Université de Liège
Faculté des Sciences
Département d'Astrophysique,
Géophysique et Océanographie

Université catholique de Louvain
Faculté des Bioingénieurs
Earth and Life Institute

Multiscale hydrodynamic modelling of the Danube Delta

Doctoral dissertation presented by

Lauranne Alaerts

in partial fulfillment of the requirements for the degree of

Doctor in Sciences
and
Doctor in Agronomical Sciences and Biological Engineering

Thesis committee:

Prof. Marilaure Grégoire (Supervisor)	ULiège
Prof. Emmanuel Hanert (Supervisor)	UCLouvain
Dr. Luc Vandenbulcke	ULiège
Dr. Olivier Gourgue	Royal Belgian Institute of Natural Sciences
Dr. Christian Ferrarin	Institute of Marine Sciences of the National Research Concil of Italy
Dr. Jonathan Lambrechts (Secretary)	UCLouvain
Prof. Xavier Fettweis (President)	ULiège

Liège, December 2025

You cannot get through a single day
without having an impact on the world around you.
What you do makes a difference, and you have to decide
what kind of difference you want to make.

Jane Goodall

Abstract

Floodplains are a key component of deltaic systems, influencing hydrodynamics, ecosystem functioning, and local socio-economic activities. Situated at the interface between the Danube River and the Black Sea, the Danube Delta forms a complex mosaic of channels, lakes, and floodplains. Despite its key role as a transition region—that filters nutrients, buffers floods, supports biodiversity, and sustains local livelihoods and economic activities—the Danube Delta remains understudied. In this thesis, we use the 2D version of the multiscale hydrodynamic model SLIM to evaluate the influence of floodplains on the hydrodynamics of the Danube Delta. We first examine the role of mesh configuration in such braided river–floodplain environments and propose hybrid curvilinear–unstructured meshes as the best compromise between accuracy and computational efficiency. We then present a first comprehensive, high-resolution, easily accessible bathymetric dataset for the three main branches of the Danube Delta, filling a key gap in available data for hydrodynamic modeling in the region. Finally, we demonstrate that including floodplains in deltaic hydrodynamic models improves hydrodynamic representation and offers alternative pathways for water flows. In the Danube Delta, we estimate that the proportion of the upstream discharge reaching the sea through routes other than the six main river mouths ranges from 10.0±4.1% (2024) to 10.8±4.8% (2021). This thesis highlights the essential role of floodplains in deltaic environments and represents an important step toward a more realistic representation of the Danube–Black Sea continuum.

Résumé

Les plaines inondables sont des composantes clés des systèmes deltaïques, influençant l'hydrodynamique, le fonctionnement des écosystèmes et les activités socio-économiques locales. Situé à l'interface entre le Danube et la mer Noire, le delta du Danube forme une mosaïque complexe de canaux, de lacs et de plaines inondables. En dépit de son rôle essentiel de région de transition—filtrant les nutriments, atténuant les crues, soutenant la biodiversité et les activités économiques locales—le delta du Danube demeure encore sous-étudié. Dans cette thèse, nous utilisons la version 2D du modèle hydrodynamique multi-échelle SLIM pour évaluer l'influence des plaines inondables sur l'hydrodynamique du delta du Danube. Nous examinons d'abord l'impact de différentes configurations de maillages dans des environnements fluvio-deltaïques composés de rivières en tresses et des plaines inondables, et proposons des maillages hybrides curvilinéaires–non structurés comme le meilleur compromis entre précision et efficacité de calcul. Nous présentons ensuite un premier jeu de données bathymétriques complet, facile d'accès et à haute résolution, couvrant les trois branches principales du delta, comblant ainsi une lacune majeure dans les données disponibles pour la modélisation hydrodynamique de la région. Enfin, nous démontrons que l'inclusion des plaines inondables dans les modèles hydrodynamiques améliore la représentation de la dynamique fluviale et ouvre des voies d'écoulement d'eau alternatives. Dans le delta du Danube, nous estimons que la proportion d'eau atteignant la mer par d'autres voies que les six embouchures principales varie entre 10.0±4.1% (2024) et 10.8±4.8% (2021). Cette thèse souligne ainsi le rôle essentiel des plaines inondables dans les environnements deltaïques et constitue une étape importante vers une représentation plus réaliste du continuum entre le Danube et la mer Noire.

Acknowledgements / Remerciements

On dit souvent qu'il faut un village pour élever un enfant. Au cours de ces quatre années de doctorat je me suis rendue compte que c'était aussi le cas pour écrire une thèse. A la fin de ce long parcours, il me semble donc naturel de remercier toutes les personnes qui ont rendu ce travail possible.

Mes premier remerciements vont à Dieu, qui est Seigneur et donne la vie, pour l'amour et la présence constante qui m'ont permis de tenir jusqu'au bout de cette thèse.

Je tiens ensuite à remercier mes promoteurices de thèse, Emmanuel Hanert et Marilaure Grégoire. Je pense pouvoir dire avec confiance que je n'aurais pas pu rêver meilleur duo d'encadran·te·s pour ma thèse. Merci à Emmanuel, qui m'a proposé ce sujet de thèse alors que j'étais mémorante chez lui, et sans qui je n'aurais probablement jamais fais de thèse. Merci pour ton optimisme sans failles—si on l'écoutait, j'aurais eu un set-up 3D sur tout mon domaine en un an—qui m'a permis de m'accrocher dans les moments où tout semblait se liguer contre l'obtention de résultats, pour ta disponibilité, que ce soit pour relire ce que j'écrivais ou discuter de mes résultats, et pour ta compréhension. Merci Marilaure pour ta confiance en moi qui dépassait souvent la mienne, ton écoute lors des moments plus difficiles et les opportunités d'apprendre et me dépasser, de l'organisation du colloque de Liège à la summer school au Chili en passant par le FRIA. Pour tout cela et bien plus, merci à tous les deux.

I would also like to thanks my jury members: Christian Ferrarin, Jonathan Lambrechts, Luc Vandenbulcke, Olivier Gourgue and Xavier Fettweis. After hearing the stories of several doctoral students whose thesis defenses had gone poorly, having a constructive scientific discussion in a supportive and respectful atmosphere was a relief. Thank you for all your questions, feedback and comments that really helped me bring the most out of this four-year work. A special thank you for those of you who were also (officially or not) in my thesis comity, for their

presence to the many meetings we had during the this thesis and their ongoing feedback and support.

Je ne peux pas écrire ces remerciements sans citer les collègues. Et ce qui est chouette quand on est en cotutelle c'est qu'on fais de rencontres des deux côtés. Ce qui veut aussi dire qu'on a plus de gens à remercier! Dans un premier lieu, j'aimerais remercier les collègues de Liège. En particulier les "Awesome ULg PhD students", pour les midis ensemble, cette belle tradition des anniversaires et les sorties à la découverte de Liège. Un merci particulier aux camarades de galères qui ont commencé en même temps que moi, et que j'ai eu l'occasion d'apprendre à connaitre dans l'organisation de ce fameux colloque de Liège, Basile, Cécile et Guillaume. Merci aussi aux membres de la team MAST pour cet environnement presque familial qui s'est établi entre nous. Un merci particulier à Loïc, pour les escapades au ski et à la découverte du Brabant Wallon.

J'aimerais ensuite remercier les collègues de Louvain-la-Neuve. Merci aux gens d'ELIE pour les afterworks, team buildings et soupers de Noël mémorables. On ne peut plus dire merci aux ENGEs, donc je dirai merci aux collègues de géomatique, pour les bons moments partagés au Mendel puis dans notre nouveau bâtiment de Serres. Merci en particulier à Barbara et Sacha pour le soutien, la positivité et la touche queerness bien nécessaires. Merci également à la team SLIM, les ancien·ne·s comme les nouveaux, pour les moments conviviaux lors de nos réunions hebdomadaires et pour les échanges toujours bienveillants et stimulants autour de nos différents projets. Un merci particulier à Jon et Miguel, pour toutes les fois où ils sont venus à ma rescousse lorsque j'étais dépassée par les mystères de SLIM. Merci enfin à mes camarades de bureau, ceux du C391 pour l'accueil dans ce monde du travail post-covid, et ceux du B315 où j'ai passé la majorité de ma thèse. Merci Antoine (que je n'ai pas cottoyé longtemps mais qui a réussi à nous transmettre sa passion des belles illustrations et des icones—on espère être à la hauteur du maître), Thomas (qui est au final celui qui m'a initié à SLIM, et répondu à mes nombreuses questions du début, toujours avec patience—du moins en apparence—et son humour tranquille), Colin (pour sa convivialité, sa disponibilité à aider—que ce soit pour organiser un souper de Noël/team-building ou pour essayer de comprendre les mystères de SLIM—et ses nombreuses

références que seul·e·s les vrai·e·s comprendront), et les derniers arrivant du bureau, Mattias et Théo. Enfin merci aux staffs administratifs des deux universités, qui ont répondu à mes nombreuses questions dans ce casse-tête qu'est le parcours d'une thèse en cotutelle. Un merci particulier à Jasmine, la maman d'ELIE, pour ta serviabilité et la vie que tu mets au sein de notre pôle.

Il me faut aussi maintenant remercier tous les gens en dehors du travail, qui m'ont aidé à rester seine d'esprit en me sortant la tête des triangles. Merci aux gens du MVG, aux ami·e·s du Nouvel an, à celles de la chorale, et à toutes ces autres amitiés individuelles; en particulier je pense à Insaf, Constance, Renaud. Un merci particulier à Valentin et Mathilde, pour m'avoir nourri lors de ma période de rush d'écriture. Merci aux habitants du chateau Lariguette, passés et présents. Alex, Alexis, Emeline, Henri, Lola, Matus, Manu, Ony, Rozenn, Samuel, merci d'avoir été mon lieu de refuge et de repos ces trois dernières années. Un merci particulier à Alex, pour son amour et son écoute de chaque instant; à Emeline, pour sa bonne humeur et son accueil chaleureux (et pour m'avoir fait découvrir FRIENDS); à Rozenn pour sa douceur et sa bienveillance. Merci aux gens de la paroisse de Court-St-Etienne, pour les moments de communion et de ressourcements hebdomadaires. Un merci particulier à Jean-Marc, pour toutes ces années où on a servi la messe ensemble. Enfin, merci à Riana. Je ne savais pas trop dans quelle catégorie te remercier, mais plus qu'une collègue tu es devenue une véritable amie, et un soutien au jour le jour quand nous galérions sur nos thèses respectives. Merci pour les sorties, les fous rires, les moments confidences, les coups de mains, les nombreuses activités que nous avons (aidé à) organisées... Je ne pense pas que j'aurais été aussi loin dans cette thèse si je ne t'avais pas eu comme compagne de galère. Donc pour tout ce que tu m'as apporté, merci.

Je voudrais également remercier ma famille, pour le soutien et l'amour dont vous m'avez entouré. Ce que je suis, je vous le dois. En particulier, merci papa, qui est définitivement la source de mon intérêt pour la science et donc, quelque part, responsable de cette thèse. Merci maman, pour la force d'affronter les obstacles que tu m'as transmise. Merci Simon et Johan, pour les moments de lacher prise et d'absurdité pure et simple.

Enfin, on fini en général des remerciements par son conjoint ou sa conjointe. Personnellement, j'adresserai ces remerciements finaux à Stitch et Bulle, pour la joie qu'iels montraient en me voyant rentrer, pour les moments calins et les longues discussions.

Merci à tou·te·s du fond du coeur.

Ce travail a été financé par le Fonds de la Recherche Scientifique—FNRS au moyen d'une bourse FRIA

Contents

Abstract iv

Acknowledgements / Remerciements vii

Contents xi

List of acronyms and abbreviations xiii

1 Introduction 1
- 1.1 Connecting the river to the sea: The Danube Delta 1
- 1.2 Modeling the Danube River-Delta-Black Sea continuum . . 11
- 1.3 Outline of the thesis 16
- 1.4 Supporting publications 16

2 Setting up SLIM on a braided river floodplain 19
- 2.1 Hydrodynamic model 19
- 2.2 First steps towards a coupled hydro-biogeochemical model 41

3 What mesh for a braided river? Mesh configurations impact on river and floodplain hydrodynamic using the SLIM model 47
- 3.1 Introduction 49
- 3.2 Material and methods 53
- 3.3 Results 57
- 3.4 Discussion and conclusion 69

4 An integrated high-resolution bathymetric model for the Danube Delta system 77
- 4.1 Introduction 79
- 4.2 Data and Method 81

4.3 Bathymetry product 86
4.4 Validation 89
4.5 Conclusion 95

Appendices **97**
4.A Parametrization 97

5 The Danube Delta: How do floodplains impact the Danube-Black Sea continuum? **103**
5.1 Introduction 105
5.2 Material and methods 107
5.3 Results 119
5.4 Discussion and conclusion 138

Appendices **145**
5.A Spatial validation for CLMF and LLMF simulations 145

6 Conclusions and perspectives **147**
6.1 Conclusion 147
6.2 Contribution to the model development 151
6.3 Perspectives for future works 152
6.4 Final thoughts 167

Bibliography **169**

List of acronyms and abbreviations

AFDJ	Galati Lower Danube River Administration
BS	Black Sea
CFL	Courant–Friedrichs–Lewy
CMEMS	Copernicus Marine Service
CRMSE	Centered Root Mean Squared Error
CRMSE'	Normalized Centered Root Mean Squared Error
DDNIRD	Danube Delta National Institute for Research and Development
DEM	Digital Elevation Model
DRB	Danube River Basin
DRBMP	Danube River Basin Management Plan
DSM	Digital Surface Model
DG	Discontinuous-Galerkin
FD	Finite Differences
FE	Finite Element
FV	Finite Volume
ICPDR	International Commission for the Protection of the Danube River

IDW	Inverse Distance Weighting
INHGA	Institutul Naţional de Hidrologie şi Gospodărire a Apelor
MAE	Mean Absolute Error
MAD	Median Absolute Deviation
MAR	Modèle Atmosphérique Régional
MBE	Mean Bias Error
NEMO	Nucleus for European Modelling of the Ocean
NDWI	Normalized Difference Water Index
NPZD	Nutrient-Phytoplankton-Zooplankton-Detritus
NWS	North-Western Shelf
OSM	OpenStreetMap
RMSE	Root Mean Squared Error
RRMSE	Relative Root Mean Squared Error
SAR	Synthetic Aperture Radar
SLIM	Second-generation Louvain-la-Neuve Ice-ocean Model
TNMN	Trans-National Monitoring Network
UkrSCES	Ukrainian Scientific Center of Ecology of the Sea
WD	Wetting and drying

Chapter 1

Introduction

1.1 Connecting the river to the sea: The Danube Delta

1.1.1 The Danube

The Danube River, Europe's second-longest river, flows over 2,800 kilometers from its source in Germany's Black Forest to its outlet in the Black Sea (Figure 1.1). Along its course, the Danube passes through ten countries and four European capitals. Its basin stretches across 19 countries, covering more than 800,000 km^2—approximately 10% of continental Europe—making it the most international river basin in the world (ICPDR, 2021; Eder et al., 2022; Sommerwerk et al., 2022). Humans have lived in the Danube River Basin (DRB) since the Paleolithic, and nowadays between 70 and 90 million people depend on the it for drinking water, agriculture, energy production, transport, recreation, and ecosystem services (ICPDR, 2021; Kovacs & Zavadsky, 2021; Mănoiu & Crăciun, 2021; Eder et al., 2022; Sommerwerk et al., 2022).

The size of the DRB makes it highly heterogeneous in terms of natural conditions (climate, hydrology, topography, geology, geomorphology),

river characteristics (discharge, sediment load, biogeochemistry, seasonality), as well as socioeconomic conditions (economic development, political situation, urbanization, land management plans) and cultural behavior (languages, traditions) (Schiller et al., 2010; Kovacs & Zavadsky, 2021; Sommerwerk et al., 2022; Probst & Mauser, 2023; Ionita et al., 2025). From this complexity emerges a need for international cooperation in the basin's management, which led in 1994 to the creation of the International Commission for the Protection of the Danube River (ICPDR), which now includes 14 countries and has published a Danube River Basin Management Plan (DRBMP) every six years since 2009 (ICPDR, 2021).

Figure 1.1: The Danube's course through Europe. The river is shown as a dark blue line. Countries and capitals along its path are labeled on the map. A small globe in the top right corner indicates the extent of the main map with a red rectangle.

Although international cooperation has improved basin-wide management, the Danube still faces numerous anthropogenic pressures. In the second half of the 20th century, water quality was negatively impacted by intensified agriculture, urbanization, and industrial development. These pressures altered the river's physical (e.g., temperature, sediment load), chemical (e.g., nutrient and contaminant loads), and biological (e.g., biodiversity, invasive species) characteristics (Mănoiu & Crăciun, 2021). The most recent DRBMP identifies the key pressures on the river as hydromorphological alterations, climate change,

and pollution from nutrients, organic substances, and hazardous compounds (ICPDR, 2021).

Among these, hydromorphological alterations are particularly significant. Dams, weirs, and navigation works have fragmented the river continuum, disrupted sediment transport, and reduced floodplain connectivity (ICPDR, 2021; Mănoiu & Crăciun, 2021). Since the 1970s, the Danube water regime have changed and sediment transport has declined by two-third, mainly because of dam construction (Sandu et al., 2025). The river's original floodplain area has been reduced by 70-80%, with uneven distribution of the loss as the Upper Danube is the most affected and the Danube Delta the most preserved (Eder et al., 2022; Sommerwerk et al., 2022; Frank et al., 2025).

In parallel, water quality has been a long-standing concern. In the 1960-1990s, nitrogen inputs to the basin increased fivefold, and phosphorus inputs doubled. While water quality has since then improved thanks to better wastewater treatment and agricultural management, nutrient and pollutant loads remain a concern. Between 2015 and 2018, the river received a yearly load of approximately 500,000 tonnes of total nitrogen and 31,000 tonnes of total phosphorus, mostly originating from agriculture and urban wastewater systems (ICPDR, 2021; Mănoiu & Crăciun, 2021; Hikov et al., 2023). In addition, contamination from heavy metals, persistent organic pollutants, and emerging hazardous substances—often linked to industrial activity or historic mining—remains an issue in some parts of the basin (Vîjdea et al., 2022; Hikov et al., 2023; Zessner et al., 2025).

Finally, climate change is expected to further exacerbate these challenges. Rising air and water temperatures have already been observed throughout the basin and are projected to continue increasing (ICPDR, 2019; Pekárová et al., 2023; Probst & Mauser, 2023). Precipitations regime will change, with projections for 2050-2100 suggesting that wet regions and seasons will become wetter, and dry ones drier. Although average annual discharge is expected to increase, variability and seasonality will also grow, and the likelihood and severity of extreme events such as floods and droughts is expected to increase (ICPDR, 2019; Stolz et al., 2025).

1.1.2 The Black Sea

At the end of its course, the Danube discharges into the Black Sea (Fig. 1.2). The Black Sea (BS) is a semi-enclosed basin located between Europe, Anatolia and the Caucasus, connected to the Mediterranean via the Bosporus Strait and to the Sea of Azov through the Kerch Strait. Its surface area is ~423,000 km^2, with an average depth of ~1240 m and a maximum depth reaching ~2500 m (Toderascu & Rusu, 2013; Bakhtyar et al., 2020). The BS receives important freshwater input at the surface through rivers and precipitations, and denser saline water inflow from the Mediterranean at depth, resulting in low overall salinity and a strong vertical stratification. A permanent halocline is present at depth between 100 and 200 meters, below which the waters are completely anoxic. This makes the Black Sea the largest anoxic water body on Earth, with anoxic conditions prevailing in roughly 90% of its volume (Bakan & Büyükgüngör, 2000; Toderascu & Rusu, 2013; Bologa & Bloesch, 2025). Interestingly, the deep waters also contain the largest natural reservoir of toxic hydrogen sulfide (H_2S), only separated from the surface by the oxic layer. During the peak eutrophication period of the 1970s and 1980s, the thickness of this oxic layer decreased significantly due to increased oxygen demand. The situation has since improved, mainly due to reductions in nutrient inputs from the rivers (Bakan & Büyükgüngör, 2000; Capet et al., 2016).

In terms of horizontal dynamics, circulation in the BS is primarily wind-driven, as tidal amplitudes are relatively small—–typically between 7 and 12 cm. The main feature of the BS's circulation is the Rim Current, a cyclonic flow that follows the continental slope of the central basin (Fig. 1.2). The circulation also includes two cyclonic gyres, called the western and eastern gyres, along with transient mesoscale structures such as eddies, meanders, dipoles, and filaments found on either side of the Rim Current. These features play an important role in shaping water transport and biogeochemical processes across the basin (Oguz & Besiktepe, 1999; Bakan & Büyükgüngör, 2000; Toderascu & Rusu, 2013; Sadighrad et al., 2021).

Most of the riverine input to the BS happens on the North-Western Shelf (NWS) (Fig. 1.2). This shallow continental shelf, spanning approximately 200 kilometers in width and reaching depth up to 200 m,

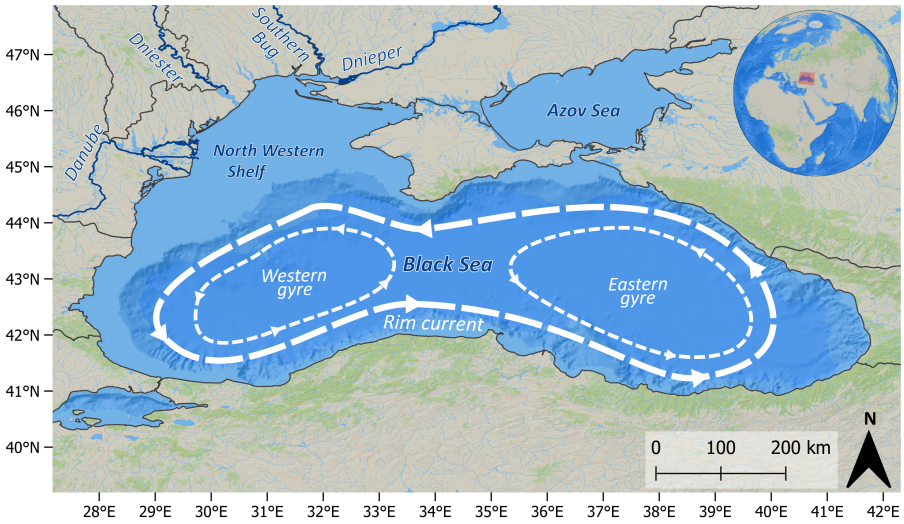

Figure 1.2: The Black Sea. General circulation patterns are illustrated with white dotted lines and arrows. The four main river contributors to the Black Sea—the Danube, Dniester, Dnieper, and Southern Bug—are shown as dark blue lines. A small globe in the top right corner indicates the extent of the main map with a red rectangle.

accounts for about 30% of the sea's surface area but only 1–2% of its total volume (Panin & Jipa, 2002). The NWS receives inputs from several large rivers—namely the Danube, Dniester, Dnieper, and Southern Bug (Fig. 1.2)—but the Danube is by far the main contributor. With an average discharge of 6000 to 6500 m^3/s, it provides almost 60% of the freshwater inflow to the Black Sea. This flow is highly seasonal, peaking in late spring (on average ~9000 m^3/s) and a minimum in autumn (on average ~4000 m^3/s) (Jaoshvili, 2022; Sommerwerk et al., 2022). Beyond freshwater, the Danube also plays a significant role in the biogeochemistry of the NWS through the large quantities of nutrients it discharges. Its nitrogen input alone is estimated to exceed the combined contributions of the Dniester and Dnieper by more than thirty-fold (Grégoire & Friedrich, 2004) and it accounts for approximately 48% of all suspended matter inputs to the Black Sea (Güttler et al., 2013). During the 1970s–1990s, high nutrient discharges from the Danube triggered widespread eutrophication and hypoxia events, leading to severe biodiversity losses in the northwestern Black Sea (ICPDR, 2021; Kovacs & Zavadsky, 2021). While the situation has improved,

and the river basin retains part of the nutrient input——reducing the load entering the sea by approximately 22% for nitrogen and 23% for phosphorus——current nutrient delivery to the sea still exceeds benchmark values from the 1960s (~2.5×10^8 kg TN and ~2×10^7 kg TP per year), showing that there is still room for improvement (ICPDR, 2021; Kovacs & Zavadsky, 2021).

Once discharged into the sea, the nutrient-rich Danube plume can influence the Black Sea biogeochemistry hundreds of kilometers from the delta, depending on shelf circulation (Miladinova et al., 2020; Ferrarin et al., 2025). The plume's dispersion is primarily governed by wind patterns and the Rim Current, the latter typically acting as a barrier between the deep BS waters from the shallower NWS. While the plume usually flows southwestward along the coast, seasonal and interannual variability can produce a range of propagation patterns (Kubryakov et al., 2018; Miladinova et al., 2020). For example, Kubryakov et al. (2018) identified four dominant summer propagation patterns: (i) western propagation, that occurs in years with prevailing north-eastern winds, where an along-shore southward current push the plume along the coast; (ii) southeastern propagation, where winds blow to the south-southeast, leading a substantial portion of the plume eastward, where it interacts with mesoscale eddies along the shelf break and can reach the central western BS; (iii) northern propagation, where anticyclonic winds form an eddy that retains the plume in the northern NWS for a considerable part of the summer; and (iv) eastern propagation, driven by an anticyclonic wind system extending over the entire western Black Sea that pushes the plume eastward toward the Rim Current and associated eddies.

In addition to these natural dynamics, the NWS is subject to multiple anthropogenic pressures. Eutrophication had major impacts in the past, with the northern NWS experiencing benthic hypoxia during the peak nutrient loads to the sea in the 1970s-1980s. It remains a key concern today, as benthic communities still show incomplete recovery from the biodiversity losses, and seasonal hypoxia events persist in some areas (Chevalier et al., 2024; Bologa & Bloesch, 2025). At the same time, reduced sediment supply——mainly due to upstream damming——leads to coastal erosion, especially in deltaic and nearshore environments (Sandu et al., 2025). Other ongoing pressures

on the NWS include climate change, intensive navigation, dredging, tourism, fisheries, pollution, land use changes, and the spread of invasive species. More recently, geopolitical instability with Russia's invasion of Ukraine has introduced additional stressors, linked to infrastructure damage and an increased military presence in the region (Bologa & Bloesch, 2025). The ongoing war has had both direct and indirect impacts on the NWS ecosystems. Direct effects include physical damage from weapons and explosions, shockwaves, intense noise, sonar use, as well as flooding and fires. Indirect effects arise from oil spills due to sinking ships and aircraft, toxic and heavy metal contamination from ammunition, and the release of untreated sewage and pathogens following the destruction of wastewater facilities. Together, these disturbances degrade water quality and threaten ecosystem services across the region (Kharchenko, 2023; Safranov et al., 2024; Kvach et al., 2025).

1.1.3 At the interface: the Danube Delta

At the interface between the Danube River and the Black Sea lies the Danube Delta (Fig. 1.3). The delta begins at Ceatal Izmail, the site of the first bifurcation of the Danube, where the river divides into the Tulcea and Chilia branches. The Chilia branch, which serves as a border between Ukraine and Romania, is the longest (117 km) and least disturbed of the three main branches of the delta. About 20 km before reaching the sea, the Chilia branch forms a smaller secondary delta (Panin et al., 2016). Approximately 17 km east of Ceatal Izmail, the Tulcea branch splits again at Ceatal Sfântu Gheorghe into the Sulina and Sfântu Gheorghe (Saint George) branches. The Sulina branch is the shortest (71.7 km, including 8 km of marine jetties) and the most transformed of the branches, as its course was straightened and deepened between 1868 and 1992 to facilitate navigation. The Sfântu Gheorghe branch, 108.8 km in length, was also altered during a "cut-off" program in the 1980s–1990s, which shortened its course by 31 km (Panin et al., 2016). Water levels and discharges in the delta fluctuate seasonally and interannually, with peak levels typically observed in late spring (April–June) and lower levels in autumn (September–November) (Güttler et al., 2013) (Fig. 1.4).

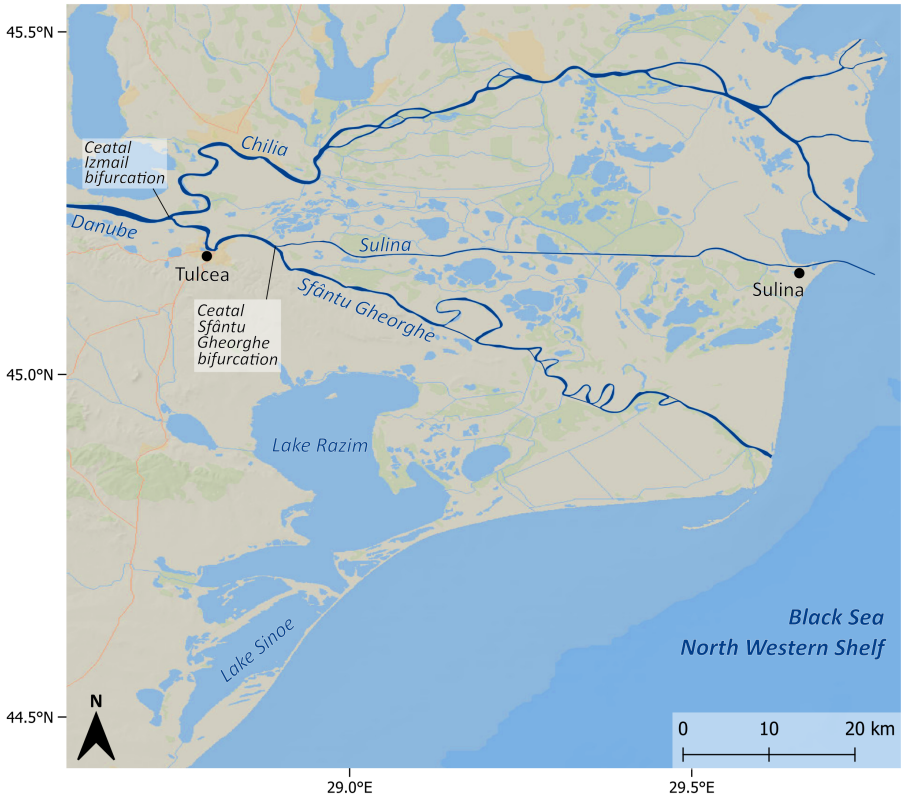

Figure 1.3: The Danube Delta. The Danube and its three main branches are shown in dark blue. The two main cities in the area—Tulcea and Sulina—are indicated on the map, as well as the two main bifurcations—Ceatal Izmail and Ceatal Sfântu Gheorghe—of the Danube

The exact Danube Delta boundaries are not fixed in the literature, and vary depending on wether Ukrainian territories, adjacent lakes, or lagoons (geologically and ecologically connected to the delta) are included. As such, reported surface areas range from approximately 4000 to 8800 km^2 (Sommerwerk et al., 2022). Regardless of delineation, the delta is predominantly flat, with more than 90% of its surface lying below 2 meters above sea level (Driga, 2008). The Danube Delta is composed of a mosaic of interconnected ecosystems, including semi-natural wetlands, marshes, lakes, reed beds, grasslands, sand dunes, forests, and human-modified landscapes such as agricultural lands, aquaculture zones, and scattered settlements. A complex network of

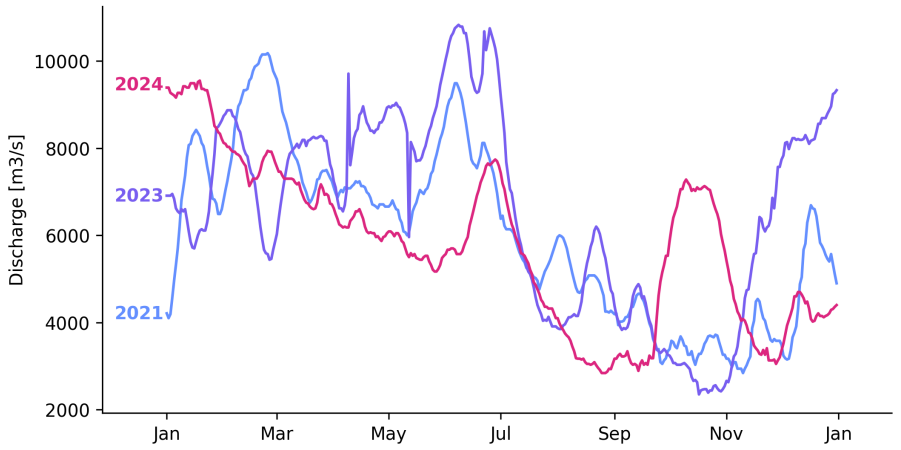

Figure 1.4: Discharge evolution at Isaccea, upstream of the Danube Delta, for years 2021, 2023 and 2024. Data collected by the Galati Lower Danube River Administration (AFDJ).

channels and backwaters connects over 300 to 500 lakes. These shallow lakes (average depths of 1.7 to 3.9 meters) vary greatly in size (0.7 to 43 km^2) and can be seasonally or permanently connected by channels or through dense reed vegetation (Güttler et al., 2013; Poncos et al., 2013; Cioacă et al., 2018). In total, the delta contains over 3,000 km^2 of river-connected wetlands, making it the largest nearly undisturbed wetland in Europe. Approximately half of this area is flooded year-round, while the remainder experiences seasonal inundation.

The Danube Delta plays a central buffering role in regulating exchanges along the Danube–Black Sea continuum. It helps attenuate discharges to the sea (Driga, 2008), processes and retains nutrients (Suciu et al., 2002; Friedrich et al., 2003), and captures sediments (Cioacă et al., 2018). In addition, the delta provides other ecosystem services, including drinking water, food supply, flood protection, and opportunities for agriculture, aquaculture, navigation, fishing, and tourism. It is also a known hotspot for biodiversity: it is famous for its abundant birdlife, with more than 310 important bird species, and it hosts countless invertebrates, valuable plant communities, and a diverse range of fishes and mammals (Lupu et al., 2022). Studies show that more than half of the 137 fish species recorded in the broader Danube-NWS region depend on the delta at some point in their life cycle (Bănăduc

et al., 2023). This ecological value has led to multiple conservation measures. Since 1990, large portions of the delta, its floodplains, the Danube River, and the Razim-Sinoe lagoon complex have been protected as the Danube Delta Biosphere Reserve. The site has been designated a Ramsar Wetland of International Importance (since 1991) and a UNESCO World Heritage Site (since 1998). In total, an area of approximately 6265 km^2 is now under protection (Güttler et al., 2013; Sommerwerk et al., 2022; Nichersu et al., 2025).

Although most of the Danube Delta is now protected, its ecosystems had already been heavily altered by human interventions throughout the 20th century. The modification of the course of the Danube's branches led to a significant redistribution of water among them. In 1902, 72% of the Danube's discharge was flowing into the Chilia branch, while the Sulina and Sfântu Gheorghe branches received 9% and 19%, respectively. By 2003, these proportions had shifted to 52, 20 and 28% (Panin et al., 2016) and in 2015, to 45, 34 and 21 (Bloesch et al., 2025). More recent data from 2021 and 2024, provided by the Institutul Naţional de Hidrologie şi Gospodărire a Apelor (INHGA) indicate a continuing shift, with roughly 45% of discharge through the Chilia branch, ~20% through Sulina, and 30–35% through Sfântu Gheorghe. Additional changes to delta hydromorphology include the construction of 8-km-long jetties at the Sulina outlet, which altered sediment transport dynamics and contributes to coastal erosion (Panin & Jipa, 2002). Beyond the main branches, more than 300 km of canals were dug throughout the delta to facilitate inland navigation, and approximately 30% of the deltaic area was dammed or polderized for fish farming, reed harvesting, agriculture, or forestry. These interventions have disrupted natural water circulation and led to extensive wetland fragmentation (Driga, 2008; Cioacă et al., 2018). Restoration efforts have been underway since 1994, but progress remains limited and many challenges persist (Cioacă et al., 2018). Today, despite its protected status, the Danube Delta remains vulnerable. Long-standing anthropogenic modifications are now being aggravated by the large-scale pressures——climate change, erosion, pollution——that affect the broader Danube-Black Sea system and do not stop at the delta's borders (Nichersu et al., 2025).

1.2 Modeling the Danube River-Delta-Black Sea continuum

1.2.1 Existing modeling efforts

Hydrodynamic modeling offers a powerful tool to investigate the functioning of aquatic systems, their interactions, and their responses to various natural and anthropogenic pressures. Given the ecological complexity and socioeconomic importance of the Danube River–Danube Delta–Black Sea continuum, such models are particularly valuable for understanding and managing this interconnected environment. While the river, delta, and sea have each been extensively studied through modeling, they are still most often treated separately. This separation reflects both practical challenges (such as computational cost or model architecture) as well as disciplinary divides. As one of Europe's major rivers, the Danube has been the subject of numerous modeling efforts in recent years. These include a wide range of applications, spanning flood risk analysis, sediment dynamics, navigability, and water quality management. Models vary in dimensionality (box models, 1D, 2D, 3D) and in spatial scope, depending on the objective and region of focus (Glock et al., 2019; Bezak et al., 2021; Liptay & Gauzer, 2021; Savu & Drobot, 2021; Gogoaşe-Nistoran et al., 2022). Similarly, various hydrodynamic models have been applied to the Danube Delta, targeting processes such as flooding, sediment transport, or restoration planning (Jugaru Tiron et al., 2009; Gogoase et al., 2011; Popescu et al., 2015; Tudor et al., 2022). However, the quasi totality of these studies focus on limited areas of the delta, and there is still a lack of high-resolution (10-100 m), system-wide models that incorporate the full floodplain network and dynamic water redistribution within the delta.

The Black Sea also has a long history of hydrodynamic modeling, with studies addressing among other things circulation, stratification, biogeochemistry, and hypoxia (Grégoire et al., 1997; Beckers et al., 2002; Grégoire & Friedrich, 2004; Enriquez et al., 2005; Capet et al., 2013; Bajo et al., 2014; Vandenbulcke & Barth, 2015; Dorofeyev & Sukhikh, 2017; Bouzaiene et al., 2021; Causio et al., 2021; Ciliberti et al., 2021). Yet, in most of these sea models, the Danube's contribution is poorly represented. River inputs are often simplified, for example by using seasonal climatological means or fixed values in time, or by reducing

them spatially to a single-point discharge. In most cases, the delta is omitted entirely. In some of the most recent studies, effort to better represent the Danube discharge has been made by splitting the observation or climatological means upstream of the delta between branches through percentages found in the literature (Bajo et al., 2014; Causio et al., 2021; Ciliberti et al., 2021). However, such approaches must be done carefully, especially in a context of changing discharge repartition, and they might also completely miss small time-scale events, such as rising water level induced by storms, that have a definite impact on river–sea exchanges. The poor representation of river-sea exchanges has been identified as a key source of uncertainty in coastal models globally (Breitburg et al., 2018; Lewis et al., 2019), and specific modeling studies in the Black Sea have pointed the poor representation of the Danube as a possible explanation for observed discrepancies with ground-truth observations (Capet et al., 2013; Bouzaiene et al., 2021).

In light of these limitations, there is a clear need for integrated models that resolve the delta not just as a boundary, but as an active zone mediating river-sea interactions. A recent effort by Ferrarin et al. (2025) has explored this continuum using a 3D setup and gave good insight on the river-sea interactions, but the study did not include the floodplain system of the delta. This thesis aims to address this gap by investigating the hydrodynamic role of those floodplains in the Danube Delta. Specifically, it tackles the following question: *What are the impacts of the Danube Delta and its floodplains on the hydrodynamics of the Danube–Black Sea continuum?*

1.2.2 Challenges in modeling the Danube-Black Sea continuum

Modeling land–sea continuum implies representing processes across a wide range of spatial and temporal scales. In particular, accurately simulating riverine and coastal hydrodynamics demands high spatial resolution to capture small-scale features such as channel networks, shoreline complexity, and complex bathymetry. However, applying such fine resolution to large domains comes with high computational cost. For instance, the Copernicus Marine Service (CMEMS) operational model for the Black Sea is based on the structured grid model Nucleus for European Modelling of the Ocean (NEMO) and has a horizontal reso-

lution of about 3 km (Ciliberti et al., 2021), which is insufficient to resolve processes in narrow river branches or complex coastal zones. Two main strategies exist to address this challenge. The first one is the use of structured nested grids, in which high-resolution grids are embedded within coarser ones (Debreu et al., 2012; Marta-Almeida et al., 2013). While effective in many contexts, nested grids lack flexibility and become increasingly difficult to apply in domains where relevant spatial scales vary from a few meters to several kilometers (Hasan et al., 2016; Haidvogel et al., 2017; Nudds et al., 2020). An alternative is the use of unstructured meshes, which allow for spatially varying resolution, with small elements in rivers and near the coast and larger elements offshore (de Brye et al., 2010; Y. J. Zhang et al., 2023). Though unstructured mesh models have historically been considered too computationally expensive, recent advances in computational power——particularly through GPU acceleration——have made them increasingly viable and competitive (Dong et al., 2025; De Le Court et al., n.d.)

In addition to spatial resolution, vertical structure is another key consideration when choosing a hydrodynamic model. As previously mentioned, the Black Sea is a highly stratified basin, with a strong permanent halocline between 100 and 200 meters, separating oxygenated surface waters from anoxic deep layers (Bologa & Bloesch, 2025). Accurately representing this stratification typically requires three-dimensional (3D) baroclinic models, which resolve density variations driven by temperature and salinity and can simulate internal waves, stratification, and density-driven flows (Cushman-Roisin & Beckers, 2011). However, in shallow and well-mixed environments such as the Danube River and Delta, a 2D barotropic model is generally sufficient (Brinkman et al., 2002). In such models, a vertically homogeneous water column is assumed and the flow is driven solely by external forces——such as river inflow, wind and tides——and by surface elevation gradients. Two-dimensional barotropic typically solve the depth-averaged shallow water equations, which are derived from the Navier–Stokes equations under the hydrostatic and incompressibility assumptions, i.e., assuming vertical accelerations are negligible and vertical pressure gradients are balanced by gravity. This approach is valid when horizontal scales of motion greatly exceed vertical scales (Cushman-Roisin & Beckers, 2011).

In this thesis, we employed the two-dimensional barotropic module of the latest version of the Second-generation Louvain-la-Neuve Ice-ocean Model (SLIM). SLIM is a discontinuous Galerkin finite element model based on unstructured meshes, designed for high-resolution simulations over complex domains. It has already been applied in several land–sea continuum studies (Gourgue et al., 2009; de Brye et al., 2010; Gourgue et al., 2013; Le Bars et al., 2016; Sampurno, Vallaeys, et al., 2022), although not yet in its latest version. SLIM 4 introduces support for GPU-based computations, enabling finer resolutions and longer simulations at significantly reduced computational times (De Le Court et al., n.d.). While SLIM also includes a 3D baroclinic version (Alaerts et al., 2022; Ishimwe et al., 2025), the choice of a 2D barotropic approach was motivated by the physical characteristics of the domain. In both the Danube River and Delta, water columns are shallow and largely vertically homogeneous, rendering 3D effects negligible in this context. Additionally, the 3D module of SLIM 4 is still under development and currently lacks support for wetting and drying processes, which are necessary when modeling floodplains. Indeed, one of the main challenges in hydrodynamic models of floodplains is the representation of flooding and drying dynamics. As water depth approaches zero, the shallow water equations become numerically unstable. This issue is commonly addressed through wetting and drying algorithms, which enable a stable transition between wet and dry states (Gourgue et al., 2009; Medeiros & Hagen, 2013). During this thesis, a new version of SLIM's wetting and drying algorithm was developed and implemented in the 2D version of the model, making this work the first to describe and use it. Details on the algorithm and its implementation can be found in Chapter 2.

Finally, every model needs data, whether for calibration, validation, or boundary conditions. Despite the ecological and geopolitical importance of the Danube Delta, open-access easy-to-use data remain scarce. This data scarcity stems from a combination of logistical and financial challenges, commercial restrictions, and the inherent complexity of the deltaic environment. A simple but telling example is the absence of discharge data at the mouths of the three main branches—-a gap that partly motivated this study. Another major limitation, which became one of the main focus of this thesis, was the absence of

an integrated, easily accessible bathymetry dataset for the three river branches of delta. Similarly, finding an easy-to-use product to validate flooding extents proved difficult, mainly due to the nature of the vegetation which interfere with satellite-based flood detection methods. This scarcity of data poses a significant challenge for modeling efforts, affecting both parameter calibration and model validation (Camacho et al., 2014). Nevertheless, in this thesis, the model was parameterized to the best of our ability, using the most reliable data available and literature-informed assumptions. It was then evaluated against available in situ and remotely sensed observations. Despite these limitations, the development of a physics-based hydrodynamic model remains valuable. As the popular saying goes "all models are wrong, but some are useful". In environments where direct measurements are sparse, numerical models can help bridge data gaps by offering estimations of ground-truth reality. They can also serve as tools to assess the plausibility of unobserved or unobservable dynamics, inform monitoring strategies, and support decision-making under uncertainty. This thesis aims to be one of many building blocks in the ongoing effort to understand the functioning of the Danube Delta.

All this leads us to refine the aforementioned research question into four more specific ones:

1. *How do different mesh-building strategies affect the representation of river–floodplain interactions?* ***(Chapter 3)***

2. *How can heterogeneous bathymetric datasets be combined to produce a coherent description of the braided river bed in the Danube Delta?* ***(Chapter 4)***

3. *How does the inclusion of floodplains influence the modeling of the hydrodynamics within the Danube Delta?* ***(Chapter 5)***

4. *How do floodplains modify the fluxes of water from the Danube to the Black Sea?* ***(Chapter 5)***

1.3 Outline of the thesis

This thesis follows the path taken to address the research questions outlined above. In Chapter 2, we first present the current version of SLIM, the hydrodynamic model used in this study, along with the necessary developments for this thesis to which I contributed. Chapter 3 discusses mesh design in complex braided river systems such as the Danube Delta, and its impact on flood simulations. Chapter 4 focuses on the development of a bathymetry product for the three main branches of the delta, highlighting the major gaps in readily available data for this region. Chapter 5 presents the full land–sea continuum model, and evaluates the influence of the Danube Delta and its flood plains on the Danube–Black Sea system under different hydrological scenarios. Finally, Chapter 6 summarizes the main findings and outlines perspectives for future research, including potential model improvements and discussions on data availability and delta management.

1.4 Supporting publications

Alaerts, L., Dobbelaere, T., Gravinese, P. M., & Hanert, E. (2022). Climate change will fragment Florida stone crab communities. *Frontiers in Marine Science - Sec. Global Change and the Future Ocean*, 9. 10.3389/fmars.2022.839767.

Alaerts, L., Lambrechts, J., Randresihaja, N. R., Vandenbulcke, L., Gourgue, O., Hanert, E., & Grégoire, M. (2025). An integrated high-resolution bathymetric model for the Danube Delta system. *Earth System Science Data*, 17(7), 3125–3140. 10.5194/essd-17-3125-2025.

Lecart, M., Dobbelaere, T., **Alaerts, L.**, Randresihaja, N. R., Mohammed, A. V., Vethamony, P., & Hanert, E. (2024). Land reclamation and its consequences: A 40-year analysis of water residence time in Doha Bay, Qatar. *PLOS ONE*, 19(1), e0296715. 10.1371/journal.pone.0296715.

Dobbelaere, T., Dekens, A., Saint-Amand, A., **Alaerts, L.**, Holstein, D. M., & Hanert, E. (2024). Hurricanes enhance coral connectivity but also superspread coral diseases. *Global Change Biology*, 30(6), e17382. 10.1111/gcb.17382.

Randresihaja, N. R., Gourgue, O., **Alaerts, L.**, Fettweis, X., Lambrechts, J., De Le Court, M., Grégoire, M., & Hanert, E. (2025). How atmospheric forcing resolution impacts storm surge model results: Insights from Xaver Storm in the North Sea-Scheldt Estuary continuum. *SSRN Preprint*. 10.2139/ssrn.5333301.

Grégoire M., Vandenbulcke L., Chevalier S., Choblet M., Drozd I., Grailet J.-F., Ivanov E., Macé L., Verezemskaya P., Yu H., **Alaerts L.**, Randresihaja N. R., Mangeleer V., Maertens de Noordhout G., Capet A., Meulders C., Mouchet A., Munhoven G., Soetaert K. (2025). The BiogeochemicAl Model for Hypoxic and Benthic Influenced areas: BAMHBI v1.0. *EGUsphere preprint*. 10.5194/egusphere-2025-4196

Chapter 2

Setting up SLIM on a braided river floodplain

In this chapter, we present the Second-generation Louvain-la-Neuve Ice-ocean Model (SLIM) model as used in this thesis, along with the developments to which I contributed. Specifically, I describe the mesh generation and bathymetry interpolation procedures designed for braided river environments, and the latest version of the wetting and drying algorithm implemented in SLIM. Finally, I introduce a simple Nutrient-Phytoplankton-Zooplankton-Detritus (NPZD) model developed as a first step toward a coupled hydro-biogeochemical model of the Danube–Black Sea continuum.

2.1 Hydrodynamic model

2.1.1 SLIM and SLIM2D

SLIM is an unstructured hydrodynamic model that uses a Discontinuous-Galerkin (DG) Finite Element (FE) method. The

model is available in one-dimensional (1D, section-averaged), two-dimensional (2D, depth-averaged), and three-dimensional (3D) configurations. Each module offers specific advantages depending on the application context, and all have been successfully applied in various environments worldwide. SLIM1D can be used for well mixed river systems or networks where the flow is mainly unidirectional (Draoui et al., 2020; Patil, 2025). SLIM2D is suited for well-mixed shallow-water environments where vertical variations of the hydrodynamics are negligible. It includes a wetting and drying algorithm that enables simulation over intertidal zones, tidal marshes, or floodplains. This 2D version of the model has been applied extensively in coastal (Saint-Amand et al., 2022; Dobbelaere, Dekens, et al., 2024; Lecart et al., 2024; Scherpereel et al., 2025) and riverine systems (Gourgue et al., 2009; Le, Gratiot, et al., 2020; Sampurno, Ardianto, & Hanert, 2022; Randresihaja et al., 2025). SLIM3D solves the hydrostatic three-dimensional baroclinic ocean circulation equations and is applicable in settings where vertical stratification plays a significant role in the dynamics. It has been applied to coastal waters (Alaerts et al., 2022), lakes (Delandmeter et al., 2018; Duquesne et al., 2021), and river estuaries (Vallaeys et al., 2018, 2021). Both SLIM2D and SLIM3D support coupling with Lagrangian particle tracking and Eulerian transport modules (Duquesne et al., 2021; Alaerts et al., 2022; Saint-Amand et al., 2022). Recent development have enabled the latest version of SLIM to run on GPUs, allowing for longer, larger and higher-resolution simulations (De Le Court et al., n.d.).

In this thesis, we employ the 2D version of SLIM, as both the river and the delta are shallow, well-mixed systems, which allows for 2D-depth averaged representation. Additionally, the wetting and drying algorithm enables the inclusion of floodplains in the simulation domain.

SLIM2D solves the barotropic shallow water equations:

$$\frac{\partial \eta}{\partial t} + \nabla_h \cdot (H\boldsymbol{u}) = 0, \tag{2.1}$$

$$\begin{aligned}\frac{\partial (H\boldsymbol{u})}{\partial t} + \nabla_h \cdot \frac{H\boldsymbol{u}H\boldsymbol{u}}{H} + f\,\boldsymbol{e}_z \times H\boldsymbol{u} = -gH\nabla_h \eta + \frac{\boldsymbol{\tau}}{\rho} \\ + \nabla_h \cdot \left(\kappa H \nabla_h \frac{H\boldsymbol{u}}{H}\right) - \frac{n^2 g |H\boldsymbol{u}|}{H^{7/3}} H\boldsymbol{u} + a_n (H\boldsymbol{u}_{\text{ext}} - H\boldsymbol{u}),\end{aligned} \tag{2.2}$$

where η [m] is the water surface elevation, $H = \eta + h$ [m] (Fig. 2.4) is the water column height, h [m] is the bathymetry, $\boldsymbol{u} = (u, v)$ [m s^{-1}] is the depth-averaged horizontal velocity, f [s^{-1}] is the Coriolis parameter, $\boldsymbol{\tau}$ [kg m^{-1} s^{-2}] is the wind stress, ρ [kg m^{-3}] is the water density, κ [m^2 s^{-1}] is the horizontal eddy viscosity, g [m s^{-2}] is the gravity acceleration, a_n [s^{-1}] is the nudging coefficient and $\boldsymbol{u}_{ext}$ [m s^{-1}] is the depth-averaged velocity from a larger-scale 3D baroclinic model used for flow relaxation.

SLIM's eddy viscosity is calculated using the Smagorinsky (1963)'s model, which accounts for the local grid size and strain rate:

$$\kappa = C_S^2 A \|\mathbf{S}\| = C_S^2 A \sqrt{2\left(\frac{\partial u}{\partial x}\right)^2 + 2\left(\frac{\partial v}{\partial y}\right)^2 + \left(\frac{\partial u}{\partial y} + \frac{\partial v}{\partial x}\right)^2}, \tag{2.3}$$

where C_S is the dimensionless Smagorinsky coefficient, usually set to $C_S = 0.1$, A [m^2] is the area of the triangular element and $\|\mathbf{S}\|$ [s^{-1}] is the norm of the strain-rate tensor. The wind stress is expressed as

$$\boldsymbol{\tau} = \rho_{air} C_w |\mathbf{u_w}| \mathbf{u_w}, \tag{2.4}$$

where ρ_{air} [kg m^{-3}] is the air density, C_w [m s^{-1}] is wind drag coefficient computed using the Smith and Banke formulation(Smith & Banke, 1975; Cushman-Roisin & Beckers, 2011) and $\mathbf{u_w}$ is the horizontal wind velocity 10 m above sea level. The bottom friction formulation is based on Chezy-Manning-Strickler's formulation for 2D shallow water equations, which defines the bottom friction γ as

$$\gamma = \frac{n^2 g |H\boldsymbol{u}|}{H^{7/3}}, \tag{2.5}$$

where n [s m$^{-1/3}$] is the Manning coefficient (Hervouet, 2007). Finally, the term $a_n(H\boldsymbol{u}_{ext} - H\boldsymbol{u})$ describes the way SLIM's velocity is relaxed towards the depth-averaged velocity of a larger-scale baroclinic model. The aim of this relaxation is to correct SLIM's barotropic velocity in deep area, where the 3D baroclinic effects are no longer negligi-

ble. Consequently, the relaxation coefficient a_n usually increases with bathymetry.

2.1.2 Meshing in braided river environment

As stated above, SLIM solves the equations on an unstructured mesh. The common practice among SLIM-users is to create such mesh by using the state-of-the-art mesh-generation software GMSH (Geuzaine & Remacle, 2009) through the Python library seamsh, which enables the construction of unstructured meshes whose resolution can vary according to different criteria, such as the distance to specific locations or the bathymetric gradient. In river models, several studies have shown the advantages of using hybrid meshes, that combine curvilinear structured meshes in unidirectional river segments with unstructured meshes in connection zones and floodplains (Horritt et al., 2006; Kim et al., 2014; Bomers et al., 2019; Bilgili et al., 2023). Such meshes had never been used in SLIM until now, and I contributed to the development of a method to generate them using GMSH. The meshes generated through this approach are a combination of structured curvilinear meshes composed of triangles elongated along the river within unidirectional segments, coupled with fully unstructured triangular meshes in the connection zones between those segments and outside the river.

The meshing process goes as follows. In a complex floodplain-river-sea environment, the river is first separated from the rest of the domain and meshed independently. The different steps of the mesh generation process for a braided river are illustrated in Fig. 2.1. First, the river is divided into unidirectional segments and connection zones (i.e. zones where the river segments splits or merge, Fig. 2.1.a.). To do so, the river is cut at a distance L [m] from the points where the river segments intersect, with L being the target length of the elongated edge of the triangles. The connection zones are meshed using triangular elements with a targeted resolution of l [m] (Fig. 2.1.b.). Each segment is then subdivided into quadrilaterals by cutting both riverbanks at L-meter intervals. To optimize this division of the segments, we create the following quality metric for each quadrilateral:

$$Q = 10(|\mathbf{b}| - L)^4 + (\mathbf{b} \cdot \hat{\mathbf{a}})^4, \tag{2.6}$$

where **b** is a vector following one of the quadrilateral edges along the riverbank, whose target length is L, and **a** is a vector following the edge of the same quadrilateral that serves as a cross section of the river, with $\hat{\mathbf{a}}$ the unit vector along that direction (Fig. 2.1.c.). Each quadrilateral therefore has two possible edges that can serve as a and two that can serve as b, leading to four possible combinations ($a_1 - b_1$, $a_1 - b_2$, $a_2 - b_1$, $a_2 - b_2$) per quadrilateral. The quality metric Q is computed for each of those combinations, and the sum of Q is minimized for each segment. The aim of this optimization is to have quadrilaterals where **b** is as close as possible to the desired length L, and where the angle between **a** and **b** is as close as possible to 90°. This way, we avoid having elements that are too small in curved river segments or near connections. The weighting factor (10) and the exponent (4) were chosen empirically through trial and error to provide a good balance between both terms of the metric. A brief sensitivity analysis (not shown) indicated that the exact values of these parameters had little influence on the final mesh structure.

To ensure smooth transitions between unidirectional segments and transition zones, the first and last quadrilaterals in each segment are further subdivided into smaller quadrilaterals using a geometric progression of their edge length along the riverbank (Fig. 2.1.d.). This avoids abrupt jumps in resolution, which would otherwise be problematic once the floodplains are included. The segments are then reassembled with the connection zones, and quadrilaterals in the segments are further subdivided into elongated triangles aligned with the flow to match the triangular elements in the connection zones (Fig. 2.1.e.).

Once the river mesh is optimized and assembled, it serves as the backbone for the mesh on the entire the domain. Unstructured meshes are used to represent the surrounding floodplains and the sea, with element sizes matching those at the river mouths and along the riverbanks. The use of unstructured mesh outside of the river also allows the use of coarser elements where fine resolution is less critical, such as in the outer floodplains or offshore in the sea, reducing computational cost while maintaining fine resolution where it matters most. The benefits of the approach developed in this section are further discussed in Chapter 3.

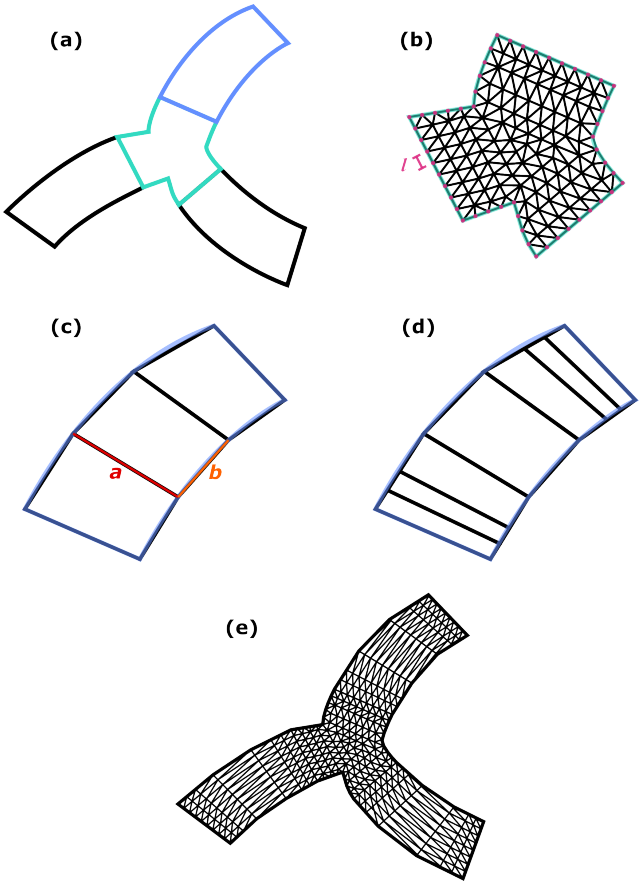

Figure 2.1: Creation of the mesh in the river. **(a)** The braided river is divided into unidirectional segments (black and blue) and connection zones (turquoise). **(b)** Connection zones are meshed with triangular elements at a resolution of approximately l m. **(c)** Segments are divided into quadrilaterals, where parameters a and b are optimized across each segment to ensure that b edges are as close as possible to the target length L, and that a and b remain as perpendicular as possible (Eq. 2.6). **(d)** The first and last quadrilaterals of each segment are subdivided using a geometric progression of their riverbank edge length. **(e)** Segments and connection zones are reassembled. Each quadrilateral is further divided into elongated triangles aligned with the river flow to match the triangular elements in the connection zones.

2.1.3 Bathymetry interpolation

Another key aspect of hydrodynamic modeling is the correct interpolation of the bathymetry on the mesh. Interpolation of bathymetry in rivers requires specific consideration due to the inherent anisotropy of the data (Merwade et al., 2006). For this reason, we used two distinct interpolation strategies in this thesis, one for the river and one in the surrounding areas. I participated in the development of a two-step bathymetry interpolation process tailored for braided rivers, using the hybrid mesh described above as a framework. The first step involves reprojecting bathymetric data into a local s,n-coordinate system, and the second consists in the interpolation itself, performed within this transformed space. A concrete example of this process and its results are presented in Chapter 4.

The projection of the bathymetry data in a segment-oriented s,n-coordinate system is a common first step in river interpolation (Merwade et al., 2005, 2006; Legleiter & Kyriakidis, 2008; Pelckmans et al., 2021). This projection improves interpolation results, as conventional cartesian interpolation methods often struggle to capture riverbed topography accurately because of the strong anisotropy of river systems. Depth variations are typically much more pronounced across the river (perpendicular to the flow) than along its course. The initial projection of bathymetric data into an s,n-coordinate system allows us to accounts for this anisotropy in the following interpolation. In this thesis, s represents the distance along the centerline of the river, while n is the distance on the perpendicular to s.

Each river segment, as defined during mesh generation, has its own s,n-coordinate system. The projection process inside a segment is described below and illustrated in Fig. 2.2:

1. **Definition of the s,n-coordinate system:**
   The river centerline is computed as the midpoint between each pair of opposing bank nodes (Fig. 2.2.a.). This centerline serves as the s axis. The s-coordinate of each pair of opposing bank node is determined by measuring the centerline distance from the segment's starting point to the line connecting the two nodes (Fig. 2.2.b.). The n-coordinate is assigned to each node on the banks,

by halving the distance between opposing nodes (Fig. 2.2.c.). Nodes on the left bank are assigned positive n-coordinate, while those on the right bank have negative ones. This results in a grid of quadrilateral elements, where each corner node has a new coordinate within the s,n-system of the segment.

2. **Reprojection of the bathymetry points:**
Each bathymetry point is assigned to the quadrilateral it falls within (Fig. 2.2.d.). The s,n-coordinates of the bathymetry point are calculated (Fig. 2.2.e.) with:

$$\begin{aligned} s &= \frac{1-\delta_x}{2} s_{x_0} + \frac{1+\delta_x}{2} s_{x_1}, \\ n &= \left(\frac{1-\delta_x}{2} n_{x_0} + \frac{1+\delta_x}{2} n_{x_1} \right) \frac{1-\delta_y}{2} \\ &\quad + \left(\frac{1-\delta_x}{2} n_{x_3} + \frac{1+\delta_x}{2} n_{x_2} \right) \frac{1+\delta_y}{2}, \end{aligned} \tag{2.7}$$

where δ_x and δ_y are the point's local coordinates within the quadrilateral, and s_{x_i} and n_{x_i} are the s,n-coordinates of the i^{th} corner node of the quadrilateral.

In a second step, we interpolate the bathymetry values on the mesh in this new s,n-coordinate system. To account for the river anisotropy during interpolation in the segments, one approach is to give more weight to points with similar n-coordinate (i.e., directly upstream or downstream), than those with similar s-coordinates (i.e. on the same transect) (Merwade et al., 2006, 2008; Wu et al., 2019). To achieve this, we multiplied the n-coordinate of each point by an, a dimensionless anisotropy factor, to artificially increase the distance between bathymetry points in the direction perpendicular to the river. Bathymetry values at mesh nodes were then computed using Inverse Distance Weighting (IDW) interpolation:

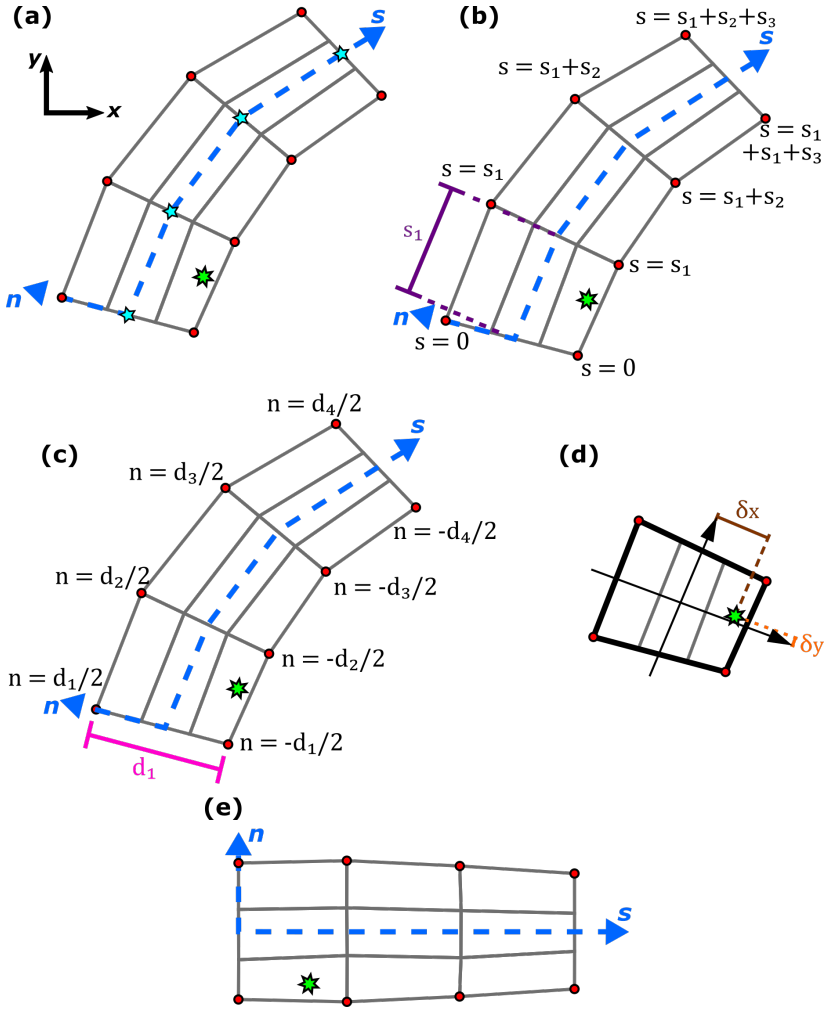

Figure 2.2: Reprojection of the bathymetry points in the s, n-coordinate system. The bathymetry point is represented by a green star. The nodes on the riverbanks are represented by red circle. The mesh is represented by gray lines. **(a)** We find the centerline (blue dotted line) of the river segment. The centerline passes in the middle (blue stars) of every pair of opposing nodes. **(b)** Every node on the riverbanks receives an s-coordinate. **(c)** Every node on the riverbanks receives an n-coordinate. **(d)** Coordinates of the bathymetry points in the quadrilateral in which it is located. **(e)** Bathymetry point in the s, n-coordinate system.

$$z^* = \sum_{i=1}^{np} w_i z_i, \tag{2.8}$$

where z^* is the interpolated depth, $i = 1,...np$ are the np bathymetry points closest to the node, z_i is the depth of the i^{th} bathymetry point, and w_i is the weight associated to this point:

$$w_i = \frac{\frac{1}{d_i^p}}{\sum_{i=1}^{np} \frac{1}{d_i^p}}, \tag{2.9}$$

where d_i is the distance between the node and the i^{th} bathymetry point and p is an exponent controlling the influence that the points have on the interpolation. A higher p value reduces the effect of distant points on the interpolation. Similar methods, where the IDW interpolation is modified to take into account the anisotropy of the river, have given good results in previous studies, even outperforming other interpolation methods, such as kriging or spline interpolation (Merwade et al., 2006; Diaconu et al., 2019; Liang et al., 2022). In this anisotropic IDW method, a new parametrization is needed for every new grid on which the bathymetry is interpolated. An example of a sensitivity study to find the optimal values for the parameters an, np, and p on a particular mesh for the entire Danube Delta is presented in Chapter 4.A.

Because of data scarcity in the Danube Delta, the parametrization is done by minimizing the error obtained through a "leave-one-out" method. This approach works well for sparse, randomly distributed or high-density input bathymetry, but is less effective when the available bathymetric data consist of widely spaced transects with many observations along each transect. In such cases, optimal an values found in the parametrization are often low, creating step-like bathymetry when the interpolation process is applied on a mesh with L value smaller than the distance between transects, thereby disrupting along-channel continuity.

To address this issue, we developed a modified two-step interpolation

technique within the s,n-coordinate system for segments where such input data dominate. The first step is based on the idea pursued by several studies that the bathymetry changes linearly following lines of constant n-coordinates (Goff & Nordfjord, 2004; Caviedes-Voullième et al., 2014; Dysarz, 2018). For each grid point of the grid used for reprojection, we computed the bathymetry by identifying the closest points from the upstream and downstream transects and then applying a simple IDW interpolation using those two points in Eqs. 2.8 and 2.9, with $np = 2$ and $p = 1$. This process results in bathymetric data whose coordinates align with the mesh within the segment but not in the connection zones. To resolve this, a second interpolation is performed using the same method as with other bathymetry sources, but with the grid-interpolated bathymetry as the source. Since the grid and the mesh coincide within the segments, the interpolated bathymetry in these areas remains unaffected by the second step, while the bathymetry on the mesh points in the connections continues smoothly from the segments. More information on this other technique and the errors it can yield can be found in Chapter 4.A.

Another challenge in braided river interpolation is handling interpolation in the connection zones, where multiple river segments converge or diverge. In these areas, the deepest parts of the river do not follow a single, easily defined direction that can be approximated by a centerline s. Instead, bathymetric features form complex patterns, often extending from adjacent segments and intersecting in "T" or "X" configurations. Few studies on river bathymetry interpolation focus on braided rivers with multiple river segments. Goff and Nordfjord (2004) included the connections zones within the river segments and took the maximum interpolated depth at points with multiple interpolation results. Hilton et al. (2019) employed an s,n-coordinate system that covered the entire braided river network, with the n-coordinate spanning from 1 at the northernmost riverbank to -1 at the southernmost riverbank, thus avoiding the need to divide the network into separate segments. Similarly, R. Lai et al. (2021) kept the whole river network and linearly interpolated the bathymetry along streamlines. In contrast, Dey et al. (2022) segmented the network, and interpolated points in connection zones using a 2- or 3-neighbor IDW approach, depending on whether the points were on the tributary side of the thalweg. While

these methods produce satisfactory results, they also present limitations in terms of complexity or compatibility with our domain.

In this thesis, we chose to elongate the segment's mesh, to create a grid that extends into the surrounding connection zones. This grid then serves as a reference grid for projecting both the mesh points and bathymetric data within the connection areas, following the procedure illustrated in Figure 2.2. Interpolation is then performed as if the mesh points of the connection zones included in this extended grid belonged to the segment. As a result, each point in a connection zone can be assigned multiple bathymetry values from the interpolation in the different neighbouring segments. To determine the final bathymetry value at these points, we average the interpolation results with weights inversely proportional to the distance from the segment generating each result. More details on this choice can be found in Chapter 4.A

In floodplains and coastal areas, bathymetry do not follow a predominant direction, and interpolation can therefore be performed isotropically. We apply here the standard interpolation procedure commonly used by SLIM users to project bathymetric data onto unstructured meshes. Bathymetry values are interpolated from structured grid datasets onto the mesh using a bilinear weighted interpolation. For each mesh node, the cell of the dataset containing the node is identified, and its normalized coordinates in that cell are computed as

$$\xi = \frac{x_i - \mathrm{lon}_0}{\mathrm{lon}_1 - \mathrm{lon}_0}, \qquad \psi = \frac{y_i - \mathrm{lat}_0}{\mathrm{lat}_1 - \mathrm{lat}_0}, \tag{2.10}$$

where x_i and y_i are the longitude and latitude of mesh node i, lon_j and lat_k are the longitude and latitude of the grid cell's sides, with j, $k = 0, 1$ corresponding respectively to the western/eastern and southern/northern side (Fig. 2.3). The interpolated bathymetry at the i^{th} mesh node is then obtained as a weighted sum of the bathymetry values at the four surrounding grid-cell corners:

$$h_i = \sum_{j=0}^{1} \sum_{k=0}^{1} w_{j,k}\, h_{j,k}, \tag{2.11}$$

where the bilinear weights are defined as

$$w_{0,0} = (1-\xi)\,(1-\psi),\;\; w_{0,1} = (1-\xi)\,\psi,\;\; w_{1,0} = \xi\,(1-\psi),\;\; w_{1,1} = \xi\,\psi. \quad (2.12)$$

In some cases, parts of the domain are covered by finer-resolution bathymetric datasets. Within the extent of such datasets, we apply the same bilinear weighted interpolation process as described above. To ensure a smooth transition between regions derived from different data sources, the interpolated bathymetric values at node i are combined using a distance-weighted formulation:

$$h_i = \lambda\, h_{i,\text{finer}} + (1-\lambda)\, h_{i,\text{coarser}}, \quad (2.13)$$

where $h_{i,\text{finer}}$ and $h_{i,\text{coarser}}$ are the interpolated bathymetry at node i based on the finer and coarser bathymetry datasets, respectively, and λ is a weighting coefficient defined as

$$\lambda = \begin{cases} \min\left(1, \frac{d_i}{d_{\text{buffer}}}\right) & \text{if inside the extent of the finer bathymetry,} \\ 0 & \text{otherwise,} \end{cases} \quad (2.14)$$

where d_i is the distance between the mesh node and nearest boundary of the finer bathymetry, and d_{buffer} is a user-defined buffer distance inside the finer bathymetry extent, beyond which the coarser dataset has no influence. This approach ensures a continuous and gradual transition between coarse and fine bathymetric datasets, preventing artificial discontinuities along dataset boundaries.

After interpolation, the resulting bathymetry may still exhibit some abrupt depth variations or local anomalies, which can have a particularly strong impact in shallow areas. To mitigate these, a smoothing algorithm is applied to the bathymetry field expressed in its continuous form, enforcing a local slope constraint within each mesh element:

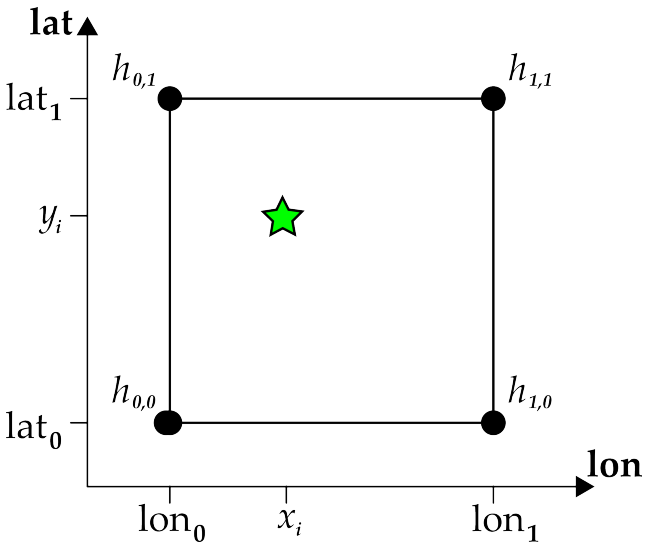

Figure 2.3: Schematic representation of the coordinate system used for the bilinear interpolation. The black square represents a cell of the bathymetric dataset, with its corner nodes (lon_j, lat_k) and corresponding bathymetric values $h_{j,k}$. The green star marks the mesh node of coordinates (x_i,y_i), for which the interpolated bathymetry h_i will be computed.

$$(h_{\max} - h_{\min}) < C_{\text{smooth}}\,|h|_{\max} + \min_{\text{delta}}, \tag{2.15}$$

where $C_{smooth} = 0.5$ is a smoothing coefficient controlling the relative slope limit, h_{max} and h_{min} are the maximal and minimal bathymetry values on the element, $|h|_{max}$ is the maximum absolute bathymetry and $min_{delta} = 0.3$ m is a minimum absolute threshold ensuring smoothness even in shallow regions. The smoothing is performed iteratively. At each iteration, the following scaling factor is computed:

$$f = \min\left(\frac{C_{\text{smooth}}\,|h|_{\max} + \min_{\text{delta}}}{\max\left((h_{\max} - h_{\min}),\ \epsilon\right)},\ 1\right), \tag{2.16}$$

where $\epsilon = 10^{-8}$ prevents division by zero. The bathymetry at each node i is then updated as

$$h_i^{\text{new}} = h_{\text{mean}} + f\ (h_i - h_{\text{mean}}), \tag{2.17}$$

where h_{mean} is the mean bathymetry of the element. The iterations continue until the convergence criterion $\max(0, 1-f) < 0.01$ is met, indicating that all local slopes satisfy the imposed constraint. This process limits depth variations within individual elements, allowing steeper gradients in deep regions while enforcing smoother transitions in shallow areas. This smoothing is not used in the river, as it tends to excessively flatten the bathymetry in the channels.

2.1.4 Wetting and drying

In hydrodynamic models, floodplains can be a source of numerical instabilities, caused by dry areas, i.e. areas where $H = 0$, within the computational domain. To mitigate these instabilities, Wetting and drying (WD) algorithms are employed. Over the years, different WD algorithms have been incorporated in SLIM, including both implicit and explicit schemes (Gourgue et al., 2009; Kärnä et al., 2011; Le, Lambrechts, et al., 2020). The kind of algorithm currently implemented in SLIM, and used in this study, is called a "thin-film" wetting and drying algorithm. The idea behind it is to ensure that a thin layer of water, with a minimal depth H_{thin}, is maintained on every element by limiting the fluxes of water when necessary (Medeiros & Hagen, 2013) (Fig. 2.4). In the current version of SLIM, this algorithm is designed for explicit time integration schemes.

Our WD algorithm consists of three main steps. The first step aims to prevent elements from becoming completely dry by limiting the outgoing fluxes through their edges. This is achieved by computing, for each element, a coefficient C_{WD}^F used afterwards to scale fluxes between elements in such way that no more water than what can be safely removed is extracted from the element. To determine this coefficient, we only consider the outgoing fluxes. Four different situations are considered (Fig. 2.5). The first situation is the case where there is not enough water in the element to sustain outflow (Fig. 2.5 (a)). To determine if this is the case, we look at the volume that can be safely removed, defined by

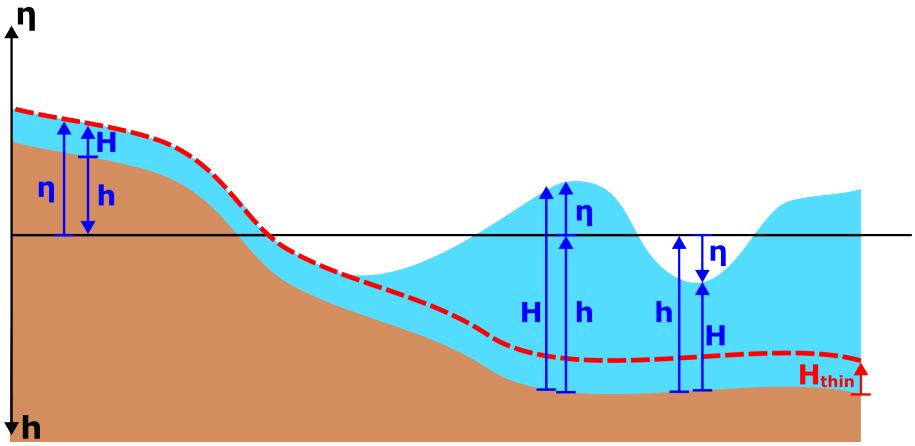

Figure 2.4: Schematic representation of the vertical reference system and height components used in SLIM. The blue area represents the water column, with total water height H, free-surface elevation η and the bathymetry h. The water elevation η and bathymetry h are both measured compared to a common reference level (horizontal black line), with η representing the vertical distance from the reference level to the water surface and h the distance from the bottom to the reference level. Upward arrows denote positive values and downward arrows denote negative values for H, η and h. In SLIM, the convention is that η increases upward, and h increases downward. In WD schemes based on thin-film approach, the water height H is constrained to remain above a minimum admissible depth H_{thin}, shown as a red dashed line.

$$\tilde{V} = \frac{A}{3} \sum_{i=0}^{3} (H_i - H_{thin}), \tag{2.18}$$

where A the area of the element and H_i is the water depth at node i of the element. If $\tilde{V} \leq 0$, the element does not contain enough water to sustain any outflow, and C^F_{WD} is set to zero. In the second situation, the element contains sufficient water, but there is no net outflow (Fig. 2.5 (b)). To ascertain whether this is the case, we compute the total outgoing volume of the element as

$$\Delta V = \sum_{j \in edges} F_j^{ext,out}, \tag{2.19}$$

where $F_j^{ext,out}$ is the outward flux through edge j of the element. By convention, $\Delta V < 0$ indicates a net outflow, while $\Delta V = 0$ means no water is leaving the element. When $\tilde{V} > 0$ and $\Delta V = 0$, there is therefore enough water in the element and no risk of emptying it, and C_{WD}^F is set to 1. In the third situation, the element contains enough water ($\tilde{V} > 0$) and part of it is leaving the element ($\Delta V < 0$), but the water leaving does not bring the water level below what is safe ($-\tilde{V} \geq \Delta V$, Fig. 2.5 (c)). As the outgoing flux does not deplete the element below the safe threshold, no limitation is required, and C_{WD}^F is also set to 1. In the last situation, there is enough water in the element, but the outgoing flux would remove too much water ($-\tilde{V} < \Delta V$, Fig. 2.5 (d)). In this case, outgoing fluxes must be scaled and C_{WD}^F is set to $-\tilde{V}/\Delta V$.

Once the coefficient are determined, each edge flux is multiplied by C_{WD}^F of the element from which the flux originates. In the configuration shown in Fig. 2.6, the flux through edge **i** is multiplied by the C_{WD}^F of triangle 1, while the fluxes through edges **ii** and **iii** are scaled by the C_{WD}^F of triangle 2. This ensures that elements at risk of drying have their outflow limited, while preserving both mass conservation and numerical stability.

After controlling the fluxes at the element scale, the next step ensures that water depth at individual nodes within each element does not go below the minimum water depth of H_{thin}. This is achieved by redistributing water within each element. However, special care is required at the interface between rivers and floodplains, where steep bathymetric gradients often occur. In such cases, one or more nodes located on the riverbank may be dry while others, typically in the channel, remain wet. A naive redistribution of water in these elements could lead to unphysical uphill flow across the bank crest and trigger artificial flooding. To avoid this, we use two distinct methods to redistribute water within the elements.

In the first case, elements have a mean water elevation that is below the minimum admissible elevation of the highest node, $\eta_{\mathrm{mean}} < H_{\mathrm{thin}} - h_{\mathrm{min}}$, where h_{min} is the lowest nodal bathymetry of the element (i.e. the bathymetry of the highest node) (Initial state in Fig. 2.7). Such a configuration typically occurs along riverbanks, when one node on the banks has its water depth going below H_{thin}. The goal here is to

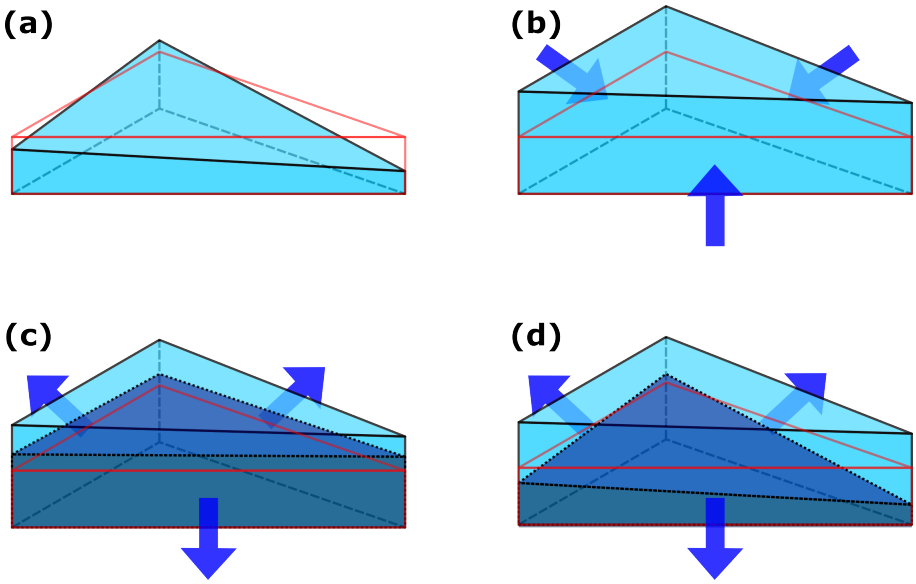

Figure 2.5: Schematic representation of the four possible situations in the determination of the flux-limiting WD coefficient C^F_{WD}. The light blue triangular-based prisms represent the water level at the beginning of the time step, the red-framed prisms represent the volume that can be safely removed ($\tilde{V}$), the dark blue prisms with dotted black edges indicate the water level at the end of the time step, obtained by applying the outgoing fluxes only (i.e. by removing the total outgoing volume ΔV from the initial volume), and the blue arrows show the net direction of the fluxes through the element edges. **(a)** The element does not contain enough water to sustain outflow ($\tilde{V} \leq 0$); $C^F_{\text{WD}} = 0$. **(b)** The element contains sufficient water, but there is no net outflow on any edge ($\tilde{V} > 0$ and $\Delta V = 0$); $C^F_{\text{WD}} = 1$. **(c)** Water is leaving the element, but the volume loss does not lower the water level below the safe threshold ($\tilde{V} > 0$, $\Delta V < 0$ and $-\tilde{V} \geq \Delta V$); $C^F_{\text{WD}} = 1$. **(d)** The element contains sufficient water, but the outgoing flux would remove too much water ($\tilde{V} > 0$, $\Delta V < 0$ and $-\tilde{V} < \Delta V$), $C^F_{\text{WD}} = -\tilde{V}/\Delta V$.

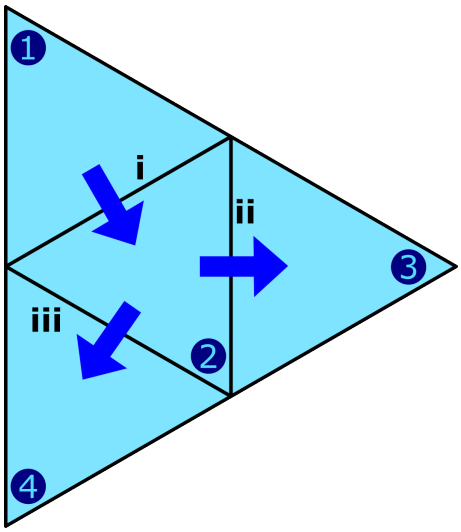

Figure 2.6: Schematic representation of the water fluxes between elements, viewed from above. Triangular elements are identified by numbers (1–4) shown in dark blue circles, while the edges of element 2 are labeled with Roman numerals (i–iii). The dark blue arrows represent the direction of water fluxes through these edges, each of which is multiplied by the C^F_{WD} of the element from which the flux originates as part of the WD algorithm.

bring the water height at that node to H_{thin} with the smallest possible transfer of water from the river, thereby preventing artificial backflow up the slope.

The nodes are first sorted according to their minimal admissible water elevation, defined as $\tilde{\eta_i} = H_{thin} - h_i$, where h_i is the bathymetry at node i. For clarity, we assign subscripts i=1,2,3 to represent the nodes with the highest, middle, and lowest values of $\tilde{\eta_i}$, respectively. As nodes on the banks have a lower bathymetric value (i.e., the ground is higher there) than those in the river, they also have higher $\tilde{\eta_i}$ values.

In a first redistribution step, the water elevation at the highest node is brought to its admissible minimum ($\eta_1 = \tilde{\eta_1}$) (Step 1 in Fig. 2.7). The water added to that node $\mathrm{diff}_1 = \tilde{\eta_1} - \eta_1$ is equally taken from the two other nodes

$$\eta_i = \eta_i - \frac{\text{diff}_1}{2} \text{ for } i = 2, 3. \tag{2.20}$$

On some elements, both nodes 1 and 2 lie on the riverbank. In this situation, removing water equally from nodes 2 and 3 may undesirably transfer water uphill, even though node 2 could alone supply the deficit at node 1. This case is identified by comparing the minimal water elevation between nodes 2 and 3 (η_{min}) with the lowest admissible elevation of node 2. If $\eta_{min} < \tilde{\eta_2}$, node 2 is considered part of the riverbank. A second redistribution step is then performed, in which node 2 is also set to its minimal admissible elevation ($\eta_2 = \tilde{\eta_2}$), and the resulting water difference $\text{diff}_2 = \tilde{\eta_2} - \eta_2$ is subtracted from the water elevation at node 3. If $H_2 > H_{\text{thin}}$ after the first step, then $\text{diff}_2 < 0$ and node 3 gains water in this second step, making node 2 the primary contributor to the filling of node 1. Conversely, if $H_2 < H_{\text{thin}}$, $\text{diff}_2 > 0$, and node 3 serves as a water source to maintain sufficient depth on both nodes along the bank. This two-step process effectively prevents spurious flooding across steep slopes while maintaining realistic mass redistribution within the element.

As a last step in this case, the momentum of each node of the element is set to 0. This step suppresses any residual motion within the element, preventing spurious flow that could otherwise cause artificial flooding along the banks after redistribution.

In other cases where water elevation of the element satisfies $\eta_{\text{mean}} \geq H_{\text{thin}} - h_{\text{min}}$, two situation can still arise (Fig. 2.8). In the first, mean water height (H_{mean}) is lower than or equal to H_{thin}. In this case, the element is considered fully dry. The water height at each node is then uniformly adjusted to the mean value by setting $\eta_i = \eta_i + H_{\text{mean}} - H_i$ (Fig. 2.8 (a)). The second situation corresponds to elements that are only partially dry, with a mean depth above the admissible threshold ($H_{\text{mean}} > H_{\text{thin}}$) but at least one node having a $H_i < H_{\text{thin}}$ (Fig. 2.8 (b)). In this case, water is redistributed from the nodes where water is in excess ($H_i \geq H_{\text{thin}}$) to those where we have a deficit of water ($H_i < H_{\text{thin}}$) to ensure a minimum water depth across the element while preserving mass conservation. The redistribution translates into

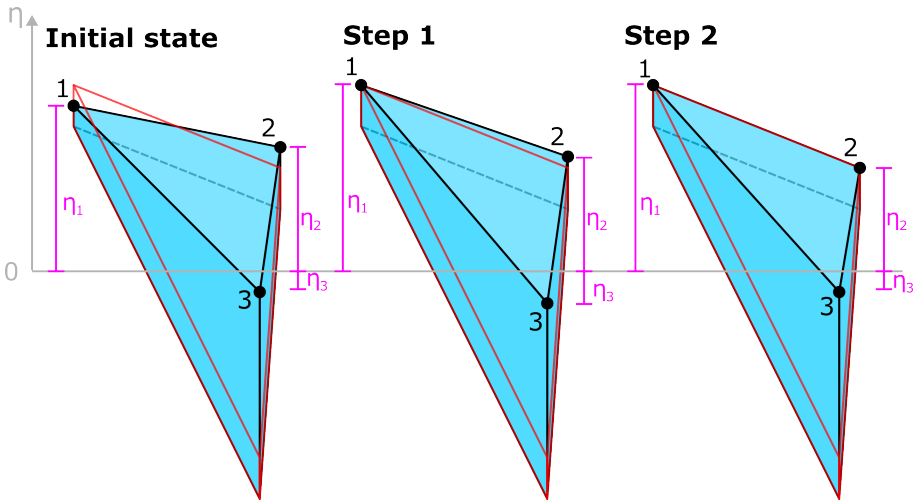

Figure 2.7: Schematic representation of the two-step water redistribution procedure of the WD algorithm in the case where two nodes lie on the riverbank. The blue prisms represent the water height (H), and the three nodes of the element are shown as black dots, numbered from highest to lowest according to their minimal admissible water elevation ($\tilde{\eta_i} = H_{thin} - h_i$). The red-framed prism indicates the minimal admissible water depth (H_{thin}). The prisms are shown from a frontal view, with nodes 1 and 2 (on the riverbank) aligned on the same plane at the back. The horizontal gray line corresponds to $\eta = 0$ and the pink vertical lines show the nodal water elevations η_i at each substep, highlighting how water is redistributed between nodes during the process. In the initial state, $\eta_{\text{mean}} < H_{\text{thin}} - h_{\text{min}} = H_{\text{thin}} - h_1$. In the first step, water is taken equally from nodes 2 and 3 to bring H_1 to H_{thin}. In second step, since both nodes 1 and 2 are on the riverbank, water is taken at node 2 to fill node 3 and limit the amount of water going uphill.

$$\eta_i = \eta_i + C^H_{\text{WD,i}} \cdot (H_{\text{thin}} - H_i), \tag{2.21}$$

where $C^H_{\text{WD,i}}$ is a nodal wetting and drying coefficient defined by

$$C^H_{\text{WD,i}} = \begin{cases} 1 & \text{if } H_i < H_{\text{thin}}, \\ \dfrac{\sum_{j \in d} \left(H_{\text{thin}} - H_j\right)}{\sum_{j \in e} \left(H_j - H_{\text{thin}}\right)} & H_i \geq H_{\text{thin}}, \end{cases} \tag{2.22}$$

with d as the set of nodes of the element experiencing a water deficit

and e the set of nodes with excess water. This formulation ensures that the total redistributed volume within the element is conserved while preventing any node from becoming artificially dry.

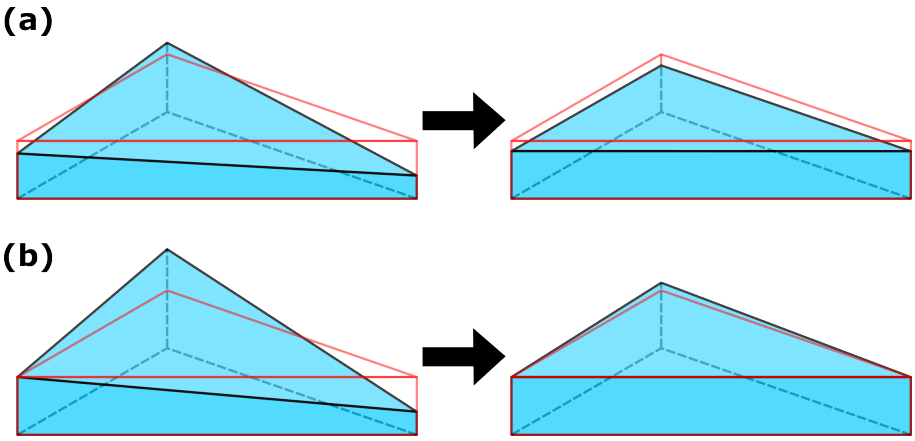

Figure 2.8: Schematic representation of the two situations requiring water redistribution in the case where no node is located on a riverbank. The blue prisms represent the water height (H), and the red-framed prism indicates the minimal admissible water depth (H_{thin}). The left column shows the state of the element at the beginning of the time step, and the right column shows the element after redistribution. **(a)** The mean water height (H_{mean}) is lower than or equal to H_{thin}; the water height is flattened toward H_{mean}. **b** At least one node has a $H_i < H_{\text{thin}}$; water is redistributed from nodes with excess water ($H_i \geq H_{\text{thin}}$) to those with a deficit ($H_i < H_{\text{thin}}$).

In the final step of our WD process, we limit the momentum $H\boldsymbol{u} = (Hu, Hv)$ at each node to avoid supercritical flow in shallow areas, which can cause numerical instabilities. In this step, we compute the new safely usable water depth at each node i, $\tilde{H}_i = \max(0, H_i - H_{\text{thin}})$ and the norm of the momentum

$$|H\boldsymbol{u}_i| = \sqrt{(Hu_i)^2 + (Hv_i)^2}. \tag{2.23}$$

The maximal allowable momentum value is defined as

$$Hu_{i,max} = \tilde{H}_i \sqrt{g\tilde{H}_i}\, Fr_{\max}, \tag{2.24}$$

where $Fr_{max} = 1$ is the maximum Froude number allowed in this case. At nodes where $|Hu_i| > Hu_{i,max}$, the momentum is set to a maximal value of

$$H\boldsymbol{u}_i = H\boldsymbol{u}_i \frac{Hu_{\mathrm{i,max}}}{|H\boldsymbol{u}_i|}. \tag{2.25}$$

This operation preserves the flow direction while reducing its magnitude to avoid numerical instabilities.

As a final safeguard, and to avoid the accumulation of numerical rounding errors that can lead to increasingly negative water depths, we also force all values of $H < H_{\mathrm{thin}}$ to be set equal to H_{thin} after each time step. This step does not affect the physical realism of the model, as the errors it targets are on the order of the machine precision. However, it enhances numerical robustness by preventing the emergence of spurious instabilities.

This three-step WD algorithm allows us to enhance the stability of hydrodynamic simulations with partially dry domains, such as those found in deltas with floodplains or estuaries with intertidal zones. It is a slightly modified version from the one described by Randresihaja et al. (2025), where the second step does not include the check on η_{mean}. This new sub-step is particularly important to avoid water going over dikes and causing excessive flooding. By ensuring a minimum water depth, redistributing water within elements, and controlling momentum in shallow regions, the method preserves physical realism while maintaining numerical robustness. Its integration into the current version of SLIM enables accurate simulation of dynamic coastal and estuarine environments where wetting and drying processes are significant.

2.2 First steps towards a coupled hydro-biogeochemical model

Beyond the scope of this thesis, I also worked on implementing a simple NPZD model, using SLIM Eulerian transport model. This is a first step in the development of a coupled hydro-biogeochemical model on the Danube-Danube Delta-Black Sea continuum. A similar approach with SLIM's 3D version has already been applied to Lake Titicaca by

Duquesne et al. (2021). We define DIN as the dissolved inorganic nitrogen, P the phytoplankton nitrogen biomass, Z the zooplankton nitrogen biomass, and D the detrital nitrogen (all in mmol N m^{-3}).

The equations used in this model are based on a lake model presented by Soetaert and Herman (2009) and read:

$$\frac{d\mathrm{DIN}}{dt} + \mathcal{A}(DIN) = \underbrace{l_{\mathrm{min}} D}_{\text{mineralization}} + \underbrace{l_{\mathrm{exc}} Z}_{\text{excretion}} - \underbrace{\mathrm{Uptake}(DIN, \mathrm{PAR})\, P}_{\text{uptake}} + \mathcal{D}(DIN), \tag{2.26}$$

$$\frac{dP}{dt} + \mathcal{A}(P) = \mathrm{Uptake}(DIN, \mathrm{PAR})\, P - \underbrace{\mathrm{Graze}(P)\, Z}_{\text{grazing}} - \underbrace{l_{\mathrm{mortP}} P}_{\text{phyto\_mortality}} + \mathcal{D}(P), \tag{2.27}$$

$$\frac{dZ}{dt} + \mathcal{A}(Z) = \underbrace{(1 - p_{\mathrm{Faeces}})\, \mathrm{Graze}(P)\, Z}_{\text{zoo\_growth}} - \underbrace{l_{\mathrm{mortZ}} Z^2}_{\text{zoo\_mortality}} - l_{\mathrm{exc}} Z + \mathcal{D}(Z), \tag{2.28}$$

$$\frac{dD}{dt} + \mathcal{A}(D) = \underbrace{p_{\mathrm{Faeces}}\, \mathrm{Graze}(P)\, Z}_{\text{faeces}} + l_{\mathrm{mortP}} P + l_{\mathrm{mortZ}} Z^2 - l_{\mathrm{min}} D + \mathcal{D}(D). \tag{2.29}$$

where $\mathcal{A}(X)$ and $\mathcal{D}(X)$ are the advection and diffusion of tracer X, respectively, and are defined as follow:

$$\mathcal{A}(X) = \nabla_h \cdot (\mathbf{u} X), \qquad \mathcal{D}(X) = \frac{1}{H} \nabla_h \cdot \left(\kappa H \nabla_h X \right) \tag{2.30}$$

with $\mathbf{u}$ as the depth-averaged velocity and κ the horizontal diffusivity.

The uptake and grazing functions are

$$\text{Uptake}(DIN, \text{PAR}) = \max_{\text{uptake}} \frac{\text{PAR}}{\text{PAR} + k_{\text{PAR}}} \frac{DIN}{DIN + k_N}, \tag{2.31}$$

$$\text{Graze}(P) = \max_{\text{graze}} \frac{P}{P + k_{\text{graze}}} \tag{2.32}$$

where $\max_{\text{uptake}}$ is the maximum DIN uptake rate by P, $\max_{\text{graze}}$ is the maximum grazing rate of Z, k_N and k_{graze} are the half saturation constant for N uptake by P and for grazing by Z, k_{PAR} is the half-saturation coefficient for PAR, and PAR is the photosynthetically active radiation at mid-depth, defined as

$$\text{PAR} = 0.5 \times \frac{\text{Light}}{3600} e^{-k_d H/2},$$

where Light is the solar radiation as provided by ERA5 ($\text{J m}^{-2}\,\text{hour}^{-1}$) (Hersbach et al., 2023), the division by 3600 is used to transform $\text{J m}^{-2}\,\text{hour}^{-1}$ into Wm^{-2}, the factor 0.5 converts shortwave to PAR (Kirk, 1994), and $k_d = 0.1\,\text{m}^{-1}$ is the light attenuation coefficient with water depth. Model parameters and their values listed in Table 2.1 are derived from Soetaert and Herman (2009), and a schematic of the fluxes is provided in Fig. 2.9. Preliminary results using those parameters can be found in Chapter 6.3.2.

Table 2.1: Parameters used in the NPZD model. Processes in parentheses refer to the fluxes in Eqs. 2.26–2.29 in which those parameters are involved.

Symbol	Description	Value
l_{min}	Mineralization rate (D $\rightarrow$ DIN)	0.10 day^{-1}
l_{exc}	Zooplankton excretion rate (Z $\rightarrow$ DIN)	0.10 day^{-1}
l_{mortP}	Phytoplankton mortality rate (P $\rightarrow$ D)	0.05 day^{-1}
p_{Faeces}	Fraction of grazed P lost as faeces (P $\rightarrow$ D)	0.30 [-]
l_{mortZ}	Zooplankton quadratic mortality rate (Z $\rightarrow$ D)	0.40 $(\text{mmol N m}^{-3})^{-1}\ \text{day}^{-1}$
$\text{max}_{\text{uptake}}$	Maximum DIN uptake rate by P (DIN $\rightarrow$ P)	1.00 day^{-1}
k_{PAR}	Half-saturation coefficient for PAR (DIN $\rightarrow$ P)	55 W m^{-2}
k_N	Half-saturation constant for DIN uptake by P (DIN $\rightarrow$ P)	1.0 mmol N m^{-3}
$\text{max}_{\text{graze}}$	Maximum grazing rate of Z on P (P $\rightarrow$ Z/D)	1.0 day^{-1}
k_{graze}	Half-saturation constant for grazing (P $\rightarrow$ Z/D)	1.0 mmol N m^{-3}
k_d	Light attenuation coefficient (DIN $\rightarrow$ P)	0.10 m^{-1}

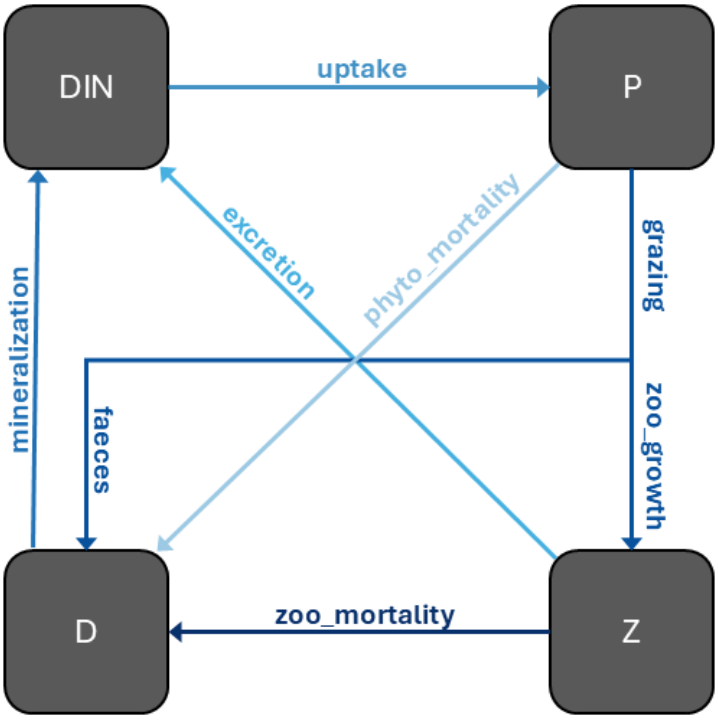

Figure 2.9: Schematic representation of the NPZD model. Boxes indicate nitrogen pools: dissolved inorganic nitrogen (DIN), phytoplankton (P), zooplankton (Z), and detritus (D). Arrows represent nitrogen fluxes between compartments, color-coded to distinguish processes and improve readability.

Chapter 3

What mesh for a braided river? Mesh configurations impact on river and floodplain hydrodynamic using the SLIM model

This chapter is based on the following article: **Alaerts, L.**, Lambrechts, J., Hanert,E., and Grégoire, M. What mesh for a braided river? Mesh configurations impact on river and floodplain hydrodynamic using the SLIM model. *In preparation.*

Abstract

Mesh type plays an important role in hydrodynamic modeling, both in terms of simulation accuracy and computational performances. In this chapter, we evaluate the impact of different mesh configurations on the representation of rivers and floodplains dynamics with the discontinuous-Galerkin (DG) finite-element hydrodynamic model SLIM. A series of six mesh configurations–—hybrid (structured-curvilinear combined with unstructured) and fully unstructured, at varying resolutions——were tested on a reach of the Sfântu Gheorghe branch of the Danube Delta, under both constant discharge and flood event scenarios. Results show that accurate representation of river geometry and riverbanks is the most critical factor in mesh performance. Hydrodynamic accuracy is primarily governed by in-river resolution and explicit riverbank delineation, while computational cost scales with the number of elements and the size of the smallest elements. We propose to combined a hybrid mesh of 20 x 20 m elements in the river and an unstructured mesh with a gradually increasing element size in the floodplain as the best trade-off between in-river hydrodynamic accurate representation, estimation of the flooded area and computational efficiency. These results can serve as a basis for mesh design in larger-scale application for braided river–floodplain systems like deltas.

3.1 Introduction

Floods are a key process in river ecosystem. They can cause devastating damage to infrastructure and human lives, and are one of the natural disaster affecting the most people worldwide (Merz et al., 2021). At the same time, floods are a necessary process in some environments, because of their impact on the transport of sediments and dissolved nutrients (Talbot et al., 2018). As a result, floods have been the focus of many studies. Hydrodynamic models are a recurrent tool in such studies, used to assess the impacts of flooding under a wide range of conditions. Such models are applied to predict flood extent and plan flood mitigation strategies (Abdella & Mekuanent, 2021; Timbadiya & Krishnamraju, 2023), investigate sediment transport and erosion processes (Yan et al., 2024; Hawez et al., 2025), assess ecological and biodiversity patterns (McCabe, 2024; Wegscheider et al., 2024) and explore biogeochemical processes (Wohl, 2021).

Numerical hydrodynamic modeling of river systems involves a wide range of approaches that differ in their mathematical formulation, numerical schemes, dimensionality and the type of computational grid employed. Each modeling approach comes with specific advantages and limitations, and the choice of a suitable model often depends on the nature of the study area, the processes of interest, and the available resources (Horritt et al., 2007; Kim et al., 2014; Samir, 2024)

In terms of numerical schemes, most hydrodynamic river models can be classified into one of three main categories: finite differences, finite volume and finite element methods. Among these, Finite Differences (FD) methods are computationally the cheapest and are relatively easy to implement, making them suitable for applications where low computational cost is a priority. However, they typically rely on structured grid, which limits their ability to represent complex geometries such as meanders, bifurcations, or detailed floodplain features. This leads to the dilemma of having to choose between accurately representing the boundaries or modifying the elements at the possible cost of stability (Fanous et al., 2023). Although less commonly used than the other two methods, FD methods are still applied in river modeling, as seen in recent studies such as Altenau et al. (2017) and Gomiz-Pascual et al. (2021).

Finite Volume (FV) methods are currently the most widely used in river modeling (Cobby et al., 2003; Bomers et al., 2019; X. Zhang et al., 2023; Gaber et al., 2025). Their strength lies in their conservation properties, particularly for mass and momentum, making them well-suited for advection-dominated flows such as those found in rivers. They are computationally efficient and robust, but highly sensitive to mesh quality. Poorly shaped or irregular elements can degrade solution accuracy or cause numerical instabilities (Kärnä et al., 2018; Vallaeys, 2018). Some popular finite volume models used for river studies are MIKE (Liu et al., 2021; X. Zhang et al., 2023), FVCOM (Chen et al., 2022; Qin et al., 2023), Delft3D (Nuhjhat et al., 2023; Rivera & Heredia, 2023) and HEC-RAS (Pilotti et al., 2020; Alipour et al., 2022), among others.

Finite Element (FE) methods, in contrast, offer higher-order discretization and hence better accuracy. They are less sensitive to mesh irregularities and support anisotropic triangular elements, which is advantageous in cases with directional flow features (Shewchuk, 2002; Kamenski et al., 2014). However, they are generally less suited to advection-dominated problems unless stabilization techniques are employed—techniques that are often computationally expensive and less scalable in parallel computing environments (Schwanenberg & Harms, 2004; Fanous et al., 2023). Popular finite element models used in river include TELEMAC (Le et al., 2023; Pelckmans et al., 2023), ADCIRC (Bacopoulos et al., 2017; Gayathri et al., 2021) and SHYFEM (Ferrarin et al., 2025).

At the interface between FV and classical continuous FE methods, lie finite element Discontinuous-Galerkin (DG) methods. Like FE schemes, they offer a higher-order accuracy and high geometrical flexibility. At the same time, they also offer local conservation properties and are well suited for advection-dominated problems, like FV methods (Dolejší & Feistauer, 2015; Kärnä et al., 2018; Vallaeys, 2018). The main disadvantage of DG methods is their computational cost: their linear stability limit (CFL condition) tends to be more restrictive than in FV methods (Vater et al., 2019), and their large number of degrees of freedom leads to higher computational and storage demands compared to traditional finite element methods (Aricò et al., 2011). However, DG schemes are well suited for parallelization, which can significantly reduce the computational time and, in turn, make them more efficient (Kubatko et al.,

2009). Their suitability for river modeling has been demonstrated in several studies (Gourgue et al., 2009; Kesserwani & Wang, 2014; Vallaeys et al., 2018; Ayog et al., 2021; Patil et al., 2025). In this study, we adopt the DG approach through the use of the hydrodynamic model Second-generation Louvain-la-Neuve Ice-ocean Model (SLIM).

Alongside the choice of numerical scheme, mesh design plays a critical role in simulation accuracy, stability, and efficiency. Three main mesh types are commonly used in river hydrodynamics: structured Cartesian grids, curvilinear grids, and unstructured meshes. Structured Cartesian grid are the easiest to implement and use. They also facilitate the integration of river into larger domains containing floodplains, whose topography are often represented on structured grids. However, these grids do not follow the river's shape, and achieving accurate representation of sinuous channels requires very high resolutions (Hodges & Imberger, 2001; Altenau et al., 2017). Curvilinear grids, in contrast, follow the riverbanks and allow for cell stretching, enabling a more accurate representation of the river without the need for small elements. A major drawback is that curvilinear grids are not well-suited for representing complex geometric features, such as bifurcations, or floodplains (Y. G. Lai, 2010; Bomers et al., 2019). Unstructured grids share the advantage of following the riverbanks and providing a more accurate representation of the river delineation. They are also more flexible than curvilinear grids, making them better suited for representing bifurcations and floodplains. However, even if they allow for larger elements than cartesian structured grids, an accurate river representation with unstructured mesh still requires many small elements (Y. G. Lai, 2010; Bomers et al., 2019).

Other mesh types found in the literature include hybrid meshes, which combine structured curvilinear grids within river channels with unstructured—typically triangular—meshes in floodplains and at the junctions between river segments. These meshes capitalize on the strength of both curvilinear and unstructured meshes. They guarantee a good representation of channel geometry and can adapt to complex features, while keeping a relatively low number of elements, reduced computational cost and smaller output sizes (Bomers et al., 2019). Within the river channels, the elements are usually either rectangular (Y. G. Lai, 2010; Bomers et al., 2019; Bilgili et al., 2023) or elongated

triangles (Bates et al., 1998; Bunya et al., 2023). The latter are mainly used in FE studies because elongated triangles do not respect the orthogonality principle. This principle states that (1) the circumcenter of each cell must lie inside the cell, and (2) the line joining the circumcenters of two adjacent cells must intersect their shared edge at a 90° angle. If these conditions are not met in FV schemes, computation time increases and accuracy decreases, which is why elongated triangles—failing to meet the second condition—are rarely used (Bilgili et al., 2023).

Several comparative studies have evaluated the influence of mesh type and resolution on the accuracy and computational cost of river simulations. For instance, Horritt et al. (2006) investigated different mesh resolutions of unstructured triangular grids on a section of the Thames River. They found that mesh resolution had a greater influence on simulation results than the resolution of the underlying bathymetric data. Kim et al. (2014) compared structured quadrilateral, structured triangular, unstructured triangular, and mixed grids containing both triangular and quadrilateral cells. Their results showed that no single mesh type consistently outperformed the others across all scenarios, and they advocated for the use of mixed meshes due to their flexibility. Parsapour-moghaddam et al. (2018) compared unstructured triangular grids and curvilinear structured grids on the 2013 flooding of the Bow River (Canada). They found that even if both model represent adequately the hydrodynamics, unstructured triangular meshes showed better accuracy at the same averaged resolution, albeit at the cost of more computational resources. Bomers et al. (2019) compared curvilinear, unstructured triangular and hybrid grids at various resolutions on the Waal River (Netherlands). They highlighted that both mesh resolution—through its effect on bathymetric accuracy and numerical friction—and element shape—through numerical viscosity—can significantly affect simulation outcomes. They also found unstructured meshes to be the most sensitive to calibration and recommended hybrid grids as a good compromise between computational efficiency and model accuracy. Similarly, Bilgili et al. (2023) compared curvilinear, triangular, and hybrid meshes using both idealized test cases and real-world applications. They concluded that resolution and bathymetric discretization—that is, how well depth is represented on the

mesh and the errors introduced by its interpolation—–had the greatest impact on results, with triangular meshes being the most sensitive to changes in resolution. However, they found numerical effects to have less impact on the hydrodynamic results.

However, these studies are all based on models employing FV methods. While DG FE methods are generally less sensitive to mesh quality than FV methods, the structure and resolution of the mesh still influence model performance. For instance, it has been shown that mesh resolution has a clear impact in the hydrodynamic of coastal models (Saint-Amand et al., 2023). To our knowledge, no study has yet investigated the influence of mesh structure—specifically, unstructured triangular versus hybrid curvilinear-unstructured triangular meshes—on river hydrodynamic simulations using the DG FE method. This study aims to address this gap by evaluating the effect of mesh design on river simulations performed with the latest version of SLIM, focusing on how mesh structure affects computational costs and flooding patterns.

3.2 Material and methods

In this section, we describe the six mesh configurations considered in this work, and the case study on which they are applied.

3.2.1 Mesh generation

To evaluate the effect of meshing spatial patterns on simulation results, we design six different mesh configurations. They can be classified into three categories. The first two mesh types are hybrid curvilinear-unstructured meshes. They combine elongated curvilinear triangles aligned with the river path in unidirectional channels, and unstructured triangular elements in the connection zones and floodplains. Their generation follow the process described in Chapter 2.1.2. We test two resolutions: a coarse resolution with elements of 20 m × 200 m in the river, and a finer one with elements of 20 m × 20 m in the river. Those simulation will be hereafter be referred to as the "H200" and "H20" configurations. The next two meshes are unstructured constrained meshes, where riverbanks are explicitly represented by the edges of the triangular elements. We test them at two resolutions, one

with a uniform resolution of 200 m across the domain, and a finer one with a uniform resolution of 20 m. It is important to note that due to the river's width being narrower than 200 m in certain locations, some elements in the coarse mesh are necessarily smaller. These two meshes will hereafter be called "C200" and "C20". The next category considers fully unstructured meshes, one with a uniform resolution of 20 m ("U20"), and one with a variable resolution that ranges from 20 m at the riverbanks to 200 m in the floodplains ("US20"). The river being narrower than 200 m in certain locations, we do not test a uniform mesh of 200 m without imposing the riverbanks, as the mesh would simply miss the river at those points.

All meshes are generated using the state-of-the-art mesh-generation software GMSH (Geuzaine & Remacle, 2009), which allows to build unstructured meshes of resolutions depending on different criteria, such as the distance to specific locations or the bathymetry. In this test case, we only used the distance to riverbanks criteria. For both constrained mesh types (H and C), the river part was meshed first to ensure accurate riverbank representation, followed by meshing of the surrounding floodplains.

3.2.2 Model testing

To compare the different mesh configurations, they are applied on a single test case. The chosen domain is a section of the Sfântu Gheorghe branch and its adjacent floodplain, including two meanders—Dunavăţ de Sus and Dunavăţ de Jos—as well as the artificial cut-off channels constructed in the 1980s to straighten the river (Fig. 3.1). These cut-off programs have had different results on the two meanders: while water still flows comparably through both the original channel and the cut-off at Dunavăţ de Sus, sediment deposition has significantly reduced flow through the Dunavăţ de Jos meander, diverting most of the discharge into its cut-off channel (Tiron Duţu et al., 2014). This section of the river therefore offers an ideal test case, featuring complex channel geometries, bifurcations, varying bathymetry and floodplains. On the eastern part of the domain, the Dunavăţ-Murighiol polders has been excluded, as we know it will not be flooded.

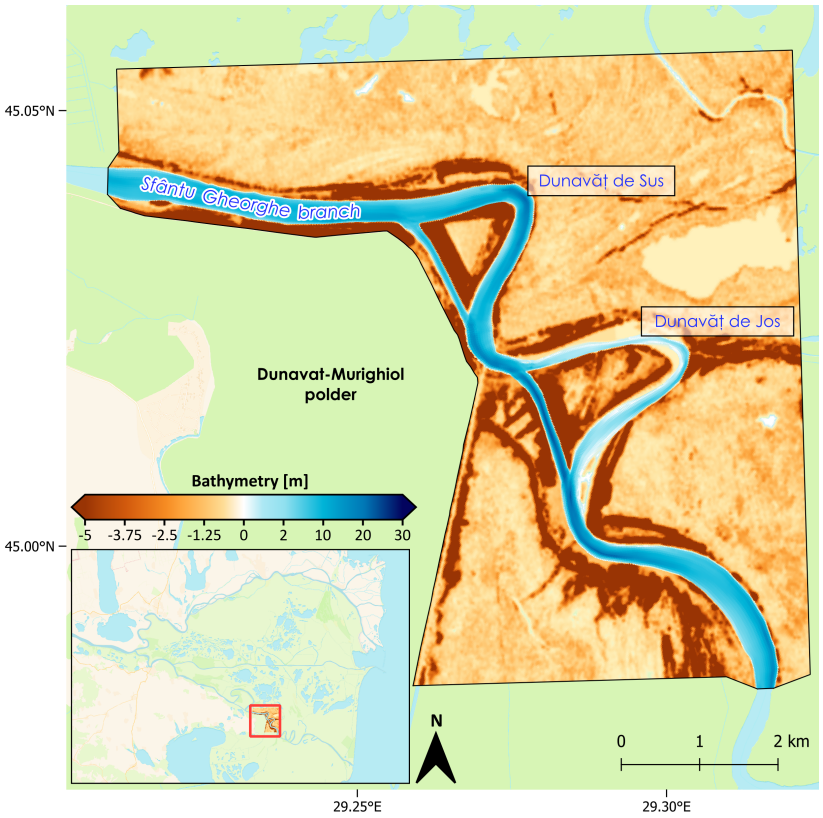

Figure 3.1: Bathymetry of the test case domain. The inset on the bottom left is the position of the domain in the Danube Delta. The black line in the figure represents the domain's boundaries.

Because mesh node positions differ between test cases, the bathymetry is computed independently on each mesh and will obviously play a role on the simulation results. To minimize discrepancies between the bathymetries, a consistent methodology where the river and the floodplains are treated separately is applied. In the river, bathymetric data from the Danube Delta National Institute for Research and Development (DDNIRD) (DDNIRD, 2015) are interpolated onto the meshes using an anisotropic interpolation method described in Chapter 2. This dataset consists of cross-sectional transects spaced ~300 m apart, with an internal resolution of ~3 m within the transects. More details on the bathymetry data can be found in Chapter 4. In the floodplain,

bathymetry from Copernicus' Digital Elevation Model (DEM) (European Space Agency, 2021) is interpolated on the meshes, and smoothed following the methodology described in Chapter 2. The original DEM is gridded at 30 m spatial resolution.

To evaluate the performance of each mesh configuration, two test scenarios are implemented. In the first one, a steady inflow of 2000 m^3/s is imposed at the upstream boundary, while the downstream boundary is set at a constant water surface elevation of $\eta = 0$. The aim of this first scenario is to assess whether the meshes allow water to flow correctly through the river system under constant conditions. The second scenario aims to evaluate the set-up's response to a flood event. To that aim, a base discharge of 2000 m^3/s is maintained upstream for six days, then gradually increased linearly over three days to 4000 $m^3\ s^{-1}$. The inflow is then abruptly raised to a peak of 10^4 $m^3\ s^{-1}$, which is sustained for one day before decreasing linearly over three days to 8000 $m^3\ s^{-1}$. Finally, the discharge is returned to its base value at day thirteen. Forcings at both open boundaries are imposed through Flather boundary conditions, while the other model boundaries are closed with weak no-slip conditions. Both scenarios use the same initial conditions, with velocities that are set to zero and the water surface elevation as $\eta = max(-h + H_{thin}, 0)$, ensuring a minimum water depth of H_{thin} across the domain. Simulations are run for a total duration of 30 days. The simulations are run without wind forcing or nudging toward an external model, and with a uniform manning coefficient of 0.025 $m^{1/3}s$.

As we aim to assess both the computational performances and hydrodynamic patterns of every mesh, all simulations are run on one single GPU NVIDIA A100-SXM4-40GB. In addition, the first scenario (constant discharge) is run twice for every mesh. A first run is made with a time step of $\Delta t = 0.1$ s, which is representative of typical simulations over the entire delta. The second run uses a time step derived from a Courant–Friedrichs–Lewy (CFL) stability condition, computed on the initial condition. The CFL-limited time step is calculated as:

$$\Delta t_{CFL} = \min\left(2\frac{A}{P\sqrt{gH_i}}\right), \tag{3.1}$$

over all the nodes of the domain. For a given node i, A and P are the area and perimeter of the triangular elements to which it belongs. The ratio $2A/P$ corresponds to the inradius of the triangle, which is used here as its characteristic length, and H_i is the water column height at node i. This formulation ensures numerical stability by accounting for both element size and water column height. Smaller elements and deeper water tend to yield smaller allowable time steps. Computing this CFL-limited time step on the initial condition provides a conservative estimate of the stable time step magnitude. Using the inradius as the characteristic length is likely too conservative for anisotropic meshes that follow the riverbanks, since the flow is mostly aligned with the element orientation. However, this conservative estimate guarantees stability even in regions where flow is not aligned with the mesh, such as bifurcations and connection zones, which typically impose the most restrictive Δt_{CFL}. In addition, because the formulation is based on the gravity-wave velocity ($\sqrt{gH}$), it may be overly conservative in advection-dominated river flows, where stability is governed more by flow velocity than by wave propagation. Nevertheless, this criterion remains the standard approach in shallow-water modeling (Kärnä et al., 2011; García-Alén et al., 2021; Herbin et al., 2023; Chopra & Oza, 2025). Using it here provides a consistent and robust stability constraint across all meshes, ensuring that the simulations remain stable even in locally supercritical or poorly aligned flow regions. For the domain used in this study, the Δt_{CFL} numbers are larger than 0.1. Running each simulation with both time steps allow us to compare the model performance for each mesh under equivalent conditions as well as under optimal mesh-adapted time steps.

3.3 Results

In this section, we first present the different meshes used in this study. We then compare the computational performances and hydrodynamic results of the simulations carried out with these meshes, under both steady discharge and flood event conditions.

3.3.1 Meshes overview

The six mesh configurations used in this study are significantly different in terms of resolution, element size distribution, and total number of elements (Fig. 3.2 and Table 3.1). The largest meshes are C20, U20 and H20, with approximately 260 000 elements each. The constrained unstructured mesh US20 includes roughly 50 000 elements, while the hybrid mesh H200 contains around 8 000 elements. The coarsest mesh, C200, is composed of only 2 000 elements. Most meshes include small elements with edge sizes between 11 and 15 m. For the hybrid meshes, these small elements can be found in the connection zones. The exception is C200, whose edge sizes do not go under 100 m. Mesh uniformity varies among the configurations. As expected, the uniform mesh U20 exhibits the lowest size standard deviation, followed by C20 and H20 meshes. Among the coarser meshes, C200 is the most uniform, followed closely by US20. Most of the variation in size for the former is due to the the conforming to the river banks, while in the latter is purely linked with the imposed variation in size according to the distance to the riverbanks. The mesh with the highest size standard variation is H200; due to the combination of small elements in connection zones, elongated elements along the river segments, and coarser triangular elements in the floodplains.

Table 3.1: Meshes characteristics. All sizes are expressed in meters.

	H20	H200	C20	C200	U20	US20
Number of elements ($\times 10^3$)	256	8.4	263	2.4	262	50.6
Minimum size	12.46	11.8	11.3	104.7	14.0	15.4
Maximum size	56.0	293.9	37.4	321.0	28.1	280.2
Mean size	20.9	116.4	20.2	221.7	20.0	37.8
Size standard deviation	3.2	85.3	0.7	28.5	0.3	30.7

3.3.2 First scenario: Constant discharge

Simulation runtimes vary significantly depending on both the mesh configuration and the chosen time step (Table 3.2). When using a fixed time step of $\Delta t = 0.1$ s, the fastest simulation is obtained with the hybrid coarse mesh H200, followed closely by C200 and US20. In contrast, the three finer meshes——H20, C20, and U20——all require more than three hours of computation.

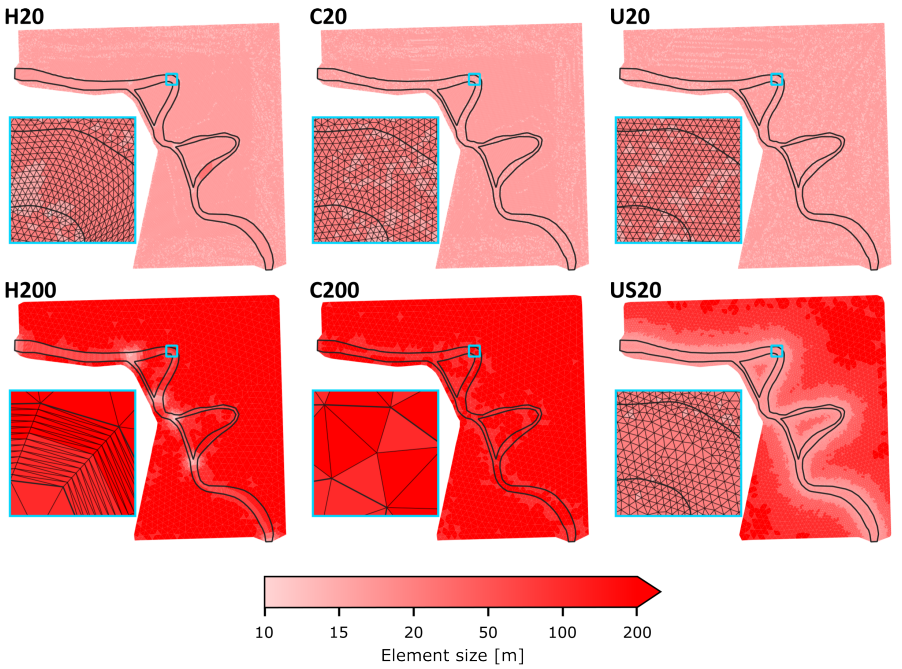

Figure 3.2: Comparison of the six mesh configurations used in the study: hybrid mesh with 20 × 20 m resolution (**H20**), constrained unstructured mesh with 20 m resolution (**C20**), uniform unstructured mesh with 20 m resolution (**U20**), hybrid mesh with 20 × 200 m resolution (**H200**), constrained unstructured mesh with 200 m resolution (**C200**), and unstructured mesh with variable resolution decreasing from 20 m near the riverbanks to 200 m in the floodplains (**US20**). The color scale shows the length of the longest edge of each triangular element. Each panel displays the full domain and a close-up view (framed in blue), with the close-up location marked on the full-domain panel. The thick black line delineates the river boundary: in H20, H200, C20, and C200 it corresponds to the mesh edges, while in U20 and US20—where the mesh does not explicitly follow the riverbanks—it is taken from the H20 mesh for consistency. In the close-ups, mesh edges are drawn as thin black lines, but they are omitted from the full-domain views to avoid masking the color patterns of the finer meshes.

When using the CFL-limited time step Δt_{CFL}, the picture changes notably. As expected, all Δt_{CFL} are bigger than 0.1, and all simulations' computational times are considerably reduced. When looking at the values of Δt_{CFL}, it ranges between 0.25 and 0.4 s for most mesh configurations. The clear exception is C200, whose relatively large and uniform elements allow for a much larger time step, with a $\Delta t_{CFL} \approx 2$ s. This results in a significant reduction in simulation time——to just over two minutes——making it by far the most computationally efficient configuration under CFL-based time stepping. Among the finer meshes, H20 and C20, which closely follow the riverbanks, produce the smallest Δt_{CFL}, due to the presence of small elements inside the river, where the water depth is the highest. Although H200 is coarser overall, its small elements in deep connection zones reduce the allowable time step, bringing it just above those of H20 and C20. US20 and U20 both perform better with Δt_{CFL} higher than 0.3 s. As a result, H200 who had the best runtime at $\Delta t = 0.1$ s, drops to second place under CFL-based time stepping, with US20 ranking third. Among the three most refined meshes, U20 benefits the most from this new time step, completing the simulation under one hour. In contrast, both C20 and H20 still require around 1 hour and 15 minutes.

Table 3.2: Constant discharge scenario simulations cost. Runtimes are expressed in HH:MM format, while Δt_{CFL} is expressed is seconds

	H20	H200	C20	C200	U20	US20
Runtime with $\Delta t = 0.1$ s	03:10	00:39	03:15	00:42	03:11	00:50
Δt_{CFL}	0.26	0.29	0.26	1.94	0.38	0.32
Runtime with $\Delta t = \Delta t_{CFL}$	01:12	00:14	01:16	00:02	00:52	00:16

The simulation outputs remain relatively stable throughout the simulation period and and are consistent across both time-stepping strategies. For this reason, we focus on the final outputs from the simulation using CFL-based time stepping to compare water column heights (Fig 3.3), velocity magnitudes (Fig 3.4) and discharge distribution across the different mesh configurations. Seeing that they exhibit similar patterns in the river, we will use the finer mesh simulations as reference.

With the exception of C200, all simulations exhibit similar global water repartition patterns and water remains confined to the river channels

(Fig. 3.3). A closer look at the river reveals that, in all cases, water extends over the first elements adjacent to the river. This is caused by the transition from the river channel to the floodplain, which happens over one element. In meshes aligned with the riverbanks (H20, C20, H200, and C200, Fig. 3.3.a, b, d, and e) this transition appears as as a band of semi-wet elements following the river's path. In meshes H200 and C200, where the resolution in the flood plains near the river is relatively low, this transition zone is more noticeable, producing a slightly blurred effect along the riverbanks. In contrast, for meshes without explicit riverbank alignment (U20 and US20, Fig. 3.3.c and f), the transition results in a horizontal step-like interface between wet and dry zones. Within the river, all meshes except C200 reproduce the same general patterns of water depth. H200, although coarser, still captures the main features but with less precision, especially in curved sections of the river.

In terms of discharge repartition between the different river segments, all simulations except C200 display similar patterns. The values reported below correspond to the mean and standard deviation computed across all configurations except C200. A small, almost negligible loss is observed before the first bifurcation, with discharge averaging 97.35±0.74% of the imposed inflow. Downstream of this point, discharge remain stable, with values of 98.00±1.78% between the two meanders and 97.25±1.41% at the downstream end of the domain. Regarding the repartition of discharge between meanders and their corresponding cut-off channels, 82.00±1.84% and 12.98±1.64% of the inflow pass through the Dunavăţ de Sus and its cut-off channel, respectively, while 0.83±0.16% and 89.78±2.73% pass through the Dunavăţ de Jos and its cut-off channel, respectively. In contrast, the C200 configuration exhibits a markedly different behavior. A strong discharge loss occurs immediately after the inflow boundary, with only 30.52% of the imposed discharge remaining in the main channel upstream of the first bifurcation. Discharge then partially comes back to the river downstream, reaching 49.86% between the two meanders and 52.38% at the downstream end. The repartition between meanders and cut-off channels also deviates strongly from the other cases, with only 31.03% and 5.87% of the inflow passing through the Dunavăţ de Sus and its cut-off channel, and 2.05% and 31.34% through the Dunavăţ de Jos

and its cut-off channel, respectively.

Looking at the velocity magnitude (Fig. 3.4), the four finer meshes (H20, C20, U20, and US20, Fig. 3.4.a, b, c, and f) globally show the same patterns. In the zoomed-in views of Fig. 3.4, an area of high velocity is visible along the inner bank of the bend, shifting laterally across the channel at the bend's exit. Some meshes, notably C20 and US20, display additional high velocities area on the inner bank downstream of the bend. H200 (Fig. 3.4.d), by contrast, tends to smooth velocity distributions across the channel width. It slightly underestimates peak velocities in the inner bend and completely fails to capture the low-velocity zones near the outer bank. Contrarily to the water depth results, we don't see velocities extending outside the river in any simulation - except the simulation with the C200 mesh.

For that mesh, we see water spillage north of the river (Fig. 3.3.e) and it fails to represent localized variations across the cross-section of the river channel (Figs. 3.3.e and 3.4.e). Both water levels and flow magnitudes appear overly smoothed when compared with the other simulations.

3.3.3 Second scenario: Flood event

In the flood event scenario, all simulations were run using Δt_{CFL} to reduce computational costs. The runtimes, presented in Table 3.3, are broadly similar to those observed in the constant discharge case, although slightly larger.

Table 3.3: Flood event scenario simulations costs. Runtimes are expressed in HH:MM format

	H20	H200	C20	C200	U20	US20
Runtime with Δt_{CFL}	01:13	00:14	01:17	00:02	00:53	00:17

The hydrodynamic response of each mesh during the flood event scenario reveals clear differences in flooding spatial patterns (Figs. 3.5 and 3.6). Among all configurations, H20 and C20 produce nearly identical inundation patterns throughout the simulation (Fig. 3.5.a and b). Water level increases over the entire river, with a more marked increase

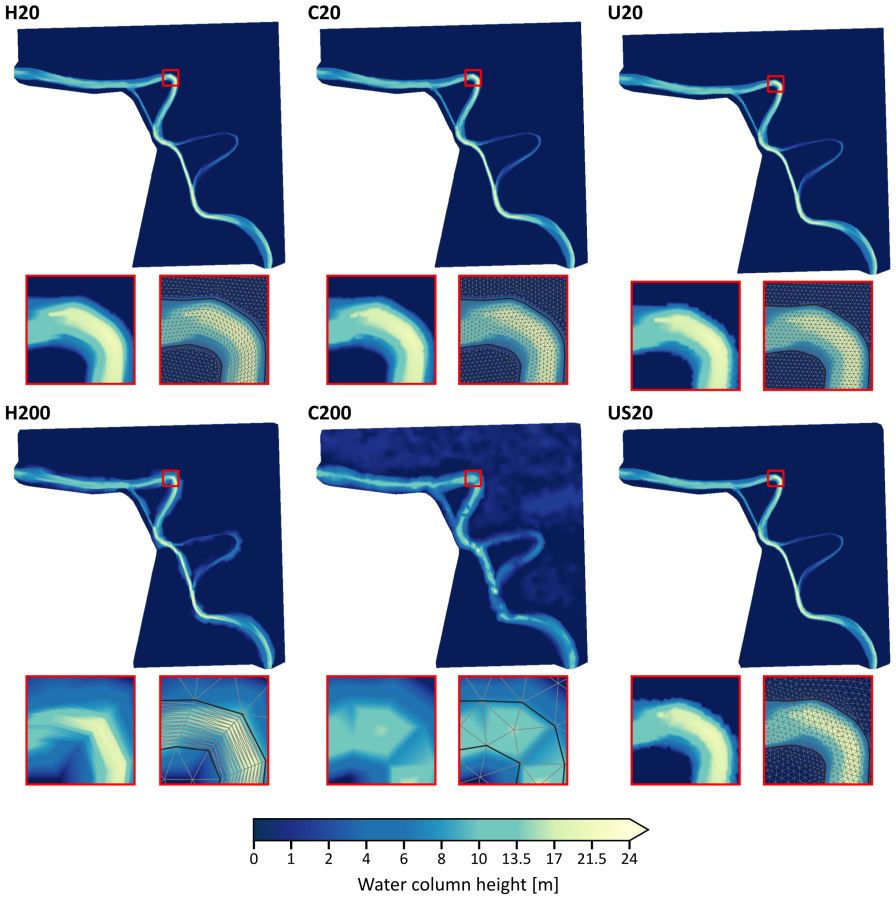

Figure 3.3: Comparison of water column height at the end of the simulation for the six mesh configurations(H20, C20, U20, H200, C200 and US20). Each subplot includes a view of the entire domain and two versions of the same close-up view. The location of the zoomed area is indicated on the domain view by a red square. Both close-ups show the same area, but in the second, the mesh is overlaid: thin gray lines represent element edges, and the wider black line delineates the river boundary. For meshes that do not follow the riverbanks, the river boundary from the H20 mesh is used.

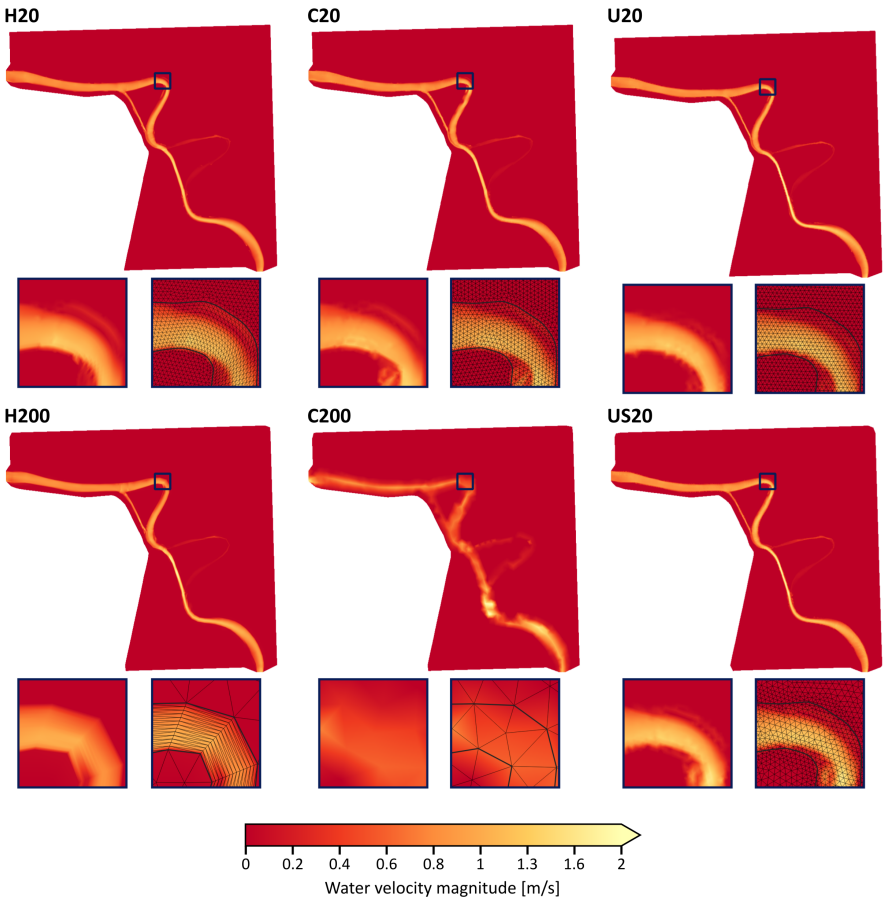

Figure 3.4: Comparison of water velocity magnitude at the end of the simulation for the six mesh configurations (H20, C20, U20, H200, C200 and US20). Each subplot is made of a view of the entire domain, and two versions of the same close-up view. The position of the close-up view is represented on the domain view by a dark blue square. Both close-ups show the same area, but in the second, the mesh is overlaid: thin black lines represent element edges, and the wider black line delineates the river boundary. For meshes that do not follow the riverbanks, the river boundary from the H20 mesh is used.

before and inside the first meander. The second meander that was almost dry in the previous scenario widens for the time of the flood, before coming back to its original shape. When looking at the flooding itself, water spills out of the river and flood the northern part of the domain. We also notice a lake filling up north-east of the second meander. After 11 days, both simulations flooded ~22 km^2, and at the end of the simulation ~20 km^2 stayed flooded. They also show consistent patterns in term of discharge distribution (Fig. 3.7). Given their high resolution, the alignment of their elements with the riverbanks and their consistent agreement, these two meshes are used as reference benchmarks for evaluating the others.

The unstructured mesh US20 reproduces similar flood extents but slightly overestimates water depth in the inundated areas (Fig. 3.5.c). It also provides a coarser representation of the flood pattern details. Despite this, the overall flooded area remains consistent with the benchmark simulations. In this configuration, ~22 km^2 are flooded after 11 days of simulation, and ~21 km^2 stayed flooded at the end. In contrast, U20 and H200 both show noticeable differences when compared to benchmark simulations (Fig. 3.6.a and b). U20 predicts additional flooded areas in the southwestern part of the domain, while H200 displays water spreading into the southeastern part of the floodplains. In addition, H200 shows some irregularities near the river channel, due to the transition zone. Both of these configurations show a flooded area of ~27 km^2 after 11 day. However, the flooding extent differs at the end, with ~20 km^2 flooded at the end of the H200 simulation, against ~25 km^2 in the U20 simulation. The coarsest mesh, C200, performs the worst in term of spatial accuracy, with excessive water spillage everywhere north of the river (Fig. 3.6.c). Its flooding extent after 11 days is of ~29 km^2, which comes down to ~27 km^2 at the end of the simulation. In all cases, once the flood peak has passed, a significant portion of the water remains stored in the floodplains.

We do not observe major differences in the average discharge repartition compared with the constant-discharge scenario, with all simulations—except C200—showing consistent patterns. However, there is a clear change in behavior during the flood event between the two reference cases (H20 and C20) and the other four configurations (Fig. 3.7). In H20 and C20, the discharge downstream of the domain

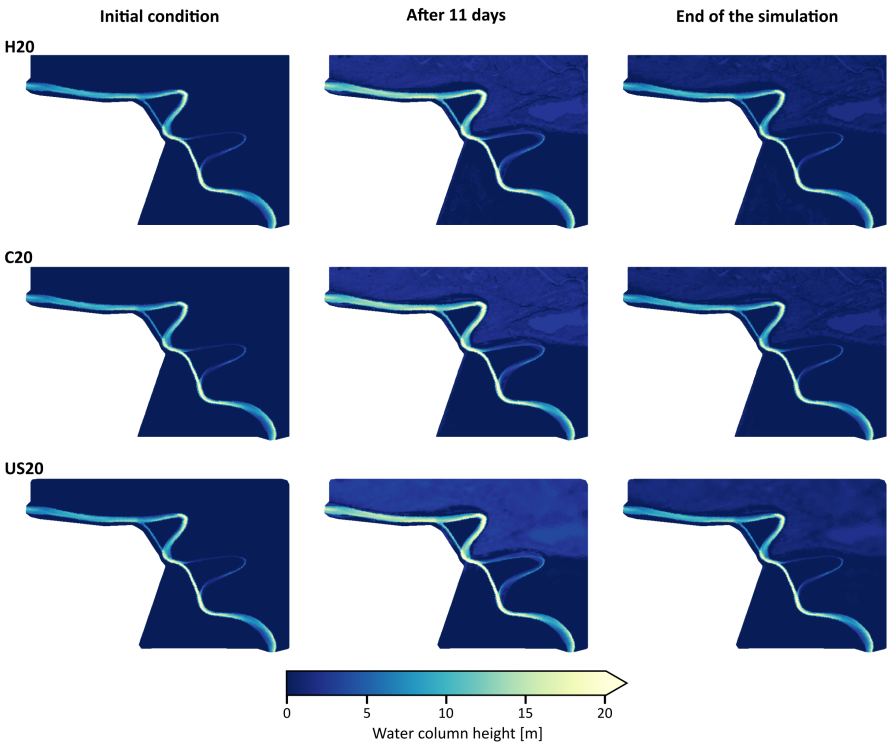

Figure 3.5: Evolution of the water column height during the flood event simulations fo H20 mesh, C20 mesh and US20 mesh. For each simulation, the first column represents the initial condition, the second column is the state of the simulation after eleven days (at the end of the flood peak) and the last column shows the water height at 30 days, the end of the simulated period.

follows the values observed upstream of the first bifurcation and between the two meanders. In contrast, the other mesh configurations produce a downstream discharge peak that temporarily exceeds the upstream values. The relative proportions of flow in the other river segments also deviate slightly from those observed in H20 and C20. In addition, the downstream discharge curves of U20 and US20 display a slightly delayed peak compared to the other cases. As in the constant discharge scenario, there is again a significant discharge loss in the C200 configuration compared with the others.

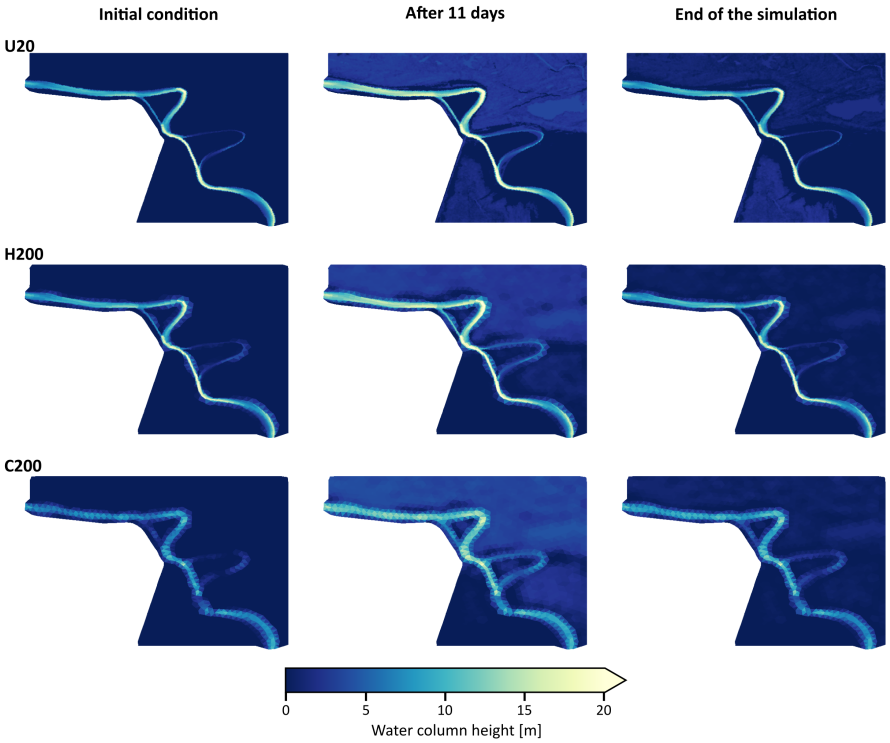

Figure 3.6: Same as Fig. 3.5 but for U20 mesh, H200 mesh and C200 mesh.

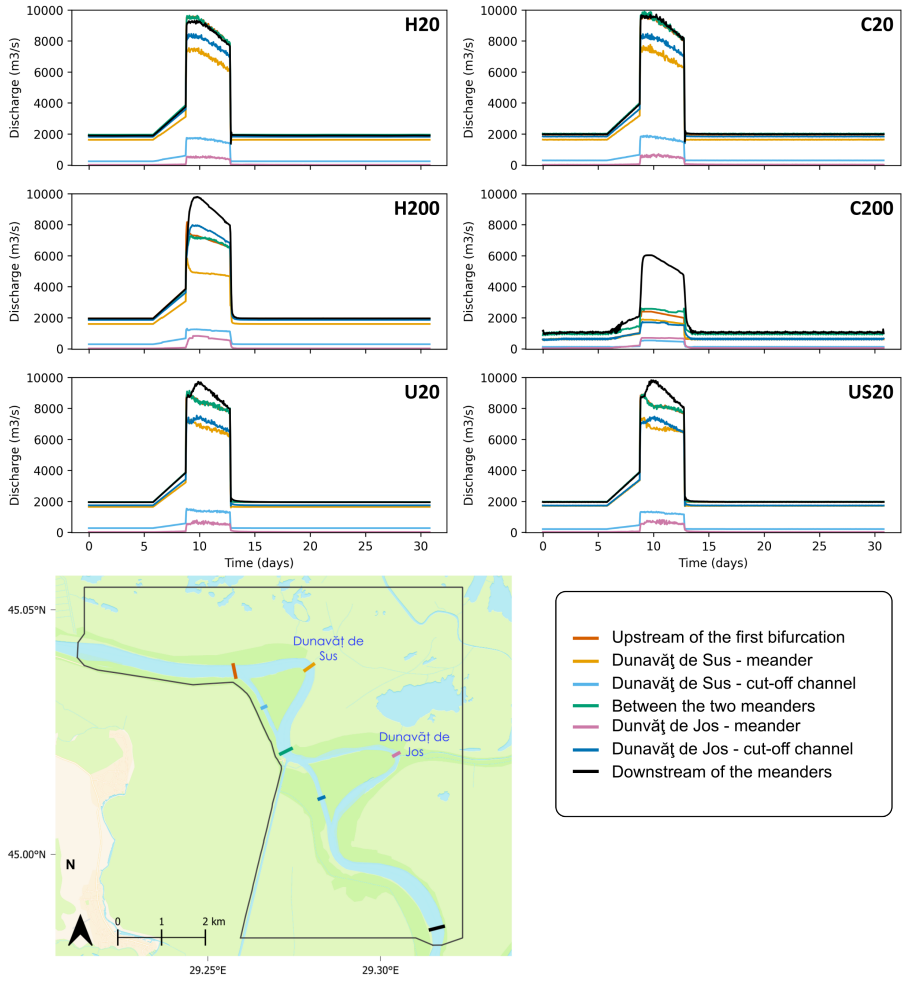

Figure 3.7: Discharge distribution between the river segments for the six mesh configurations (H20, C20, H200, C200, U20 and US20). Each color corresponds to one transect, as described in the legend. The map below shows the location of the transects used to compute discharges, consistently color-coded with the plots, with the model domain boundary is shown in gray. The name of each simulation is indicated in the top-right corner of its respective panel.

3.4 Discussion and conclusion

In this study, we evaluated the hydrodynamic and computational performances of different mesh configurations for river–floodplain simulations using a DG FE model. We found that in-channel hydrodynamic representation and discharge distribution under non-flooding conditions are primarily controlled by the in-river resolution, whereas flood extent and discharge repartition during flooding events depend on the representation of the riverbanks. On the other hand, computational cost increases with the total number of elements and with decreasing size of the smallest element. Based on these findings, we propose to combine a hybrid mesh of 20 x 20 m elements in the river and an unstructured mesh with a gradually increasing element size in the floodplain as the best compromise between accurate in-river representation, best estimation of the flooding extent and computational efficiency.

Our results show that accurate representation of in-channel hydrodynamics in non-flooding scenarios requires sufficiently high resolution within the river; in our case, 200 m was too coarse to capture the patterns reproduced at 20 m. With a 20 m in-channel resolution, all mesh types tested——hybrid (H20), constrained unstructured (C20), uniform unstructured (U20), and unstructured with graded resolution (US20)——produce consistent water depth, velocity patterns and discharge repartition. This aligns with prior findings in studies made with FV models, who showed that mesh resolution, and through it accurate bed shape representation, has greater impact on hydrodynamics models than input bathymetry resolution (Horritt et al., 2007), mesh structure (Bilgili et al., 2023) or other typical calibration parameters (Hardy et al., 1999).

At high resolution (20 m), differences between hybrid and constrained unstructured meshes are minor. While some local deviations occur——particularly in bends or near complex bathymetry——they do not significantly affect the global hydrodynamic behavior. However, at coarser resolution, hybrid meshes clearly outperforms constrained ones. Similar observations were made by Bilgili et al. (2023) and Y. G. Lai (2010), who reported that unstructured meshes require higher resolution to achieve accuracy comparable to curvilinear grids. It must be noted that in our case, the marked differences between H200 and C200 mainly

stem from the fact that hybrid meshes retain higher resolution across the river's width, whereas constrained unstructured meshes reduce resolution more uniformly.

That being said, and while across-channel resolution remains more important than along-channel resolution in river modeling due to the inherent anisotropy of fluvial systems, our results show that high cross-section resolution alone is not sufficient. Along-the-flow resolution must also be adapted to the geometry and flow conditions, particularly in bends and areas with variable bathymetry. In these zones in particular, too coarse along-channel resolution can degrade the representation of the flow velocity. However, the H200 mesh, despite its lower resolution along the river, still performs reasonably well in reproducing the water column height. This is in contradiction with the significant increase in water depth that Bilgili et al. (2023) observed with coarser meshes, but aligns with the findings of Y. G. Lai (2010), who also concluded that water depth is generally less sensitive to mesh structure and resolution than flow velocity. As a results, hybrid meshes with lower longitudinal resolution may remain useful in studies focused solely on water levels, particularly in relatively straight river sections where complex flow dynamics are limited.

For overbank flooding scenarios, our results show that an accurate and explicit representation of the riverbanks is essential. In our study, meshes that do not align with the riverbanks—U20 and US20—either show excessive water spillage or misplaced flooding, as well as a delayed downstream discharge peak. In the case of the uniform mesh, the lack of alignment likely results in an inaccurate representation of bank elevations, creating artificial pathways for water to spill south of the channel. The US20 mesh, even if it is not explicitly constrained by the riverbanks, still has a resolution depending on the distance to the riverbanks, allowing for a more accurate representation of the flooded area. However, it still overestimates the amount of water going into the floodplains. This overestimation is likely due to an inaccurate representation of the bank geometry, which lets more water going out of the river. Yet, explicitly following the riverbanks is not sufficient if resolution near the channel is too coarse. Both H200 and C200, while aligned with the river geometry, provide insufficient resolution at the bank interface. This results in water over-spilling, wrong evaluation of

flooded area and spatially irregular flooding patterns along the channel banks. The excessive spilling observed in these four configurations is reflected in the downstream discharge, which temporarily exceeds the discharge upstream of the first bifurcation, indicating that part of the flow transited through the floodplains rather than the river. These findings aligns with those of Kim et al. (2014), who highlighted that higher resolution and ability to follow riverbanks lead to higher model accuracy.

As expected and seen in the literature (Kim et al., 2014; Bomers et al., 2019), computational cost increases with the total number of elements and decreases with larger minimum element sizes. When using a fixed time step for all simulations, hybrid meshes are slightly more efficient than constrained unstructured meshes at the same resolution. While the difference is small on this small-scale test case, it could translate into significant time savings in large-scale or long-duration simulations. It should however be noted that, while flow-oriented structure of hybrid meshes may offer slightly better memory locality and numerical conditioning (Bomers et al., 2019), the difference in number of elements in the coarsest meshes (~8000 for H200 and ~2000 for C200) is sufficiently marked that C200 should have shown better times. However, in both those meshes, the total number of elements is too small to fully exploit the computational capacity of the GPU (Brodtkorb et al., 2012; Ma et al., 2025). In this under-utilization regime, kernel-launch and memory-management overheads dominate runtime, which makes the small difference observed between C200 and H200 (42 min vs 39 min) not meaningful. When using CFL-based time stepping, the benefits of hybrid meshes depend on their resolution. At high resolution, they remain slightly faster than constrained meshes. However, at lower resolution, the inclusion of small elements in connection zones where the water is deep, significantly reduces the CFL-constrained time step of the hybrid mesh, leading to longer simulation times than their constrained counterparts. Despite its computational performances, the C200 mesh is not a viable option for this test case, as its coarse resolution causes a substantial loss of accuracy, both in river and flooding representation.

Overall, while hybrid meshes show a slight advantage in computational time over triangular fully unstructured meshes, the performance gain

is less pronounced than reported in other mesh comparison studies (Kim et al., 2014; Bomers et al., 2019). This difference may be explained by the nature of our test case: these studies focused on single channel non-braided rivers, meaning they do not have to deal with river segment connections and the resulting small elements in deep water. As a result, their allowable time step for hybrid meshes is higher than for their fully unstructured meshes, leading to significant gains in computational times. In contrast, our domain includes bifurcations and connection zones, where hybrid meshes introduce small triangles in deep water, ultimately limiting their computational advantage. Interestingly, the unstructured mesh with variable resolution (US20) consistently ranks third in terms of computational performance, achieving a good balance between speed and accuracy. Although not the most accurate or the fastest, its adaptability makes it an appealing compromise for many practical applications.

It's worth noting that our performance evaluation focused on runtime. We did not include disk space or memory usage, but these are non-negligible in large domains—especially for high-resolution meshes that require significantly more storage. It must also be noted that we use an explicit scheme, where the allowable time step is constrained by the smallest elements. An implicit scheme would remove this constraint and allow larger time steps, which might give hybrid meshes a clearer performance advantage. However, this would come at the cost of the drawbacks associated with implicit schemes, and a detailed comparison falls beyond the scope of this study.

Based on the meshes we tested in this study and our subsequent findings, we suggest that the most suitable mesh configuration would be a combination of a hybrid high-resolution mesh (similar to H20) in the river, with an unstructured mesh whose resolution decreases with the distance to the riverbanks (like US20) in the floodplains (see example in Fig. 3.8). This approach would explicitly represent the riverbanks, ensure sufficient in-channel resolution for accurate hydrodynamics, and limits computational cost by reducing resolution away from the main flow paths while still capturing flood patterns realistically. The use of this configuration should, however, be approached with caution, as our results are based on simulations performed with a single DG model and may not be directly generalizable to other models or numerical

schemes. Nevertheless, our findings are consistent with previous studies conducted using FV approaches (Hardy et al., 1999; Horritt et al., 2007; Kim et al., 2014; Bilgili et al., 2023). It should also be noted that the comparison between configurations is sensitive to the underlying bathymetry and to the bathymetry smoothing applied, which can influence both local flow distribution and floodplain connectivity.

As is often the case, there are several opportunities to extend or improve this study. First, it should be noted that our results were not validated against observational data. As a result, we cannot say with absolute certainty that simulations using the H20 and C20 meshes reproduce reality more accurately than others. Nevertheless, the consistency of the trends we observe and their agreement with previous studies, give us confidence in our conclusions. In addition, several other mesh configurations could have been tested. While our results clearly favor the finest resolutions in terms of accuracy, we only tested two discrete resolutions——20 m and 200 m. Intermediate resolutions, such as 50 m or 100 m, could potentially have offered better accuracy–cost trade-offs. These alternatives were not explored here in order to limit the number of test cases. Another possibility would be to vary the along-the-flow resolution based on river morphology. For example, coarser hybrid meshes may be sufficient for straight channels, while meanders or areas with complex bathymetry would benefit from finer along-channel resolution. A further improvement that could be tested, would be to introduce an additional row of elements along the riverbanks in the hybrid meshes, which would serve as a transition zone between the river and the floodplains. This could be particularly beneficial for the H200 mesh, potentially reducing excessive water spillage. Beyond these adjustments, alternative mesh types could also be explored. Flow-aligned meshes, for example, have been used successfully for bathymetry reconstruction in rivers (R. Lai et al., 2021) and hydrodynamic modeling in coastal systems (Kernkamp et al., 2011). Another possibility would be adaptive mesh refinement, where spatial resolution is dynamically adjusted during the simulation to refine the mesh in regions of strong gradients or active flooding and coarsen it elsewhere (W. Huang et al., 2015; Hu et al., 2019). These approaches may provide improved representation of flow dynamics while maintaining computational efficiency. Finally, further studies could also

benefit from local time stepping, which assigns to element its own time step, reducing the global computational time (Wang et al., 2024; Ping et al., 2025). This approach would prevent the smallest elements—often located near bifurcations or banks—from imposing unnecessarily restrictive time steps on the entire domain.

Ultimately, the "best" resolution depends on the goals of the study. Our results confirm that high resolution in the river is essential for accurate in-channel hydrodynamics, while proper representation of riverbanks is critical for reliable flood modeling. However, the level of resolution required may vary depending on domain size, computational constraints, and the physical processes being modeled. Above all, this study reinforces a central idea: for reliable riverine hydrodynamics, accurate river and riverbank representation are paramount——regardless of mesh type. Building on these findings, we apply a hybrid strategy in chapter 5 for the hydrodynamic modeling of the Danube Delta, using a hybrid mesh with fine (20 m) resolution in the river and gradually coarsening unstructured elements in the floodplains to balance accuracy of river morphology representation and computational efficiency.

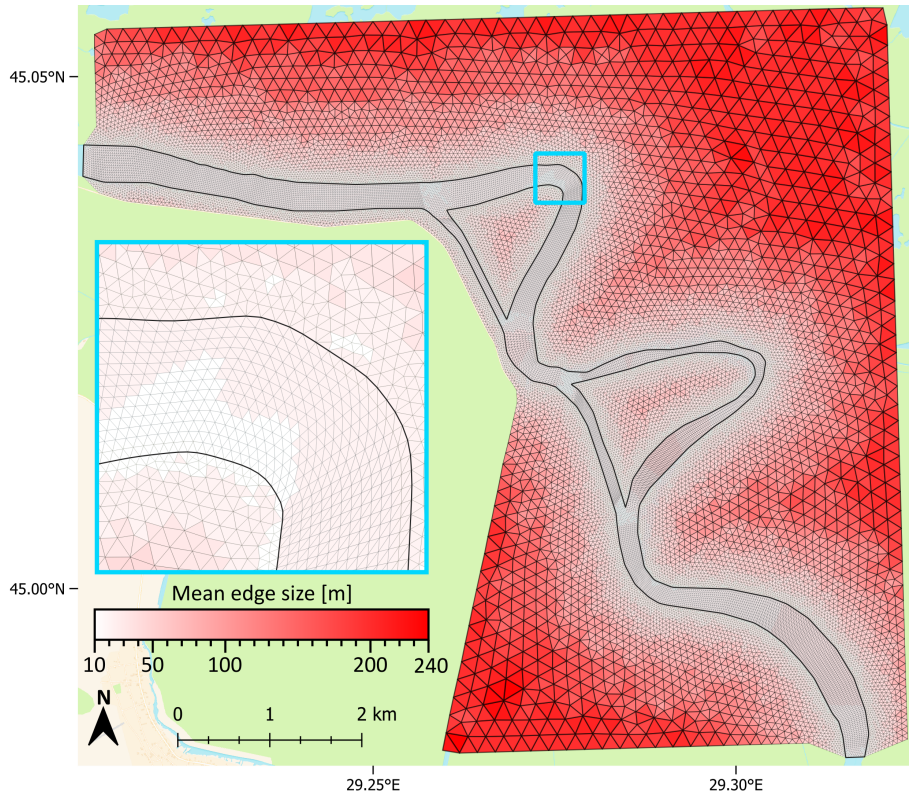

Figure 3.8: Illustration of the hybrid–unstructured mesh configuration recommended based on this study's findings. The main panel shows the full model domain, while the inset on the left (outlined in blue) provides a close-up view of the area highlighted in the full-domain panel. Colors represent the mean edge length of each triangular element, with edge thickness also scaled to the mean edge length for improved visual clarity. The thick black line delineates the river boundaries.

Chapter 4

An integrated high-resolution bathymetric model for the Danube Delta system

This chapter is based on the following article: **Alaerts, L.**, Lambrechts, J., Randresihaja, N. R., Vandenbulcke, L., Gourgue, O., Hanert,E., and Grégoire, M. (2025). An integrated high-resolution bathymetric model for the Danube Delta system. Earth System Science Data, 17 (7), 3125–3140. https://doi.org/10.5194/essd-17-3125-2025

Abstract

Acting as a buffer between the Danube and the Black Sea, the Danube Delta plays an important role in regulating the hydro-biochemical flows of this land-sea continuum. Despite its importance, very few studies have focused on the impact of the Danube Delta on the different fluxes between the Danube and the Black Sea. One of the first step to characterize this land-sea continuum is to describe the bathymetry of the Delta. However, there is no complete, easily accessible bathymetric data on all three branches of the Delta to support hydrodynamic, biogeochemical or ecological studies. In this study, we aim to fill this gap by combining 4 different datasets, three in the river and one for the riverbanks, each varying in density and spatial distribution, to create a high-resolution bathymetry dataset. The bathymetric data was interpolated on a hybrid curvilinear-unstructured mesh with an anisotropic Inverse Distance Weighting (IDW) interpolation method. The resulting product offers resolutions ranging from 2 m in a connection zone to 100 m in one of the straight unidirectional channel. Cross validation of the dataset underlined the importance of the data source spatial pattern, with average Root Mean Square Error (RRMSE) of 0.55 %, 6.3 % and 27.6%, for river segments covered by the densest to the coarsest dataset. These error rates are comparable to those observed in bathymetry interpolation in rivers with similar source datasets. The bathymetry presented in this study is the first unique, high-resolution, comprehensive and easily accessible bathymetric model covering all three branches of the Danube Delta. The dataset is available at https://doi.org/10.5281/zenodo.14055741 (Alaerts et al., 2024).

4.1 Introduction

The Danube, Europe's second-largest river, flows through ten countries and drains an extensive catchment area of ~800,000 km^2 before emptying into the Black Sea, where it is the primary source of water and nutrients. About 110 km before reaching the coast, the river divides into three main branches: the Chilia, Sulina and Sfantu Gheorghe branches (Fig. 4.1). Between those three branches, spanning ~ 5000 km^2, lies the Danube Delta (Driga, 2008; Romanescu, 2013; Bănăduc et al., 2023). The Danube Delta is a complex system of lakes, channels and flood plains. It acts as a crucial buffer zone for water, nutrients and sediments between the Danube river and the Black Sea (Cristofor et al., 1993; Suciu et al., 2002; Sommerwerk et al., 2022). The delta is also a biodiversity hotspot and holds substantial importance for local inhabitants, providing essential resources such as drinkable water, fishing, aquaculture, agricultural lands, transport and recreational activities (Bănăduc et al., 2016; Lazar et al., 2022; Bănăduc et al., 2023).

Among the three branches, Chilia is the northernmost and serves as natural boundary between Ukraine and Romania. It is the youngest and least transformed of the three branches, and includes numerous meanders and islands. It divides into four smaller branches before reaching the sea, creating a secondary delta within the Danube Delta (Romanescu, 2013; Bănăduc et al., 2023). The Sulina branch is located in the center of the delta. It is the shortest and most altered by anthropogenic activities of the three branches. The rectification of the branch, during a so-called 'cut-offs' program, took place at the end of the 19^{th} century and greatly impacted the path and discharge of the Sulina branch, now linking the cities of Tulcea and Sulina in an almost straight line. The branch is the main shipping route of the delta (Panin & Jipa, 2002; Driga, 2008; Duţu et al., 2018). Sfantu Gheorghe is the southernmost branch. Like the Chilia branch, it meanders a lot, but an other 'cut-offs' program was carried-out in the 1980s to rectified all the meander bends, shortening the total length of the branch (Panin & Jipa, 2002).

Despite its ecological and socio-economic importance, comprehensive studies on the delta dynamics and ecological status as a whole are scarce. In terms of bathymetry, some studies have focused on spe-

Figure 4.1: Map of the Danube Delta. The zoomed-out view (bottom left) displays the countries through which the Danube flows, with the river represented by a black line. The red rectangle outlines the area covered by the close-up view. In the close-up view of the delta, the black line marks the boundaries of the zone of interest, while the dashed line indicates the national borders. The basemaps are the Ocean Basemap (Esri, 2018) for the zoomed-out view, and for the close-up view the Voyager map tile by CartoDB, under CC BY 3.0. Data by OpenStreetMap © OpenStreetMap contributors 2019. Distributed under the Open Data Commons Open Database License (ODbL) v1.0.

cific channels (Jugaru Tiron et al., 2009; Roşu et al., 2022) and broader campaigns have covered entire branches (DDNIRD, 2015; Duţu et al., 2018). There is however no publicly available bathymetry product covering the entirety of the three branches to support hydrodynamic, biogeochemical or ecological studies on the Danube Delta as a whole. Bathymetry plays an important role in the description of aquatic environment. Overly coarse resolution or poor-quality bathymetric data can result in substantial errors in predicting water column heights, flood extents, velocities, and shear stress. In larger systems like deltas

and estuaries, these inaccuracies can substantially affect the distribution of water (Merwade et al., 2005; Dey et al., 2022; Fuchs et al., 2022).

Our goal in this study is to produce a complete bathymetry model of the three branches of the Danube Delta, from the city of Issacea to the Black Sea (Fig. 4.1). To achieve that objective, we will use four different datasets that will be interpolated on a hybrid curvilinear-unstructured mesh. The resulting product will subsequently be used in hydrodynamic models to better represent the role of the delta within the Danube-Black Sea land-continuum.

4.2 Data and Method

4.2.1 Data sources

We used data coming from four different sources. The first source is Copernicus' Digital Elevation Model (DEM) (European Space Agency, 2021). We used it to determine the riverbanks' position and height. It has a resolution of 30 m, and the data dates from 2021. The three other sources describe the bathymetry inside the river (Table 4.1). For the section of the Danube upstream of the delta and the Chilia branch (represented in yellow in Fig. 4.2), the data come from measurements made by the Ukrainian Scientific Center of Ecology of the Sea (UkrSCES) between 2014 and 2017. The data points were collected without adhering to a specific sampling pattern, resulting in variable distances between points and inconsistent sampling density (Fig. 4.2.b.). The averaged distance between two points is 160 m but can decrease down to $\sim$ 50 m. With 1925 data points, this dataset has an averaged point density of 3.2×10^{-5} points/m^2, which is rather low compared to datasets used in other studies (Legleiter & Kyriakidis, 2008; Merwade, 2009; Liang et al., 2022). The section upstream of the Sulina-Sfantu Gheorghe separation and the Sulina branch (Fig 4.2.c.) are covered by data from the Galati Lower Danube River Administration (AFDJ). This data is composed of measurements made on a regular grid of $\sim$ 1 m resolution and dates from 2018. This dataset is composed of 14.5×10^6 points, which gives a data point density of 0.4 points/m^2, which is a very high density for a bathymetric survey (Legleiter & Kyriakidis, 2008; Merwade, 2009; Liang et al., 2022). Data for the Sfantu Gheorghe branch

comes from the Danube Delta National Institute for Research and Development (DDNIRD) (DDNIRD, 2015). This data is made of transects spaced 300 m apart on average (Fig 4.2.d.). The distance between two points within each transect is ~ 3 m. The measurement campaign was carried out in 2015. There are 5.23×10^4 points in this dataset, and the point density is 1.7×10^{-3} points/m^2. This density is in the lower range of what is normally observed in bathymetry interpolation studies (Legleiter & Kyriakidis, 2008; Merwade, 2009; Liang et al., 2022). Due to data scarcity in the region, it was impossible to obtain bathymetric data of the same year for the entire domain.

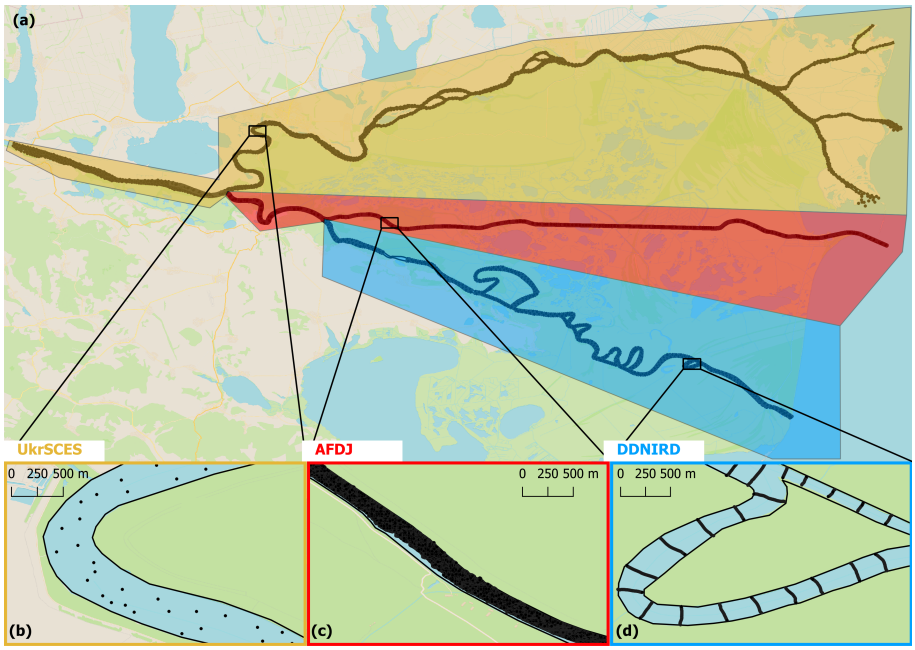

Figure 4.2: (a) Distribution of bathymetry sources within the delta. Each color represents a different source: UkrSCES in yellow, AFDJ in red, and DDNIRD in blue. Each black dot represents an individual bathymetry data point. **(b-d)** The bottom three panels provide close-up views at the same scale, displaying the bathymetry sampling points and highlighting the variations in sampling density among the three distinct bathymetry sources. The background image is the Voyager map tile by CartoDB, under CC BY 3.0. Data by OpenStreetMap © OpenStreetMap contributors 2019. Distributed under the Open Data Commons Open Database License (ODbL) v1.0.

Table 4.1: Characteristics of the different bathymetry data sources within the river. Averaged spacing for the DDNIRD dataset corresponds to resolution within a transect/resolution between transects.

Source	Sampling strategy	No. of points	Density of points [points/m^2]	Averaged spacing [m]	Sampling years
UkrSCES	Random points	1925	3.2×10^{-5}	160	2014-2017
AFDJ	Regular grid	14.5×10^{6}	0.4	~ 1	2018
DDNIRD	Transects	5.23×10^{4}	1.7×10^{-3}	$\sim 3/300$	2015

4.2.2 Bathymetry interpolation

Given the diverse data sources, a certain degree of standardization was necessary. First, we had to transition most of the data from their local vertical datum to the WGS84 vertical datum. The UkrSCES data were referenced to the Odessa datum, which is 0.17 m below the WGS84 vertical datum. For AFDJ data, most of the Sulina channel was referenced to the Marea Neagra Sulina datum, 0.03 m above WGS84, while data upstream of Tulcea and the beginning of the Sulina channel used the Tulcea datum, 0.33 m above WGS84. DDNIRD data were referenced to the Marea Neagra 75 datum, 0.25 m above WGS84 (Anastasiu, 2014).

To merge the different bathymetry sources into a unified bathymetry product, a grid spanning the entire delta is required. In this study, we used a hybrid curvilinear-unstructured mesh (Fig. 4.3). The mesh consists of quadrilateral elements elongated along the flow in the unidirectional river segments (Figs. 4.3.b. and 4.3.d.), combined with unstructured triangular elements in the connection zones between segments (Fig. 4.3.c.). This configuration provides an accurate representation of both the river's course and the bottom topography, while minimizing disk space requirements (Y. G. Lai, 2010; Bomers et al., 2019). As the mesh elements adapt to follow the shape of the river, the resolution is not constant. Perpendicular to the river, resolution varies between 2 and 12 m, with an average of 5 m. Along the river, element sizes range from 37 to 102 m, averaging 52 m. In the connection zones, smaller elements are used, ranging from 2 to 9 m, with an average resolution of 5

m. Overall, mesh resolution varies from 2 m (in a connection zone) and 102 m (on an edge along the riverbank). Further details on the mesh construction can be found in Chapter 3.

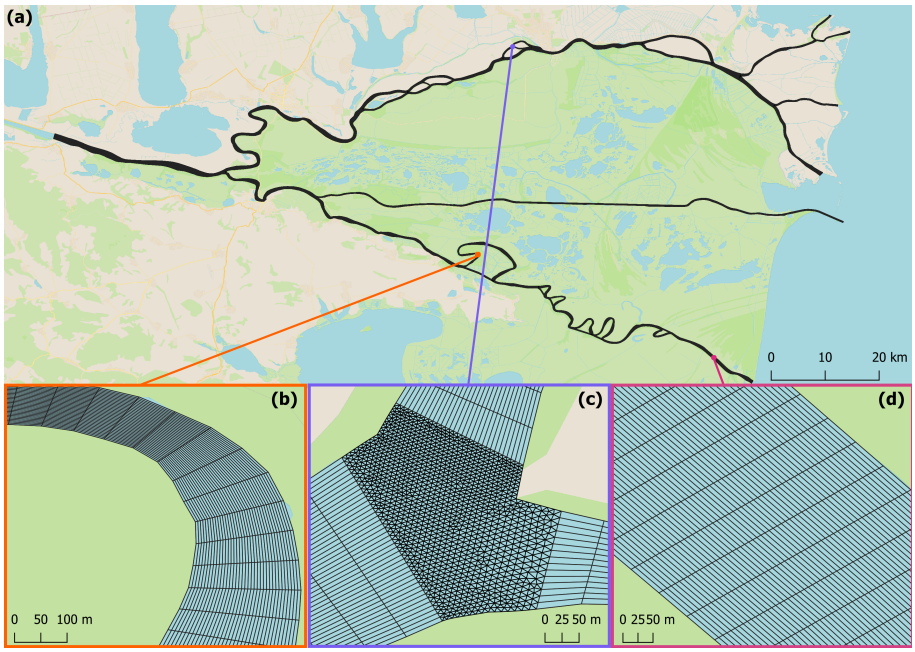

Figure 4.3: **(a)** Illustration of the hybrid curvilinear-unstructured mesh on the Danube, with zooms on **(b)** a bend in the river followed by a narrowing of the river,**(c)** a connection zone between segments with its unstructured meshing and **(d)** a straight portion of the river. The background image is the Voyager map tile by CartoDB, under CC BY 3.0. Data by OpenStreetMap © OpenStreetMap contributors 2019. Distributed under the Open Data Commons Open Database License (ODbL) v1.0.

The data was then interpolated onto the generated mesh. Interpolation in river systems present unique challenges due to their inherent anisotropy: bathymetric variations tend to be more pronounced across the river than along its course. To address this, most present-day methods involve projection into a channel-centered coordinate system, often referred as an s,n-coordinate system or curvilinear coordinate system. In this system, s either represents the centerline or the thalweg of the river, and n its perpendicular. Further explanations on the projection can be found in Chapter 2.1.3. Once the bathymetric data is

projected in the s,n-coordinate system, an anisotropic interpolation is performed. In this study, we chose an anisotropic Inverse Distance Weighting (Inverse Distance Weighting (IDW)) interpolation method, as it is easy to implement and has shown good results in previous studies (Merwade et al., 2006; Diaconu et al., 2019; Liang et al., 2022). Each unidirectional river segment was assigned its own s,n-coordinate system, and interpolation was performed segment by segment. To ensure smooth transitions between adjacent segments, the connections zones were included in the projection and interpolation processes of each of their neighbouring segment. As a result, each point in the connection zones was assigned multiple bathymetry values, which were then combined using a weighted mean, with weights inversely proportional to the distance from the corresponding segment. Further details on the interpolation method can be found in the Appendix 2.1.3.

4.2.3 Validation

Cross-validation

The lack of data in the Danube Delta means that there was no independent dataset to validate our bathymetry product. As a result, we chose to use a 'leave-one-out' cross-validation technique (Wu et al., 2019; Liang et al., 2022). In this method, one observation point is iteratively removed, and the interpolation is applied to estimate the bathymetry at that location. The estimated value is then compared to the actual observed data and this process is repeated for each point in the dataset. We chose this technique because it is best suited for datasets with low point density where every observation point is valuable. It is however time-consuming since the process has to be repeated for each point of the dataset. This becomes particularly challenging with very large datasets, like the one from AFDJ, that contains 14.5×10^6 data points. To counter this problem, we chose to use a randomly selected subset of the points where the number of points is too high. As the validation is done segment by segment, we took a random sample of 1000 points for every segment that is covered by more than 1000 data points. In segments with less than 1000 points, all the points were used. Errors in the connection zones were calculated separately from those in the segments. The error metrics we used in the valida-

tion are the Root Mean Squared Error (RMSE) and Relative Root Mean Squared Error (RRMSE):

$$RMSE = \sqrt{\frac{1}{n}\sum_{i=1}^{n}(z_{obs,i} - z_{predicted,i})^2}, \tag{4.1}$$

$$RRMSE = \frac{RMSE}{\frac{1}{n}\sum_{i=1}^{n} z_{obs}, i} \times 100\%, \tag{4.2}$$

where $i = 1, ...n$ are the n points tested on the segment, $z_{obs,i}$ represents the observed value at the i^{th} point, $z_{predicted,i}$ represents the interpolated bathymetry at the same point. The error in the connection was computed separately from the error in the segments, to be able to find the optimum combination method in the connection zone.

Comparison with global models

At present, there is no unique high-resolution bathymetry dataset easily available for the Danube Delta. In areas where such data is lacking, hydrodynamic models can use global bathymetry models as an alternative. To ensure that the bathymetry product developed in this study offers a clear improvement over existing resources, we compared it against two widely-used global bathymetry models: ETOPO 2022 (NOAA National Centers for Environmental Information, 2022) and GEBCO 2024 (GEBCO Compilation Group, 2024). Both models provide bathymetric data on a global scale, delivered on a grid with a resolution of 15 arc-seconds (~330 m).

4.3 Bathymetry product

The final bathymetry product of this study covers the three main branches of the Danube Delta, including all the channels and meanders for which data were available, from Issacea to the Black Sea (Fig. 4.4). Detailed views of three areas, each covered by a different bathymetry data source, demonstrate the consistency between the interpolation and the observed data (Fig. 4.4.b-d). The dataset includes over 5.8×10^5

points. The bathymetry values range from -3.4 m (negative values indicate points above the reference level) on a dike, to 38.8 m in the river near Tulcea, with an average depth of 8.2 ± 5.06 m.

Our results align with general river morphology. The bathymetry displays anisotropic patterns, with more pronounced depth variations across the river than along its flow (Fig. 4.4 b., c. and d.). Greater depths are observed at the center of straight channels (Fig. 4.4 c.), and on the outer bends of the curves (Fig. 4.4 b. and d.). The meanders of the Sfantu Gheorghe branch tend to be shallower than the man-made straight channels created during the cut-off programs (Fig. 4.5). These patterns derive from hydrodynamic forces and sediment transport processes. Erosion tend to be more pronounced in areas with higher water velocities, such as outer bends and the center of straights channels. By contrast, sediment deposition is higher in slower-moving regions, like inner bends and meanders. In meandering channels, secondary helical flows, which transfer water from the outer bend near the surface downward toward the inner bend near the riverbed, further contribute to sediment accumulation in the inner bend (Bridge, 2003; Nelson et al., 2003).

Not all of the Sfantu Gheorghe branch meanders exhibit the same behaviours (Fig. 4.5). For example, while M1 and M3 meanders are indeed shallower than their respective artificial canals, the M2 meander displays the opposite pattern. Tiron Duţu et al., 2014 observed the same phenomenon, attributing it to the fact that the M2 meander has retained much of its activity, with its artificial canal being comparatively less active than those associated with M1 and M3. This unequal distribution of flow between the meander and the man-made channel is attributed to several geomorphological control factors, including the channel length ratios, the diversion angle (i.e. angle between the main channel and the entrance of the diversion channel) and the bed level differences.

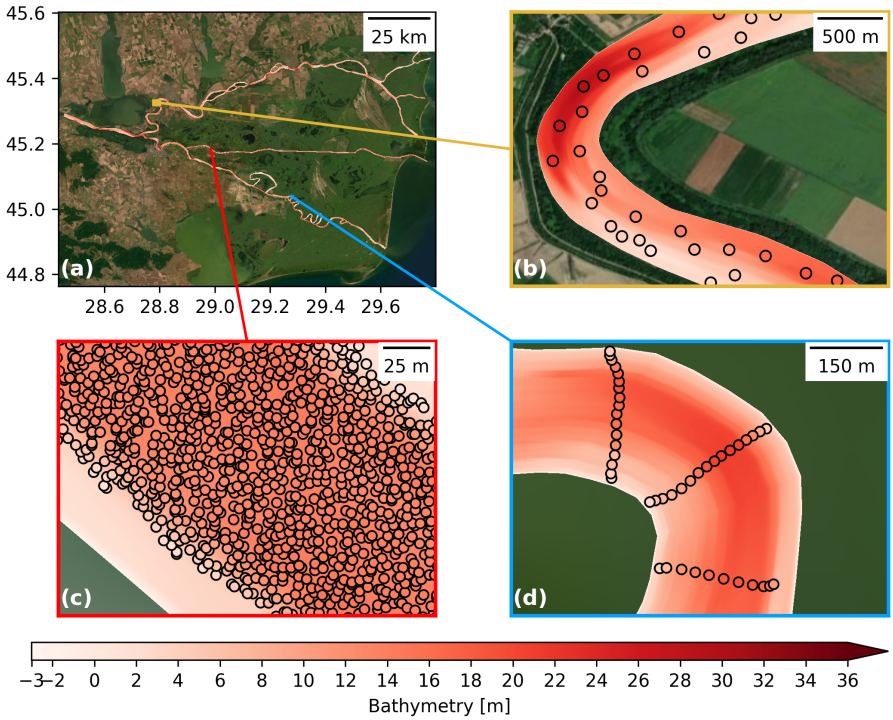

Figure 4.4: (a) Map of the interpolated bathymetry in the Danube Delta, with close-up views **(b-d)** showing the interpolated bathymetry in the background and observations as colored dots. The modeled and observed bathymetry share the same colorbar in all the panels. **(b)** Close-up on the Chilia branch. **(c)** Close-up on the Sulina branch, where the observation data have been resampled to display 1/15 of the points for clarity. **(d)** Close-up on the Sfantu Gheorghe branch, where the observation data have been resampled to display 1/7 of the points for clarity. The background image is the Esri World Imagery basemap (ESRI, 2025).

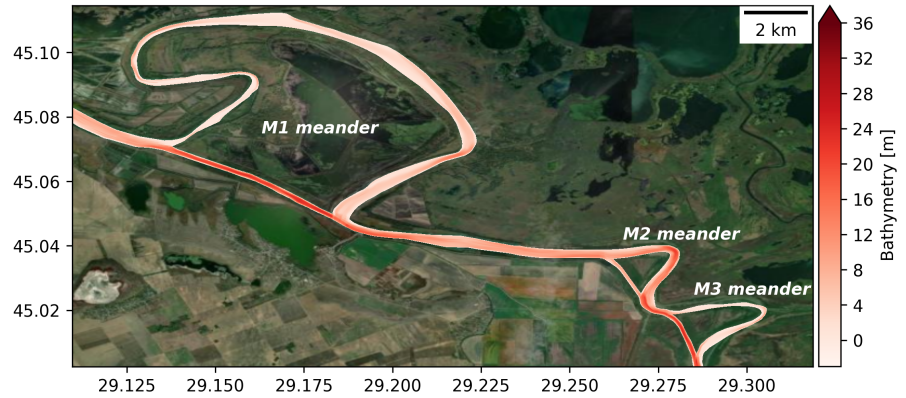

Figure 4.5: Map of the interpolated bathymetry in a section of the Sfantu Gheorghe branch. M1 and M3 meanders present a shallower bathymetry than their respective artificial canal, while M2 meander is deeper than its man-made cut-off channel. The background image is the Esri World Imagery basemap (ESRI, 2025)

4.4 Validation

4.4.1 Validation

The RRMSE for each segment is strongly influenced by the primary bathymetric source (Fig. 4.6). Segments predominantly based on UkrSCES data show an average RRMSE of 27.6 ± 13.4 % (RMSE = 1.78 m). In contrast, segments primarily using AFDJ data exhibit a lower average RRMSE of 0.55 ± 0.34 % (RMSE = 0.07 m). In segments where the DDNIRD serves as the primary data source, the average RRMSE is 6.3 ± 2.55 % (RMSE = 0.5 m). In the connection zones, where a weighted mean was performed to ensure smooth transitions between segments, the average RRMSE is 1.90% (RMSE = 0.26 m).

Those results are comparable to those reported in studies using similar interpolation techniques. We did not find any studies that used datasets with a point resolution as low as that of the UkrSCES dataset. However, the RRMSE obtained for UkrSCES covered segments are similar to those of Merwade, 2009 for two rivers with a random point distribution and a density approximately 3000 times higher than the UkrSCES dataset. For the DDNIRD dataset, our results are on par with or better than those found in the literature with transect and similar

point densities (Merwade, 2009; Liang et al., 2022). We also found no studies using datasets with a point density as high as that of the AFDJ, but our RRMSE in AFDJ dominated segments is close to 0, indicating excellent alignment with the observed data. Additionally, our results conform to well-established river morphological patterns. They present a greater variation in depth across the river than along its flow, and deeper areas on the outer bends. The bathymetry in the Sfantu Gheorghe meanders reflects what has been observed by Tiron Duţu et al., 2014. As a result, we consider the bathymetric product to be of the highest possible quality with the available data sources.

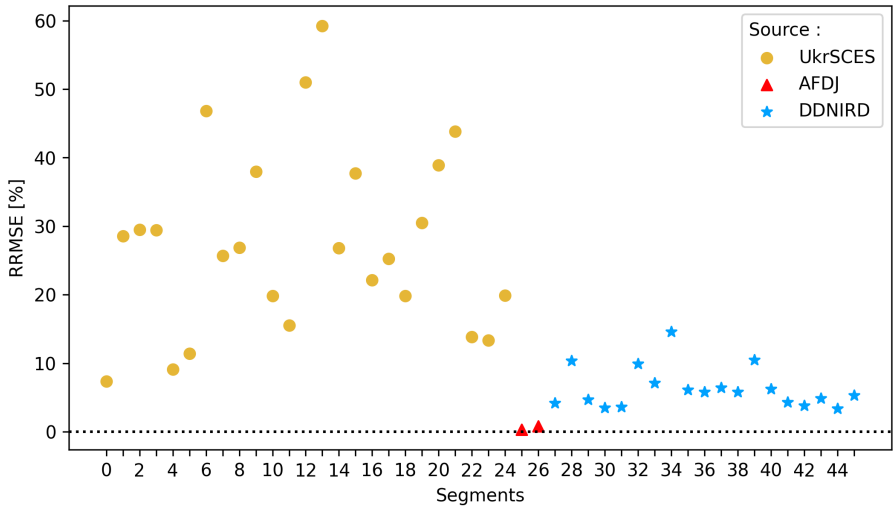

Figure 4.6: RRMSE for the bathymetry of each segment. The color and shape of the markers correspond to the main bathymetry data source covering the segment. The horizontal dotted line highlights the 0% RRMSE line.

4.4.2 Comparison with global bathymetry models

Our bathymetry product presents a significant improvement in representing the Danube Delta over global bathymetry models like ETOPO 2022 and GEBCO 2024 (Fig. 4.7). With a grid resolution of ~ 330 m, these global models struggle to represent the river bathymetry. In many cases, they either fail to capture the river's course or significantly underestimate its depth. Due to the coarse pixel size, which frequently ex-

ceeds the width of the river, they are unable to represent the depth variations within the river channel. While ETOPO 2022 and GEBCO 2024 are good bathymetry product for oceanographic applications, they lack the necessary resolution to represent river processes. In contrast, our bathymetry product, which has a much higher resolution, is specifically tailored to capture these critical riverine dynamics, making it a more suitable tool for river-related studies and models.

4.4.3 Limitations

The most obvious limitation of this study comes from the data used. The first problem is linked with the data resolution. In particular, additional bathymetric data would be beneficial for river segments covered by the UkrSCES and DDNIRD datasets, and a higher-resolution DEM could improve shoreline delineation. For the UkrSCES dataset, the overall number of points is too low, and more data points should be taken, with special care to take points all across the width of the river. In the case of the DDNIRD, the overall density is good but the spacing between transects is too high to ensure correct representation of the continuity of the bed between measurements. To improve the quality of the results, the best solution would be to increase the density of points in the river, particularly for the UkrSCES dataset, and to a lesser extent for the DDNIRD dataset. For the former, any input of bathymetry point would be useful, as random-based bathymetry datasets can achieve performance comparable to transect-based data, if the density is high enough and points are correctly distributed across the width of the river (Merwade, 2009). For segments covered by the DDNIRD dataset, we suggest increasing transect frequency or adding longitudinal profiles parallel to the shores, as proposed by Diaconu et al., 2019. Concerning the topography data, the 30 m resolution of Copernicus' DEM may be insufficient to precisely define the riverbank positions. A higher-resolution DEM could improve accuracy, but to our knowledge, no such dataset is publicly available for this region.

The other limitation linked with the data initiates from the temporal disparity between datasets. The different measurements used in this study were taken between 2024 and 2021. The AFDJ and DDNIRD datasets were each collected within a single year, in 2018 and 2015,

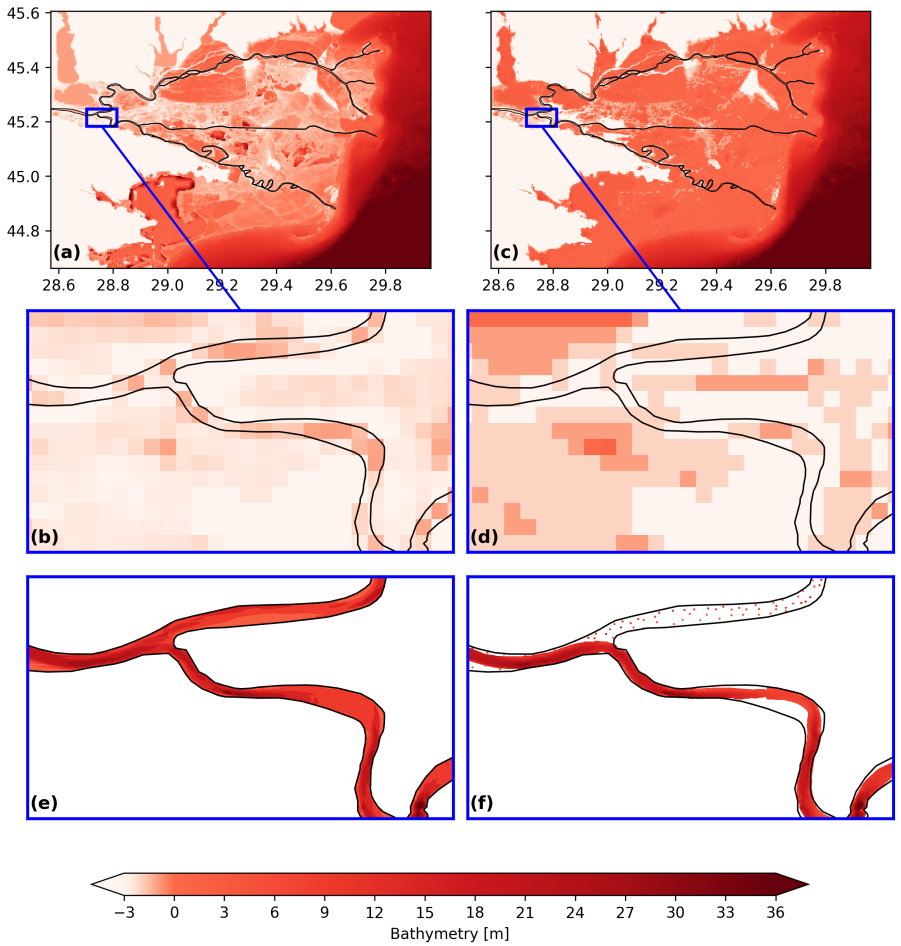

Figure 4.7: Comparison of ETOPO 2022 and GEBCO 2024 bathymetry of the delta with this study's results and observations. The Black line represent the Danube riverbanks. (a) Delta bathymetry according to ETOPO 2022 (NOAA National Centers for Environmental Information, 2022), with (b) a close-up view on ETOPO 2022 data in the Danube. (c) Delta bathymetry according to GEBCO 2024 (GEBCO Compilation Group, 2024), with (d) a close-up view on GEBCO 2024 data in the Danube. (e) Bathymetry product presented in this study. (f) Observations data points used in this study.

respectively. This is not the case for the UkrSCES dataset, whose data spans three years (2014-2017). The topography readings originate from the 2021 Copernicus DEM. Rivers are very dynamic ecosystem, and the Danube is no exception, with both natural erosion/deposition of sediments and man-made dredging happening at different points along the river (Jugaru Tiron et al., 2009; Habersack et al., 2016; FAIRway Danube, 2021). It is therefore highly unlikely that the bathymetry and position of the riverbanks remained the same during the entire sampling period. As such, it is only natural that we observed discrepancies at places where two different bathymetry sources meet. Despite this, the datasets used in this study were carefully selected to minimize temporal gaps while prioritizing the highest available spatial resolution and accessibility, ensuring the best possible representation of the riverbed for an easy-access bathymetry product. Regarding the Copernicus DEM, since no product was available for the years corresponding to the bathymetry measurements, we used the latest available dataset at the time of data collection, as it provided the best possible topographic coverage for the region.

The "by segment" interpolation used to allow reprojection in s,n-coordinate system is also a source of discontinuities between segments. The use of a weighted mean combination method in the connection zones reduced those discontinuities in the interpolation results and allow for more realistic transitions.

4.4.4 Applications

This work presents the first bathymetry dataset that comprehensively covers all three branches of the Danube Delta, marking a significant advancement in the characterization and understanding of the delta.

One of the possible applications for this dataset is its use in a hydro-biogeochemical model of the Danube-Black Sea continuum. The Danube Delta plays an important buffering role between the river and the sea, but most present-day models do not represent the delta (Beckers et al., 2002; Grégoire & Friedrich, 2004; Kara et al., 2008; Kubryakov et al., 2018; Lima et al., 2020). This oversimplification can lead to inaccuracies in the representation riverine inputs to the sea,

which can in turn significantly impact the simulation of coastal processes (Rose et al., 2017; Breitburg et al., 2018; Ivanov et al., 2020; Bonamano et al., 2024). Therefore, having a high-resolution, easily accessible bathymetry dataset for the Danube Delta's branches is an important step toward improving the Black Sea coastal models and better understanding interactions within the Danube-Black Sea continuum. With that application in mind, future improvements to this dataset could include extending coverage to the shallow coastal waters in front of the delta.

Our bathymetry product could also be useful for flood risk assessment in the Danube Delta. The region is characterized by low elevations and minor altitude variations, with ~ 93% of its surface lying between 0 and 2 m above sea level. As a results, and despite the moderate rainfall in that area, the Danube Delta experience annual flooding (Niculescu et al., 2015). Coupled with a high-precision DEM, our bathymetry dataset could be used to represent the flooding processes within the delta. It could also support evaluations of infrastructure impacts, such as those of dikes and floodplain modifications, on flood extent and dynamics.

In addition, this bathymetry dataset can be used in ecosystem and habitat modeling. Designated a UNESCO World Heritage Site since 1990, the Danube Delta is Europe's largest nearly undisturbed wetland and is considered a major biodiversity hotspot (Sommerwerk et al., 2022; Simon & Andrei, 2023). Water depth, and by extension underwater topography, are key components of habitat suitability models. They influence many wildlife activities, including fish breeding, benthic communities distribution, reed bed development and bird nesting (Zigler et al., 2008; Sultanov, 2019; Y. Zhang et al., 2024). High-resolution bathymetry can help pinpoint areas of ecological importance and guide conservation efforts.

While this dataset is currently only available through conventional repositories, future developments could focus on integrating it into an interactive WebGIS platform. WebGIS tools are getting increasingly used for disseminating scientific datasets in various fields (Dragićević, 2004; Pasquaré Mariotto et al., 2021; Foglini et al., 2025). They allow for an easy access and a larger dissemination of the information, providing broader accessibility beyond the scientific community that

typically engages with data repositories. Web-based platform enable intuitive visualization, exploration, and interaction with the data, often incorporating tools for processing, analysis, and modeling. Although implementing such a system would require additional technical development and falls beyond the scope of this study, it could be a logical step toward enhancing the usability and impact of this dataset for a wider range of users, including policymakers, environmental managers, and researchers.

4.5 Conclusion

This dataset is the first unique, high-resolution, comprehensive and easily accessible bathymetric model covering all three branches of the Danube Delta. We combined four different datasets of varying density and spatial patterns on a hybrid curvilinear-unstructured mesh using an anisotropic IDW interpolation method. The resulting product is made of 5.8×10^5 elements, with a resolution ranging from 2 to 100 m. Cross-validation confirmed that the error rates are comparable to those reported in similar interpolation studies, leading us to conclude that this product is as accurate as possible, given the available data. By offering better resolution and accuracy, this product will allow more precise simulations of river-coastal dynamics, providing essential insights for both scientific research and environmental management in the region.

Appendix

4.A Parametrization

A sensitivity analysis was carried out to identify the optimal values for the parameters *an*, *np*, and *p* of the interpolation method (Eqs. 2.8 and 2.9) in the river segments. For the anisotropy factor *an*, we tested integers between 1 and 20, followed by multiples of 10 up to 100. The maximum value of 100 was chosen based on the Danube Delta National Institute for Research and Development (DDNIRD) data, where the distance within a transect is approximately 3 m, while the distance between transects is about 300 m. The values tested for the number of neighbors *np* and the exponent *p* are respectively integers between 2 and 8, and integers between 1 and 3. To select the best set of parameters, we looked for the set of parameters that minimized the error obtained with the 'leave-one-out' cross-validation technique. For segments with more than 1000 points, where a random sample of 1000 points was used for testing, the same 1000 points were tested for each parameter set.

The optimal parameters for each segments are presented in Tables 4.A.1 and 4.A.2. Overall, we did not find any definitive rule to define the optimum values of *an*, *np* and *p* parameters of the segments. However, certain trends can be observed regarding the dimensionless anisotropic factor *an*. Segments covered by bathymetry primarily sourced from Ukrainian Scientific Center of Ecology of the Sea (UkrSCES) data tend to require a higher *an* value, with a median of 18. Segments relying on Galati Lower Danube River Administration (AFDJ) or DDNIRD data have lower median *an* of 1 and 2, respectively. We observed no clear trend between the optimal values of the other

parameters and the source of the observation data. Segments mainly relying on AFDJ data appear to be insensitive to variations in parameter values.

Table 4.A.1: Combination of parameters for the interpolation of the bathymetry that gives the lowest error for each segment covered by the UkrSCES dataset.

Segment ID	*np*	*p*	*an*	RMSE *[m]*	RRMSE *[%]*	Source
0	3	2	14	1.21	7.35	UkrSCES
1	5	3	8	2.48	28.52	UkrSCES
2	7	1	18	2.10	29.50	UkrSCES
3	2	1	15	1.57	29.45	UkrSCES
4	2	3	90	0.60	9.09	UkrSCES
5	4	1	13	1.02	11.39	UkrSCES
6	2	3	30	1.54	46.81	UkrSCES
7	4	1	8	1.44	25.68	UkrSCES
8	3	3	6	2.69	26.89	UkrSCES
9	5	3	40	3.58	37.94	UkrSCES
10	6	2	14	1.54	19.84	UkrSCES
11	8	2	100	0.97	15.49	UkrSCES
12	3	3	100	2.09	51.00	UkrSCES
13	5	1	50	4.30	59.24	UkrSCES
14	5	2	100	1.57	26.81	UkrSCES
15	3	2	5	3.06	37.75	UkrSCES
16	4	2	20	1.25	22.10	UkrSCES
17	2	1	18	1.64	25.22	UkrSCES
18	4	2	15	1.50	19.82	UkrSCES
19	6	2	8	1.61	30.48	UkrSCES
20	4	1	1	1.29	38.89	UkrSCES
21	4	1	20	1.91	43.83	UkrSCES
22	4	1	30	1.04	13.82	UkrSCES
23	2	3	9	1.14	13.34	UkrSCES
24	3	2	18	1.44	19.89	UkrSCES

This initial parametrization worked well for sparse, randomly distributed bathymetric data and high-density bathymetry, such as the data from the UkrSCES and the AFDJ. For the DDNIRD data, where

Table 4.A.2: Combination of parameters for the interpolation of the bathymetry that gives the lowest error for each segment covered by the AFDJ or the DDNIRD datasets.

Segment ID	*np*	*p*	*an*	RMSE *[m]*	RRMSE *[%]*	Source
25	2	1	1	0.04	0.31	AFDJ
26	2	1	1	0.09	0.79	AFDJ
27	6	3	7	0.31	4.13	DDNIRD
28	2	1	14	0.32	12.66	DDNIRD
29	2	2	1	0.51	3.50	DDNIRD
30	3	2	1	0.42	5.09	DDNIRD
31	4	3	2	0.27	3.02	DDNIRD
32	3	2	1	0.35	6.72	DDNIRD
33	6	2	1	0.47	4.59	DDNIRD
34	2	1	4	0.14	9.79	DDNIRD
35	2	2	9	0.63	4.38	DDNIRD
36	4	2	2	0.40	4.15	DDNIRD
37	4	1	1	0.28	7.01	DDNIRD
38	6	2	40	0.64	4.47	DDNIRD
39	4	2	1	0.37	3.07	DDNIRD
40	4	2	1	0.19	5.88	DDNIRD
41	2	1	8	0.65	4.51	DDNIRD
42	2	1	13	0.27	2.76	DDNIRD
43	4	2	1	0.40	4.09	DDNIRD
44	2	1	3	0.29	2.95	DDNIRD
45	2	2	1	0.54	7.56	DDNIRD

points within transects are densely packed and transects are widely spaced, this method led to interpolation errors on the higher-resolution grid. When optimizing parameters in segments with DDNIRD data by sequentially removing points, the optimal *an* value was often low. This is due to the fact that points within the same transect are very close to each other and have similar bathymetry values, unlike the more distant points in other transects. As a result, when the mesh resolution along the *s*-axis is finer than the distance between transects, the *np* closest bathymetric points to the mesh nodes are often all from the same tran-

sect. This created a step-like interpolation, disrupting along-bed continuity.

To address this issue, we employed a modified two-step interpolation technique within the s,n-coordinate system for segments where DDNIRD data predominates. The first step is based on the idea pursued by several studies that the bathymetry changes linearly following lines of constant n-coordinates (Goff & Nordfjord, 2004; Caviedes-Voullième et al., 2014; Dysarz, 2018). For each grid point of the grid used for reprojection, we computed the bathymetry by identifying the closest points from the upstream and downstream transects and then applying a simple Inverse Distance Weighting (IDW) interpolation using those two points in Eqs. 2.8 and 2.9, with $np = 2$ and $p = 1$. This process results in bathymetric data whose coordinates align with the mesh within the segment but not in the connection zones. To resolve this, a second interpolation is performed using the same method as with other bathymetry sources, but with the grid-interpolated bathymetry as the source. Since the grid and the mesh coincide within the segments, the interpolated bathymetry in these areas remains largely unaffected by the second step, while the bathymetry on the mesh points in the connections continues smoothly from the segments. To estimate the error with this method, we used a "leave-one-out" cross-validation technique to compute the Relative Root Mean Squared Error (RRMSE) on the observation points. It is important to note that this approach does not provide an error estimation for the mesh nodes between the transects.

In the connection zones, as each mesh point can receive one bathymetry value per segment adjacent to the connection zone, we tested three different combination methods to determine the final bathymetry value at these points. The first method followed Goff and Nordfjord, 2004's approach, selecting the maximum value among the results. In the second method, we calculated the mean of the values. In the third approach, we averaged the interpolation results with weights inversely proportional to the distance from the segment generating each result. Those three methods are hereafter referred to as the Max, Mean and Weighted mean methods, respectively. In addition to the Root Mean Squared Error (RMSE) and RRMSE, we also look here at the Mean Absolute Error (MAE) and Median Absolute Deviation (MAD), defined by:

$$\mathrm{MAE} = \frac{1}{n}\sum_{i=1}^{n}\left|z_{obs,i} - z_{predicted,i}\right| \tag{4.3}$$

$$\mathrm{MAD} = \mathrm{median}\left(\left|z_{obs,i} - z_{predicted,i}\right|\right) \tag{4.4}$$

The three tested combination methods have similar errors (Table 4.A.3). They all gave low error metrics, with at least 50% of the tested points with an absolute error below 3.5 cm. The Max method gives the poorest results. Although the Mean method resulted in the lowest overall error, the Weighted Mean method provided smoother transitions between the segments and has a lower MAD.

Table 4.A.3: Error metrics in connection zones corresponding to the different combination methods

Combination method	RMSE *[m]*	RRMSE *[%]*	MAE *[m]*	MAD *[m]*
Max	0.29	2.14	0.09	0.035
Mean	0.22	1.64	0.08	0.033
Weighted mean	0.26	1.90	0.08	0.032

Chapter 5

The Danube Delta: How do floodplains impact the Danube-Black Sea continuum?

This chapter is based on the following article: **Alaerts, L.**, Lambrechts, J., De Le Court, M., Randresihaja, N. R., Vandenbulcke, L., Gourgue, O., Hanert,E., and Grégoire, M. The Danube Delta: How do floodplains impact the Danube-Black Sea continuum? *In preparation.*

Abstract

Floods are both a necessary natural process and a threat to local populations in deltas. Floodplains play a central role in flood mitigation and water circulation in those environments, and the Danube Delta is no exception. Yet no numerical model has so far evaluated the contribution of floodplains to the flow dynamics of this region. Here, we use the unstructured hydrodynamic model SLIM to assess how floodplains influence water levels, discharge distribution, and coastal circulation along this continuum. In this study, we investigate the role of floodplains in the Danube Delta and their impact on the regional hydrodynamics using the unstructured hydrodynamic model SLIM. Simulations were conducted with and without explicit floodplain representation, and with different values of Manning coefficients to assess the sensitivity of results to channel and floodplain roughness. Our results show that including floodplains improves agreement with discharge and water level observations in the Delta, and alters flow distribution. In 2024, about 10% of upstream discharge entered floodplains and reached the sea through pathways other than the six main rivermouths. Floodplains reduce water levels and buffer peak discharges, particularly during sustained high flows, while their effect on coastal circulation is limited to within ~10 km of the shoreline. Channel Manning coefficients has a stronger influence on water levels and discharges than floodplain inclusion, underlining the importance of parameterization. The model still shows signs that river-floodplain connectivity could be improved, particularly through better representation of the topography and the inclusion of channels in the inner delta. These findings highlight the importance of explicitly representing floodplains in deltaic hydrodynamic models. They also provide a basis for future applications coupling hydrodynamic processes with sediment, nutrient, and pollutant dynamics along the Danube River-Delta-Black Sea continuum.

5.1 Introduction

Flooding has posed a threat to human settlements since the dawn of time, and remains a major issue today. In 2024 alone, storms and flooding in Europe affected 413 000 people, causing more than €18 billion in damages (Copernicus ECMWF, 2025). Notably, Storm Boris brought one of the most devastating and widespread flood events in recent European history, impacting major river basins such as the Danube, Elbe, and Oder, and affecting countries including Germany, Poland, Austria, Hungary, Czechia, Slovakia, Romania, and Italy (Copernicus ECMWF, 2025). While such events are not unprecedented, projections indicate that both fluvial and pluvial flood risks are likely to increase across Europe in the coming decades (Bednar-Friedl et al., 2022).

Among all ecosystems, deltas are particularly vulnerable to flooding. Their flat topography, location at the interface between rivers and the sea, and often high population density contribute to this sensitivity (Wolters & Kuenzer, 2015). In addition, deltas are under intense anthropogenic pressure: agricultural development, river engineering for navigation, upstream dam construction, and altered river flows all degrade their natural capacity to buffer floods (Syvitski et al., 2009; Wolters & Kuenzer, 2015). These pressures also disrupt sediment transport, contributing to land subsidence in many deltas worldwide and further exacerbating flood risk (Syvitski et al., 2009).

The Danube Delta, with its average altitude of 0.52 m and 93% of its surface below 2 m, is not an exception (Güttler et al., 2013). Studies show that flooding in the Danube Delta typically occurs when river discharge exceeds 10,000 m^3/s or in case of high waves in the coastal areas (Jugaru Tiron et al., 2009; Gogoase et al., 2011). Between 1840 and 2000, 89 flood events were recorded in the region, with the most severe in recent memory occurring in 2006 (Jugaru Tiron et al., 2009; Güttler et al., 2013) and 2010 (Hackl, 2010; Niculescu et al., 2015). While 2024 was not classified as a high flood year in the delta, the Danube River discharge observed after Storm Boris was unusually high for a month of September, even if such values could be considered normal at other times of the year (Fig 1.4). Projections indicate that flood frequency and intensity in the Danube Delta will increase in the coming decades, with scenarios assessed for both mid- (2050) and late-century

(2100) horizons (Ciobotaru et al., 2025). Observations already suggest rising discharges in recent decades, attributed to climate change, upstream damming, and loss of wetland storage capacity (Jugaru Tiron et al., 2009).

Beyond these documented flood events, seasonal flooding is a natural and recurring phenomenon in the Danube Delta. Although precipitation levels in the delta itself are low, the area experiences inundation every year as part of its natural hydrological cycle (Niculescu et al., 2015). The Danube Delta's intricate network of channels, lakes, and floodplains forms a highly connected system that buffers the effects of high river discharge (Poncos et al., 2013). The more than 300 lakes scattered throughout the delta, along with the surrounding swamps, marshes, and floodplains act as natural buffers. They absorb excess water in spring, when melting snow from upstream regions raises Danube discharge, and gradually release it as water levels recede (Gâştescu, 2009; Güttler et al., 2013; Niculescu et al., 2015). Depending on the water levels, some lakes are connected by the means of canals or directly through the vegetation (Gâştescu, 2021), while other, completely isolated during low-water periods, rely on seasonal floods to renew their waters and sustain ecological health (Güttler et al., 2013). However, these natural dynamics have been increasingly disrupted by anthropogenic activities, including channelization, damming, and polderization. Although large portions of the delta remain relatively undisturbed due to limited accessibility, the region has nonetheless lost approximately 30% of its natural area since the early 20th century (Poncos et al., 2013; Gâştescu, 2021). The delta's natural capacity to store and redistribute water still remains important in mitigating the destructive potential of extreme discharge events.

There have been many studies on flooding in the Danube Delta, including both damaging and natural inundation events. Some have focused on specific areas within the delta (Jugaru Tiron et al., 2009; Gogoase et al., 2011; Niculescu et al., 2015; Banescu et al., 2020), while others have assessed flood susceptibility across the entire delta (Mierla et al., 2015; Crăciun et al., 2022; Costache et al., 2024; Ciobotaru et al., 2025). Beyond physical inundation, several studies have explored the role of floodplains in shaping key environmental processes in the Danube Delta, such as nutrient dynamics (Cristofor et al., 1993), heavy

metal retention (Keller et al., 1998; Burada et al., 2015), water quality (Pinay, 1992), flow and sediment transport (Jugaru Tiron et al., 2009), and biodiversity (Navodaru et al., 2002).

While all these studies underline the importance of the Danube Delta in the Danube–Black Sea continuum, none so far has evaluated the contribution of the delta's floodplains on the flow dynamics along this continuum. In this study, we use the unstructured hydrodynamic model Second-generation Louvain-la-Neuve Ice-ocean Model (SLIM)to investigate how the Danube Delta's floodplain system responds to both typical conditions and discharge surges. We compare simulations with and without integrated floodplains to assess their influence on water level distribution and outflows at the rivermouths. In addition, we evaluate the impact of bottom friction through different values of Manning coefficients.

5.2 Material and methods

5.2.1 Area of interest

For this study, our region of interest encompasses the Danube Delta and the North-Western Shelf (NWS) of the Black Sea (Fig. 5.1). The offshore boundary of the domain follows the 120 m isobath, to capture the entire shelf and its dynamics. Coastlines were extracted from OpenStreetMap (OSM). In the configuration without floodplains, the domain stops at the coastline and extends upstream along the riverbanks. In that configuration, features in front of the delta included in the coastline dataset (such as sandbanks and the Sakhalin barrier island) were removed and therefore excluded from the mesh. In the configuration with floodplains, the inland boundary corresponds to the 10 m elevation contour (i.e., the −10 m isobath). In both configurations, the upstream boundary of the river is set at Isaccea, 30 km upstream of the Danube Delta. The river network includes the three main branches of the delta——Chilia, Sulina, and Sfântu Gheorghe——along with all associated meanders covered by the available bathymetric data (see Chapter 4).

The Danube Delta includes five major polders—Pardina, Sireaşa, Tătaru, Carasuhat and Dunavăţ-Murighiol, Fig. 5.1)—that are isolated

from the regional hydrodynamics. These areas are primarily agricultural and are protected against flooding by surrounding dikes and desiccation channels (Niculescu et al., 2017). Although no information was found confirming that the polders are never flooded, and occasional overtopping or managed inundation events can therefore not be fully excluded, they are generally designed to remain dry. Detailed topographic data describing the surrounding dikes are not available, and their narrow embankments are not resolved in the available elevation datasets covering the region. To avoid introducing uncertain or artificial structures and unrealistic flooding, the polders were therefore removed from the domain rather than represented explicitly. Their boundaries are drawn based on the map provided by Tănăsescu and Constantinescu (2020), although their exact extents remain approximate due to the lack of detailed distribution data.

5.2.2 Hydrodynamic model

To run the simulations, we use the unstructured finite element model SLIM, as described in Chapter 2. To evaluate the impact of the floodplains on the Danube-Black Sea continuum, two set-ups were tested: one with the floodplains (Fig. 5.2.b.), and one without (Fig. 5.2.a.). Both configurations use the same mesh in the river (Figs. 5.2 a-3 and b-3). This mesh is a hybrid curvilinear-unstructured grid. It is made of a structured curvilinear mesh with elongated triangles in unidirectional river segments, and fully unstructured triangular meshes at intersections between segments. This approach offers several advantages, as discussed in Chapter 3. The mesh is constructed with targeted across-channel and along-channel resolutions of 20 m. The resulting mesh in the river is made of $\sim 6 \times 10^5$ triangles. Because the mesh adapts to the river's shape, its resolution is not constant. On average, elements in river have a size of $\sim$ 26 m, but edge length ranges from 9.5 to 71 m (see Table 5.1 for details). For both configurations, the river mesh is constructed first, followed by the mesh for the rest of the computational domain, which is built around it.

In the sea, both configurations follow similar rules for element sizing and share the same open boundary. At the river mouths, element sizes match those in the river (Figs. 5.2 a—4 and b—4). Beyond this, element size increases linearly with distance from the river mouths and

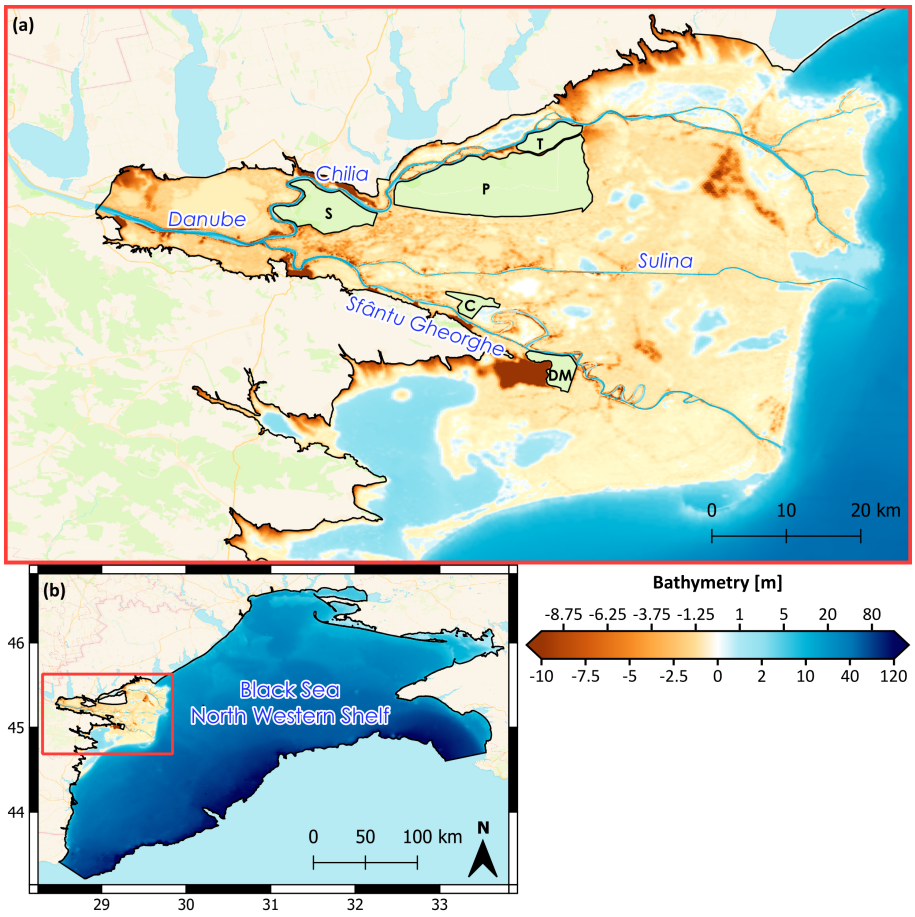

Figure 5.1: Map of the study domain. The black line represents the model boundaries in both panels. Inside this boundary, the color indicates bathymetry. **(a)** provides a close-up of the Danube Delta, and **(b)** shows the full domain, extending to the northwestern shelf of the Black Sea. In panel (a), polders excluded from the simulation are outlined in black, colored green, and labeled with initials: P (Pardina), S (Sireaşa), T (Tătaru), C (Carasuhat), and DM (Dunavăţ–Murighiol). The red frame in panel (b) indicates the extent of panel (a).

the coastline (Figs. 5.2 a—1, a—2, b—1, b—2). The resulting meshes of the NWS consists of $\sim 3.5 \times 10^5$ elements, with sizes ranging from ~15 m at the river mouths to ~200 m along the coast and ~1.5 km offshore.

The floodplains are meshed starting from the elements adjacent to the river, which are defined to match the size of those at the edges of the river mesh (Figs. 5.2 b—3 and b—4). The element size in the floodplains is then set to be inversely proportional to the distance from the riverbanks, the polders and domain boundaries, and the coastlines (Figs. 5.2 b—2 and b—3). Consequently, element sizes range from ~9 m near the riverbanks to ~200 m near the coastlines, polders and floodplain boundaries, and up to ~600 m in the interior floodplains.

The final meshes contain approximately 9.6×10^5 and 1.6×10^6 elements for the first and second configurations, respectively, with element sizes ranging from ~9 m to ~1.5 km. These additional elements in the floodplain configuration lead to higher computational costs. With a time step of $\Delta t = 0.1$ s, a one-year simulation without floodplains runs in 48 hours on four NVIDIA A100 GPUs (192 GPU hours in total). The same period simulated with floodplains requires 44 h 30 min on eight GPUs (354 GPU hours), corresponding to about 1.8 times the computational cost of the simulation without floodplains.

An accurate representation of the bathymetry is crucial for hydrodynamic models (Merwade et al., 2005; Dey et al., 2022; Fuchs et al., 2022). In the sea we use data from (EMODnet Bathymetry consortium, 2021), which has a resolution of 1/16 arc-minutes (~115 m), completed at places east of the NWS outside the Emodnet grid (i.e. the Karkinit Gulf and the coast near Sevastopol) by the GEBCO 2024 bathymetry, which has a resolution of 15 arc-seconds (~460 m) (GEBCO Compilation Group, 2024). In the river, we combine bathymetry from the Ukrainian Scientific Center of Ecology of the Sea (UkrSCES), the Galati Lower Danube River Administration (AFDJ) and the Danube Delta National Institute for Research and Development (DDNIRD) (DDNIRD, 2015). The bathymetry in the river is interpolated on the mesh following the method presented in Chapter 4, to take the anisotropic nature of the river depth into account (Alaerts et al., 2025). For the bathymetry in the floodplains, we use Copernicus' Digital Elevation Model (DEM) (European Space Agency, 2021), which as a 30 m reso-

Table 5.1: Comparison of mesh configurations in terms of number of elements and element sizes for different regions of the domain. Two mesh setups are compared: Danube–Black Sea (DBS) and Danube–Floodplains–Black Sea (DFBS). Element sizes are reported as mean ± standard deviation, with the with the range (minimum–maximum) given in parentheses. For the river, "CS edges" refer to cross-section edges (across the channel), "AF edges" to along-flow edges (along the channel), and "CZ edges" to edges in connection zones between river segments.

Characteristics	DBS mesh	DFBS mesh
Number of elements		
River	605 612	605 612
Sea	350 058	352 926
Floodplains	-	687 051
Entire mesh	**958 670**	**1 645 607**
Elements size [m]		
River		
CS edges	26.1 ± 9.6	26.1 ± 9.6
	(9.5 – 71.0)	(9.5 – 71.0)
AF edges	25.6 ± 4.7	25.6 ± 4.7
	(14.6 – 62.6)	(14.6 – 62.6)
CZ edges	26.4 ± 8.2	26.4 ± 8.2
	(13.1 – 64.5)	(13.1 – 64.5)
Sea	604.6 ± 318.8	598.9 ± 329.0
	(18.8 – 1406.1)	(11.3 – 1546.3)
Floodplains	-	96.0 ± 102.4
		(9.4 – 619.4)
Entire mesh	$\mathbf{241.3 \pm 337.9}$	$\mathbf{179.5 \pm 276.6}$
	(**8.9 – 1406.1**)	(**8.9 – 1546.3**)

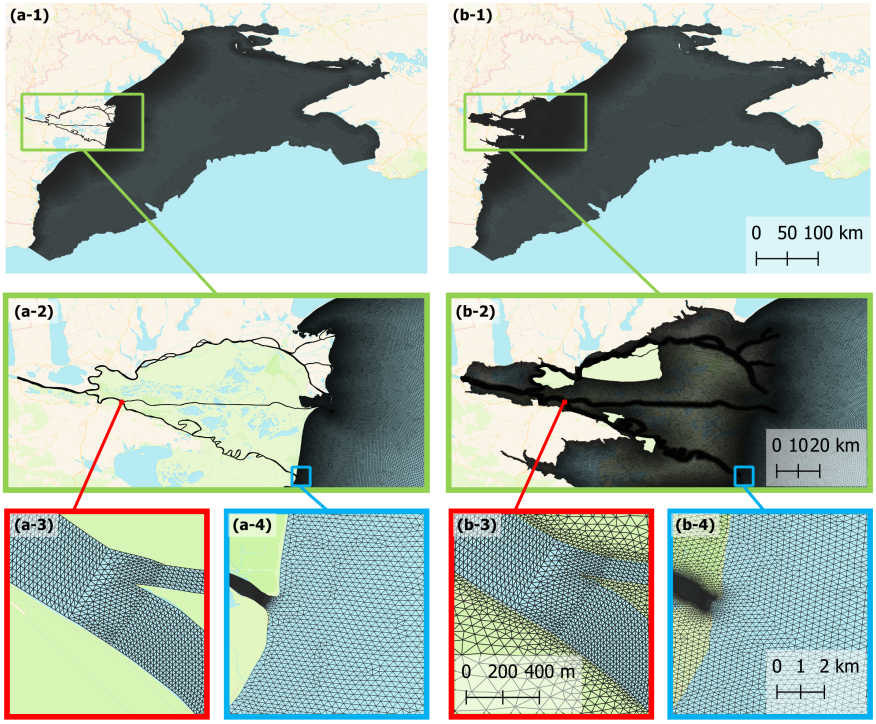

Figure 5.2: Mesh configurations. **(a—1-4)** Configuration without floodplains, and **(b—1-4)** configuration including floodplains. Panel 1 shows the mesh over the full domain. Panel 2 provides a zoomed view of the Danube Delta. Panels 3 and 4 show close-ups of a connection zone between river segments and one of the river mouths, respectively. Colored frames in Panels 1 and 2 indicate the spatial extent of the close-up views, which are framed with the corresponding colors.

lution. The bathymetry of the lakes present in the floodplains comes from the DDNIRD (DDNIRD, 2011).

To better understand the dynamic between the river and the floodplains, we test different parameterizations of the bottom friction (see eqs. 2.2 and 2.5 for the formulation of bottom friction). In the river part of the domain, we try three configurations. In the first one, we apply a uniform Manning coefficient of $n = 0.025\ \mathrm{s\,m^{1/3}}$ throughout the entire river network, which is in the range of values commonly used in the delta (Banescu et al., 2020; Roşu et al., 2022). The second config-

uration uses spatially varying coefficients, assigning $n = 0.0345\ \mathrm{s\,m^{1/3}}$ to the main river sections and $n = 0.043\ \mathrm{s\,m^{1/3}}$ to secondary segments. Main sections were defined as navigable channels or, in the absence of such information, the deepest or widest branches. The Manning values in this scenario come from Horvat et al. (2020), based on their calibration of a 2D hydrodynamic model for a section of the Danube and one of its meanders. The third configuration also uses spatially varying coefficients based on the same criteria (main and secondary river sections), but the Manning values were obtained from the empirical relations of Arcement and Schneider (1989), which allow Manning values to be computed from channel and floodplain characteristics. The resulting values are $n = 0.013\ \mathrm{s\,m^{1/3}}$ for the main sections and $n = 0.026\ \mathrm{s\,m^{1/3}}$ for secondary segments.

Two configurations are tested in the floodplains. In the first, a constant Manning coefficient of $n = 0.025\ \mathrm{m^{1/3}s}$ was applied uniformly. In the second, the Manning coefficient varied spatially according to land cover, based on the LifeWatch land cover 10 m (version 2) product for 2018. The land cover classifications are translated into Manning values using the approach of Arcement and Schneider (1989), as detailed in Table 5.2.

Combined with the two mesh configurations (with and without floodplains), we produce 7 simulation scenarios (Table 5.3). For the mesh excluding floodplains, three cases are tested, each corresponding to one of the river Manning configurations. They are hereafter referred to as CM (Constant Manning), HM (High Manning), and LM (Low Manning) scenarios. For the mesh including floodplains, four configurations were used: one with constant Manning in both the river and floodplains (CMF - Constant Manning with Floodplains), and three in which floodplain Manning was derived from land-use data. Those three last scenarios correspond to the three river Manning configurations. They are hereafter called CLMF (Constant river and Land-cover-based Manning with Floodplains), HLMF (High river and Land-cover-based Manning with Floodplain), and LLMF (Low river and Land-cover-based Manning with Floodplains). In all simulations, the Manning in the sea is set to $0.025\ \mathrm{s\,m^{1/3}}$.

The last information the model need to run are boundary conditions

Table 5.2: Manning values for the different land covers in the Danube delta. Land-cover categories come from the LifeWatch land cover 10 m (version 2) product and Manning coefficient values are determined using the approach of Arcement and Schneider (1989).

Land covers	Manning values $[s\,m^{1/3}]$
Water	0.023
Recently disturbed area	0.011
Natural material (< 10% vegetation)	0.015
Artificially sealed ground surface	0.005
Buildings	0.054
Crops	0.034
Intensively managed grassland	0.022
Grassland and scrubs	0.032
Inundated grassland and scrubs	0.017
Small coniferous (< 3 m)	0.053
Coniferous (> 3 m)	0.054
Small deciduous (< 3 m)	0.053
Deciduous (> 3 m)	0.054

and external forcings. We apply a weak no-slip conditions along all closed boundaries, including coastlines (except along the Danube Delta in configurations with floodplains), the outer limits of floodplains in the floodplain configurations, and riverbanks in simulations without floodplains. At the open boundary in the sea, water surface elevation and depth-averaged velocity are imposed through a Flather boundary condition, adding tidal forcing from TPXO9v5 (Egbert et al., 1994) to depth-averaged velocities from NEMO Black Sea (Grégoire et al., 2020a, 2020b). River inputs are also imposed via Flather conditions. For the Danube river, discharges measured by the AFDJ at Isaccea are imposed at the upstream boundary. The discharges of the next three largest rivers contributing to the NWS freshwater input—the Dnieper, Dniestr and Southern Bug—are also imposed at the domain's boundary. These values are obtained from the GEOGloWS ECMWF Streamflow Service (Hales et al., 2025). The model is initialized with water surface elevation (η) and velocities set to 0, with two notable exceptions. The first one concerns areas where the terrain elevation is above 0 m ($h < 0$), as setting $\eta = 0$ would result in a negative water

Table 5.3: Summary of the Manning bottom friction coefficient values (s $m^{1/3}$) for the different hydrodynamic configurations. In the "Manning in river" column, MS = main sections and SS = secondary sections.

Configurations	Manning in river	Manning in floodplains
LM (Low Manning)	0.013 in MS 0.026 in SS	/
CM (Constant Manning)	0.025	/
HM (High Manning)	0.0345 in MS 0.043 in SS	/
CMF (Constant Manning with Floodplain)	0.025	0.025
LLMF (Low river and Land-cover-based Manning with Floodplains)	0.013 in MS 0.026 in SS	Land-cover-based (Table 5.2)
CLMF (Constant river and Land-cover-based Manning with Floodplains)	0.025	Land-cover-based (Table 5.2)
HLMF (High river and Land-cover-based Manning with Floodplains)	0.0345 in MS 0.043 in SS	Land-cover-based (Table 5.2)

depth since $H = \eta + h$. The second exception concerns areas where terrain elevation is below 0 m ($h > 0$), but inundation is not expected. These areas are identified using the LifeWatch land cover product and correspond to regions classified as neither "Water bodies" nor "Inundated grassland and scrub of biological interest." For both exceptions, initial velocities remain 0, but initial η is adjusted so that $H = H\text{thin}$, which represents the minimum acceptable water depth below which the model considers the area dry and the wetting–drying algorithm takes effect (see Chapter 2). The wind velocity at 10 m is taken from the European Center for Medium-range Weather Forecast (ECMWF) ERA5 reanalysis (Hersbach et al., 2018). Precipitations are not taken into account, as the region has a low precipitation regime, and the

water level variations in the Danube Delta are mainly driven by river discharge. Since this discharge already integrates precipitation effects from the entire Danube Basin, the local impact of precipitation within the delta is considered negligible (Niculescu et al., 2015; Crăciun et al., 2022). During the simulation, the model is relaxed toward the sea surface elevation and depth-averaged velocity from NEMO Black Sea. The aim of this relaxation is to correct the model's barotropic velocity in deep areas, where the 3D baroclinic effects are no longer negligible. Consequently, the nudging is set to 0 in the entire Danube Delta. In the sea, the coefficient increases with depth, from 0 in coastal areas shallower than 30 m to 3×10^{-5} s^{-1} near the shelf break.

Model validation

The model validation focuses on surface elevation, discharge, flooding extent, and circulation on the NWS. For the first three, observational datasets were available, while circulation could only be assessed qualitatively against descriptions from the literature, as no dataset is available to validate circulation near the delta shoreline.

The simulated surface elevation values are compared with satellite-derived water surface elevations from the Copernicus Land Monitoring Service (European Union's Copernicus Land Monitoring Service information, 2024). These measurements are available at six validation points along the river (hereafter referred to as stations 1–6) with a temporal resolution of 27 days (see location on Fig. 5.3). Stations 1–5 are located along the Chilia branch, numbered from the most upstream (eastward) to the most downstream (westward), and station 6 is located on the Sfântu Gheorghe branch, approximately 20 km upstream from its mouth. Coordinates of all validation points are listed in Table 5.4. Discharge measurements were provided by the Institutul Naţional de Hidrologie şi Gospodărire a Apelor (INHGA). Data were collected just downstream of the city of Tulcea, at the upstream end of each of the three main branches (Chilia, Sulina, and Sfântu Gheorghe), and on the Danube just upstream of the delta (see location on Fig. 5.5). Exact locations are listed in Table 5.4.

To assess the model's accuracy with these two datasets, we compute three common statistical metrics between simulated and observed val-

ues: the Root Mean Squared Error (RMSE), the Relative Root Mean Squared Error (RRMSE), and the Mean Bias Error (MBE), defined as

$$RMSE = \sqrt{\frac{1}{n}\sum_{i=1}^{n}(m_i - o_i)^2}, \tag{5.1}$$

$$RRMSE = \frac{RMSE}{\overline{o}} \times 100\%, \tag{5.2}$$

$$MBE = \frac{1}{n}\sum_{i=1}^{n}(m_i - o_i) \tag{5.3}$$

where $i = 1,...n$ are the time steps for which observations are available, m_i is the simulated value of the variable of interest (here, discharge or water elevation), o_i is the corresponding observed value, and $\overline{o}$ is the mean observed value.

Surface elevation is also validated using Taylor diagrams. Such diagram allows us to evaluate how well the model reproduces the pattern and variability of the observations by representing, on the same plot, the standard deviation of the modeled variable (σ_m), the correlation coefficient (R) and the Centered Root Mean Squared Error (CRMSE), defined as

$$\sigma_m^2 = \frac{1}{n}\sum_{i=1}^{n}(m_i - \overline{m})^2 \tag{5.4}$$

$$R = \frac{1}{\sigma_o \sigma_m}\frac{1}{n}\sum_{i=1}^{n}(m_i - \overline{m})(o_i - \overline{o}) \tag{5.5}$$

$$\begin{aligned} \mathrm{CRMSE}^2 &= \tfrac{1}{n}\textstyle\sum_{i=1}^{n}((m_i - \overline{m}) - (o_i - \overline{o}))^2 \\ &= \sigma_o^2 + \sigma_m^2 - 2\,\sigma_o\,\sigma_m \end{aligned} \tag{5.6}$$

According to the Law of Cosines, in a triangle with sides a, b, and c,

where $a = \sigma_m$, $b = \sigma_o$, and the angle between them is $\theta = \arccos(R)$, the length of edge c is equal to the CRMSE. Using this property, model performance can be represented in a Taylor diagram, which is a polar coordinate plot where the radial coordinate is $r = \sigma_m$ and the angular coordinate is $\theta = \arccos(R)$. As a result, CRMSE is the distance between the position corresponding to the observation (or a perfect model, located at $r = \sigma_o, \theta = 0$) and the model point of coordinate $r = \sigma_m$, $\theta = \arccos(R)$.

To compare simulations across stations with different σ_o values, we use a normalized Taylor diagram, where each quantity is divided by σ_o to make them dimensionless:

$$\text{CRMSE}' = \frac{\text{CRMSE}}{\sigma_o}, \quad \sigma_m' = \frac{\sigma_m}{\sigma_o}, \quad \sigma_o' = \frac{\sigma_o}{\sigma_o} = 1 \tag{5.7}$$

In this normalized space, a perfect match with the observations lies at $r = 1$ and $\theta = 0$, allowing direct comparison between simulations with different variability scales since all reference datasets are mapped to a unit standard deviation.

Table 5.4: Location and number of observations for each validation station for year 2021.

Station name	Coordinates		Number of observations
Elevation validation			
Station 1	28.8464°E	45.3170°N	14
Station 2	28.9299°E	45.2808°N	14
Station 3	29.0061°E	45.3594°N	13
Station 4	29.2704°E	45.4283°N	12
Station 5	29.5004°E	45.4191°N	14
Station 6	29.4429°E	44.9742°N	13
Discharge validation			
Danube	28.7285°E	45.2270°N	5
Chilia	28.7512°E	45.2346°N	5
Tulcea	28.8394°E	45.2030°N	5
Sulina	28.8963°E	45.1870°N	8
Sfântu Gheorghe	28.8954°E	45.1820°N	6

Finally, flooding patterns were compared with the LifeWatch land cover

10 m (version 2) product for 2018. Although this dataset does not provide direct flood extent, it gives useful information on wether or not areas are expected to be flooded, thereby providing a useful reference for model validation. Other potential datasets, including the GloFAS Global Flood Monitoring product (Copernicus Emergency Management Service, 2025), Sentinel-2 Normalized Difference Water Index (NDWI) imagery (European Space Agency, 2025), and surface soil moisture from the Copernicus Land Monitoring Service (European Union's Copernicus Land Monitoring Service information, 2025), were also considered. However, they exhibited unrealistic patterns (e.g. flooding within polders) and were therefore excluded from the analysis.

5.3 Results

In this section, we first present the validation of the different simulations for year 2021, to find which of our model setups performs best. The best set-ups with and without floodplains are then applied in 2024, to see how well they are faring with the unusual increase of discharge in September caused by storm Boris passing over Central Europe, and to evaluate the impact of floodplains on the hydrodynamics in the delta.

5.3.1 Validation 2021

Validation of river water surface elevation shows that the best results are generally associated with simulations where floodplains are included (Fig. 5.8 and Tab. 5.5). CMF produces the lowest error metrics at stations 1–3, while LLMF performs best at stations 5–6, indicating that CMF captures upstream dynamics more accurately, whereas LLMF tends to perform better downstream. The exception is station 4, where the lowest errors are obtained with a configuration without floodplains (LM). On average, CMF yields the lowest RMSE (0.27 m) and MBE (0.14 m) values, while LM shows the lowest RRMSE (31.8 %).

The Manning coefficient in the river is the most determinant factor of water level. As expected, a higher Manning coefficient in the river leads to an increased water level. The inclusion of floodplains is the next most influential factor, generally lowering water levels in the river.

This decrease is however not uniform, being more pronounced in time and places where water level is higher. The influence of floodplains on water levels also becomes stronger as the river Manning coefficient increases. Differences in the floodplain Manning coefficient values have little impact on water elevation in the river, at least in the case tested where the Manning coefficient is constant in the river: CMF and CLMF produce very similar results, though CMF performs slightly better.

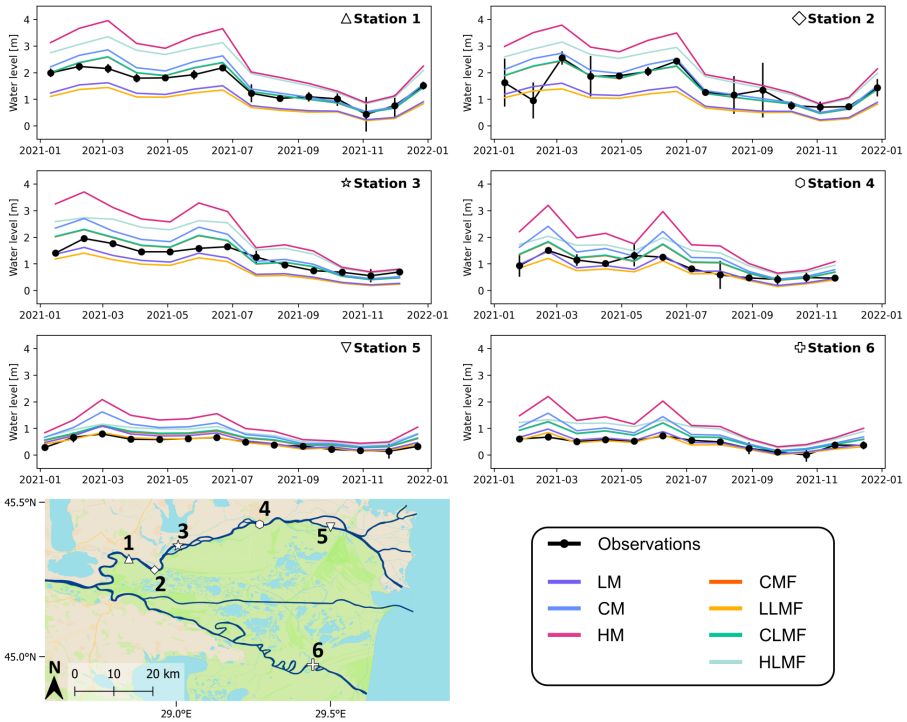

Figure 5.3: Validation of water surface elevation for all simulations in 2021, at six stations along the Danube Delta. A map (bottom left) shows the location of the six stations with numbered symbols, which are repeated in the top-right corner of each corresponding plot.

Validation of the variability of river water surface elevation shows that including floodplains generally improves model performance (Fig. 5.4 and Table 5.6). In the normalized Taylor diagram, model performance is assessed through the normalized modeled standard deviation (σ'_m), the centered root mean square error (Normalized Centered Root Mean

Table 5.5: Error metrics (RMSE, RRMSE, MBE) on water elevation at each station for simulations without and with floodplains in 2021. RMSE and MBE are expressed in meters, while RRMSE are expressed in % of the observed values. The mean across all stations of each error metric is presented at the bottom of the table. For each combination of station-error metric, the lowest value across all simulations is written in bold font. The background color indicates relative performance across models for each line, from dark green (best) to white (worst), with shades varying linearly according to the metric value.

		Without floodplains			With floodplains			
Stations	Metrics	CM	LM	HM	CMF	LLMF	CLMF	HLMF
1	RMSE	0.33	0.55	1.08	**0.17**	0.66	0.18	0.77
	RRMSE	21.5	36.6	71.4	**11.4**	43.7	11.8	51.1
	MBE	0.23	-0.53	0.97	**0.08**	-0.63	0.09	0.72
2	RMSE	0.47	0.64	1.07	**0.38**	0.73	**0.38**	0.76
	RRMSE	31.7	43.3	72.4	**25.7**	49.6	25.8	51.3
	MBE	0.18	-0.53	0.89	**0.02**	-0.63	0.03	0.62
3	RMSE	0.49	0.37	1.15	**0.29**	0.47	0.30	0.74
	RRMSE	39.2	30.2	92.6	**23.3**	38.2	24.0	59.9
	MBE	0.32	-0.35	0.97	**0.13**	-0.46	0.14	0.65
4	RMSE	0.53	**0.20**	1.02	0.29	0.27	0.30	0.57
	RRMSE	61.6	**23.6**	118.0	33.0	31.4	34.5	66.6
	MBE	0.42	**−0.11**	0.90	0.20	-0.21	0.21	0.53
5	RMSE	0.42	0.14	0.68	0.20	**0.06**	0.23	0.35
	RRMSE	95.6	31.6	154.6	46.1	**13.8**	51.6	79.7
	MBE	0.38	0.11	0.62	0.19	**0.02**	0.21	0.34
6	RMSE	0.42	0.11	0.79	0.29	**0.10**	0.29	0.51
	RRMSE	95.5	25.8	179.1	66.7	**22.4**	64.9	116.2
	MBE	0.35	**0.04**	0.69	0.25	**−0.04**	0.24	0.48
Mean	RMSE	0.44	0.34	0.96	**0.27**	0.38	0.28	0.62
	RRMSE	57.5	**31.8**	114.7	34.4	33.2	35.4	70.8
	MBE	0.31	-0.23	0.84	**0.14**	-0.33	0.15	0.56

Squared Error (CRMSE')), and the correlation coefficient (R). The ideal model corresponds to $\sigma'_m = 1$, CRMSE' = 0, and $R = 1$. In that respect, the best representations of variability are obtained with the LLMF and LM configurations, followed by CMF, while HM consistently performs the worst.

Our results show that R is primarily station-dependent, varying between 0.8 and 0.99, which indicates a very good overall agreement in temporal variability. For a given Manning configuration in the river, σ'_m decreases when floodplains are included, showing that floodplain connectivity dampens water level variability. Conversely, σ'_m increases with the Manning coefficient in the river, with high or constant Manning configurations systematically overestimating the observed variability.

In terms of discharge validation, simulations including floodplains generally provide the best agreement with observations, with four out of five stations showing the lowest errors with simulations accounting for floodplains (HLMF in most cases, CMF at the start of the Sulina branch—Fig. 5.5 and Tab. 5.7). A notable exception is Sfântu Gheorghe, where LM produces lower RMSE and RRMSE values. On average, CMF provides the best overall error metrics (RMSE: 266 m^3/s, RRMSE: 12.8%, MBE: 186 m^3/s), with CLMF and HLMF showing equally good MBE values.

As observed for water levels, the Manning coefficient in the river is the main factor influencing simulated discharges, followed by the inclusion of floodplains, whose effect becomes more pronounced during high-flow periods. Results show clear differences between different Manning configurations. Lower Manning coefficients tend to amplify the observed bias, leading to larger overestimations of discharge in the Tulcea and Sulina branches and stronger underestimations in the Chilia branch. The main exceptions are at the stations before the delta (Danube), where all simulations produce very similar results, and at Sfântu Gheorghe, where the ordering of simulations in terms of discharge magnitude changes throughout the year. Sfântu Gheorghe also stands out because, unlike other locations which show a consistent tendency to over- or underestimate observations, simulations at Sfântu Gheorghe display no systematic bias. Concerning the impact of

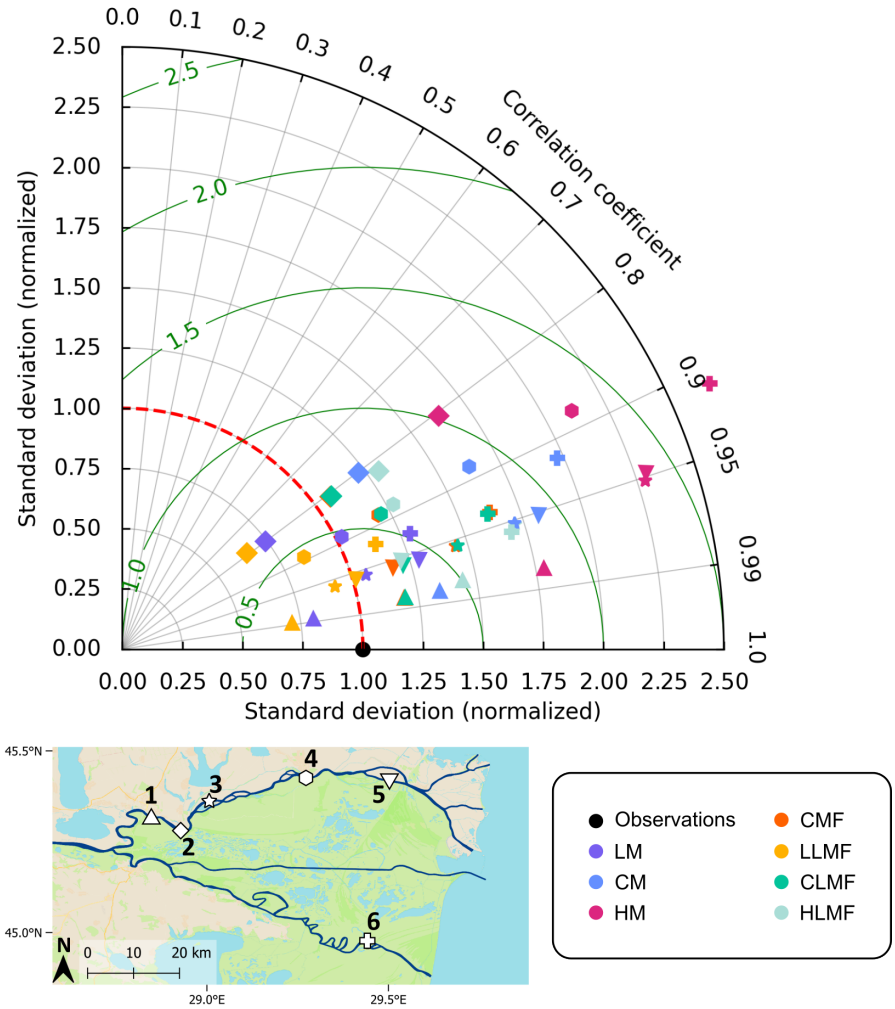

Figure 5.4: Taylor diagram of water surface elevation for all simulations in 2021, at six stations along the Danube Delta. In the polar plot above, the radial distance from the origin represents the normalized model standard deviation (σ'_m), with the red dashed circle at $\sigma'_m = 1$ indicating the case where the model has the same standard deviation as the observations. The angular coordinate represents the correlation coefficient (R). A model that perfectly matches the observed variability and is fully correlated with the observations would lie at the point of coordinates $\sigma'_m = 1$, $R = 1$, shown as a black dot. The distance from this point, depicted here by the green concentric circles, corresponds to the normalized centered root mean square error (CRMSE'). Marker shape indicates the validation station (locations shown on the map below), and marker color identifies the model configuration.

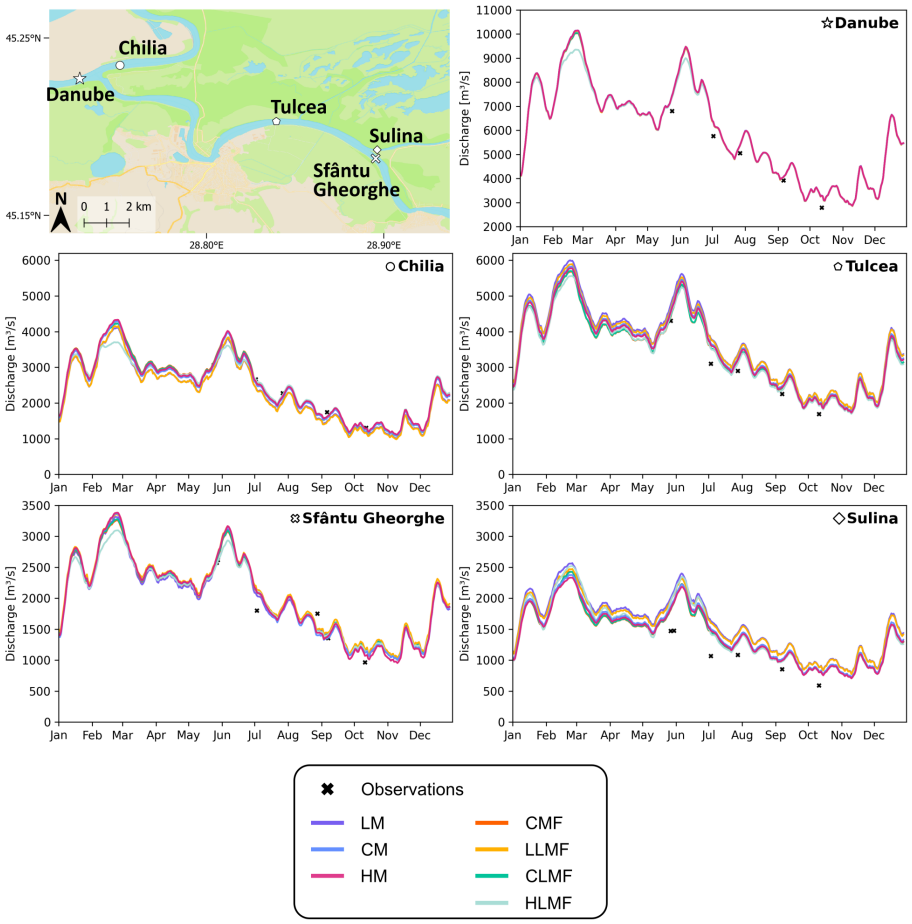

Figure 5.5: Validation of the water discharge for all simulations in 2021, at five locations: upstream of the delta (Danube), downstream of Tulcea city (Tulcea), and at the entry points of the three main branches (Chilia, Sulina, and Sfântu Gheorghe). A map (top left) shows the five validation points with symbols and names, which are repeated in the top-right corner of each corresponding plot.

Table 5.6: Error metrics (σ'_m, CRMSE') on water elevation variability at each station for simulations without and with floodplains in 2021. All metrics are dimensionless: σ'_m represents the normalized model standard deviation and should ideally be close to one, while CRMSE' should be close to zero. For each station–metric pair, the best value among all simulations is highlighted in bold. The background color indicates relative performance across models for each line, from dark green (best) to white (worst), with shades varying linearly according to the metric value.

		Without floodplains			With floodplains			
Stations	Metrics	CM	LM	HM	CMF	LLMF	CLMF	HLMF
1	σ'_m	1.341	0.804	1.785	**1.191**	0.715	1.195	1.444
	CRMSE'	0.40	**0.24**	0.82	0.27	0.31	0.28	0.50
2	σ'_m	1.223	0.744	1.633	**1.071**	0.654	1.075	1.297
	CRMSE'	0.73	**0.60**	1.02	0.65	0.63	0.65	0.74
3	σ'_m	1.711	**1.058**	2.282	1.451	0.921	1.459	1.713
	CRMSE'	0.82	0.31	1.37	0.58	**0.28**	0.58	0.82
4	σ'_m	1.628	**1.025**	2.114	1.200	0.845	1.212	1.275
	CRMSE'	0.88	0.48	1.32	0.56	**0.46**	0.57	0.61
5	σ'_m	1.817	1.287	2.296	1.174	**1.013**	1.217	1.216
	CRMSE'	0.92	0.44	1.39	0.36	**0.29**	0.39	0.40
6	σ'_m	1.974	1.288	2.678	1.630	**1.140**	1.619	1.689
	CRMSE'	1.13	0.52	1.81	0.78	**0.44**	0.76	0.79

floodplains inclusion, it is particularly noticeable when the Manning coefficient is increased, the most telling example being the HLMF case, where a clear buffering effect on peak flows is observed.

In terms of discharge distribution, all simulations show similar patterns: about 40% of the flow is directed into the Chilia branch and 60% into Tulcea, with the four floodplain configurations losing 1–2% in this initial separation. From Tulcea, the flow further splits into roughly 40% toward Sulina (i.e. ~25% of the discharge value at the Danube station) and 60% for Sfântu Gheorghe (~35%), with no systematic loss between Tulcea and these two downstream branches.

Spatial validation of flooding for 2021 was performed for two contrasting hydrological states (Figs. 5.6 and 5.7): the end of the "wet" season

Table 5.7: Error metrics for discharges upstream of the delta (Danube), at the start of each branch (Chilia, Sulina, Sfântu Gheorghe) and downstream of the city Tulcea (Tulcea) for all different simulations in 2021. RMSE and MBE are expressed in m^3/s, while RRMSE are expressed in % of the observed values. The mean across all stations of each error metric is presented at the bottom of the table. For each combination of branch-error metric, the lowest value across all simulations is written in bold font. The background color indicates relative performance across models for each line, from dark green (best) to white (worst), with shades varying linearly according to the metric value.

		Without floodplains			With floodplains			
Stations	Metrics	CM	LM	HM	CMF	LLMF	CLMF	HLMF
Danube	RMSE	465	455	460	458	473	446	**441**
	RRMSE	9.5	9.4	9.4	9.4	9.7	9.2	**9.1**
	MBE	420	414	412	409	420	401	**393**
Chilia	RMSE	115	231	87	98	238	111	**78**
	RRMSE	5.2	10.4	4.0	4.4	10.8	5.0	**3.5**
	MBE	-93	-215	-57	-60	-227	-68	**−47**
Tulcea	RMSE	359	511	338	281	454	277	**263**
	RRMSE	12.6	17.9	11.8	9.9	15.9	9.7	**9.2**
	MBE	334	489	306	247	437	237	**226**
Sulina	RMSE	344	467	319	**302**	434	315	362
	RRMSE	34.4	46.7	31.9	**30.2**	43.4	31.5	36.2
	MBE	325	447	325	**285**	418	297	323
Sf. Gheorghe	RMSE	205	**178**	192	190	220	197	198
	RRMSE	11.1	**9.7**	10.4	10.3	11.9	10.7	10.7
	MBE	44	54	48	48	103	61	**36**
Mean	RMSE	297	368	279	**266**	364	269	268
	RRMSE	14.6	18.8	13.5	**12.8**	18.3	13.2	13.7
	MBE	206	238	207	**186**	230	**186**	**186**

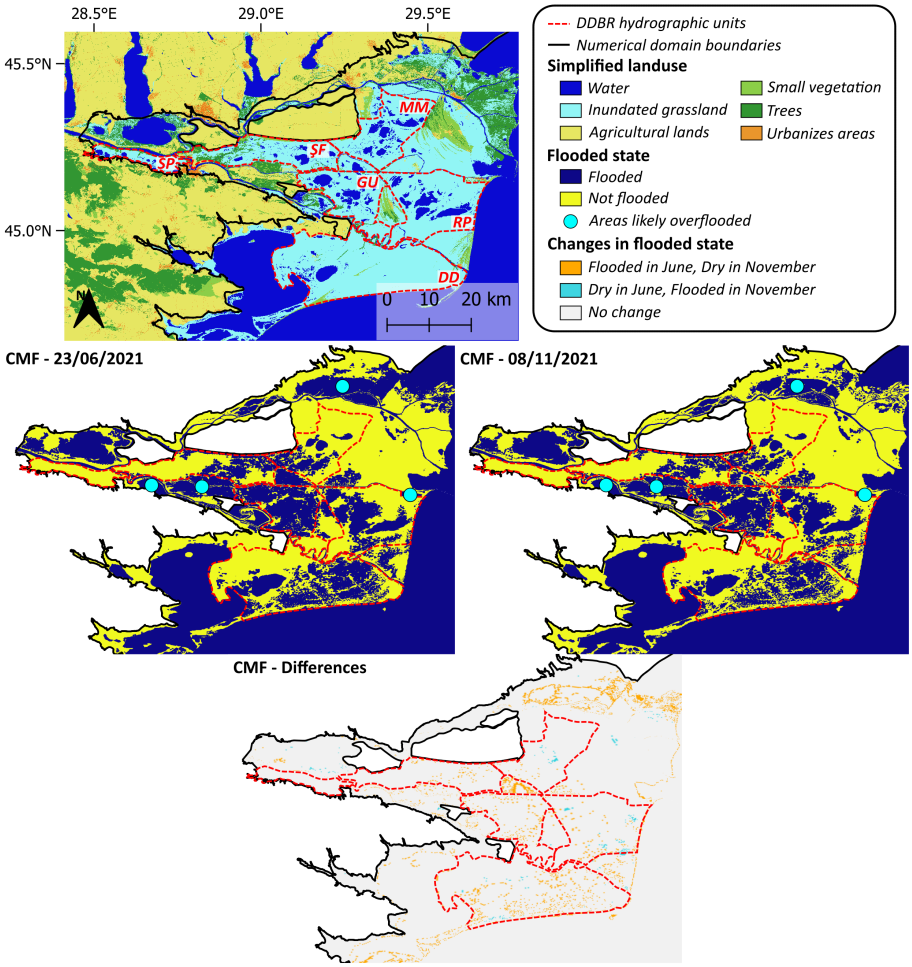

Figure 5.6: Changes in flooded areas between 23 June 2021 and 8 November 2021 for the CMF configuration. The red dotted line marks the boundaries of the Danube Delta Biosphere Reserve (DDBR) hydrographic units: SP – Somova-Parches, ŞF – Şontea-Fortuna, MM – Matiţa-Merhei, GU – Gorgova-Uzlina, RP – Roşu-Puiu, DD – Dunavăţ-Dranov. The top panel shows a simplified LifeWatch land-cover map and the location of hydrographic units. The second row displays the flooded states for each date, and the third row shows their differences.

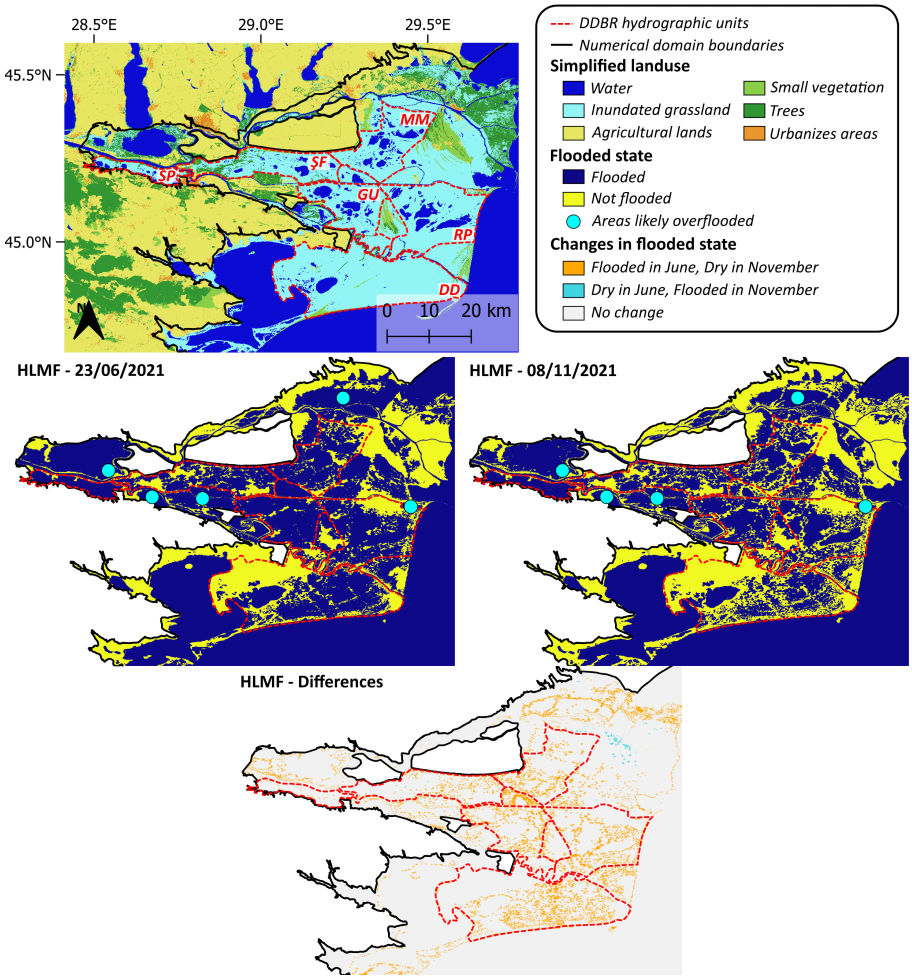

Figure 5.7: Same as Fig. 5.6, but for the HLMF configuration.

(23 June 2021), when upstream discharges began to decrease after several months of high flow (~8000 m^3/s), and the end of the "dry" season (8 November 2021), when discharges started to rise again after a prolonged low-flow period (~4000 m^3/s, Fig. 1.4). Results from the CLMF simulation were nearly identical to those of CMF, while the LLMF configuration produced almost no flooding. These two cases are therefore presented in the Appendix (Fig. 5.A.1) and not discussed further in the main text.

Both CMF and HLMF produce flooding mainly in areas expected to be inundated. Depending on the time of the year, between 83.7–84.4% (CMF) and 84.2–84.6% (HLMF) of the flooded areas correspond to LifeWatch land-cover classes “water” or “inundated grassland”. Spatially, CMF tends to underestimate flooding, with several lakes missing in the western Şontea–Fortuna unit and no water predicted in the Somova–Parcheş unit (Fig. 5.6). In total, the CMF simulation flood 2336 km^2 on the 23rd of June and 2158 km^2 on the 8th of November. In contrast, HLMF presents a larger inundated area (3287 km^2 and 2868 km^2, respectively), with water present in all hydrographic units and all the lakes represented (Fig. 5.7).

However, both configurations also predict permanent flooding in areas that are expected to remain dry for at least part of the year (highlighted by blue circles in Figs. 5.6 and 5.7), as those areas are either used for crops or as agricultural grassland according to LifeWatch land-cover. Those wrongly flooded areas represents about 7.3% (at least 157 km^2) of the total flooded area in CMF, and about 6.2% (at least 180 km^2) in HLMF. Overall it is difficult to identify a clearly superior configuration: CMF underestimates flood extent in some regions, while HLMF appears to flood more areas that should remain dry.

Since the depth-averaged barotropic model we consider does not include all the physical processes required to simulate the flow on the NWS, we consider a more qualitative validation of that area examine yearly averaged circulation patterns (Fig. 5.8). All simulations present very similar patterns. Currents follow a southwestward direction along the shelf break and the western coast, with mesoscale eddies forming in the northern part of the domain. Higher velocities are observed near the delta’s rivermouths and along the shelf break, and all simulations

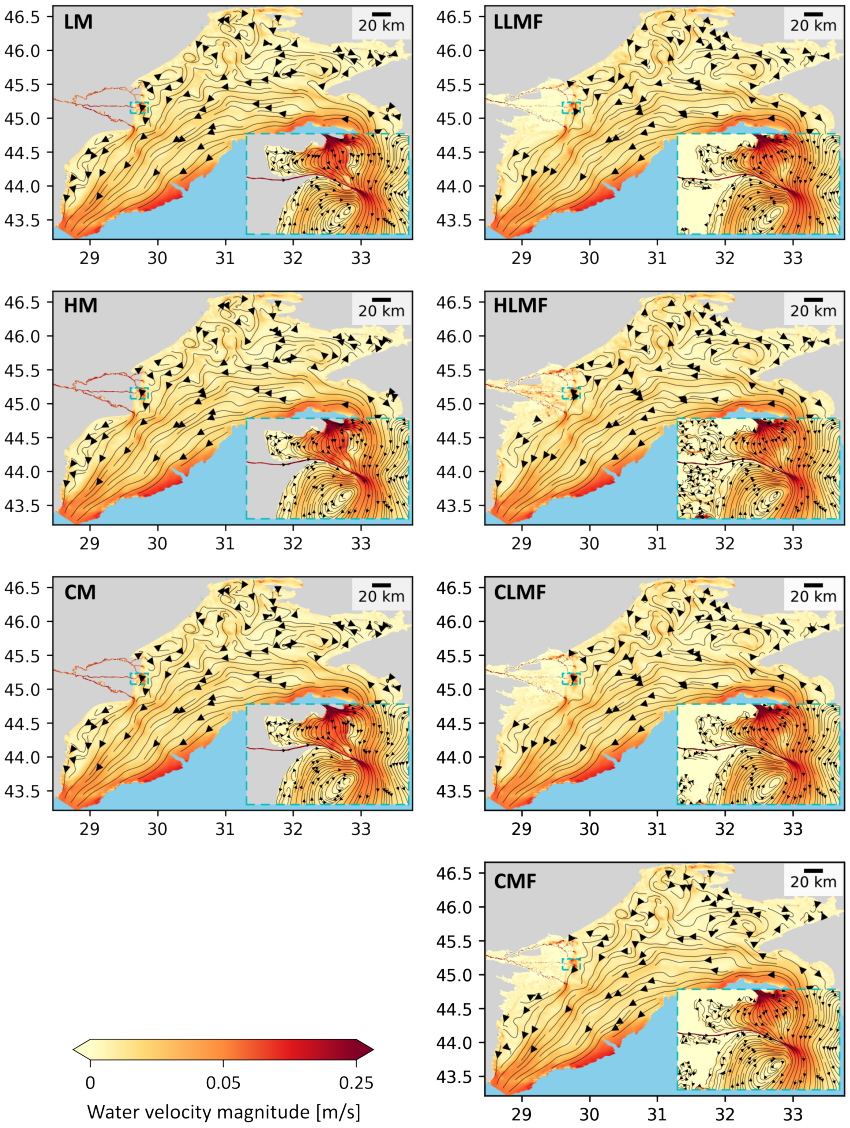

Figure 5.8: Annual mean circulation on the NWS for all simulations. Simulations without floodplains are shown in the left column, and simulations with floodplains in the right. For each simulation, a close-up of the Sulina and Chilia mouths is displayed in the bottom-right corner, outlined by a blue dotted frame; the corresponding area is indicated by a dotted blue rectangle in the main panel. Land and sea outside the domain are represented in gray and blue, respectively.

reproduce an eddy south of the Sulina channel. The influence of the river on the velocities is particularly clear at the mouth of the Sfântu Gheorghe branch, where water velocity is increased in a plume extending ~20 km south.

Some differences can be seen between configurations with and without floodplains, near the coast and the delta's rivermouth. In particular, we can see differences around the sand bank in front of the Chilia mouth, which is excluded from simulations without floodplains, as well as direct communications between the sea and the floodplains. Differences are also visible between floodplain configurations, with stronger activity in the floodplain areas as Manning coefficients in the river increase.

5.3.2 Floodplain impact in 2024

For 2024, we focus on the two best-performing model setups with and without floodplains, namely the LM and CMF configurations, as they show the smallest overall errors in their respective categories for 2021. In this section, we examine the impact of floodplains on discharge distribution between the distributary branches and on coastal circulation. We also analyze the spatial response of the floodplains to a sudden increase in water level by comparing the flooding extent in 2024 after storm Boris with that of the same period in 2021.

Before conducting the analyses for 2024, we perform a final validation for the surface elevation. We choose to only show the validation for this dataset, as it provides the most complete assessment of the simulation on the entire DD due to its broad spatial coverage (Fig. 5.9). Results for CMF are even better than in 2021 and confirm that CMF reproduces water levels more accurately than LM. Averaged over all six stations, CMF achieves an RMSE of 0.18 m, an RRMSE of 20%, and an MBE of 0.02 m. It also captures the increase in water level following storm Boris at every station except station 3, where it overestimates water elevation. By comparison, LM yields an RMSE of 0.38 m, an RRMSE of 33%, and a MBE of –0.34 m. As illustrated by its negative MBE, it almost systematically underestimates water levels, with the only exception occurring at certain times at station 5. As in 2021, LM performs better at downstream stations than at upstream ones.

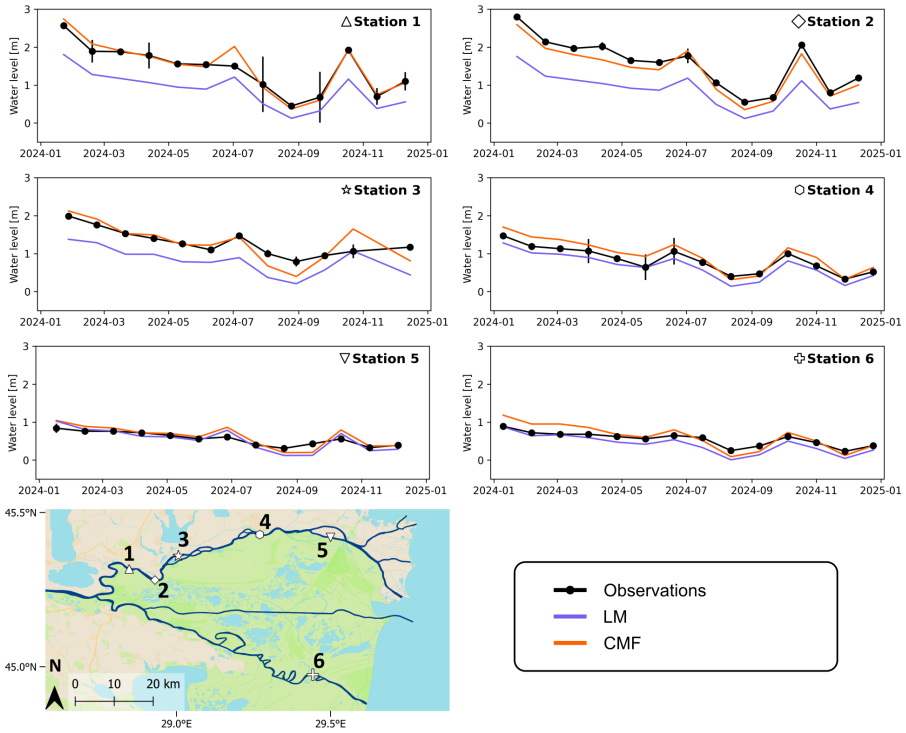

Figure 5.9: Validation of water surface elevation from the LM and CMF simulations in 2024, at six stations along the Danube Delta. A map (bottom left) shows the location of the six stations with numbered symbols, which are repeated in the top-right corner of each corresponding plot.

The effect of floodplains on the Danube discharge in the delta is clearly visible (Fig. 5.10). In the LM simulation (top panel in Fig. 5.10), almost no differences are observed between inflow and outflow at the branches: the mean sum of all branch discharges equals 100% of the upstream Danube input. In terms of discharge distribution, approximately 38% of the flow is directed to the Chilia branch, 27% to Sulina, and 34% to Sfântu Gheorghe. With no communication between branches and no discharge loss to the floodplains, these percentages remain identical between the branch entry points and their river mouths.

In contrast, the CMF simulation shows reduced outflows compared to the upstream inflow, with an average annual loss of 10.0±4.1% between the delta entrance and the river mouths (bottom panel in Fig.

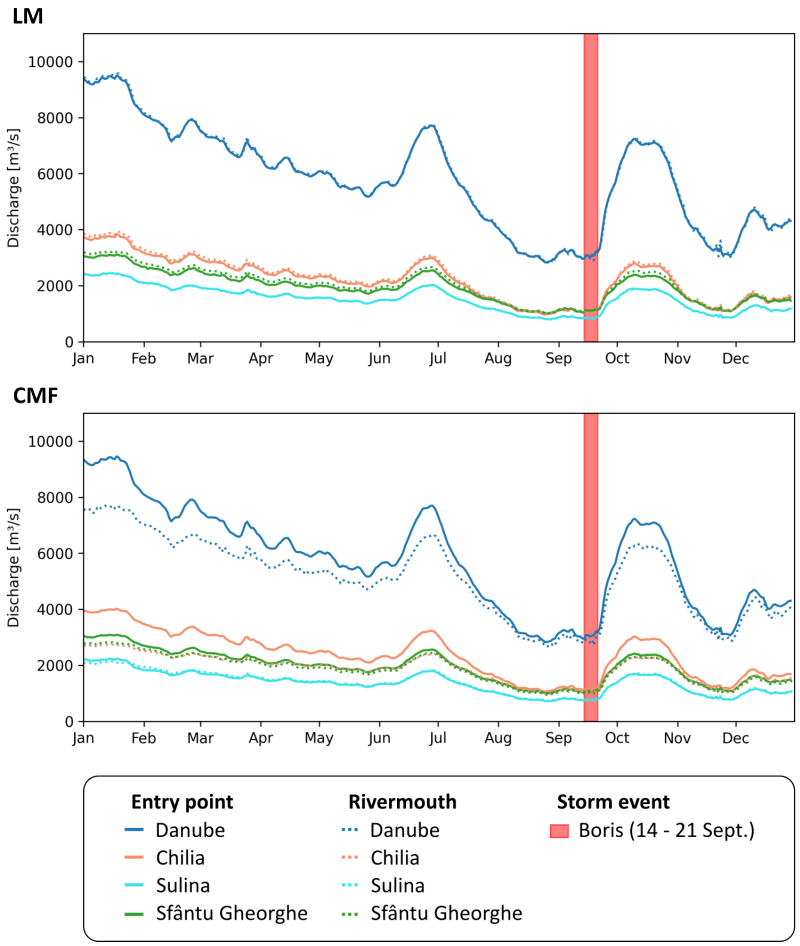

Figure 5.10: Discharges distribution simulated by CMF and LM for 2024. The figure shows the discharge at the entry point and rivermouths of the three main branches (Chilia, Sulina and Sfântu Gheorghe), and just upstream of the delta (Danube). The Danube outflow is obtained by summing the discharges at the six distributary mouths (four for Chilia and one for each of Sulina and Sfântu Gheorghe). The duration of storm Boris is indicated by a red rectangle.

5.10). This value is very close to that obtained in 2021 ($10.8 \pm 4.8\%$). Losses are particularly pronounced during high-flow periods, such as the surge following storm Boris, when discharge losses reached ~14%. They occur mainly in the Chilia branch, while the other two branches show only minimal changes. In terms of distribution, discharge in the Chilia branch decreases from 41% at the bifurcation to 33% at the mouths, Sulina remains roughly constant at 24% of the upstream flow, and Sfântu Gheorghe decreases slightly from 34% to 32%.

In both simulations, the relative contribution of each branch varies over time. During low-flow periods (e.g. August-September and late November), discharges in Chilia and Sfântu Gheorghe are nearly identical. In contrast, in higher discharges period (e.g. the first half if the year up until July, or during the peak right after Boris), the Chilia branch clearly carries a larger proportion of the Danube discharge than Sfântu Gheorghe.

To assess the impact of floodplains on circulation, we examine two dates characterized by distinct wind patterns: 8 February 2024, with winds blowing from the south-west in front of the delta and 21 September 2024, with winds blowing from the north-east (Fig. 5.11). In both cases, simulated surface circulation follows the prevailing wind direction, and the general patterns are similar. We observe the formation of a clockwise eddy south of the Sulina jetties under winds coming from the northwest, while an anticlockwise current forms northeast of the Sulina mouth under winds coming from the southeast.

Differences between the two configurations are mainly found near the delta's shoreline, and are primarily linked to the presence/absence of closed boundaries at the shoreline. In the LM simulation, the exclusion from the computational domain of the sand banks in front of the Chilia mouth (north of the Sulina jetties) and of the Sakhalin barrier island (south of the Sfântu Gheorghe mouth) produces localized recirculation patterns (second column in Fig. 5.11). In the CMF scenario, additional flow is visible from the floodplains to the sea, particularly north of the secondary Chilia delta on 8 February 2024 (first row and column in Fig. 5.11). The discharges at the rivermouth being different, the intensity of the resulting currents also varies slightly, leading to minor differences in circulation features. For instance, the eddy northeast

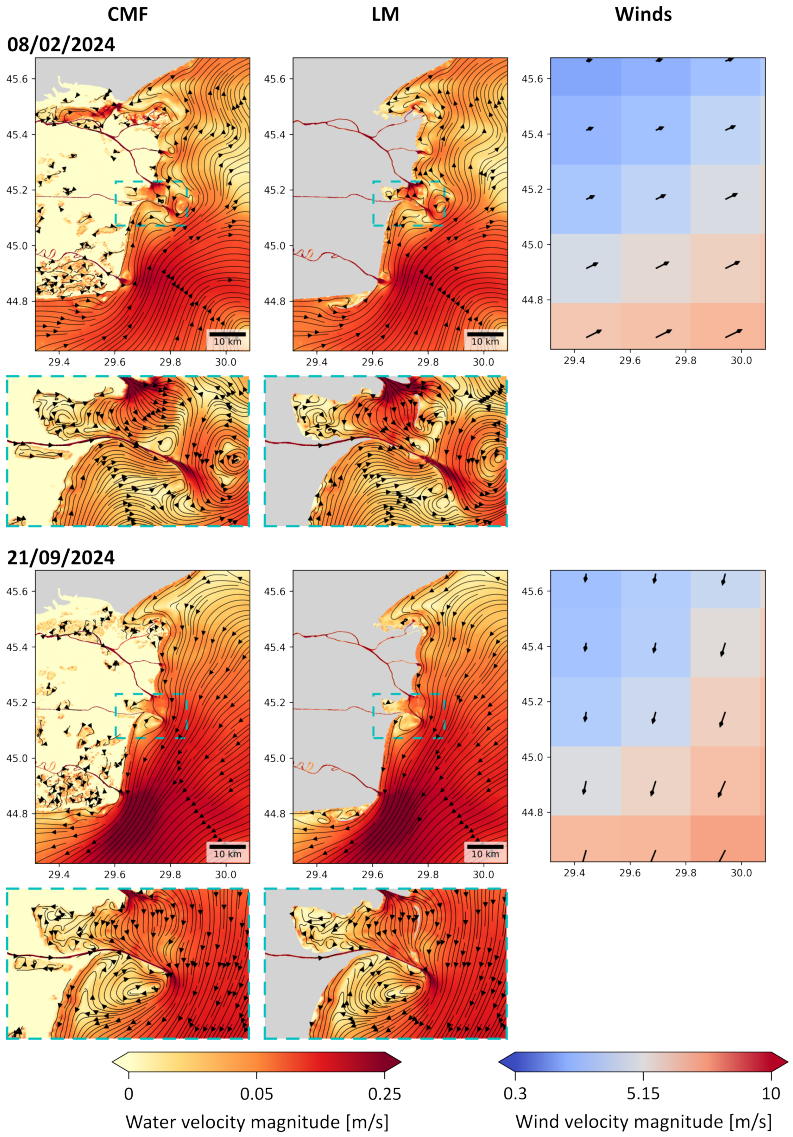

Figure 5.11: Circulation from the CMF (left) and LM (center) simulations and ERA5 winds (right), shown as daily averages for 8 February and 21 September 2024. Maps are centered on the delta shoreline. Below each circulation panel, a close-up of the Sulina and Chilia mouths is displayed in a blue dotted frame, with the corresponding area indicated by a blue rectangle in the main map. Land outside the domain is represented in gray.

of the Sulina jetty on 8 February has a more circular shape in the LM simulation (first row in Fig. 5.11). Overall, the influence of floodplains on circulation seems restricted to the coastal zone and does not extend beyond approximately 10 km offshore.

To assess the impact of floodplains during high-flow peak events, we compare spatial flooding patterns two days after the peak discharge caused by the storm Boris in 2024 (12 October), with the same date in 2021 (Fig. 5.12). This two-days delay is chosen because, according to our simulations, it takes between one and two days for water to flow from the upstream boundary at Isaccea to the sea.

The overall patterns are very similar, but the delta in 2024 is generally drier than in 2021, particularly in the Roşu–Puiu unit. In total, 2282 km^2 of the delta area were flooded in 2021 against 2062 km^2 in 2024. Despite this overall reduction, about 70 km^2 were inundated on the 12 October 2024 that were not flooded on the same date in 2021. These areas are located close to the main channels: between the Şontea–Fortuna, Matiţa–Merhei, and Gorgova–Uzlina units, north of Matiţa–Merhei, and in the eastern part of Dunavăţ–Dranov. All of these areas correspond to floodplains that are easily connected to the river and were also inundated in the LLMF simulation, where we only see minimal flooding (Fig. 5.A.1).

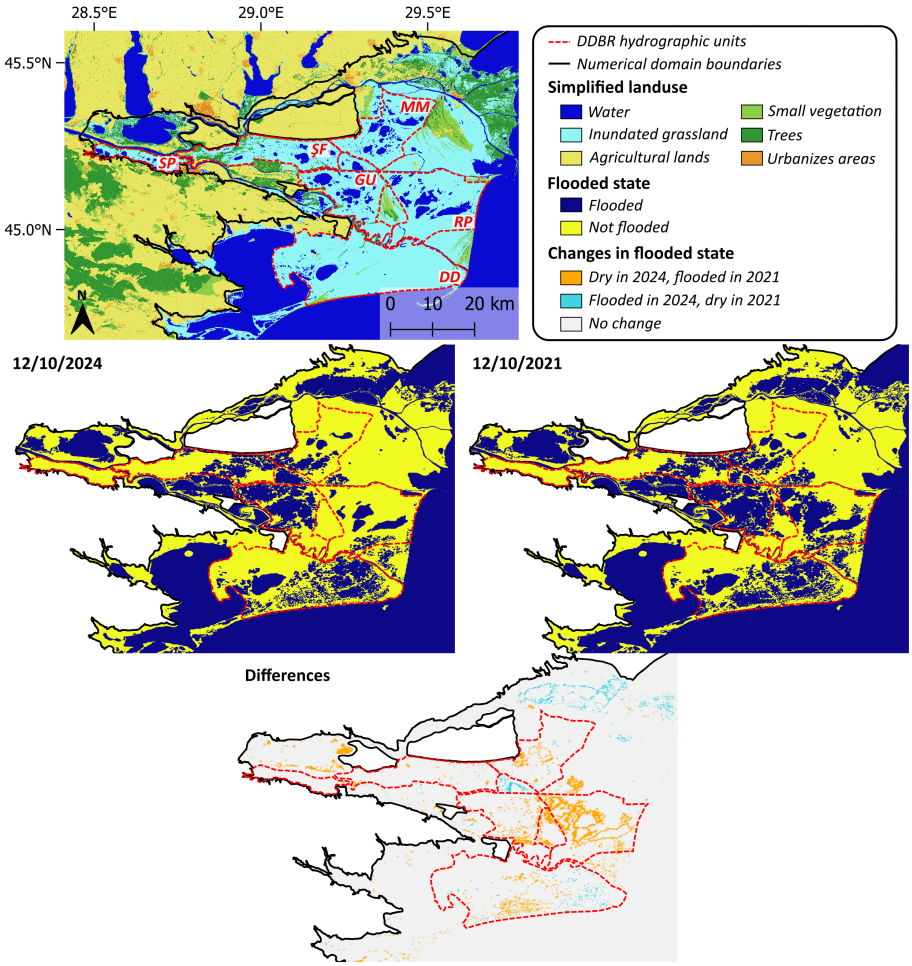

Figure 5.12: Comparison of flooded areas between 12 October 2024 and 12 October 2021. The red dotted line marks the boundaries of the Danube Delta Biosphere Reserve (DDBR) hydrographic units: SP – Somova-Parches, ŞF – Şontea-Fortuna, MM – Matiţa-Merhei, GU – Gorgova-Uzlina, RP – Roşu-Puiu, DD – Dunavăţ-Dranov. The top panel shows a simplified LifeWatch land-cover map and the location of hydrographic units. The second row displays the flooded states for each date, and the third row shows their differences.

5.4 Discussion and conclusion

In this study, we used the unstructured hydrodynamic model SLIM to evaluate the role of floodplains in the Danube Delta and their influence on the Danube–Black Sea continuum. Our simulations show that floodplains play a significant role in the system. On average, in the year we simulated, the proportion of upstream discharge reaching the sea through routes other than the six main rivermouths represented 10.0±4.1% (2024) and 10.8±4.8% (2021). Including floodplains also improved agreement with observed water levels and discharges compared to simulations without them. At the same time, the influence of floodplains on coastal circulation appears spatially limited, with minor differences between simulations confined to within ∼10 km of the shoreline. The river Manning coefficient values exerted an even stronger control on water levels than floodplain inclusion, underlining the importance of parameter choices in model calibration.

Our results indicate that including floodplains in the modeling framework of the Danube–Black Sea continuum has a clear impact on simulation results in the delta, and that it allows for a better representation of the reality, notably by improving agreement with observed water levels and discharge distributions among the branches. For a fixed Manning coefficient value, the presence of floodplains tends to lower water levels and buffer discharges, particularly under high-flow conditions. This buffering role is well documented in the literature, with both modeling studies and field observations reporting that the removal of floodplains leads to higher in-channel water levels, higher discharge peaks and faster recession limbs, particularly in high-flow situations (Shankman & Pugh, 1992; Clilverd et al., 2016; Fleischmann et al., 2019; Suchara, 2019). Based on our simulations, we estimate that on average about 10% (10.0±4.1% for 2024 and 10.8±4.8% for 2021) of the discharge upstream of the delta is buffered by the floodplains and reaches the sea through other pathways than the six monitored rivermouths. This proportion is hydrologically significant, as it represents roughly one third of the combined inputs of the three other major rivers entering the Black Sea (namely the Dnieper, Dniestr and Southern Bug), and exceeds the discharge of the Dniestr or Southern Bug combined. This amount of water loss to the floodplains is in agreement, although

slightly higher, than values reported in previous studies ——2.2–7% according to Driga (2008) and about 8% in Gâştescu (2009). However, Gâştescu (2009) also highlighted substantial interdecadal variability over the last century, with discharge loss to the floodplains ranging from 4% of upstream discharge in the 1950s to 10% in the 1980s. In addition, Popescu et al. (2015) reports a steady increase in discharges to the delta over the past 150 years, which may partly explain our higher estimate. Our results also show that this proportion increases during high-flow periods, such as the surge following storm Boris in September 2024, when discharge losses to the floodplains reached ~14%.

The influence of floodplains also depends on whether high discharges occur as short peaks or as prolonged periods of elevated flow. The comparison of flooding extent on 12 October 2021 and 12 October 2024 (Fig. 5.12) illustrates this contrast. Although 2021 was relatively dry on that date, the flooded area was larger than in 2024. This difference reflects the fact that 2021 was overall a wetter year than 2024 : according to the AFDJ data (Fig. 1.4), average discharge in 2021 was about 6010 m^3/s (range 2840–10 180), compared to 5775 m^3/s in 2024 (range 2840–9550). Over the year, discharges in 2021 were consistently higher than in 2024, except for the surge following storm Boris and a short period in January. As a result, floodwaters in 2021 penetrated farther into the delta interior plains. This also reflects in the slightly higher proportion of water lost to the floodplains in 2021 compared to 2024 ($10.8 \pm 4.8\%$ and $10.0 \pm 4.1\%$, respectively). In contrast, flooding on 12 October 2024 was concentrated along the river, with inundated areas absent on the same day in 2021. These differences are consistent with the idea that short high-discharge surges primarily fill floodplains adjacent to the river, while sustained high discharges allow water to spread farther into the delta (Poncos et al., 2013).

While floodplains have a definite impact on in-river water level, they seem to exert little influence on the general circulation over the NWS. All simulations reproduce circulation patterns consistent with the literature, regardless of whether floodplains are included. They all present a yearly averaged southwestward current along the shelf break and coast (Tolmazin, 1985; Lima et al., 2021), with mean velocities on the shelf below 0.1 m/s (Oguz & Besiktepe, 1999), stronger currents near

the shelf break and rivermouths (Causio et al., 2021), and the formation of a clockwise eddy south of the Sulina piers (Romanescu, 2013). On shorter daily time scales, current direction is primarily wind-driven (Oguz & Besiktepe, 1999; Kubryakov et al., 2018) and velocities on the shelf reach values of 0.2-0.3 m/s (Causio et al., 2021). The high spatial resolution of our model allows us to resolve the detailed hydrodynamic features around key coastal structures, such as the Sulina jetties and nearby shoreline, where localized eddies and velocity gradients are particularly sensitive to bathymetry and boundary conditions. The observed differences between simulations with and without floodplains appear to be confined to within about 10 km around the delta's shoreline. This is not surprising given that the amount lost to the floodplains amounts to roughly 10 % (~650 m^3/s) of the of the 6000-6500 m^3 entering the delta. On the other hand, as the circulation on the NWS is partly driven by baroclinic processes resulting from density contrasts between freshwater and seawater (Miladinova et al., 2020; Ferrarin et al., 2025), it is possible that the influence of the floodplains is not fully captured by our 2D barotropic model configuration. In any case, hydrodynamic models such as ours are rarely an end in themselves, and floodplain–river exchanges remain critical for sediment dynamics, nutrient fluxes, and salinity in the NWS. In particular, floodplains can act not only as pathways that delay or reroute material, but also as sinks that retain sediments and nutrients before they reach the sea (Cristofor et al., 1993; Popescu et al., 2015; Nichersu et al., 2025). Once in the sea, the influence of the Danube plume can extend tens to hundreds of kilometers into the Black Sea (Panin, 2011; Kubryakov et al., 2018; Ferrarin et al., 2025), which underlines the importance of including the delta and its floodplains in broader NWS and Black Sea modeling frameworks.

Besides the inclusion of floodplains, our results show that the Manning coefficient value in the river has the most impact on simulation results. Increasing this coefficient in the river leads to increased water levels. This means that in configuration with floodplains, increasing the Manning coefficient also leads to more water going into the floodplains and larger flooded areas, as water will overtop the riverbanks at a lower input discharge threshold. As a result, the impact of floodplains is more pronounced under higher Manning values. Although our Man-

ning configurations differ not only in magnitude but also in their spatial distribution, with the inclusion of main and secondary channels in high- and low-manning scenarios, the trends we observe are sufficiently consistent and marked to support our conclusions. In addition, the responses we identify are in agreement with established hydraulic principles and previous studies that highlight the importance of channel roughness for flood dynamics in numerical models (Yamazaki et al., 2011; Al Mehedi et al., 2024).

Although the CMF configuration provides the best overall agreement with observations, its performance is not without limitations. Discharges are slightly overestimated at both Danube and Tulcea stations (by ∼10%, corresponding to RMSE of ∼450 m^3/s and ∼280 m^3/s, respectively) and more strongly overestimated at Sulina (∼30%, RMSE of ∼300 m^3/s). Similar patterns are also reported by Ferrarin et al. (2025), who overestimates flow towards the Tulcea branch and underestimated flow towards the Chilia branch (RMSE ∼165 m^3/s for both branches). In our case, the overestimation at Tulcea is slightly more pronounced, while the bias at Chilia is almost negligible (RRMSE ∼4%, RMSE ∼100 m^3/s). These discharges overestimations are likely related to an imperfect representation of the complex system of channels, lakes and floodplains in the different hydrological units of the delta. For instance, the error observed at the Danube station is probably linked to the absence of water into the Somova–Parcheş unit (upstream of the delta), leading to an overestimation of the water discharge reaching the delta. Similarly, the lack of water into the western part of the Şontea-Fortuna unit (between the Tulcea and Chilia branches) likely contributes to the overestimation of the discharge in the Tulcea and Sulina branches. We also observe an overestimation of the water levels at the downstream end of the river, which is probably due to the fact that not enough water is entering the inner delta (e.g. into the Matiţa-Merhei unit, between the Chilia and Sulina branches). As a result, the artificial lowering of the water level caused by the lower Manning coefficient values in the LM scenario leads to better agreement with observations at the downstream stations, while this configuration strongly underestimates water levels upstream. Lastly, there is also the issue of some agricultural areas remaining inundated throughout the year. Together, these shortcomings suggest that the network of channels, lakes and floodplains

are not being adequately represented and used by the model, and that river-delta connectivity could be further improved.

A likely cause of this inadequate communication with the floodplains lies in data limitations, particularly regarding the representation of topography. The Copernicus DEM used in this study is in fact a Digital Surface Model (DSM), which does not filter out vegetation or built structures. Many delta banks are wooded, and tree cover is interpreted by the DSM as topographic features several meters high, which can transform small protective dikes into barriers and artificially block water exchange between the river and the floodplains. In addition, with a horizontal resolution of 30 m, the DSM fails to capture smaller levees around agricultural fields, which could be the reason behind the observed spurious flooding. Previous studies have highlighted that such errors in riverbanks elevation can be decisive in flood dynamic: Cliverd et al. (2016), for instance, found that removing a one-meter embankment in a small catchment was the difference between no flooding over a decade and regular flooding. Similarly, sensitivity analyses rank topography above in-channel roughness in terms of influence on flood dynamics (Oubennaceur et al., 2019; Alipour et al., 2022). This also echoes the conclusions of Chapter 3, where we emphasized the importance of accurately representing riverbanks in flood dynamics. Access to a DEM that filters vegetation would therefore greatly improve representation of river–floodplain exchanges.

This misrepresentation of the floodplains topography could also explain the limited impact of the Manning coefficient values in the floodplains, as inundation patterns are likely already largely determined by the terrain. This echoes the findings of several other studies, which, although they identified bottom friction as one of the most decisive factors in determining the extent of flooding, emphasize that topography—through bank elevation, slope orientation, and relative height— exerts an even greater control over flood dynamics (Alipour et al., 2022; Crăciun et al., 2022). Another possible explanation, which is not mutually exclusive, is that the Manning bottom drag parametrization is not well suited to represent floodplain friction. Several studies have shown that vegetation–flow interactions are not driven by homogeneous friction value, but depends on vegetation density, leaf area, as well as stem diameter, height and flexibility (Harvey et al., 2009; White

et al., 2025). Incorporating such physically based descriptions of vegetation parameters in friction coefficient could provide a more realistic representation of floodplain hydraulics than assigning a uniform Manning coefficient by land use class. That said, since topography seems to exert a stronger control over floodplain inundation than bottom friction (Alipour et al., 2022; Crăciun et al., 2022), the largest improvements in representing water extent would likely come from better topographic data, while refinements of floodplain bottom friction could then provide an additional level of accuracy.

Another possible improvement would be to explicitly account for channels within the delta. Those small connectors play a crucial role in surface-water exchanges in wetland environment, as they can fill and redirect water or delay floodplain inundation (Czuba et al., 2019). In the Danube Delta, such channels are known to be the entry points for water to go into the different units of the delta, which they can then flood by overtopping. For example, water mainly enters and exits the Şontea-Fortuna unit though canals, including the Mila 35 that connects Chilia and Tulcea branches (Popescu et al., 2015). While incorporating every channel would be a major and not always necessary task, accounting for the main channels could substantially improve the representation of water fluxes within the delta. These channels could be fully discretized in 2D, or, given that some are quite narrow, represented more efficiently by coupling the 1D SLIM module with the 2D floodplain mesh (Draoui et al., 2024).

In addition to these structural limitations, validation data remain limited, validation data are limited, both for assessing floodplain inundation extent and for evaluating the broader impact of floodplains on coastal circulation. Satellite observations are probably the most promising for flood extent validation, but no dataset currently provides dedicated coverage for the Danube Delta, and global products either display unrealistic inundation patterns or require heavy preprocessing. While there are some hydrodynamic validation data in the Black Sea, very few observations are available over the NWS and none near the Danube Delta shoreline. Nevertheless, the model shows good agreement with the available observations, giving confidence that the conclusions drawn here remain robust despite these limitations.

Looking ahead, the model developed here could be used as a basis for coupled applications, for instance with biogeochemical models (Duquesne et al., 2021) or sediment transport models (Saint-Amand et al., 2022). Such extensions would be particularly relevant in the Danube Delta coastal zone, where both eutrophication (Capet et al., 2013; Chevalier et al., 2024) and sediment dynamics (Tătui et al., 2019) remain pressing issues. By explicitly accounting for river–floodplain exchanges, the model provides a useful platform for assessing how these processes influence nutrient and sediment fluxes at the land–sea interface.

Overall, our results highlight the importance of explicitly accounting for floodplains when assessing the Danube–Black Sea continuum. While their influence on large-scale circulation is modest, floodplains substantially shape local hydrodynamics by buffering high flows, redistributing discharge, and creating alternative pathways to the sea. These functions are central to the delta's natural capacity to mitigate floods, a role that is increasingly critical in the context of rising discharge trends and projected increases in flood frequency across Europe. Beyond these hydrodynamic effects, floodplains play a critical role in regulating the transport and retention of nutrients, sediments, and pollutants, further underlining their importance for the continuum. By demonstrating how floodplain processes can be represented in a basin-to-coast modeling framework, this study provides a step toward more integrated assessments of flood risk and environmental change in deltas.

Appendix

5.A Spatial validation for CLMF and LLMF simulations

Spatial validation of flooding for 2021 was performed for two contrasting hydrological states (Fig. 5.A.1): the end of the "wet" season (23 June 2021), when upstream discharges began to decrease after several months of high flow (~8000 m^3/s), and the end of the "dry" season (8 November 2021), when discharges started to rise again after a prolonged low-flow period (~4000 m^3/s). Results from the CLMF simulation were nearly identical to those of CMF presented in Chapter 5.3.1, while the LLMF configuration produced almost no flooding. This is the reason why they are presented here and not in the main text. CLMF produce flooding mainly in areas expected to be inundated. Depending on the time of the year, between 83.5–84.3% of the flooded areas correspond to LifeWatch land-cover classes “water” or “inundated grassland”. Spatially, it tends to underestimate flooding, with several lakes missing in the western Şontea–Fortuna unit and no water predicted in the Somova–Parcheş unit (left column in Fig. 5.A.1). In total, the CLMF simulation flood 2342 km^2 on the 23rd of June and 2156 km^2 on the 8th of November. In contrast, LLMF presents a smaller inundated area (1248 and 1138, respectively), with no water in the Somova-Parches and Şontea-Fortuna units, and many lakes absent from the others (right column in Fig. 5.A.1). Both configurations also predict permanent flooding in areas that are expected to remain dry for at least part of the year (highlighted by blue stars in Fig. 5.A.1), as those areas are either used for crops or as agricultural grassland. Those wrongly flooded areas represents about 7.3% (at least 157 km^2) of the total flooded area in CLMF, and about 6.1% (at least 67 km^2) in LLMF.

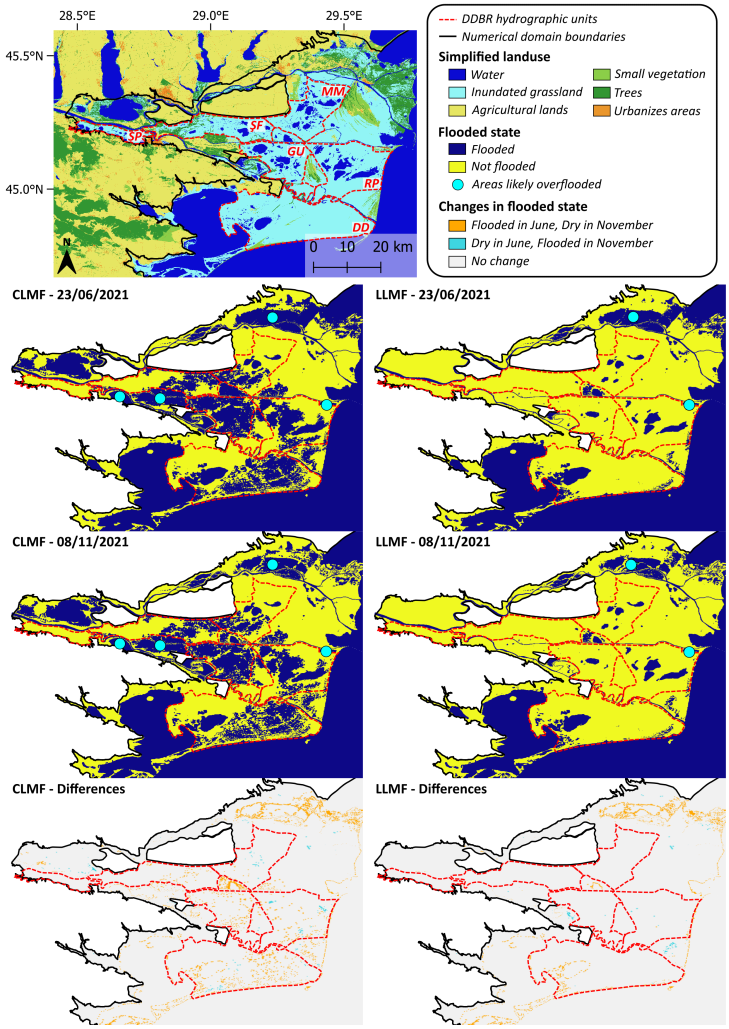

Figure 5.A.1: Changes in flooded areas between 23 June 2021 and 8 November 2021. The red dotted line marks the boundaries of the Danube Delta Biosphere Reserve (DDBR) hydrographic units: SP – Somova-Parches, ŞF – Şontea-Fortuna, MM – Matiţa-Merhei, GU – Gorgova-Uzlina, RP – Roşu-Puiu, DD – Dunavăţ-Dranov. The top panel shows a simplified LifeWatch land-use map and the location of hydrographic units. In the next three rows, left panels show CLMF results, right panels LLMF results: rows 2–3 display flooded states for each date, and row 4 shows their differences.

Chapter 6

Conclusions and perspectives

6.1 Conclusion

In this thesis, we investigated the role of the Danube Delta and its floodplains in shaping the regional hydrodynamics using a hydrodynamic modeling approach. To that aim, we needed a model capable of capturing processes across multiple scales, from riverine dynamics (tens of meters) to large-scale circulation on the North-Western Shelf (NWS) of the Black Sea (several kilometers and above). For this purpose, we employed the unstructured-mesh discontinuous-Galerkin finite-element ocean model SLIM presented in Chapter 2. First, we examined how different meshing strategies influence model performance on a localized section of the Danube Delta (Chapter 3). We then developed a bathymetric dataset for the three main branches of the delta (Chapter 4). Finally, we implemented the model across the entire delta and its floodplains, and assessed the contribution of floodplains to the hydrodynamics of Danube Delta (Chapter 5).

We found that the mesh configuration plays a decisive role in river-floodplain hydrodynamic modeling. Three aspects proved particularly

important. The first one is mesh resolution inside the river: higher resolution (20 m in our case) allows for a better representation of river morphology and, through it, in-channel hydrodynamics. Second, explicitly following riverbanks—and thereby accurately representing their elevation—is necessary to reproduce the overtopping and flooding dynamics. Third, as expected, the total number of elements and the size of the smallest elements directly controls the computational performances. Based on these findings, we propose a mesh configuration that combines a hybrid curvilinear–unstructured triangular mesh with 20 × 20 m resolution in the river channels, and a fully unstructured triangular mesh in the floodplains, whose resolution decreases with distance from the riverbanks. Our results suggest that this configuration would offer the best compromise between an accurate representation of in-channel hydrodynamics, flood extent, and computational performance, and it was subsequently adopted for the Danube Delta simulations in Chapter 5.

The next step was to obtain bathymetric data for interpolation on the mesh. Since no comprehensive dataset existed for the three main distributary branches of the Danube Delta, we combined three different sources to construct the first unified, high-resolution, and accessible bathymetric model covering all branches of the system. Bathymetric data were interpolated onto a hybrid curvilinear–unstructured triangular mesh using an anisotropic Inverse Distance Weighting (IDW) method. The mesh is similar to the one designed for the river in Chapter 3, but its resolution was adjusted to balance numerical accuracy and ease of use for other studies. The resolution of the resulting product ranges from 2 m in complex connection zones between unidirectional segments to 100 m in segments, where bathymetry variations along the flow are small. On average, the resolution is about 5 m across the flow and 50 m along the flow. Cross-validation highlighted the importance of data source density, with relative root mean square errors of 0.55%, 6.3%, and 27.6%, depending on the coverage of the datasets used. Beyond its use in this thesis, this final product provides a valuable resource for other hydrodynamic models in the Danube Delta, with potential applications in studies of biogeochemistry, sediment transport, ecology, and flood protection. The interpolation technique developed for its creation was subsequently applied to represent the bathymetry

in the full Danube Delta model in Chapter 5.

Building on the results of the previous chapters, we implemented the first hydrodynamic model covering the entire Danube Delta and its floodplains. Our simulations showed that explicitly including floodplains leads to better agreement for both water level and discharge observations in the delta. Floodplains were shown to lower water levels and buffer discharges, particularly during high-flow events, and to provide alternative pathways for water transfer to the sea. In the year we simulated, the proportion of the upstream discharge reaching the sea through routes other than the six river mouths explicitly represented in the model ranged from 10.0±4.1% (2024) to 10.8±4.8% (2021). At the same time, the calibration of the river Manning coefficient proved to exert an even stronger influence on model outcomes than the inclusion of floodplains, underlining the critical role of the bottom roughness parametrization. In the end, though we are confident in our results and conclusions, further improvements in river–floodplain interactions are possible, particularly through a more accurate physical description of the inner delta. Employing high-quality topography (e.g., a Digital Elevation Model (DEM) rather than a Digital Surface Model (DSM)), more precise riverbank elevations, and the inclusion of some of the main inner delta's channels would be key steps in this direction. In our simulations, the influence of floodplains on velocities was mostly confined to a zone extending about 10 km offshore. However, hydrodynamic models such as the one developed here are rarely an end in themselves: floodplains strongly affect nutrient and sediment fluxes, with impacts that may extend up to hundreds of kilometers into the Black Sea (Panin, 2011; Kubryakov et al., 2018). The model presented in this thesis can thus serve as a foundation for future work, providing a robust hydrodynamic framework for coupling with biogeochemical or sediment transport models to more fully capture the role of the Danube Delta and its floodplains in the Danube–Black Sea continuum.

At the end of this thesis, we can return to the research questions defined in the introduction (Chapter 1):

1. **How do different mesh-building strategies affect the representation of river–floodplain interactions?**

Mesh design in river-floodplain hydrodynamic models strongly influences in-river hydrodynamic accuracy, flooding patterns and computational costs. For a reliable river-floodplains exchanges description, focus should be on resolution inside the river and on explicitly defining the riverbanks. In our work we found that a 20 m resolution in the river gave the best results. In contrast, resolution in the floodplains can be gradually decreased with the distance to the riverbanks to reduce computational costs.

2. **How can heterogeneous bathymetric datasets be combined to produce a coherent description of the braided river bed in the Danube Delta?**
   Due to the inherent anisotropy of river bathymetry, conventional interpolation methods are unsuitable and must be adapted. In this work, we first projected the raw data into a channel-centered s,n-coordinate system, and then interpolated it on a hybrid curvilinear-unstructured grid using an anisotropic IDW method. To ensure smooth transitions between unidirectional river segments, connection zones were included in the interpolation of adjacent segments, and their final bathymetry was computed as a weighted mean based on proximity to the segment. This approach produced a consistent and accurate representation of the delta's braided river bed.

3. **How does the inclusion of floodplains influence the modeling of the hydrodynamics within the Danube Delta?**
   Including floodplains clearly improved the agreement between simulated and observed water levels and discharges observations. The presence of floodplains helps lower in-channel water level and buffer discharges by allowing overbank flow. The effect is especially pronounced during periods of elevated discharge, when floodplains attenuate peaks and slow recessions. In contrast, neglecting floodplains forces the model to rely more heavily on channel roughness calibration, which does not reproduce the same high-flow dampening effect.

4. **How do floodplains modify the fluxes of water from the Danube to the Black Sea?**
   Floodplains integration leads to a net decrease of the discharge

leaving the the delta through the six modeled river mouths. In 2024, an average of approximately 10±4.1% of the discharge entering the delta reached the Black Sea through pathways not explicitly represented in the river network. This proportion increases in high-flow conditions, such as after storm Boris in 2024, when discharge losses to the floodplains reached ~14%. A comparable pattern is observed for 2021, which was a wetter year than 2024 overall, and showed slightly higher but still consistent average losses of 10.8±4.8%. These discharge losses to the floodplains reduce the share of water carried by the main branches, with the Chilia branch particularly affected, while Sulina remains nearly constant and Sfântu Gheorghe decreases slightly. Floodplains therefore not only reduce total outflow through the main river mouths, but also change the relative importance of fluxes between the river's branches.

6.2 Contribution to the model development

Answering the above research questions required the development and adaptation of several modeling tools. While many of these advances were not developed by me directly, I played a central role in testing, refining, and applying them within the context of the Danube–Black Sea continuum.

First, mesh generation was a key methodological challenge. Within the SLIM user community, the Python library seamsh, which is based on the open-source mesh generator GMSH (Geuzaine & Remacle, 2009), is the most commonly used tool for mesh creation. I contributed to the design of the meshing procedures behind the hybrid curvilinear-unstructured meshes used in this thesis, tested their performance, and provided feedback that led to significant improvements. I also evaluated the resulting meshes with respect to both hydrodynamic accuracy and computational cost.

Second, anisotropic bathymetry interpolation in rivers represented a novel development within our team. My idea to project bathymetric data into channel-centered s, n-coordinates was implemented using the meshing tools developed for our curvilinear grids. Building on this,

I implemented and tested an anisotropic IDW interpolation method, which proved effective in producing a coherent bathymetric dataset for the Danube Delta.

Third, Wetting and drying (WD) proved to be a crucial feature for including floodplains in our computational domain. Although I did not design the current WD scheme in SLIM, I worked on an earlier implicit version, aiming to integrate and improve upon the algorithm presented by Le, Lambrechts, et al. (2020). However, the complexity of its multiple parameters limited its robustness and usefulness. With the transition of SLIM to GPU-adapted code, the model was restructured around explicit time integration schemes, and a more reliable explicit WD algorithm was developed. While much of this effort came from other developers, I was among the first users to test the new scheme in realistic configurations, and my feedback directly motivated several modifications compared to the algorithm described in Randresihaja et al. (2025).

Finally, I intended to exploit SLIM's Eulerian tracer framework to implement a biogeochemical model for the Danube–Black Sea continuum. Due to time constraints, I only implemented a simple NPZD model, which I was not able to calibrate on the Danube Delta. Preliminary results are nevertheless presented in Section 6.3.2, providing a first step toward future coupling of hydrodynamics and biogeochemistry in this system.

6.3 Perspectives for future works

At the end of this thesis, we can identify several directions that could be taken to further improve the study of the Danube Delta–Black Sea continuum. The results obtained in this thesis provide a useful basis, but also point to limitations that future studies may address. In the following, we outline some possible paths for further development.

6.3.1 Improving the hydrodynamic model

While this thesis primarily focused on the Danube Delta, it is important to consider its position within the broader Danube-Black Sea

continuum. Previous studies have shown that the Danube's influence can extend hundreds of kilometers offshore, affecting the hydro-biogeochemistry properties of the entire NWS and beyond (Panin, 2011; Kubryakov et al., 2018; Ferrarin et al., 2025). In this context, an important next step would be to study the overall impact of the delta on the Black Sea. However, a depth-averaged (2D) model such as the one presented in this thesis is not ideally suited to represent the processes governing water circulation on the NWS. As there are virtually no tides on the Black Sea, the hydrodynamics on the shelf is mainly driven by wind and freshwater inputs from the rivers. The latter create strong salinity and density gradients, leading to baroclinic behavior (Miladinova et al., 2020; Dorofeyev & Sukhikh, 2021; Ferrarin et al., 2025). Accurately representing the hydrodynamics of the NWS therefore requires a fully three-dimensional, baroclinic model on the coastal and shelf domain.

Building on the present work, different modeling strategies could be developed to bridge the delta and shelf dynamics. The first one is to build a 3D model covering the entire Danube Delta-NWS continuum. However, even though WD algorithm can in principle be incorporated in 3D models, this approach is generally avoided for large systems because of the high computational cost, numerical instabilities, and the complexity of such scheme (Choudhary et al., 2025). Another possibility is to couple a 2D-model on the floodplains with a 3D-model in the coastal areas (G. Huang et al., 2022; Carlotto & Chaffe, 2023; Choudhary et al., 2025). Such hybrid 2D-3D model has not been yet developed in SLIM, but would allow to combine the mixing of freshwater with saline sea, without significantly increasing computational cost due to the inclusion of floodplains and their associated WD processes. Developing such a coupled system would therefore represent a logical continuation of the present work.

Beyond density-driven stratification, wind forcing also plays a dominant role in shaping the circulation on the NWS (Oguz & Besiktepe, 1999). Winds over this region are generally from the north, although western and southern winds become more frequent during spring and summer, and average annual wind speeds is above 4 m/s (Causio et al., 2021). The result is an average south-eastward circulation along the

coast, with high variability and even periodic reversal of current direction depending on wind conditions (Kubryakov et al., 2018). Additionally, storm events—about 30 storms/year on the Romanian coast—occurring mainly in winter play a major role in shaping the circulation, shoreline dynamics, flooding and erosion of the region (Gogoase et al., 2011; Zăinescu et al., 2017).

In this thesis, wind forcing was provided by the ERA5 reanalysis dataset (Hersbach et al., 2018), which offers a spatial resolution of 0.25° × 0.25° (~20 km × 29 km at Black Sea latitudes) and an hourly temporal resolution. This is relatively coarse compared to the hydrodynamic mesh used in this thesis, which has a resolution of 1.5 km at its coarsest and reaches down tens of meters in the river. Such a mismatch in scale may limit the model's ability to resolve fine-scale circulation patterns near the delta shoreline, to capture storm dynamics accurately, and to represent the exchanges between the river mouth and the NWS. Several studies have shown that improving wind forcing resolution can improve hydrodynamic model prediction capabilities, and this in various environments and meteorological conditions (Stanev et al., 1997; Quattrocchi et al., 2014; Xue et al., 2022; Agulles et al., 2024; Randresihaja et al., 2025). In addition, the spatial resolution of ERA5 is coarser than the distance from the coast (~10 km) within which we found floodplains to influence the circulation. It must also be noted that, ERA5 typically does not resolve changes in wind dynamics at the land–sea interface, such as the land–sea breeze system or the reduction in wind speed over land, which are particularly relevant in the vicinity of river deltas (Potisomporn et al., 2023; Alkhalidi et al., 2025).

To overcome these limitations, a regional atmospheric model such as Modèle Atmosphérique Régional (MAR) (Gallée & Schayes, 1994; Grailet et al., 2025) could be used as an alternative forcing source. MAR has already been tested over the Black Sea (Macé et al., 2025) and used successfully to force SLIM on the Scheldt–North Sea continuum (Randresihaja et al., 2025). It can be run at resolutions down to 2 km spatially and 15 minutes temporally (Grailet et al., 2025; Randresihaja et al., 2025), which would better match our hydrodynamic model's resolution and enable a more realistic representation of nearshore circulation. In particular, it could enhance our ability to represent circula-

tion changes induced by floodplains and resolve wind-driven dynamics more accurately at the land–sea interface.

6.3.2 Integrating a biogeochemical model

Several studies have underlined the important role of the Danube Delta in the biogeochemistry of the Danube-Black Sea continuum. Overall, the delta acts as a nutrient filter, reducing the total amount of phosphorus and nitrogen coming from the Danube that reaches the Black Sea (Cristofor et al., 1993; Suciu et al., 2002; Friedrich et al., 2003). Wetlands and lakes have also been identified as hotspots for nutrient transformation to organic compounds, acting as sources of organic nitrogen and phosphorus for downstream ecosystems and the coastal sea (Suciu et al., 2002; Durisch-Kaiser et al., 2011). These processes are strongly seasonal, with increased nutrient uptake during the growing season and potential nutrient release in winter. Discharge variability also plays a critical role: lakes tend to be most effective at nutrient retention during low to moderate flows, while floodplains become active at higher discharges, their contribution depending on the extent and duration of inundation. Nutrient retention appears to be optimal during average water levels (Cristofor et al., 1993; Suciu et al., 2002; Friedrich et al., 2003; Nichersu et al., 2025).

The filtering role of the Danube Delta is especially important since the primary production in the Black Sea is mainly dominated by riverine input—more than half of which are from the Danube alone—and by spring and autumn precipitations (Tuğrul et al., 2014). In the 1970s and 1980s, high nutrient loads from the rivers due to intensive fertilizer use and livestock production led to intense eutrophication, hypoxia events, major shifts in biogeochemical regimes, and significant biodiversity loss on the NWS (Konovalov & Murray, 2001; Yunev et al., 2002; Voss et al., 2011; Tuğrul et al., 2014). While the situation has since then improved, NWS ecosystems still have not completely recovered (Chevalier et al., 2024), and seasonal hypoxia still occurs—closely linked to nutrient and organic matter inputs from the Danube and high temperatures (Capet et al., 2013). As shown by Capet et al. (2013), hydrodynamic–biogeochemical models are valuable tools to assess these events, especially since field observations can miss local hypoxia events and be over-generalized. That study also underlines the

importance of properly representing the Danube Delta outputs to the sea, as their model that represent the Danube inputs without distinguishing the three branches of the delta failed to capture the entire hypoxic area in some extreme events. In a context where climate change and increased anthropogenic pressure are a reality in many coastal environments, high resolution hydro-biogeochemical models could help understand and inform on possible future situations for a better management.

As a first step toward a coupled hydro–biogeochemical framework for the Danube River-Delta–Black Sea continuum, we used SLIM's Eulerian tracer module to run a simple depth-averaged Nutrient-Phytoplankton-Zooplankton-Detritus (NPZD) model coupled with the hydrodynamic model developed in Chapter 5 for the CMF set-up. A similar approach with SLIM's 3D version has already been applied to Lake Titicaca by Duquesne et al. (2021). The details of the equations and parameters of the NPZD model can be found in Chapter 2.2.

The coupled hydro-biogeochemical model was run on one year from July 2020 to January 2022, using biogeochemical characteristics from Soetaert and Herman (2009). The biogeochemical model is initialized with uniform concentrations of DIN = 2.5, $P = 0.05$, $Z = 0.03$ and $D = 0.5$ mmol N m^{-3}. A constant input concentration of DIN = 1 mmol N m^{-3} is set at Isaccea, and all other tracers are set to zero at the different open boundaries. In this test case, horizontal diffusivity is set to zero. No calibration was performed compared to Soetaert and Herman (2009)'s test case. Results are therefore only presented here as a proof of concept, and should not be interpreted as a realistic representation of the system.

The simulation's results show that river discharge is the main driver of both inorganic nitrogen (DIN) and the total nitrogen budget (DIN$+P+Z+D$) (Fig. 6.1), with peaks in tracer quantities following peaks in discharges. This is expected, since the only nitrogen input in the domain is DIN from the upstream boundary. Nevertheless, the time series also reveal variations that cannot be attributed to discharge alone, but rather to interactions between the different pools. Periods of elevated DIN stimulate phytoplankton (P) growth, which in turn reduces DIN concentrations. Zooplankton (Z) dynamics were not well calibrated: after

an initial peak following a P peak in August 2020, their biomass rapidly declined to near-zero values. This likely reflects a combination of too little DIN input to the system together with excessively high values of k_{graze} and k_N. Low DIN inputs, added to a high k_N, limits P growth. In turn, restricted P availability and a high value for k_{graze} results in very weak Z growth through grazing, which is quickly outweighed by Z mortality and excretion. Consequently, the Z pool remains very small, and detritus (D) production in the model is mostly the consequence of P natural mortality, with D temporal dynamics mirroring those of P, but with lower values.

We examine the spatial distribution of nitrogen in the different pools on 1 July 2021 (Fig. 6.2), as it corresponds to peak values of total nitrogen, P and D (Fig. 6.1). This time frame is the perfect example of the combined effect of hydrology and biological interactions: a high discharge brought more DIN into the domain, but its accumulation was dampened by the subsequent growth of P, which is mirrored by an increase in D. Higher nitrogen concentrations are observed near the coast for all pools, consistent with the DIN input at the upstream boundary of the delta and the zero-concentration boundary condition imposed for all NPZD variables at the offshore open boundary. Offshore, the accumulation of DIN results from the decrease in PAR with increasing bathymetry, which limits DIN uptake by P. This accumulation, however, remains confined to the inner shelf, as DIN concentrations are constrained to zero at the open boundary. Although temporal evolution suggests that P should exceed DIN at this time (Fig. 6.1), it looks like the opposite when looking at the entire domain. This apparent mismatch is due to the fact that elevated P values are restricted to small areas within the delta, which become indistinguishable when viewed at the domain scale. As observed in the temporal patterns, spatial distributions of D closely mirrors those of P, but with lower values. Z values are very small compared to the other pools, but some biomass persists in the northern part of the domain.

The present NPZD setup is only a preliminary step toward a more realistic hydro-biogeochemical model for the Danube–Black Sea continuum, and there are many ways to go on. Calibration is a priority, as the current parameter values and initial concentrations resulted in near-total depletion of the Z pool. We also observed small negative tracer

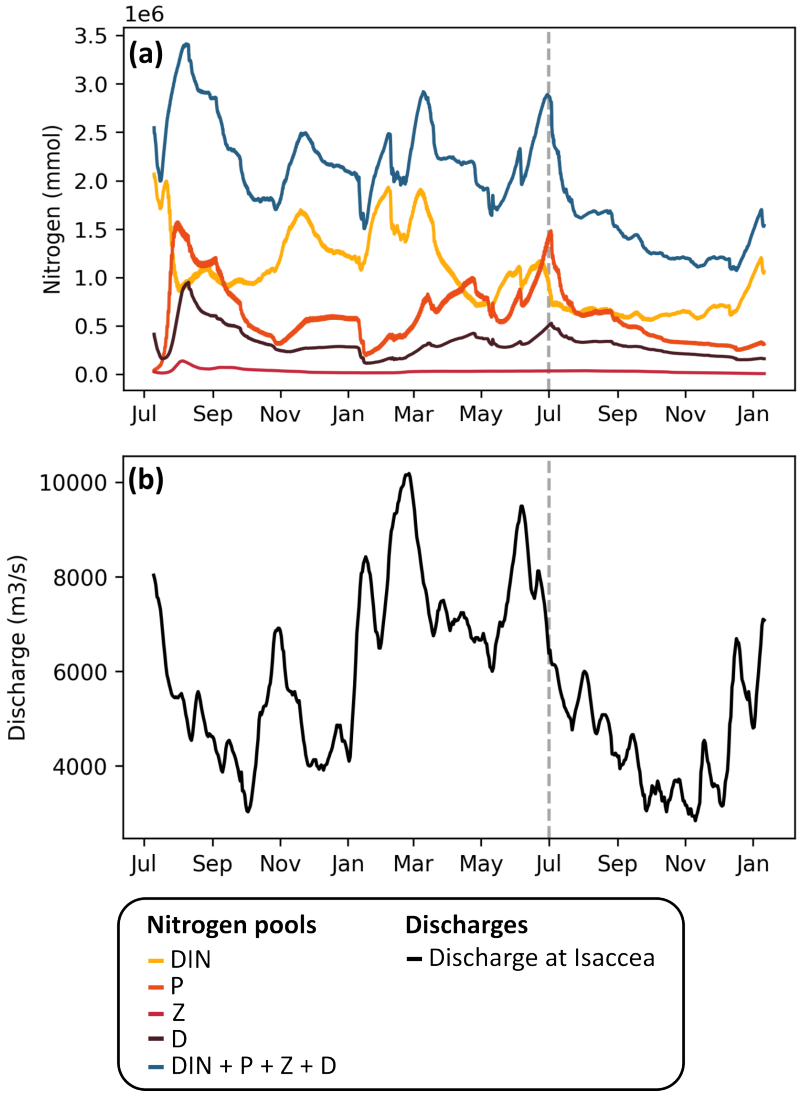

Figure 6.1: Temporal evolution of **(a)** the amount of nitrogen in the different pools over the entire domain and **(b)** water discharges imposed at Isaccea. The simulation covers the period from July 2020 to January 2022. The vertical gray dotted line represent the time at which we show the spatial distribution ins Fig. 6.2

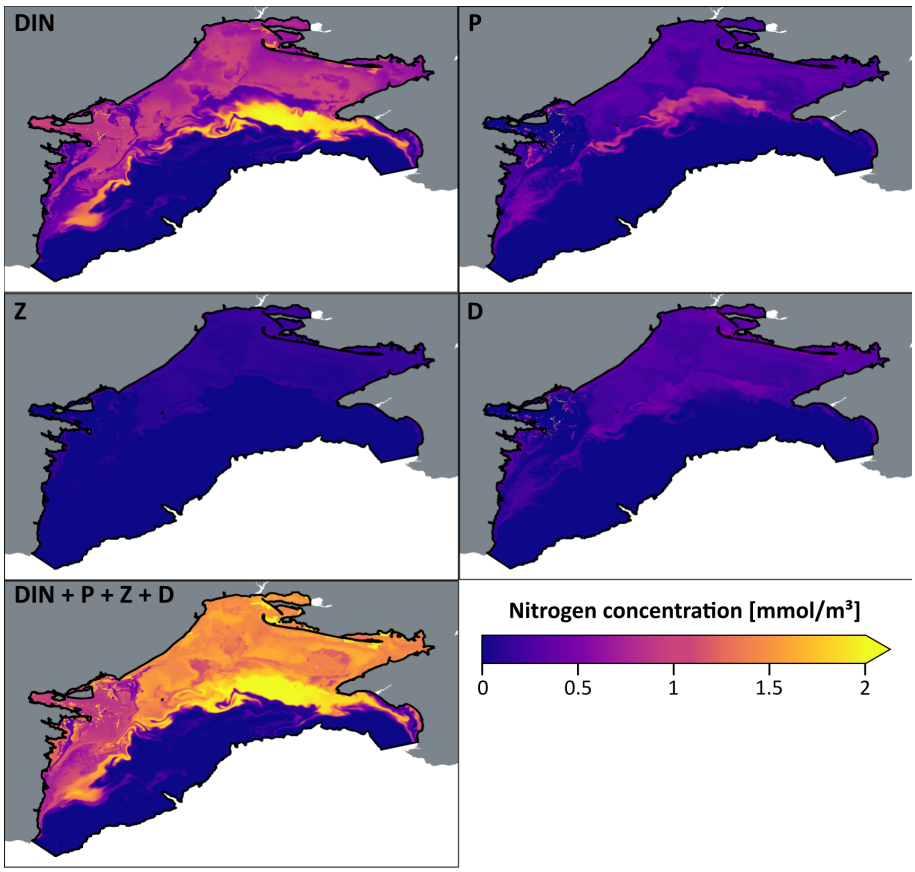

Figure 6.2: Spatial distribution of nitrogen in the different pools (DIN, P, Z, D) across the entire domain on 1 July 2021. The bottom panel shows the total nitrogen content in the domain. The black line indicates the model boundaries, while white and gray areas correspond to the sea and land outside the domain, respectively.

values in certain locations, which stem from the absence of positivity-preserving schemes for the reaction part of the biogeochemical equations. This issue could be addressed by implementing such a scheme, like the Modified Patankar-Runge-Kutta scheme (Burchard et al., 2005; Izgin et al., 2021). Another improvement of the hydro-biogeochemical configuration could be achieved by forcing SLIM with a model such as the BAMHBI biogeochemical model (Grégoire & Friedrich, 2004; Grégoire & Soetaert, 2010; Grégoire et al., 2025) at the offshore open boundary, which is the current biogeochemical module of the CMEMS product for the Black Sea (Ciliberti et al., 2021). Input from the rivers could also be more realistic, for example by using the monthly observations of chlorophyll and nutrients from the Trans-National Monitoring Network (TNMN). Another improvement would be to include the contribution of floodplain vegetation and land cover in inundated areas to nitrogen dynamics, in order to capture the filtering function of floodplains (Cristofor et al., 1993; Friedrich et al., 2003; Wohl, 2021). We should also take the temperature into account in the reactions, to better represent the seasonality (Soetaert & Herman, 2009). Finally, a more complete representation of NPZD dynamics would also call for a 3D setup to resolve vertical variability. Once calibrated, the hydro-biogeochemical model could serve as a flexible tool for scenario analysis. It could serve to simulate the effects of sudden increase in nutrient loads on the Danube River-Delta-Black Sea continuum, test different nutrient management strategies, and couple all this with different discharge regimes as the water height has a significant impact on nutrient retention in the delta (Cristofor et al., 1993; Nichersu et al., 2025).

6.3.3 Sediment dynamics and coastal erosion

Beyond eutrophication and seasonal hypoxia, the NWS coast is also strongly affected by coastal erosion. While it is a natural geomorphological process, erosion can cause substantial damage, even more so when its intensity is amplified by human activities (Pang et al., 2023). In the Black Sea, the Romanian coast—in particular the Danube Delta coastline—has been identified as especially vulnerable (Tătui et al., 2019), with estimates suggesting that about 55 % of the Romanian shoreline (Vespremeanu-Stroe et al., 2017) and over 60 % of the deltaic littoral (Romanescu, 2013) are currently undergoing erosion. In

the NWS, erosion is driven by a combination of factors: storm events (Vespremeanu-Stroe et al., 2017; Tătui et al., 2019), sea-level rise (Tătui et al., 2019; Pang et al., 2023), reduced sediment supply from rivers (Panin et al., 2016; Görmüş et al., 2021), and anthropogenic pressures such as coastal development and poorly designed protection structures (Romanescu, 2013; Panin et al., 2016).

The Danube and its delta play a central role in this dynamic. Over the past century, the sediment load delivered to the Black Sea has dramatically decreased. The construction of the Iron Gates Dams in the 1970s alone reduced sediment discharge by 30–40% (Panin & Jipa, 2002), and additional modifications of the river flow, both upstream and in the Danube Delta, further altered sediment dynamics (Ungureanu & Stanica, 2000; Tiron Duţu et al., 2014). Today, it is estimated that less than one-third of the sediment load that reached the sea a century ago is still delivered (Vespremeanu-Stroe et al., 2017; Görmüş et al., 2021). Coastal structures directly linked with the delta's dynamics have also contributed to coastal erosion. One notable example is 8 km-long Sulina jetties: originally built to prevent sedimentation in the navigation channel, these dikes disrupt the southward littoral drift from the Chilia branch, redirect Sulina's sediments offshore (where they settle before reaching the coast), and generate persistent eddy-like circulation patterns that modify sediment transport. Combined with offshore disposal of dredged sediments, these changes have triggered severe erosion along the Sulina–Sfântu Gheorghe coastline (Panin & Jipa, 2002). Erosion is now observed everywhere along the deltaic shoreline. In the south, estimations of coastal retreat rates between Sulina and Sfântu Gheorghe range from 10±2.5 m yr^{-1} (Görmüş et al., 2021) to 5–30 m yr^{-1} (Panin & Jipa, 2002), while in the north the Chilia lobe is showing signs of a morphological transition from a fluvial-dominated to a wave-dominated delta front (Vespremeanu-Stroe et al., 2017). Consequences for the area are manifold: damage to coastal infrastructure, loss of beaches and associated tourism revenue, reduced shoreline accessibility, and the destruction of coastal ecosystems (Romanescu, 2013; Efremova, 2021; Pang et al., 2023).

In a context where climate change is expected to accelerate erosion through sea-level rise, increased storminess, and further damage to

coastal ecosystems, understanding sediment dynamics becomes essential for effective mitigation and adaptation strategies (Tătui et al., 2019; Pang et al., 2023). Hydrodynamic modeling offers a powerful approach to investigate these processes. For example, SLIM's sediment transport model could be coupled with our model setup to explore sediment pathways under current and future scenarios, and to assess the efficiency of potential mitigation measures. Such approach has already been used to understand the environmental impacts of modified sediment fluxes in Australia (Saint-Amand et al., 2022) and sediment-borne disease dispersal in the Gulf of Mexico (Dobbelaere, Holstein, et al., 2024). As waves are a key driver in sediment transport, further improvements could include coupling our model with a wave model such as SWAN, which has already been used in several studies on the Black Sea (Surkova et al., 2013; Rusu, 2018), and has already been successfully coupled with a SLIM model set-up in the Gulf of Mexico (Dobbelaere et al., 2022). In the longer term, model developments could aim to explicitly simulate erosion–deposition processes, providing a more complete representation of sediment budgets and morphological change.

6.3.4 Data collection

Another important perspective for future work concerns the acquisition of new datasets. As stated several times throughout this thesis, the reliability of hydrodynamic and flooding simulations in the Danube River–Delta–Black Sea continuum is constrained by data availability. Despite progress in the comprehension of the continuum made in this thesis, limitations in available data remain a major constrain. We underline here several gaps that, if addressed, could significantly improve future modeling efforts.

Bathymetric data remain one of the most critical needs. In Chapter 4, we produce the first easy-to-access harmonized bathymetry dataset of the delta's three main branches, but the resulting product inevitably reflect the quality of the underlying input data. Firstly, the different input datasets were produced on different years, whereas bathymetry in the delta is highly dynamic. While it is unrealistic to ask for a continuous high resolution mapping of the river, even a unified dataset

for a single year would represent a step forward. In addition, spatial coverage remains uneven: the Chilia branch in particular would benefit from additional measurements, while the Sfântu Gheorghe branch could be better resolved by increasing transect density or adding longitudinal profiles parallel to the shore, as suggested by Diaconu et al. (2019).

Equally important is the representation of floodplain topography. The Copernicus DEM employed in this study is a Digital Surface Model that includes vegetation and built structures, which can produce artificial barriers to flow along riverbanks. This is a well-known issue in flood modeling using DEM based on Synthetic Aperture Radar (SAR) or stereoscopic imaging products (Meadows et al., 2024). While there is no perfect solutions, several approaches can be considered, including machine-learning filtering (Meadows & Wilson, 2021; Hawker et al., 2022), LiDAR mapping (Meng et al., 2010; Esin et al., 2021) or hybrid methods combining different datasets (Vijith et al., 2015).

Validation is also a limitation in our current modeling framework. While we were able to validate discharges and water elevation, easy to access and to use datasets to validate flood extent and nearshore circulation are missing for a complete assessment of modeling on the continuum. For flooding, satellite observations are probably the best approach, but require careful post-processing and comparison with ground-truth data to avoid unrealistic patterns such as those observed in freely available products like GloFAS GFM (Copernicus Emergency Management Service, 2025) or Sentinel-2 Normalized Difference Water Index (NDWI) (European Space Agency, 2025). One promising dataset is SWOT Mask Pixel Cloud Data Product (PIXC) (Surface Water Ocean Topography (SWOT), 2024), which provides water elevation estimates since 16 December 2022 at a theoretical horizontal resolution of ~22 m. However, as with many satellite products, the data requires pre-processing to remove artifacts and and low-quality pixels, resulting in a fragmented dataset (Figure. 6.3). Consequently, the dataset can be used to validate general spatial patterns but we were not able to exploit its high resolution to its full potential. In addition, data retrieval remains cumbersome: visualization of data and quality metrics are not possible without downloading large data files, making the selection of suitable validation scenes a challenging and time-consuming

task. Finally, this product should ideally be validated against ground-truth data within the Danube Delta before being used operationally, as the complex morphology and variable vegetation cover in the delta make satellite-based water height detection particularly challenging. Overall, while the SWOT PIXC dataset is promising for future flood validation, it is not yet user-friendly and would require further refinement that lies beyond the scope of this work. Datasets to validate circulation on the NWS are scarce, and none can be found in the vicinity of the Danube Delta shoreline. However, the growing development of affordable and easy-to-deploy instruments opens new perspectives for future monitoring campaigns, which would provide helpful comparison for future hydrodynamic models on the continuum (Collins et al., 2024).

Finally, a better representation of lakes and connecting channels inside the delta could be very useful to correctly represent the internal circulation. The Danube Delta National Institute for Research and Development (DDNIRD) has already compiled an important dataset of lake bathymetry (DDNIRD, 2011), but several large lakes are missing from their inventory, such as lake Fortuna (~9 km^2) in the Şontea-Fortuna unit, Gorgova (~15 km^2) in the Gorgova-Uzlin unit, and a series of smaller lakes in the western part of the Şontea-Fortuna unit. In addition, we did not find any data on the Kuhurluy lake (~90 km^2), situated north of the Somova-Parches unit in Ukrainian territory, right before the delta. For the channels, information on the location and bathymetry of the main ones connecting the delta branches, such as Mila 35 (linking Tulcea and Chilia) and Caraoman-Litcov (linking Sfântu Gheorghe and Sulina), could help better represent flow between branches. Those channels could be integrated in the 2D model setup with elements following their banks, or, if too narrow, represented with a 1D model coupled to the 2D domain (Draoui et al., 2024).

6.3.5 Floodplain dynamics and delta resilience

In this thesis, we highlight that floodplains are an essential component of Danube Delta dynamics. Their inclusion in the hydrodynamic model reveals that they significantly modify water pathways and redistribution within the delta. Beyond their physical influence on water flow,

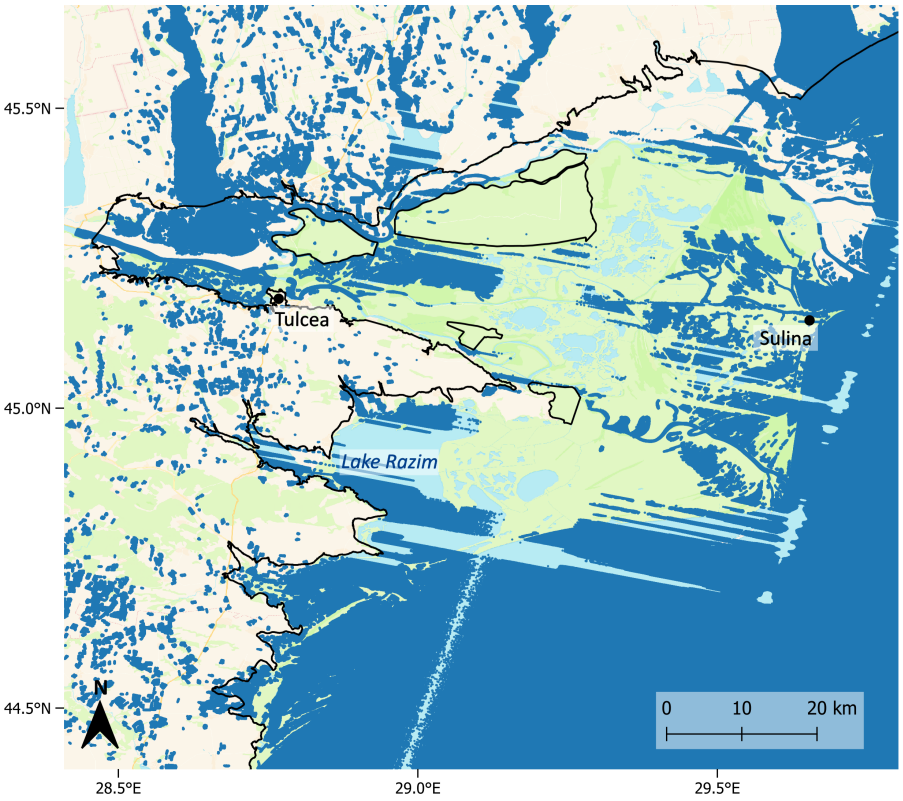

Figure 6.3: SWOT Mask Pixel Cloud Data Product (PIXC) data on the Danube Delta on 14 October 2024. Dark blue pixels represent water classified as "good" based on classification and geolocation quality flags. The data exhibit large spatial gaps, particularly visible over permanent water bodies such as Lake Razim. The black line delineates the model domain boundaries.

floodplains provide key ecosystem services. Our results, together with those of previous studies, underline that they buffer floods by attenuating peak discharges and lowering water levels, and act as temporary water storage areas that sustain baseflow during low-flow periods. Beyond these hydrodynamic effects, previous studies have shown that floodplains contribute to the filtering and retention of nutrients (Suciu et al., 2002; Friedrich et al., 2003) and sediments (Cioacă et al., 2018), processes that are critical for maintaining water quality and sustaining delta morphology. In addition to their ecological functions, floodplains in the Danube Delta support multiple human activities, offer-

ing opportunities for agriculture, aquaculture, navigation, fishing, and tourism, while also serving as biodiversity hotspots and drinking-water reserves.

The role of the inner delta and floodplains in the Danube Delta is particularly important in the context of the ongoing climate change. Projections for 2050-2100 suggest that the delta region may become drier but at the same time suffer from more frequent extreme events such as storms and floods (ICPDR, 2019). In this context, the floodplains and lakes of the inner delta play a dual role as both buffers and reservoirs, contributing to the resilience of the delta to hydrological variability. At the same time, as previously mentioned, the inner delta has undergone extensive modification over the past century through the construction of dykes, damming, channel rerouting, and polderization (Driga, 2008; Cioacă et al., 2018). These alterations have disrupted natural hydrological connectivity and altered floodplain dynamics, reducing their capacity to perform these regulating functions.

Efforts to restore floodplain connectivity are already being discussed and, in some areas, implemented (Niculescu et al., 2017). Since the 1990s, several rehabilitation initiatives have been launched, such as canal ecological reconstruction, drainage and unclogging projects, and the hydrological reconnection of certain polders (e.g., Babina, Cernovca) to the natural flood regime by opening sections of existing dykes (Niculescu et al., 2017). However, restoration is a slow process, partly due to the numbers of parties involved and the socio-economic stakes at play. For example, the flooding of the Pardina polder has been an ongoing debate for several years: the DDNIRD supports flooding, claiming that 50–60% of the area is no longer cultivated, whereas the Tulcea General Council argues that flooding the polder would cause significant economic losses for the local population (Niculescu et al., 2017). This example underlines that sound decision-making for inner delta management requires a comprehensive understanding of the social, ecological and economic values at stake. In this regard, further modeling studies could quantify the hydrodynamic and environmental impacts of potential restoration scenarios, as demonstrated in other systems (Clilverd et al., 2016; Ahilan et al., 2018; Caruso et al., 2019).

6.4 Final thoughts

Throughout this work, the central role of bathymetry emerged repeatedly as a controlling factor in the accurate representation of river and delta hydrodynamics. High-resolution bathymetry is essential to reproduce water levels and velocities; explicit mesh alignment with riverbanks requires precise topographic information; and realistic riverbank heights are indispensable to capture river–floodplain exchanges and flooding dynamics. The Danube Delta is not unique in this regard. Many deltas and flood-affected regions worldwide still lack accurate bathymetric data (Kinzel et al., 2013; Pelckmans et al., 2021; Kechnit et al., 2024). Several strategies have been proposed to overcome this limitation, including calibration of Manning coefficients (Garrote et al., 2021), iterative adjustments of floodplain elevations (Pelckmans et al., 2021), or the use of conceptual and interpolation-based methods to estimate bathymetry (Dey et al., 2019). While such approaches can yield valuable insights in data-scarce regions, they risk overfitting and may limit the transferability of model results. The most reliable path forward remains the production of accurate bathymetric datasets. Recent advances in acquisition techniques are making high-resolution bathymetry increasingly accessible (Gafurov, 2021; Choi et al., 2023), but sustained effort is still required to make such data routinely available for sensitive environments.

Ultimately, improving data quality and model realism serves a broader goal: advancing our understanding of how deltas function and respond to environmental change. Deltas are among the most densely populated and socio-economically important regions on Earth, yet they are also among the most vulnerable (Wolters & Kuenzer, 2015; Rahman et al., 2022; Scown et al., 2023). Their ecological, social, and economic components are exposed to a wide range of natural and anthropogenic pressures, from altered river discharges and sediment fluxes to accelerated sea-level rise and climate change (Wolters & Kuenzer, 2015; Loucks, 2019; Scown et al., 2023). In this context, numerical models represent invaluable tools to explore these pressures, test scenarios, and inform management. By focusing on the hydrodynamic role of floodplains and their integration into the Danube–Black Sea continuum, this thesis makes a significant contribution toward a more

complete understanding of how deltas function as transitional systems, and underscores the importance of incorporating floodplains into future modeling efforts.

Bibliography

Abdella, K., & Mekuanent, F. (2021). Application of hydrodynamic models for designing structural measures for river flood mitigation: The case of Kulfo River in southern Ethiopia. *Modeling Earth Systems and Environment*, *7*(4), 2779–2791.

Agulles, M., Marcos, M., Amores, A., & Toomey, T. (2024). Storm surge modelling along European coastlines: The effect of the spatio-temporal resolution of the atmospheric forcing. *Ocean Modelling*, *192*, 102432.

Ahilan, S., Guan, M., Sleigh, A., Wright, N., & Chang, H. (2018). The influence of floodplain restoration on flow and sediment dynamics in an urban river. *Journal of Flood Risk Management*, *11*(S2), S986–S1001.

Al Mehedi, M. A., Saki, S., Patel, K., Shen, C., Cohen, S., Smith, V., Rajib, A., Anagnostou, E., Bindas, T., & Lawson, K. (2024). Spatiotemporal Variability of Channel Roughness and its Substantial Impacts on Flood Modeling Errors. *Earth's Future*, *12*(7), e2023EF004257.

Alaerts, L., Dobbelaere, T., Gravinese, P. M., & Hanert, E. (2022). Climate Change Will Fragment Florida Stone Crab Communities. *Frontiers in Marine Science - Sec. Global Change and the Future Ocean*, *9*.

Alaerts, L., Lambrechts, J., Randresihaja, N. R., Vandenbulcke, L., Gourgue, O., Hanert, E., & Grégoire, M. (2024, November). Comprehensive bathymetry of the Danube Delta three branches.

Alaerts, L., Lambrechts, J., Randresihaja, N. R., Vandenbulcke, L., Gourgue, O., Hanert, E., & Grégoire, M. (2025). An integrated

high-resolution bathymetric model for the Danube Delta system. *Earth System Science Data*, *17*(7), 3125–3140.

Alipour, A., Jafarzadegan, K., & Moradkhani, H. (2022). Global sensitivity analysis in hydrodynamic modeling and flood inundation mapping. *Environmental Modelling & Software*, *152*, 105398.

Alkhalidi, M., Al-Dabbous, A., Al-Dabbous, S., & Alzaid, D. (2025). Evaluating the Accuracy of the ERA5 Model in Predicting Wind Speeds Across Coastal and Offshore Regions. *Journal of Marine Science and Engineering*, *13*(1), 149.

Altenau, E. H., Pavelsky, T. M., Bates, P. D., & Neal, J. C. (2017). The effects of spatial resolution and dimensionality on modeling regional-scale hydraulics in a multichannel river. *Water Resources Research*, *53*(2), 1683–1701.

Anastasiu, M. C. (2014). *Evoluţia sistemelor de altitudini utilizate în România şi Europa* [Doctoral dissertation, Universitatea Tehnică de Construcţii Bucureşti, Facultatea de Geodezie. With the Ministerul Educaţiei, Certcetării, Tineretului şi Sportului.].

Arcement, G. J., & Schneider, V. R. (1989). *Guide for selecting Manning's roughness coefficients for natural channels and flood plains* (tech. rep. No. 2339). U.S. Geological Survey.

Aricò, C., Sinagra, M., Begnudelli, L., & Tucciarelli, T. (2011). MAST-2D diffusive model for flood prediction on domains with triangular Delaunay unstructured meshes. *Advances in Water Resources*, *34*(11), 1427–1449.

Ayog, J. L., Kesserwani, G., Shaw, J., Sharifian, M. K., & Bau, D. (2021). Second-order discontinuous Galerkin flood model: Comparison with industry-standard finite volume models. *Journal of Hydrology*, *594*, 125924.

Bacopoulos, P., Tang, Y., Wang, D., & Hagen, S. C. (2017). Integrated Hydrologic-Hydrodynamic Modeling of Estuarine-Riverine Flooding: 2008 Tropical Storm Fay. *Journal of Hydrologic Engineering*, *22*(8), 04017022.

Bajo, M., Ferrarin, C., Dinu, I., Umgiesser, G., & Stanica, A. (2014). The water circulation near the Danube Delta and the Romanian coast modelled with finite elements. *Continental Shelf Research*, *78*, 62–74.

Bakan, G., & Büyükgüngör, H. (2000). The Black Sea. *Marine Pollution Bulletin*, *41*(1), 24–43.

Bakhtyar, R., Maitaria, K., Velissariou, P., Trimble, B., Mashriqui, H., Moghimi, S., Abdolali, A., Van der Westhuysen, A. J., Ma, Z., Clark, E. P., & Flowers, T. (2020). A New 1D/2D Coupled Modeling Approach for a Riverine-Estuarine System Under Storm Events: Application to Delaware River Basin. *Journal of Geophysical Research: Oceans*, *125*(9), e2019JC015822.

Bănăduc, D., Afanasyev, S., Akeroyd, J. R., Năstase, A., Năvodaru, I., Tofan, L., & Curtean-Bănăduc, A. (2023). The Danube Delta: The Achilles Heel of Danube River–Danube Delta–Black Sea Region Fish Diversity under a Black Sea Impact Scenario Due to Sea Level Rise—A Prospective Review. *Fishes*, *8*(7), 355.

Bănăduc, D., Rey, S., Trichkova, T., Lenhardt, M., & Curtean-Bănăduc, A. (2016). The Lower Danube River–Danube Delta–North West Black Sea: A pivotal area of major interest for the past, present and future of its fish fauna — A short review. *Science of The Total Environment*, *545–546*, 137–151.

Banescu, A., Arseni, M., Georgescu, L. P., Rusu, E., & Iticescu, C. (2020). Evaluation of Different Simulation Methods for Analyzing Flood Scenarios in the Danube Delta. *Applied Sciences*, *10*(23), 8327.

Bates, P. D., Horritt, M., & Hervouet, J.-M. (1998). Investigating two-dimensional, finite element predictions of floodplain inundation using fractal generated topography. *Hydrological Processes*, *12*(8), 1257–1277.

Beckers, J. M., Gregoire, M., Nihoul, J. C. J., Stanev, E., Staneva, J., & Lancelot, C. (2002). Modelling the Danube-influenced Northwestern Continental Shelf of the Black Sea. I: Hydrodynamical Processes Simulated by 3-D and Box Models. *Estuarine, Coastal and Shelf Science*, *54*(3), 453–472.

Bednar-Friedl, B., Biesbroek, R., Schmidt, D. N., Alexander, P., Børsheim, K. Y., Carnicer, J., Georgopoulou, E., Haasnoot, M., Le Cozannet, G., Lionello, P., Lipka, O., Möllmann, C., Muccione, V., Mustonen, T., Piepenburg, D., & Whitmarsh, L. (2022). Europe. In H.-O. Pörtner, D. C. Roberts, M. Tignor, E. S. Poloczanska, K. Mintenbeck, A. Alegría, M. Craig, S. Langsdorf, S. Löschke, V. Möller, A. Okem, & B. Rama (Eds.), *Climate change 2022: Impacts, adaptation and vulnerability. contribution of working group ii to the sixth assessment report of the intergovernmental*

panel on climate change (pp. 1817–1927). Cambridge University Press.

Bezak, N., Petan, S., Kobold, M., Brilly, M., Bálint, Z., Balabanova, S., Cazac, V., Csík, A., Godina, R., Janál, P., Klemar, Ž., Kopáčiková, E., Liedl, P., Matreata, M., Korniienko, V., Vladiković, D., & Šraj, M. (2021). A catalogue of the flood forecasting practices in the Danube River Basin. *River Research and Applications*, *37*(7), 909–918.

Bilgili, E., Bomers, A., van Lente, G. J.-W., Huthoff, F., & Hulscher, S. J. M. H. (2023). The effect of a local mesh refinement on hydraulic modelling of river meanders. *River Research and Applications*, *39*(5), 832–846.

Bloesch, J., Lenhardt, M., & Ionescu, C. (2025, January). Chapter 8 - Hydromorphological alterations and overexploitation of aquatic resources. In J. Bloesch, B. Cyffka, T. Hein, C. Sandu, & N. Sommerwerk (Eds.), *The Danube River and The Western Black Sea Coast* (pp. 147–164). Elsevier.

Bologa, A. Ş., & Bloesch, J. (2025, January). Chapter 7 - The coast and the shelf of the Black Sea. In J. Bloesch, B. Cyffka, T. Hein, C. Sandu, & N. Sommerwerk (Eds.), *The Danube River and The Western Black Sea Coast* (pp. 123–144). Elsevier.

Bomers, A., Schielen, R. M. J., & Hulscher, S. J. M. H. (2019). The influence of grid shape and grid size on hydraulic river modelling performance. *Environmental Fluid Mechanics*, *19*(5), 1273–1294.

Bonamano, S., Federico, I., Causio, S., Piermattei, V., Piazzolla, D., Scanu, S., Madonia, A., Madonia, N., De Cillis, G., Jansen, E., Fersini, G., Coppini, G., & Marcelli, M. (2024). River–coastal–ocean continuum modeling along the Lazio coast (Tyrrhenian Sea, Italy): Assessment of near river dynamics in the Tiber delta. *Estuarine, Coastal and Shelf Science*, *297*, 108618.

Bouzaiene, M., Menna, M., Elhmaidi, D., Dilmahamod, A. F., & Poulain, P.-M. (2021). Spreading of Lagrangian Particles in the Black Sea: A Comparison between Drifters and a High-Resolution Ocean Model. *Remote Sensing*, *13*(13), 2603.

Breitburg, D., Levin, L. A., Oschlies, A., Grégoire, M., Chavez, F. P., Conley, D. J., Garçon, V., Gilbert, D., Gutiérrez, D., Isensee, K., Jacinto, G. S., Limburg, K. E., Montes, I., Naqvi, S. W. A., Pitcher, G. C., Rabalais, N. N., Roman, M. R., Rose, K. A., Seibel,

B. A., … Zhang, J. (2018). Declining oxygen in the global ocean and coastal waters. *Science*, *359*(6371), eaam7240.

Bridge, J. S. (2003). *Rivers and Floodplains: Forms, Processes, and Sedimentary Record*. Wiley-Blackwell.

Brinkman, R., Wolanski, E., Deleersnijder, E., McAllister, F., & Skirving, W. (2002). Oceanic inflow from the Coral Sea into the Great Barrier Reef. *Estuarine, Coastal and Shelf Science*, *54*(4), 655–668.

Brodtkorb, A. R., Sætra, M. L., & Altinakar, M. (2012). Efficient shallow water simulations on GPUs: Implementation, visualization, verification, and validation. *Computers & Fluids*, *55*, 1–12.

Bunya, S., Luettich, R. A., & Blanton, B. O. (2023). Techniques to embed channels in finite element shallow water equation models. *Advances in Engineering Software*, *185*, 103516.

Burada, A., Maria-Catalina, T., Georgescu, L., Teodorof, L., Despina (Nastase), C., Seceleanu-Odor, D., & Iticescu, C. (2015). Heavy Metals Environment Accumulation in Somova - Parches Aquatic Complex from the Danube Delta Area. *Revista de Chimie -Bucharest- Original Edition-*, *66*, 48–54.

Burchard, H., Deleersnijder, E., & Meister, A. (2005). Application of modified Patankar schemes to stiff biogeochemical models for the water column. *Ocean Dynamics*, *55*(3), 326–337.

Camacho, R. A., Martin, J. L., Diaz-Ramirez, J., McAnally, W., Rodriguez, H., Suscy, P., & Zhang, S. (2014). Uncertainty analysis of estuarine hydrodynamic models: An evaluation of input data uncertainty in the weeks bay estuary, alabama. *Applied Ocean Research*, *47*, 138–153.

Capet, A., Beckers, J.-M., & Grégoire, M. (2013). Drivers, mechanisms and long-term variability of seasonal hypoxia on the Black Sea northwestern shelf – is there any recovery after eutrophication? *Biogeosciences*, *10*(6), 3943–3962.

Capet, A., Stanev, E. V., Beckers, J.-M., Murray, J. W., & Grégoire, M. (2016). Decline of the Black Sea oxygen inventory. *Biogeosciences*, *13*(4), 1287–1297.

Carlotto, T., & Chaffe, P. L. B. (2023). A coupled 2D-3D catchment-lake model with a parallel processing framework. *RBRH*, *28*, e2.

Caruso, B. S., Newman, B., & Econopouly, T. (2019). Hydrodynamic Modeling Improves Green River Reconnection with Floodplain

Wetlands for Endangered Fish Species Recovery. *JAWRA Journal of the American Water Resources Association*, *55*(3), 622–640.

Causio, S., Ciliberti, S. A., Clementi, E., Coppini, G., & Lionello, P. (2021). A Modelling Approach for the Assessment of Wave-Currents Interaction in the Black Sea. *Journal of Marine Science and Engineering*, *9*(8), 893.

Caviedes-Voullième, D., Morales-Hernández, M., López-Marijuan, I., & García-Navarro, P. (2014). Reconstruction of 2D river beds by appropriate interpolation of 1D cross-sectional information for flood simulation. *Environmental Modelling & Software*, *61*, 206–228.

Chen, C., Huang, H., Lin, H., Blanton, J., Li, C., & Andrade, F. (2022). A Wet/Dry Point Treatment Method of FVCOM, Part II: Application to the Okatee/Colleton River in South Carolina. *Journal of Marine Science and Engineering*, *10*(7), 982.

Chevalier, S., Beauchard, O., Teacă, A., Soetaert, K., & Grégoire, M. (2024). Partial recovery of macrozoobenthos on the northwestern shelf of the Black Sea. *Marine Pollution Bulletin*, *207*, 116857.

Choi, S.-K., Ramirez, R. A., & Kwon, T.-H. (2023). Acquisition of high-resolution topographic information in forest environments using integrated UAV-LiDAR system: System development and field demonstration. *Heliyon*, *9*(9).

Chopra, M., & Oza, R. B. (2025). Numerical hydrodynamic modeling of free surface flow by solving shallow water equations. *Modeling Earth Systems and Environment*, *11*(6), 383.

Choudhary, G. K., Trahan, C. J., Pettey, L., Farthing, M., Berger, C., Savant, G., Inanc, E., Dawson, C., & Loveland, M. (2025). Strongly Coupled 2D and 3D Shallow Water Models: Theory and Verification. *Journal of Hydraulic Engineering*, *151*(1), 04024049.

Ciliberti, S. A., Grégoire, M., Staneva, J., Palazov, A., Coppini, G., Lecci, R., Peneva, E., Matreata, M., Marinova, V., Masina, S., Pinardi, N., Jansen, E., Lima, L., Aydoğdu, A., Creti', S., Stefanizzi, L., Azevedo, D., Causio, S., Vandenbulcke, L., … Agostini, P. (2021). Monitoring and Forecasting the Ocean State and Biogeochemical Processes in the Black Sea: Recent Developments in the Copernicus Marine Service. *Journal of Marine Science and Engineering*, *9*(10), 1146.

Cioacă, E., Mierlă, M., Doroftei, M., Marinov, M., Doroşencu, A., Alexe, V., Lupu, G., Năstase, A., Tudor, M., & Ibram, O. (2018). Ecological restoration of the Danube Delta wetland fragmented ecosystems. Şontea-Fortuna area case study. *Geomorphologia Slovaca et Bohemica*, *18*(1), 23–31. Retrieved August 3, 2025, from http://www.asg.sav.sk/gfsb/v0181/gfsb0180104.pdf

Ciobotaru, N., Crăciun, A., & Costache, R.-D. (2025). Assessing Flood Risk in the Danube Delta Using 2D Hydraulic Modeling Under Climate Change: Near-Term and High-End Projections. *THE XXXII-nd SCIENTIFIC SYMPOSIUM*.

Clilverd, H. M., Thompson, J. R., Heppell, C. M., Sayer, C. D., & Axmacher, J. C. (2016). Coupled Hydrological/Hydraulic Modelling of River Restoration Impacts and Floodplain Hydrodynamics. *River Research and Applications*, *32*(9), 1927–1948.

Cobby, D. M., Mason, D. C., Horritt, M. S., & Bates, P. D. (2003). Two-dimensional hydraulic flood modelling using a finite-element mesh decomposed according to vegetation and topographic features derived from airborne scanning laser altimetry. *Hydrological Processes*, *17*(10), 1979–2000.

Collins, C. O., Dickhudt, P., Thomson, J., de Paolo, T., Otero, M., Merrifield, S., Terrill, E., Schonau, M., Braasch, L., Paluszkiewicz, T., & Centurioni, L. (2024). Performance of moored GPS wave buoys. *Coastal Engineering Journal*, *66*(1), 17–43.

Copernicus ECMWF. (2025). *Flooding in 2024* (tech. rep.).

Copernicus Emergency Management Service. (2025). GloFAS Global Flood Monitoring Product [Accessed in 2025 via the Copernicus Emergency Management Service. Available at https://www.globalfloods.eu/].

Costache, R., Crăciun, A., Ciobotaru, N., & Bărbulescu, A. (2024). Intelligent Methods for Estimating the Flood Susceptibility in the Danube Delta, Romania. *Water*, *16*(23), 3511.

Crăciun, A., Costache, R., Bărbulescu, A., Pal, S. C., Costache, I., & Dumitriu, C. S. (2022). Modern Techniques for Flood Susceptibility Estimation across the Deltaic Region (Danube Delta) from the Black Sea's Romanian Sector. *Journal of Marine Science and Engineering*, *10*(8), 1149.

Cristofor, S., Vadineanu, A., & Ignat, G. (1993). Importance of flood zones for nitrogen and phosphorus dynamics in the Danube Delta. *Hydrobiologia*, *251*(1), 143–148.

Cushman-Roisin, B., & Beckers, J.-M. (2011, August). *Introduction to Geophysical Fluid Dynamics: Physical and Numerical Aspects*. Academic Press.

Czuba, J. A., David, S. R., Edmonds, D. A., & Ward, A. S. (2019). Dynamics of Surface-Water Connectivity in a Low-Gradient Meandering River Floodplain. *Water Resources Research*, *55*(3), 1849–1870.

DDNIRD. (2011). Dataset: SBES_ddni_bathy_danube_delta_lakes. https://cdi.seadatanet.org/search

DDNIRD. (2015). Dataset: SBES_Sf_Gh_DDNI_2015. https : / / cdi . seadatanet.org/search

de Brye, B., de Brauwere, A., Gourgue, O., Kärnä, T., Lambrechts, J., Comblen, R., & Deleersnijder, E. (2010). A finite-element, multi-scale model of the Scheldt tributaries, river, estuary and ROFI. *Coastal Engineering*, *57*(9), 850–863.

De Le Court, M., Legat, V., Scherpereel, C., Hanert, E., & Lambrechts, J. (n.d.). *An efficient multi-gpu implementation for the discontnuous galerkin ocean model slim* [Manuscript in preparation].

Debreu, L., Marchesiello, P., Penven, P., & Cambon, G. (2012). Two-way nesting in split-explicit ocean models: Algorithms, implementation and validation. *Ocean Modelling*, *49–50*, 1–21.

Delandmeter, P., Lambrechts, J., Legat, V., Vallaeys, V., Naithani, J., Thiery, W., Remacle, J.-F., & Deleersnijder, E. (2018). A fully consistent and conservative vertically adaptive coordinate system for SLIM 3D v0.4 with an application to the thermocline oscillations of Lake Tanganyika. *Geoscientific Model Development*, *11*(3), 1161–1179.

Dey, S., Saksena, S., & Merwade, V. (2019). Assessing the effect of different bathymetric models on hydraulic simulation of rivers in data sparse regions. *Journal of Hydrology*, *575*, 838–851.

Dey, S., Saksena, S., Winter, D., Merwade, V., & McMillan, S. (2022). Incorporating Network Scale River Bathymetry to Improve Characterization of Fluvial Processes in Flood Modeling. *Water Resources Research*, *58*(11), e2020WR029521.

Diaconu, D. C., Bretcan, P., Peptenatu, D., Tanislav, D., & Mailat, E. (2019). The importance of the number of points, transect location and interpolation techniques in the analysis of bathymetric measurements. *Journal of Hydrology*, *570*, 774–785.

Dobbelaere, T., Curcic, M., Le Hénaff, M., & Hanert, E. (2022). Impacts of Hurricane Irma (2017) on wave-induced ocean transport processes. *Ocean Modelling*, *171*, 101947.

Dobbelaere, T., Dekens, A., Saint-Amand, A., Alaerts, L., Holstein, D. M., & Hanert, E. (2024). Hurricanes enhance coral connectivity but also superspread coral diseases. *Global Change Biology*, *30*(6), e17382.

Dobbelaere, T., Holstein, D. M., Gramer, L. J., McEachron, L., & Hanert, E. (2024). Investigating the link between the Port of Miami dredging and the onset of the stony coral tissue loss disease epidemics. *Marine Pollution Bulletin*, *207*, 116886.

Dolejší, V., & Feistauer, M. (2015). *Discontinuous Galerkin Method: Analysis and Applications to Compressible Flow*. Springer International Publishing.

Dong, B., Huang, B., Tan, C., Xia, J., Lin, K., Gao, S., & Hu, Y. (2025). Multi-GPU parallelization of shallow water modelling on unstructured meshes. *Journal of Hydrology*, *657*, 133105.

Dorofeyev, V. L., & Sukhikh, L. I. (2017). Modeling of Long-Term Evolution of Hydrophysical Fields of the Black Sea. *Oceanology*, *57*(6), 784–796.

Dorofeyev, V. L., & Sukhikh, L. I. (2021). Features of Currents on the Black Sea Northwestern Shelf Based on the Numerical Simulation Results. *Physical Oceanography*, *28*(4), 426–437.

Dragićević, S. (2004). The potential of Web-based GIS. *Journal of Geographical Systems*, *6*(2), 79–81.

Draoui, I., Lambrechts, J., Legat, V., & Deleersnijder, E. (2024). The discontinuous Galerkin method for river-delta continuum by means of a coupled 1D-2D shallow water model. In *River Flow 2022*. CRC Press.

Draoui, I., Lambrechts, J., Legat, V., Soares-Frazao, S., Hoitink, T., & Deleersnijder, E. (2020). Discontinuous Galerkin method for 1D river flows. In *River Flow 2020*. CRC Press.

Driga, B.-V. (2008). The hidrological relationship between Danube arms and lake complexis in the Danube Delta. *Lakes reservoirs and ponds*, *1–2*(1), 61–71.

Duquesne, F., Vallaeys, V., Vidaurre, P. J., & Hanert, E. (2021). A coupled ecohydrodynamic model to predict algal blooms in Lake Titicaca. *Ecological Modelling*, *440*.

Durisch-Kaiser, E., Doberer, A., Reutimann, J., Pavel, A., Balan, S., Radan, S., & Wehrli, B. (2011). Organic matter governs N and P balance in Danube Delta lakes. *Aquatic Sciences*, *73*(1), 21–33.

Duţu, F., Panin, N., Ion, G., & Tiron Duţu, L. (2018). Multibeam Bathymetric Investigations of the Morphology and Associated Bedforms, Sulina Channel, Danube Delta. *Geosciences*, *8*(1), 7.

Dysarz, T. (2018). Development of RiverBox—An ArcGIS Toolbox for River Bathymetry Reconstruction. *Water*, *10*(9), 1266.

Eder, M., Perosa, F., Hohensinner, S., Tritthart, M., Scheuer, S., Gelhaus, M., Cyffka, B., Kiss, T., Van Leeuwen, B., Tobak, Z., Sipos, G., Csikós, N., Smetanová, A., Bokal, S., Samu, A., Gruber, T., Gălie, A.-C., Moldoveanu, M., Mazilu, P., & Habersack, H. (2022). How Can We Identify Active, Former, and Potential Floodplains? Methods and Lessons Learned from the Danube River. *Water*, *14*(15), 2295.

Efremova, T. (2021). Anthropogenic Impact on the Lithodynamics of the Coastal Zone of the Southern and Western Black Sea Coast (Review). *Ekologicheskaya bezopasnost pribrezhnoy i shel fovoy zon morya*, 5–29.

Egbert, G. D., Bennett, A. F., & Foreman, M. G. G. (1994). TOPEX/POSEIDON tides estimated using a global inverse model. *Journal of Geophysical Research: Oceans*, *99*(C12), 24821–24852.

EMODnet Bathymetry consortium. (2021). EMODnet Bathymetry WMTS service [Available at https://tiles.emodnet-bathymetry.eu/].

Enriquez, C. E., Shapiro, G. I., Souza, A. J., & Zatsepin, A. G. (2005). Hydrodynamic modelling of mesoscale eddies in the Black Sea. *Ocean Dynamics*, *55*(5), 476–489.

Esin, A. İ., Akgul, M., Akay, A. O., & Yurtseven, H. (2021). Comparison of LiDAR-based morphometric analysis of a drainage basin with

results obtained from UAV, TOPO, ASTER and SRTM-based DEMs. *Arabian Journal of Geosciences*, *14*(5), 340.

Esri. (2018, October). Ocean Basemap [Available at https://www.arcgis.com/home/item.html?id=67ab7f7c535c4687b6518e6d2343e8a2].

European Space Agency. (2021). Copernicus Global Digital Elevation Model [Available at https://doi.org/10.5270/ESA-c5d3d65].

European Space Agency. (2025). Sentinel-2 Level-2A Imagery [Modified Copernicus Sentinel data [2025] processed in Copernicus Browser. Available at https://browser.dataspace.copernicus.eu/].

European Union's Copernicus Land Monitoring Service information. (2024, December). River Water Level 2002-present (vector), global, Near Real Time – version 2 [Available at https://doi.org/10.2909/fa9d1d46-70a4-4f85-bed7-6e1af8e1ff36].

European Union's Copernicus Land Monitoring Service information. (2025, April). Surface Soil Moisture 2014-present (raster 1 km), Europe, daily – version 1 [Available at https://doi.org/10.2909/e934b15f-7d48-4c6d-a9c6-6484488aa58f].

FAIRway Danube. (2021). *Fairway Rehabilitation and Maintenance Master Plan for the Danube and its navigable tributaries: NATIONAL ACTION PLANS UPDATE MAY 2021* (tech. rep. No. v. 16.11.2021). Connecting Europe Facility of the European Union. https://navigation.danube-region.eu/wp-content/uploads/sites/10/sites/10/2022/01/FRMMP_national_action_plans_May-2021

Fanous, M., Daneshkhah, A., Eden, J. M., Remesan, R., & Palade, V. (2023). Hydro-morphodynamic modelling of mangroves imposed by tidal waves using finite element discontinuous Galerkin method. *Coastal Engineering*, *182*, 104303.

Ferrarin, C., Bellafiore, D., Paladio Hernandez, A., Dinu, I., & Stanica, A. (2025). Modelling river-sea continuum: The case of the Danube Delta. *EGUsphere*, 1–27.

Fleischmann, A., Collischonn, W., Paiva, R., & Tucci, C. E. (2019). Modeling the role of reservoirs versus floodplains on large-scale river hydrodynamics. *Natural Hazards*, *99*(2), 1075–1104.

Foglini, F., Rovere, M., Tonielli, R., Castellan, G., Prampolini, M., Budillon, F., Cuffaro, M., Di Martino, G., Grande, V., Innangi, S., Loreto, M. F., Langone, L., Madricardo, F., Mercorella, A., Montagna, P., Palmiotto, C., Pellegrini, C., Petrizzo, A., Petracchini, L., … Trincardi, F. (2025). A new multi-grid bathymetric dataset of the Gulf of Naples (Italy) from complementary multibeam echo sounders. *Earth System Science Data*, *17*(1), 181–203.

Frank, G., Funk, A., Becker, I., Schneider, E., & Egger, G. (2025, January). Chapter 16 - The key role of floodplains in nature conservation: How to improve the current status of biodiversity? In J. Bloesch, B. Cyffka, T. Hein, C. Sandu, & N. Sommerwerk (Eds.), *The Danube River and The Western Black Sea Coast* (pp. 335–364). Elsevier.

Friedrich, J., Dinkel, C., Grieder, E., Radan, S., Secrieru, D., Steingruber, S., & Wehrli, B. (2003). Nutrient uptake and benthic regeneration in Danube Delta Lakes. *Biogeochemistry*, *64*(3), 373–398.

Fuchs, M., Palmtag, J., Juhls, B., Overduin, P. P., Grosse, G., Abdelwahab, A., Bedington, M., Sanders, T., Ogneva, O., Fedorova, I. V., Zimov, N. S., Mann, P. J., & Strauss, J. (2022). High-resolution bathymetry models for the Lena Delta and Kolyma Gulf coastal zones. *Earth System Science Data*, *14*(5), 2279–2301.

Gaber, M. M., AboulAtta, N. M., Shafik, N. M., Salama, R. A., & El-Molla, D. A. (2025). Evaluating the impact of flow variations on the inundated areas around the Nile River in Egypt using 2D hydraulic modeling. *Modeling Earth Systems and Environment*, *11*(4), 274.

Gafurov, A. (2021). The Methodological Aspects of Constructing a High-Resolution DEM of Large Territories Using Low-Cost UAVs on the Example of the Sarycum Aeolian Complex, Dagestan, Russia. *Drones*, *5*(1), 7.

Gallée, H., & Schayes, G. (1994). Development of a Three-Dimensional Meso-γ Primitive Equation Model: Katabatic Winds Simulation in the Area of Terra Nova Bay, Antarctica. *Monthly Weather Review*, *122*(4), 671–685.

García-Alén, G., García-Fonte, O., Cea, L., Pena, L., & Puertas, J. (2021). Modelling Weirs in Two-Dimensional Shallow Water Models. *Water*, *13*(16), 2152.

Garrote, J., González-Jiménez, M., Guardiola-Albert, C., & Díez-Herrero, A. (2021). The Manning's Roughness Coefficient Calibration Method to Improve Flood Hazard Analysis in the Absence of River Bathymetric Data: Application to the Urban Historical Zamora City Centre in Spain. *Applied Sciences*, *11*(19), 9267.

Gâştescu, P. (2009). The Danube Delta Biosphere Reserve. Geography, Biodiversity, Protection, Management. *Romanian Journal of Geography*, *53*(2), 139–152.

Gâştescu, P. (2021). The biodiversity of the Danube Delta Biosphere Reserve reflected in the structure of the ecosystems. *Water Resources and Wetlands*, 1–19.

Gayathri, R., Bhaskaran, P. K., & Murty, P. (2021). River-tide-storm surge interaction characteristics for the Hooghly estuary, East coast of India. *ISH Journal of Hydraulic Engineering*, *27*(sup1), 483–495.

GEBCO Compilation Group. (2024). GEBCO 2024 Grid [Available at https : / / doi . org / 10 . 5285 / 1c44ce99 - 0a0d - 5f4f - e063 - 7086abc0ea0f].

Geuzaine, C., & Remacle, J.-F. (2009). Gmsh: A 3-D finite element mesh generator with built-in pre- and post-processing facilities. *International Journal for Numerical Methods in Engineering*, *79*(11), 1309–1331.

Glock, K., Tritthart, M., Gmeiner, P., Pessenlehner, S., & Habersack, H. (2019). Evaluation of engineering measures on the Danube based on numerical analysis. *Journal of Applied Water Engineering and Research*, *7*(1), 48–66.

Goff, J. A., & Nordfjord, S. (2004). Interpolation of Fluvial Morphology Using Channel-Oriented Coordinate Transformation: A Case Study from the New Jersey Shelf. *Mathematical Geology*, *36*(6), 643–658.

Gogoase, D. E. N., Armaş, I., & Ionescu, C. S. (2011). Inundation Maps for Extreme Flood Events at the Mouth of the Danube River. *International Journal of Geosciences*, *2*(1), 68–74.

Gogoașe-Nistoran, D.-E., Marin, A. F., Armaș, I., Ionescu, C. S., Tudor, G.-M., & Cozma, A. (2022). Hydro-sedimentary Modeling and Fluvial Morphological Processes Along the Lower Danube River (Giurgiu-Oltenița-Călărași Reach). In A. Negm, L. Zaharia,

& G. Ioana-Toroimac (Eds.), *The Lower Danube River: Hydro-Environmental Issues and Sustainability* (pp. 69–111). Springer.

Gomiz-Pascual, J. J., Bolado-Penagos, M., Gonzalez, C. J., Vazquez, A., Buonocore, C., Romero-Cozar, J., Perez-Cayeiro, M. L., Izquierdo, A., Alvarez, O., Mañanes, R., & Bruno, M. (2021). The fate of Guadalquivir River discharges in the coastal strip of the Gulf of Cádiz. A study based on the linking of watershed catchment and hydrodynamic models. *Science of The Total Environment*, *795*, 148740.

Görmüş, T., Ayat, B., Aydoğan, B., & Tătui, F. (2021). Basin scale spatiotemporal analysis of shoreline change in the Black Sea. *Estuarine, Coastal and Shelf Science*, *252*, 107247.

Gourgue, O., Baeyens, W., Chen, M. S., de Brauwere, A., de Brye, B., Deleersnijder, E., Elskens, M., & Legat, V. (2013). A depth-averaged two-dimensional sediment transport model for environmental studies in the Scheldt Estuary and tidal river network. *Journal of Marine Systems*, *128*, 27–39.

Gourgue, O., Comblen, R., Lambrechts, J., Kärnä, T., Legat, V., & Deleersnijder, E. (2009). A flux-limiting wetting–drying method for finite-element shallow-water models, with application to the Scheldt Estuary. *Advances in Water Resources*, *32*(12), 1726–1739.

Grailet, J.-F., Hogan, R. J., Ghilain, N., Bolsée, D., Fettweis, X., & Grégoire, M. (2025). Inclusion of the ECMWF ecRad radiation scheme (v1.5.0) in the MAR (v3.14), regional evaluation for Belgium, and assessment of surface shortwave spectral fluxes at Uccle. *Geoscientific Model Development*, *18*(6), 1965–1988.

Grégoire, M., Beckers, J.-M., Nihoul, J. C. J., & Stanev, E. (1997). Coupled Hydrodynamic Ecosystem Model of the Black Sea at Basin Scale. In E. Özsoy & A. Mikaelyan (Eds.), *Sensitivity to Change: Black Sea, Baltic Sea and North Sea* (pp. 487–499). Springer Netherlands.

Grégoire, M., & Friedrich, J. (2004). Nitrogen budget of the northwestern Black Sea shelf inferred from modeling studies and in situ benthic measurements. *Marine Ecology Progress Series*, *270*, 15–39.

Grégoire, M., & Soetaert, K. (2010). Carbon, nitrogen, oxygen and sulfide budgets in the Black Sea: A biogeochemical model of the whole water column coupling the oxic and anoxic parts. *Ecological Modelling*, *221*(19), 2287–2301.

Grégoire, M., Vandenbulcke, L., & Capet, A. (2020a). Black sea biogeochemical analysis and forecast (cmems near-real time blacksea biogeochemistry) [Copernicus Monitoring Environment Marine Service (CMEMS). Available at https://doi.org/10.48670/mds-00354].

Grégoire, M., Vandenbulcke, L., & Capet, A. (2020b). Black sea biogeochemical reanalysis (cmems bs-biogeochemistry) (version 1) [Copernicus Monitoring Environment Marine Service (CMEMS). Available at https://doi.org/10.25423/CMCC/BLKSEA_MULTIYEAR_BGC_007_005_BAMHBI].

Grégoire, M., Vandenbulcke, L., Chevalier, S., Choblet, M., Drozd, I., Grailet, J.-F., Ivanov, E., Macé, L., Verezemskaya, P., Yu, H., Alaerts, L., Randresihaja, N., Mangeleer, V., Maertens de Noordhout, G., Capet, A., Meulders, C., Mouchet, A., Munhoven, G., & Soetaert, K. (2025). The biogeochemical model for hypoxic and benthic influenced areas: Bamhbi v1.0. *EGUsphere*.

Güttler, F. N., Niculescu, S., & Gohin, F. (2013). Turbidity retrieval and monitoring of Danube Delta waters using multi- sensor optical remote sensing data: An integrated view from the delta plain lakes to the western–northwestern Black Sea coastal zone. *Remote Sensing of Environment*, *132*, 86–101.

Habersack, H., Hein, T., Stanica, A., Liska, I., Mair, R., Jäger, E., Hauer, C., & Bradley, C. (2016). Challenges of river basin management: Current status of, and prospects for, the River Danube from a river engineering perspective. *Science of The Total Environment*, *543*, 828–845.

Hackl, T. (2010, July). *Situation Report 2: Floods in Romania - June/July 2010* (tech. rep.). Caritas.

Haidvogel, D., Curchitser, E., Danilov, S., & Fox-Kemper, B. (2017). Numerical modelling in a multiscale ocean. *Journal of Marine Research*, *75*(6).

Hales, R. C., Nelson, E. J., Souffront, M., Gutierrez, A. L., Prudhomme, C., Kopp, S., Ames, D. P., Williams, G. P., & Jones, N. L. (2025). Advancing global hydrologic modeling with the GEOGloWS

ECMWF streamflow service. *Journal of Flood Risk Management*, *18*(1), e12859.

Hardy, R. J., Bates, P. D., & Anderson, M. G. (1999). The importance of spatial resolution in hydraulic models for floodplain environments. *Journal of Hydrology*, *216*(1), 124–136.

Harvey, J. W., Schaffranek, R. W., Noe, G. B., Larsen, L. G., Nowacki, D. J., & O'Connor, B. L. (2009). Hydroecological factors governing surface water flow on a low-gradient floodplain. *Water Resources Research*, *45*(3).

Hasan, G. M. J., van Maren, D. S., & Ooi, S. K. (2016). Hydrodynamic modeling of Singapore's coastal waters: Nesting and model accuracy. *Ocean Modelling*, *97*, 141–151.

Hawez, D. M., Füstös, V., Pomázi, F., Tamás, E. A., & Baranya, S. (2025). Simulation of Sediment Dynamics in a Large Floodplain of the Danube River. *Water*, *17*(16), 2399.

Hawker, L., Uhe, P., Paulo, L., Sosa, J., Savage, J., Sampson, C., & Neal, J. (2022). A 30 m global map of elevation with forests and buildings removed. *Environmental Research Letters*, *17*(2), 024016.

Herbin, R., Latché, J.-C., Nasseri, Y., & Therme, N. (2023). A consistent quasi–second-order staggered scheme for the two-dimensional shallow water equations. *IMA Journal of Numerical Analysis*, *43*(1), 99–143.

Hersbach, H., Bell, B., Berrisford, P., Biavati, G., Horányi, A., Muños Sabater, J., Nicolas, J., Peubey, C., Radu, R., Rozum, I., Schepers, D., Simmons, A., Soci, C., Dee, D., & Thépaut, J.-N. (2018). ERA5 hourly data on single levels from 1979 to present. [Available at https://doi.org/10.24381/cds.adbb2d47].

Hersbach, H., Bell, B., Berrisford, P., Biavati, G., Horányi, A., Muñoz Sabater, J., Nicolas, J., Peubey, C., Radu, R., Rozum, I., Schepers, D., Simmons, A., Soci, C., Dee, D., & Thépaut, J.-N. (2023). Era5 hourly data on single levels from 1940 to present [Accessed on 10-07-2025. Available at https://doi.org/10.24381/cds.adbb2d47].

Hervouet, J.-M. (2007, April). *Hydrodynamics of Free Surface Flows: Modelling with the finite element method* (1st ed.). Wiley.

Hikov, A., Vîjdea, A.-M., Peytcheva, I., Jordan, G., Marjanović, P., Milakovska, Z., Filipov, P., Vetseva, M., Baltres, A., Alexe, V. E., Bălan, L.-L., Marjanović, M., Cvetković, V., Sarić, K., & Team,

T. S. P. (2023). Assessment of river sediment quality according to the EU Water Framework Directive in large river fluvial conditions. A case study in the Lower Danube River Basin. *Carpathian Journal of Earth and Environmental Sciences*, *18*(1), 195–211.

Hilton, J. E., Grimaldi, S., Cohen, R. C. Z., Garg, N., Li, Y., Marvanek, S., Pauwels, V. R. N., & Walker, J. P. (2019). River reconstruction using a conformal mapping method. *Environmental Modelling & Software*, *119*, 197–213.

Hodges, B. R., & Imberger, J. (2001). Simple Curvilinear Method for Numerical Methods of Open Channels. *Journal of Hydraulic Engineering*, *127*(11), 949–958.

Horritt, M. S., Bates, P. D., & Mattinson, M. J. (2006). Effects of mesh resolution and topographic representation in 2D finite volume models of shallow water fluvial flow. *Journal of Hydrology*, *329*(1), 306–314.

Horritt, M. S., Di Baldassarre, G., Bates, P. D., & Brath, A. (2007). Comparing the performance of a 2-D finite element and a 2-D finite volume model of floodplain inundation using airborne SAR imagery. *Hydrological Processes*, *21*(20), 2745–2759.

Horvat, Z., Horvat, M., Majer, F., & Koch, D. (2020). Hydraulic analysis of a meander on the Danube River using a 2D flow model. *Environmental Monitoring and Assessment*, *192*(2), 149.

Hu, R., Fang, F., Salinas, P., Pain, C. C., Sto.Domingo, N. D., & Mark, O. (2019). Numerical simulation of floods from multiple sources using an adaptive anisotropic unstructured mesh method. *Advances in Water Resources*, *123*, 173–188.

Huang, G., Falconer, R., Lin, B., & Xu, C. (2022). Dynamic tracing of fecal bacteria processes from a river basin to an estuary using a 2D/3D model. *River*, *1*(2), 149–161.

Huang, W., Cao, Z., Pender, G., Liu, Q., & Carling, P. (2015). Coupled flood and sediment transport modelling with adaptive mesh refinement. *Science China Technological Sciences*, *58*(8), 1425–1438.

ICPDR. (2019). Climate change adaptation strategy [Available at https://www.icpdr.org]. *International Commission for the Protection of the Danube River*.

ICPDR. (2021). Danube river basin management plan – update 2021 [Available at https://www.icpdr.org]. *International Commission for the Protection of the Danube River*.

Ionita, M., Toroimac, G., Sandor, I.-A., & Nagavciuc, V. (2025, January). Chapter 2 - Hydrology and hydromorphology. In J. Bloesch, B. Cyffka, T. Hein, C. Sandu, & N. Sommerwerk (Eds.), *The Danube River and The Western Black Sea Coast* (pp. 13–39). Elsevier.

Ishimwe, A. P., Deleersnijder, E., Legat, V., & Lambrechts, J. (2025). A multi-scale IMEX second order Runge-Kutta method for 3D hydrodynamic ocean models. *Journal of Computational Physics*, *520*, 113482.

Ivanov, E., Capet, A., Barth, A., Delhez, E. J. M., Soetaert, K., & Grégoire, M. (2020). Hydrodynamic variability in the Southern Bight of the North Sea in response to typical atmospheric and tidal regimes. Benefit of using a high resolution model. *Ocean Modelling*, *154*, 101682.

Izgin, T., Kopecz, S., & Meister, A. (2021). Recent Developments in the Field of Modified Patankar-Runge-Kutta-methods. *PAMM*, *21*(1), e202100027.

Jaoshvili, S. (2022). *The rivers of the Black Sea* (I. Khomerki, G. Gigineishvili, & Kordzadze, Eds.; Technical Report No. 71). European environment Agency.

Jugaru Tiron, L., Le Coz, J., Provansal, M., Panin, N., Raccasi, G., Dramais, G., & Dussouillez, P. (2009). Flow and sediment processes in a cutoff meander of the Danube Delta during episodic flooding. *Geomorphology*, *106*(3), 186–197.

Kamenski, L., Huang, W., & Xu, H. (2014). Conditioning of Finite Element Equations with Arbitrary Anisotropic Meshes. *Mathematics of Computation*, *83*(289), 2187–2211.

Kara, A. B., Wallcraft, A. J., Hurlburt, H. E., & Stanev, E. V. (2008). Air–sea fluxes and river discharges in the Black Sea with a focus on the Danube and Bosphorus. *Journal of Marine Systems*, *74*(1-2), 74–95.

Kärnä, T., de Brye, B., Gourgue, O., Lambrechts, J., Comblen, R., Legat, V., & Deleersnijder, E. (2011). A fully implicit wetting–drying method for DG-FEM shallow water models, with an application to the Scheldt Estuary. *Computer Methods in Applied Mechanics and Engineering*, *200*(5), 509–524.

Kärnä, T., Kramer, S. C., Mitchell, L., Ham, D. A., Piggott, M. D., & Baptista, A. M. (2018). Thetis coastal ocean model: Discontinuous Galerkin discretization for the three-dimensional hydrostatic equations. *Geoscientific Model Development*, *11*(11), 4359–4382.

Kechnit, D., Tshimanga, R. M., Ammari, A., Trigg, M. A., Carr, A. B., Bahmanpouri, F., Barbetta, S., & Moramarco, T. (2024). Bathymetry and discharge estimation in large and data-scarce rivers using an entropy-based approach. *Hydrological Sciences Journal*, *69*(15), 2109–2123.

Keller, B. E. M., Lajtha, K., & Cristofor, S. (1998). Trace metal concentrations in the sediments and plants of the Danube Delta, Romania. *Wetlands*, *18*(1), 42–50.

Kernkamp, H. W. J., Van Dam, A., Stelling, G. S., & de Goede, E. D. (2011). Efficient scheme for the shallow water equations on unstructured grids with application to the Continental Shelf. *Ocean Dynamics*, *61*(8), 1175–1188.

Kesserwani, G., & Wang, Y. (2014). Discontinuous Galerkin flood model formulation: Luxury or necessity? *Water Resources Research*, *50*(8), 6522–6541.

Kharchenko, V. (2023). The impact of full-scale war on the Black Sea ecosystems of Ukraine and the entire sea in general. *European Dimensions of the Sustainable Development and Academic–Business Forum: Let's Revive Ukraine Together. Selected Papers of the V International Conference, June 1–2, 2023*, 149–158. https://dspace.nuft.edu.ua/handle/123456789/45628

Kim, B., Sanders, B. F., Schubert, J. E., & Famiglietti, J. S. (2014). Mesh type tradeoffs in 2D hydrodynamic modeling of flooding with a Godunov-based flow solver. *Advances in Water Resources*, *68*, 42–61.

Kinzel, P. J., Legleiter, C. J., & Nelson, J. M. (2013). Mapping River Bathymetry With a Small Footprint Green LiDAR: Applications and Challenges. *JAWRA Journal of the American Water Resources Association*, *49*(1), 183–204.

Kirk, J. T. O. (1994). *Light and photosynthesis in aquatic ecosystems* (2nd ed.). Cambridge University Press.

Konovalov, S. K., & Murray, J. W. (2001). Variations in the chemistry of the Black Sea on a time scale of decades (1960–1995). *Journal of Marine Systems*, *31*(1), 217–243.

Kovacs, A., & Zavadsky, I. (2021). Success and sustainability of nutrient pollution reduction in the Danube River Basin: Recovery and future protection of the Black Sea Northwest shelf. *Water International*, *46*(2), 176–194.

Kubatko, E. J., Bunya, S., Dawson, C., Westerink, J. J., & Mirabito, C. (2009). A Performance Comparison of Continuous and Discontinuous Finite Element Shallow Water Models. *Journal of Scientific Computing*, *40*(1), 315–339.

Kubryakov, A. A., Stanichny, S. V., & Zatsepin, A. G. (2018). Interannual variability of Danube waters propagation in summer period of 1992–2015 and its influence on the Black Sea ecosystem. *Journal of Marine Systems*, *179*, 10–30.

Kvach, Y., Stepien, C. A., Minicheva, G. G., & Tkachenko, P. (2025). Biodiversity effects of the Russia–Ukraine War and the Kakhovka Dam destruction: Ecological consequences and predictions for marine, estuarine, and freshwater communities in the northern Black Sea. *Ecological Processes*, *14*(1), 22.

Lai, R., Wang, M., Zhang, X., Huang, L., Zhang, F., Yang, M., & Wang, M. (2021). Streamline-Based Method for Reconstruction of Complex Braided River Bathymetry. *Journal of Hydrologic Engineering*, *26*(5), 04021012.

Lai, Y. G. (2010). Two-Dimensional Depth-Averaged Flow Modeling with an Unstructured Hybrid Mesh. *Journal of Hydraulic Engineering*, *136*(1), 12–23.

Lazar, L., Rodino, S., Pop, R., Tiller, R., D'Haese, N., Viaene, P., & De Kok, J.-L. (2022). Sustainable Development Scenarios in the Danube Delta—A Pilot Methodology for Decision Makers. *Water*, *14*(21), 3484.

Le, H.-A., Gratiot, N., Santini, W., Ribolzi, O., Tran, D., Meriaux, X., Deleersnijder, E., & Soares-Frazão, S. (2020). Suspended sediment properties in the Lower Mekong River, from fluvial to estuarine environments. *Estuarine, Coastal and Shelf Science*, *233*, 106522.

Le, H.-A., Lambrechts, J., Ortleb, S., Gratiot, N., Deleersnijder, E., & Soares-Frazão, S. (2020). An implicit wetting–drying algorithm for the discontinuous Galerkin method: Application to the Tonle Sap, Mekong River Basin. *Environmental Fluid Mechanics*, *20*(4), 923–951.

Le, H.-A., Nguyen, T., Gratiot, N., Deleersnijder, E., & Soares-Frazão, S. (2023). The Multi-Channel System of the Vietnamese Mekong Delta: Impacts on the Flow Dynamics under Relative Sea-Level Rise Scenarios. *Water*, *15*(20), 3597.

Le Bars, Y., Vallaeys, V., Deleersnijder, É., Hanert, E., Carrere, L., & Channelière, C. (2016). Unstructured-mesh modeling of the Congo river-to-sea continuum. *Ocean Dynamics*, *66*(4), 589–603.

Lecart, M., Dobbelaere, T., Alaerts, L., Randresihaja, N. R., Mohammed, A. V., Vethamony, P., & Hanert, E. (2024). Land reclamation and its consequences: A 40-year analysis of water residence time in Doha Bay, Qatar. *PLOS ONE*, *19*(1), e0296715.

Legleiter, C. J., & Kyriakidis, P. C. (2008). Spatial prediction of river channel topography by kriging. *Earth Surface Processes and Landforms*, *33*(6), 841–867.

Lewis, H. W., Siddorn, J., Castillo Sanchez, J. M., Petch, J., Edwards, J. M., & Smyth, T. (2019). Evaluating the impact of atmospheric forcing and air–sea coupling on near-coastal regional ocean prediction. *Ocean Science*, *15*(3), 761–778.

Liang, Y., Wang, B., Sheng, Y., & Liu, C. (2022). Two-Step Simulation of Underwater Terrain in River Channel. *Water*, *14*, 3041.

Lima, L., Aydogdu, A., Escudier, R., Masina, S., Cilibert, S., Azevedo, D., Peneva, E., Causio, S., Cipollone, A., Clementi, E., Cretí, S., Stefanizzi, L., Lecci, R., Palermo, F., Coppini, G., Pinardi, N., & Palazov, A. (2020). Black Sea Physical Reanalysis (CMEMS BS-Currents) (Version 1) [Available at https://doi.org/10.25423/CMCC/BLKSEA_MULTIYEAR_PHY_007_004].

Lima, L., Ciliberti, S. A., Aydoğdu, A., Masina, S., Escudier, R., Cipollone, A., Azevedo, D., Causio, S., Peneva, E., Lecci, R., Clementi, E., Jansen, E., Ilicak, M., Cretì, S., Stefanizzi, L., Palermo, F., & Coppini, G. (2021). Climate Signals in the Black Sea From a Multidecadal Eddy-Resolving Reanalysis. *Frontiers in Marine Science*, *8*.

Liptay, Z., & Gauzer, B. (2021). A tailor-made 1D hydrodynamic modelling solution for flood forecasting on the Danube catchment. *FLOODrisk 2020 - 4th European Conference on Flood Risk Management*.

Liu, J. C., Hu, Z. Q., & Zhu, M. Y. (2021). Comparison and analysis of calculation of Bridge backwater based on Mike21 hydrodynamic model. *E3S Web of Conferences*, *233*, 03043.

Loucks, D. P. (2019). Developed river deltas: Are they sustainable? *Environmental Research Letters*, *14*(11), 113004.

Lupu, G., Doroftei, M., Covaliov, S., Mierlă, M., Năstase, A., Cenişencu, I., Doroşencu, A., Bolboacă, L., Marinov, M., Alexe, V., Balaican, D., Ene, L., Bota, D., & Năvodaru, I. (2022). Status of biodiversity, habitats, sustainable exploitation of natural resources and socio-economic implications in Danube Delta Biosphere Reserve in 2020. *Scientific Annals of the Danube Delta Institute*, *27*, 77–98.

Ma, R., Han, H., & Zhang, Z. (2025). An Integrated Hydrological–Hydrodynamic Model Based on GPU Acceleration for Catchment-Scale Rainfall Flood Simulation. *Atmosphere*, *16*(7), 809.

Macé, L., Vandenbulcke, L., Brankart, J.-M., Brasseur, P., & Grégoire, M. (2025). Characterisation of uncertainties in an ocean radiative transfer model for the Black Sea through ensemble simulations. *Biogeosciences*, *22*(15), 3747–3768.

Mănoiu, V.-M., & Crăciun, A.-I. (2021). Danube river water quality trends: A qualitative review based on the open access web of science database. *Ecohydrology & Hydrobiology*, *21*(4), 613–628.

Marta-Almeida, M., Hetland, R. D., & Zhang, X. (2013). Evaluation of model nesting performance on the Texas-Louisiana continental shelf. *Journal of Geophysical Research: Oceans*, *118*, 2476–2491.

McCabe, C. L. (2024). *Biophysical connections in free-flowing floodplain river systems* [Doctoral dissertation, University of Otago].

Meadows, M., Jones, S., & Reinke, K. (2024). Vertical accuracy assessment of freely available global DEMs (FABDEM, Copernicus DEM, NASADEM, AW3D30 and SRTM) in flood-prone environments. *International Journal of Digital Earth*, *17*(1), 2308734.

Meadows, M., & Wilson, M. (2021). A Comparison of Machine Learning Approaches to Improve Free Topography Data for Flood Modelling. *Remote Sensing*, *13*(2), 275.

Medeiros, S. C., & Hagen, S. C. (2013). Review of wetting and drying algorithms for numerical tidal flow models. *International Journal for Numerical Methods in Fluids*, *71*(4), 473–487.

Meng, X., Currit, N., & Zhao, K. (2010). Ground Filtering Algorithms for Airborne LiDAR Data: A Review of Critical Issues. *Remote Sensing*, *2*(3), 833–860.

Merwade, V. M. (2009). Effect of spatial trends on interpolation of river bathymetry. *Journal of Hydrology*, *371*(1-4), 169–181.

Merwade, V. M., Cook, A., & Coonrod, J. (2008). GIS techniques for creating river terrain models for hydrodynamic modeling and flood inundation mapping. *Environmental Modelling & Software*, *23*(10), 1300–1311.

Merwade, V. M., Maidment, D. R., & Goff, J. A. (2006). Anisotropic considerations while interpolating river channel bathymetry. *Journal of Hydrology*, *331*(3), 731–741.

Merwade, V. M., Maidment, D. R., & Hodges, B. R. (2005). Geospatial Representation of River Channels. *Journal of Hydrologic Engineering*, *10*(3), 243–251.

Merz, B., Blöschl, G., Vorogushyn, S., Dottori, F., Aerts, J. C. J. H., Bates, P., Bertola, M., Kemter, M., Kreibich, H., Lall, U., & Macdonald, E. (2021). Causes, impacts and patterns of disastrous river floods. *Nature Reviews Earth & Environment*, *2*(9), 592–609.

Mierla, M., Romanescu, G., Nichersu, I., & Grigoras, I. (2015). Hydrological Risk Map for the Danube Delta—A Case Study of Floods Within the Fluvial Delta. *IEEE Journal of Selected Topics in Applied Earth Observations and Remote Sensing*, *8*(1), 98–104.

Miladinova, S., Stips, A., Macias Moy, D., & Garcia-Gorriz, E. (2020). Pathways and mixing of the north western river waters in the Black Sea. *Estuarine, Coastal and Shelf Science*, *236*, 106630.

Navodaru, I., Buijse, A. D., & Staras, M. (2002). Effects of Hydrology and Water Quality on the Fish Communityin Danube Delta Lakes. *International Review of Hydrobiology*, *87*(2-3), 329–348.

Nelson, J. M., Bennett, J. P., & Wiele, S. M. (2003, June). Flow and Sediment-Transport Modeling. In G. M. Kondolf & H. Piégay

(Eds.), *Tools in Fluvial Geomorphology* (1st ed., pp. 539–576). Wiley.

Nichersu, I., Livanov, O., Mierlă, M., Trifanov, C., Simionov, M., Lupu, G., Ibram, O., Burada, A., Despina, C., Covaliov, S., Doroftei, M., Doroşencu, A., Bolboacă, L., Năstase, A., Ene, L., & Balaican, D. (2025, January). Chapter 6 - The Danube Delta – The link between the Danube River and the Black Sea. In J. Bloesch, B. Cyffka, T. Hein, C. Sandu, & N. Sommerwerk (Eds.), *The Danube River and The Western Black Sea Coast* (pp. 107–122). Elsevier.

Niculescu, S., Lardeux, C., & Hanganu, J. (2017, July). Alteration and Remediation of Coastal Wetland Ecosystems in the Danube Delta. A Remote-Sensing Approach. In *Coastal Wetlands: Alteration and Remediation* (pp. 513–553).

Niculescu, S., Lardeux, C., Hanganu, J., Mercier, G., & David, L. (2015). Change detection in floodable areas of the Danube delta using radar images. *Natural Hazards*, *78*(3), 1899–1916.

NOAA National Centers for Environmental Information. (2022). ETOPO 2022 15 Arc-Second Global Relief Model [Available at https://doi.org/10.25921/fd45-gt74].

Nudds, S., Lu, Y., Higginson, S., Haigh, S. P., Paquin, J.-P., O'Flaherty-Sproul, M., Taylor, S., Blanken, H., Marcotte, G., Smith, G. C., Bernier, N. B., MacAulay, P., Wu, Y., Zhai, L., Hu, X., Chanut, J., Dunphy, M., Dupont, F., Greenberg, D., . . . Page, F. (2020). Evaluation of Structured and Unstructured Models for Application in Operational Ocean Forecasting in Nearshore Waters. *Journal of Marine Science and Engineering*, *8*(7), 484.

Nuhjhat, M., Mahalder, B., & Khan, S. M. (2023). Application of Delft3D FM Suite for Simulating the Hydrodynamic Characteristics of Karnafuli River. *Proceedings of International Conference on Planning, Architecture and Civil Engineering, 12 - 14 October 2023*.

Oguz, T., & Besiktepe, S. (1999). Observations on the Rim Current structure, CIW formation and transport in the western Black Sea. *Deep Sea Research Part I: Oceanographic Research Papers*, *46*(10), 1733–1753.

Oubennaceur, K., Chokmani, K., Nastev, M., Gauthier, Y., Poulin, J., Tanguy, M., Raymond, S., & Lhissou, R. (2019). New Sensitivity

Indices of a 2D Flood Inundation Model Using Gauss Quadrature Sampling. *Geosciences*, *9*(5), 220.

Pang, T., Wang, X., Nawaz, R. A., Keefe, G., & Adekanmbi, T. (2023). Coastal erosion and climate change: A review on coastal-change process and modeling. *Ambio*, *52*(12), 2034–2052.

Panin, N., & Jipa, D. (2002). Danube River Sediment Input and its Interaction with the North-western Black Sea. *Estuarine, Coastal and Shelf Science*, *54*(3), 551–562.

Panin, N. (2011). The Danube Delta - The mid term of the geo-system Danube River-Danube Delta-Black Sea. *Romanian Journal of Geology*, *55*, 41–82.

Panin, N., Tiron Duţu, L., & Duţu, F. (2016). The Danube Delta an Overview of its Holocene Evolution. *Méditerranée*, (126), 37–54.

Parsapour-moghaddam, P., Rennie, C. D., & Slaney, J. (2018). Hydrodynamic Simulation of an Irregularly Meandering Gravel-Bed River: Comparison of MIKE 21 FM and Delft3D Flow models. *E3S Web of Conferences*, *40*, 02004.

Pasquaré Mariotto, F., Antoniou, V., Drymoni, K., Bonali, F. L., Nomikou, P., Fallati, L., Karatzaferis, O., & Vlasopoulos, O. (2021). Virtual Geosite Communication through a WebGIS Platform: A Case Study from Santorini Island (Greece). *Applied Sciences*, *11*(12), 5466.

Patil, A. R. (2025). *Modeling the impact of potential radioactive releases into the Meuse and Scheldt aquatic systems.* [Doctoral dissertation, UCLouvain].

Patil, A. R., Perez, F. F., Lambrechts, J., Draoui, I., Deleersnijder, E., & Dewals, B. (2025). Numerical modelling of navigable waterways using a discontinuous Galerkin method: Study of Meuse River – Campine canal flow. *International Journal of River Basin Management*.

Pekárová, P., Bajtek, Z., Pekár, J., Výleta, R., Bonacci, O., Miklánek, P., Belz, J. U., & Gorbachova, L. (2023). Monthly stream temperatures along the Danube River: Statistical analysis and predictive modelling with incremental climate change scenarios. *Journal of Hydrology and Hydromechanics*, *71*(4), 382–398.

Pelckmans, I., Belliard, J.-P., Dominguez-Granda, L. E., Slobbe, C., Temmerman, S., & Gourgue, O. (2023). Mangrove ecosystem prop-

erties regulate high water levels in a river delta. *Natural Hazards and Earth System Sciences*, *23*(9), 3169–3183.

Pelckmans, I., Gourgue, O., Belliard, J.-P., Dominguez-Granda, L. E., Slobbe, C., & Temmerman, S. (2021). Hydrodynamic modelling of the tide propagation in a tropical delta: Overcoming the challenges of data scarcity [October 2021]. In W. A. Breugem, L. Frederickx, T. Koutrouveli, K. Chu, R. Kulkarni, & B. Decrop (Eds.), *2020 TELEMAC-MASCARET User Conference October 2021* (pp. 34–39). International Marine; Dredging Consultants (IMDC).

Pilotti, M., Milanesi, L., Bacchi, V., Tomirotti, M., & Maranzoni, A. (2020). Dam-Break Wave Propagation in Alpine Valley with HEC-RAS 2D: Experimental Cancano Test Case. *Journal of Hydraulic Engineering*, *146*(6), 05020003.

Pinay, G. (1992). Chapter 5: Trophic status of the Danube Delta: A water quality assessment. In *Conservation Status of the Danube Delta*. IUCN East European.

Ping, Y., Xu, H., Song, L., Chen, J., Zhang, Z., & Hu, Y. (2025). Research on Acceleration Methods for Hydrodynamic Models Integrating a Dynamic Grid System, Local Time Stepping, and GPU Parallel Computing. *Water*, *17*(18), 2662.

Poncos, V., Teleaga, D., Bondar, C., & Oaie, G. (2013). A new insight on the water level dynamics of the Danube Delta using a high spatial density of SAR measurements. *Journal of Hydrology*, *482*, 79–91.

Popescu, I., Cioaca, E., Pan, Q., Jonoski, A., & Hanganu, J. (2015). Use of hydrodynamic models for the management of the Danube Delta wetlands: The case study of Sontea-Fortuna ecosystem. *Environmental Science & Policy*, *46*, 48–56.

Potisomporn, P., Adcock, T. A. A., & Vogel, C. R. (2023). Evaluating ERA5 reanalysis predictions of low wind speed events around the UK. *Energy Reports*, *10*, 4781–4790.

Probst, E., & Mauser, W. (2023). Climate Change Impacts on Water Resources in the Danube River Basin: A Hydrological Modelling Study Using EURO-CORDEX Climate Scenarios. *Water*, *15*(1), 8.

Qin, H., Shi, H., Gai, Y., Qiao, S., & Li, Q. (2023). Sensitivity Analysis of Runoff and Wind with Respect to Yellow River Estuary Salinity Plume Based on FVCOM. *Water*, *15*(7), 1378.

Quattrocchi, G., De Mey, P., Ayoub, N., Vervatis, V. D., Testut, C. E., Reffray, G., Chanut, J., & Drillet, Y. (2014). Characterisation of errors of a regional model of the Bay of Biscay in response to wind uncertainties: A first step toward a data assimilation system suitable for coastal sea domains. *Journal of Operational Oceanography*, *7*(2), 25–34.

Rahman, M. K., Crawford, T. W., & Islam, M. S. (2022). Shoreline Change Analysis along Rivers and Deltas: A Systematic Review and Bibliometric Analysis of the Shoreline Study Literature from 2000 to 2021. *Geosciences*, *12*(11), 410.

Randresihaja, N. R., Gourgue, O., Alaerts, L., Fettweis, X., Lambrechts, J., De Le Court, M., Grégoire, M., & Hanert, E. (2025, June). How Atmospheric Forcing Resolution Impacts Storm Surge Model Results: Insights from Xaver Storm in the North Sea-Scheldt Estuary Continuum.

Rivera, A. R., & Heredia, M. W. (2023). Application of Delft3D computational model to estimate the influence of El Bala run-of-the-river dam on the morphological activity of Beni River, Bolivia. *IOP Conference Series: Earth and Environmental Science*, *1136*(1), 012030.

Romanescu, G. (2013). Alluvial transport processes and the impact of Anthropogenic intervention on the Romanian littoral of the Danube Delta. *Ocean & Coastal Management*, *73*, 31–43.

Rose, K. A., Justic, D., Fennel, K., & Hetland, R. D. (2017). Numerical Modeling of Hypoxia and Its Effects: Synthesis and Going Forward. In D. Justic, K. A. Rose, R. D. Hetland, & K. Fennel (Eds.), *Modeling Coastal Hypoxia: Numerical Simulations of Patterns, Controls and Effects of Dissolved Oxygen Dynamics* (pp. 401–421). Springer International Publishing.

Roşu, A., Arseni, M., Roşu, B., Petrea, Ş.-M., Iticescu, C., & Georgescu, P. L. (2022). Study of the influence of manning parameter variation for waterflow simulation in Danube Delta, Romania. *Scientific Papers. Series E. Land Reclamation, Earth Observation & Surveying, Environmental Engineering*, *11*, 374 to 381.

Rusu, E. (2018). An analysis of the storm dynamics in the Black Sea. *The Romanian Journal of Technical Sciences. Applied Mechanics.*, *63*(2), 127–142.

Sadighrad, E., Fach, B. A., Arkin, S. S., Salihoğlu, B., & Hüsrevoğlu, Y. S. (2021). Mesoscale eddies in the Black Sea: Characteristics and kinematic properties in a high-resolution ocean model. *Journal of Marine Systems*, *223*, 103613.

Safranov, T., Chugai, A., & Stepova, O. (2024). Impact of military activities and hostilities on the ecoystem services of the North-Weastern Black Sea coastal zone. *Ukrainian hydrometeorological journal*, 81–87.

Saint-Amand, A., Grech, A., Choukroun, S., & Hanert, E. (2022). Quantifying the environmental impact of a major coal mine project on the adjacent Great Barrier Reef ecosystems. *Marine Pollution Bulletin*, *179*, 113656.

Saint-Amand, A., Lambrechts, J., Thomas, C. J., & Hanert, E. (2023). How fine is fine enough? Effect of mesh resolution on hydrodynamic simulations in coral reef environments. *Ocean Modelling*, *186*.

Samir, F. (2024). Evaluate the numerical models' performance in the Nile River. *ISH Journal of Hydraulic Engineering*, *30*(5), 696–704.

Sampurno, J., Ardianto, R., & Hanert, E. (2022). Integrated machine learning and GIS-based bathtub models to assess the future flood risk in the Kapuas River Delta, Indonesia. *Journal of Hydroinformatics*, *25*(1), 113–125.

Sampurno, J., Vallaeys, V., Ardianto, R., & Hanert, E. (2022). Modeling interactions between tides, storm surges, and river discharges in the Kapuas River delta. *Biogeosciences*, *19*(10), 2741–2757.

Sandu, C., Wolter, C., Pöppl, R., Hein, T., Sommerwerk, N., Cyffka, B., & Bloesch, J. (2025, January). Chapter 3 - The sediments of the Danube River. In J. Bloesch, B. Cyffka, T. Hein, C. Sandu, & N. Sommerwerk (Eds.), *The Danube River and The Western Black Sea Coast* (pp. 41–53). Elsevier.

Savu, E.-A., & Drobot, R. (2021). 2D Hydrodynamic model development for a critical sector of the Danube River. *Modelling in civil and environmental engineering*, *16*(1), 12–24.

Scherpereel, C., Alosairi, Y., Lambrechts, J., & Hanert, E. (2025). Hydrodynamic impacts of bridge construction and land reclamation on water residence time and flushing processes in Kuwait Bay. *Marine Pollution Bulletin*, *214*, 117716.

Schiller, H., Miklós, D., & Sass, J. (2010). The Danube River and its Basin Physical Characteristics, Water Regime and Water Balance. In M. Brilly (Ed.), *Hydrological Processes of the Danube River Basin: Perspectives from the Danubian Countries* (pp. 25–77). Springer Netherlands.

Schwanenberg, D., & Harms, M. (2004). Discontinuous Galerkin Finite-Element Method for Transcritical Two-Dimensional Shallow Water Flows. *Journal of Hydraulic Engineering*, *130*(5), 412–421.

Scown, M. W., Dunn, F. E., Dekker, S. C., van Vuuren, D. P., Karabil, S., Sutanudjaja, E. H., Santos, M. J., Minderhoud, P. S. J., Garmestani, A. S., & Middelkoop, H. (2023). Global change scenarios in coastal river deltas and their sustainable development implications. *Global Environmental Change*, *82*, 102736.

Shankman, D., & Pugh, T. B. (1992). Discharge response to channelization of a coastal plain stream. *Wetlands*, *12*(3), 157–162.

Shewchuk, J. R. (2002). What is a Good Linear Element? Interpolation, Conditioning, and Quality Measures. *Proceedings of the 11th International Meshing Roundtable*.

Simon, T., & Andrei, M.-T. (2023). The Danube Delta and its tourism development between 1989 and 2022. *6th International Hybrid Conference Water Resources and Wetlands*.

Smagorinsky, J. (1963). General circulation experiments with the primitive equations: I. the basic experiment. *Monthly Weather Review*, *91*(3), 99–164.

Smith, S. D., & Banke, E. G. (1975). Variation of the sea surface drag coefficient with wind speed. *Quarterly Journal of the Royal Meteorological Society*, *101*(429), 665–673.

Soetaert, K., & Herman, P. M. (Eds.). (2009). *A Practical Guide to Ecological Modelling*. Springer Netherlands.

Sommerwerk, N., Bloesch, J., Baumgartner, C., Bittl, T., Čerba, D., Csányi, B., Davideanu, G., Dokulil, M., Frank, G., Grecu, I., Hein, T., Kováč, V., Nichersu, I., Mikuska, T., Pall, K., Paunović, M., Postolache, C., Raković, M., Sandu, C., … Ungureanu, L. (2022, January). Chapter 3 - The Danube River Basin. In K.

Tockner, C. Zarfl, & C. T. Robinson (Eds.), *Rivers of Europe (Second Edition)* (pp. 81–180). Elsevier.

Stanev, E. V., Staneva, J. V., & Roussenov, V. M. (1997). On the Black Sea water mass formation. Model sensitivity study to atmospheric forcing and parameterizations of physical processes. *Journal of Marine Systems*, *13*(1), 245–272.

Stolz, R., Mauser, W., & Probst, E. (2025, January). Chapter 10 - Climate change—Specific consequences for the Danube River Basin and the Black Sea Coast. In J. Bloesch, B. Cyffka, T. Hein, C. Sandu, & N. Sommerwerk (Eds.), *The Danube River and The Western Black Sea Coast* (pp. 195–222). Elsevier.

Suchara, I. (2019). The Impact of Floods on the Structure and Functional Processes of Floodplain Ecosystems. *Journal of Soil and Plant Biology*, *1*, 44–60.

Suciu, R., Constantinescu, A., & David, C. (2002). The Danube delta: Filter or bypass for the nutrient input into the Black Sea? *Large Rivers*, 165–173.

Sultanov, E. (2019). The Glossy Ibis Plegadis falcinellus in Azerbaijan. *SIS Conservation*, *1*(Special Issue: Glossy Inis ecology & conservation), 10–15.

Surface Water Ocean Topography (SWOT). (2024). Swot level 2 water mask pixel cloud data product, version c [Dataset accessed 2025-11-05].

Surkova, G., Arkhipkin, V., & Kislov, A. (2013). Atmospheric circulation and storm events in the Black Sea and Caspian Sea. *Open Geosciences*, *5*(4), 548–559.

Syvitski, J. P. M., Kettner, A. J., Overeem, I., Hutton, E. W. H., Hannon, M. T., Brakenridge, G. R., Day, J., Vörösmarty, C., Saito, Y., Giosan, L., & Nicholls, R. J. (2009). Sinking deltas due to human activities. *Nature Geoscience*, *2*(10), 681–686.

Talbot, C. J., Bennett, E. M., Cassell, K., Hanes, D. M., Minor, E. C., Paerl, H., Raymond, P. A., Vargas, R., Vidon, P. G., Wollheim, W., & Xenopoulos, M. A. (2018). The impact of flooding on aquatic ecosystem services. *Biogeochemistry*, *141*(3), 439–461.

Tănăsescu, M., & Constantinescu, S. (2020). The human ecology of the Danube Delta: A historical and cartographic perspective. *Journal of Environmental Management*, *262*, 110324.

Tătui, F., Pîrvan, M., Popa, M., Aydogan, B., Ayat, B., Görmüș, T., Korzinin, D., Văidianu, N., Vespremeanu-Stroe, A., Zăinescu, F., Kuznetsov, S., Luminița Preoteasa, Shtremel, M., & Saprykina, Y. (2019). The Black Sea coastline erosion: Index-based sensitivity assessment and management-related issues. *Ocean & Coastal Management*, *182*, 104949.

Timbadiya, P. V., & Krishnamraju, K. M. (2023). A 2D hydrodynamic model for river flood prediction in a coastal floodplain. *Natural Hazards*, *115*(2), 1143–1165.

Tiron Duţu, L., Provansal, M., Le Coz, J., & Duţu, F. (2014). Contrasted sediment processes and morphological adjustments in three successive cutoff meanders of the Danube delta. *Geomorphology*, *204*, 154–164.

Toderascu, R., & Rusu, E. (2013). Evaluation of the Circulation Patterns in the Black Sea Using Remotely Sensed and *in Situ* Measurements. *International Journal of Geosciences*, *4*(7).

Tolmazin, D. (1985). Changing Coastal oceanography of the Black Sea. I: Northwestern Shelf. *Progress in Oceanography*, *15*(4), 217–276.

Tudor, G., Deák, G., Arsene, M., Danalache, T. M., Petculescu, B., Tuca, D. M., Bratfanof, E., & Zainol, M. R. R. M. A. (2022). Hydrodynamic Modelling for the Chilia—Bystroe Danube Sector: Model Calibration and Validation. In N. Mohamed Noor, S. T. Sam, & A. Abdul Kadir (Eds.), *Proceedings of the 3rd International Conference on Green Environmental Engineering and Technology* (pp. 147–153, Vol. 214). Springer Nature.

Tuğrul, S., Murray, J. W., Friederich, G. E., & Salihoğlu, İ. (2014). Spatial and temporal variability in the chemical properties of the oxic and suboxic layers of the Black Sea. *Journal of Marine Systems*, *135*, 29–43.

Ungureanu, V. G., & Stanica, A. (2000). Impact of human activities on the evolution of the Romanian Black Sea beaches. *Lakes & Reservoirs: Science, Policy and Management for Sustainable Use*, *5*(2), 111–115.

Vallaeys, V. (2018). *Discontinuous Galerkin finite element modelling of estuarine and plume dynamics* [Doctoral dissertation, UCL - Université Catholique de Louvain].

Vallaeys, V., Kärnä, T., Delandmeter, P., Lambrechts, J., Baptista, A. M., Deleersnijder, E., & Hanert, E. (2018). Discontinuous Galerkin modeling of the Columbia River's coupled estuary-plume dynamics. *Ocean Modelling*, *124*, 111–124.

Vallaeys, V., Lambrechts, J., Delandmeter, P., Pätsch, J., Spitzy, A., Hanert, E., & Deleersnijder, E. (2021). Understanding the circulation in the deep, micro-tidal and strongly stratified Congo River estuary. *Ocean Modelling*, *167*, 101890.

Vandenbulcke, L., & Barth, A. (2015). A stochastic operational forecasting system of the Black Sea: Technique and validation. *Ocean Modelling*, *93*, 7–21.

Vater, S., Beisiegel, N., & Behrens, J. (2019). A limiter-based well-balanced discontinuous Galerkin method for shallow-water flows with wetting and drying: Triangular grids. *International Journal for Numerical Methods in Fluids*, *91*(8), 395–418.

Vespremeanu-Stroe, A., Tătui, F., Constantinescu, Ș., & Zăinescu, F. (2017). Danube Delta Coastline Evolution (1856–2010). In M. Radoane & A. Vespremeanu-Stroe (Eds.), *Landform Dynamics and Evolution in Romania* (pp. 551–564). Springer International Publishing.

Vîjdea, A.-M., Alexe, V. E., Bălan, L.-L., Bogdevich, O., Čeru, T., Dević, N., Dobnikar, M., Dudás, K. M., Hajdarević, I., Halířová, J., Hikov, A., Humer, F., Ivanišević, D., Jankulár, M., Jordan, G., Koret, K., Marjanović, M., Marjanović, P., Mikl, L., … The SIMONA Project Team. (2022). Assessment of the quality of river sediments in baseline national monitoring stations of 12 countries in the Danube river basin. *Carpathian Journal of Earth and Environmental Sciences*, *17*(2), 425–440.

Vijith, H., Seling, L. W., & Dodge-Wan, D. (2015). Comparison and Suitability of SRTM and ASTER Digital Elevation Data for Terrain Analysis and Geomorphometric Parameters: Case Study of Sungai Patah Subwatershed (Baram River, Sarawak, Malaysia). *Environmental Research, Engineering and Management*, *71*(3), 23–35.

Voss, M., Baker, A., Bange, H. W., Conley, D., Cornell, S., Deutsch, B., Engel, A., Ganeshram, R., Garnier, J., Heiskanen, A.-S., Jickells, T., Lancelot, C., McQuatters-Gollop, A., Middelburg, J., Schiedek, D., Slomp, C. P., & Conley, D. P. (2011). Nitrogen

processes in coastal and marine ecosystems [© Cambridge University Press 2011, with sections © authors/European Union]. In M. A. Sutton, C. M. Howard, J. W. Erisman, G. Billen, A. Bleeker, P. Grennfelt, H. van Grinsven, & B. Grizzetti (Eds.), *The european nitrogen assessment* (pp. 148–176). Cambridge University Press.

Wang, J., Hou, J., Li, S., Sun, J., Jing, J., & Wang, J. (2024). Advancements in enhancing flood evolution and urban inundation predictions: A study of local time stepping algorithm and GPU-accelerated hydrodynamic model. *Journal of Hydrology*, *641*, 131744.

Wegscheider, B., Linnansaari, T., Ndong, M., Haralampides, K., St-Hilaire, A., Schneider, M., & Curry, R. A. (2024). Fish habitat modelling in large rivers: Combining expert opinion and hydrodynamic modelling to inform river management. *Journal of Ecohydraulics*, *9*(1), 68–86.

White, D. C., Morrison, R. R., & Nelson, P. A. (2025). Floodplain Vegetation Density Effects on Meandering Channel Flow Patterns and Channel-Floodplain Hydraulic Exchange. *Journal of Geophysical Research: Earth Surface*, *130*(7), e2024JF008038.

Wohl, E. (2021). An Integrative Conceptualization of Floodplain Storage. *Reviews of Geophysics*, *59*(2), e2020RG000724.

Wolters, M. L., & Kuenzer, C. (2015). Vulnerability assessments of coastal river deltas - categorization and review. *Journal of Coastal Conservation*, *19*(3), 345–368.

Wu, C.-Y., Mossa, J., Mao, L., & Almulla, M. (2019). Comparison of different spatial interpolation methods for historical hydrographic data of the lowermost Mississippi River. *Annals of GIS*, *25*(2), 133–151.

Xue, P., Ye, X., Pal, J. S., Chu, P. Y., Kayastha, M. B., & Huang, C. (2022). Climate projections over the Great Lakes Region: Using two-way coupling of a regional climate model with a 3-D lake model. *Geoscientific Model Development*, *15*(11), 4425–4446.

Yamazaki, D., Kanae, S., Kim, H., & Oki, T. (2011). A physically based description of floodplain inundation dynamics in a global river routing model. *Water Resources Research*, *47*(4).

Yan, C., Boota, M. W., Soomro, S.-e.-h., Xia, H., Qin, Y., Azeem, S. S., Dou, M., Yan, X., & Wang, L. (2024). Predicting possible bank erosion and bed incision in the Zhengzhou Reach of the Yellow River with hydrodynamic modeling. *Journal of Water and Climate Change*, *16*(1), 92–111.

Yunev, O. A., Vedernikov, V. I., Basturk, O., Yilmaz, A., Kideys, A. E., Moncheva, S., & Konovalov, S. K. (2002). Long-term variations of surface chlorophyll a and primary production in the open Black Sea. *Marine Ecology Progress Series*, *230*, 11–28.

Zăinescu, F. I., Tătui, F., Valchev, N. N., & Vespremeanu-Stroe, A. (2017). Storm climate on the Danube delta coast: Evidence of recent storminess change and links with large-scale teleconnection patterns. *Natural Hazards*, *87*(2), 599–621.

Zessner, M., Slobodnik, J., Gericke, A., van Gils, J., Alygizakis, N., Ng, K., Kovacs, A., Zoboli, O., & Venohr, M. (2025, January). Chapter 4 - Water quality of the Danube River and the Black Sea. In J. Bloesch, B. Cyffka, T. Hein, C. Sandu, & N. Sommerwerk (Eds.), *The Danube River and The Western Black Sea Coast* (pp. 55–81). Elsevier.

Zhang, X., Lu, Y., Wu, X., Wang, T., & He, S. (2023). Simulation study on the influence of the number of bridge piers on the flow regime of the lower Yellow River. *Arabian Journal of Geosciences*, *16*(2), 115.

Zhang, Y. J., Fernandez-Montblanc, T., Pringle, W., Yu, H.-C., Cui, L., & Moghimi, S. (2023). Global seamless tidal simulation using a 3D unstructured-grid model (SCHISM v5.10.0). *Geoscientific Model Development*, *16*(9), 2565–2581.

Zhang, Y., Yaak, W. B., Wang, N., Li, Z., Wu, X., Wang, Q., Wang, Y., & Yao, W. (2024). Evaluation of the highly sinuous bend sequences using an ecohydraulic model to ascertain the suitability of fish habitats for river ecological conservation. *Journal for Nature Conservation*, 126750.

Zigler, S. J., Newton, T. J., Steuer, J. J., Bartsch, M. R., & Sauer, J. S. (2008). Importance of physical and hydraulic characteristics to unionid mussels: A retrospective analysis in a reach of large river. *Hydrobiologia*, *598*(1), 343–360.